Addressing individual electronic spins with a microwave superconducting resonator

Zhiren Wang

To cite this version:

Zhiren Wang. Addressing individual electronic spins with a microwave superconducting resonator. Quantum Physics [quant-ph]. Université Paris-Saclay; Université de Sherbrooke (Québec, Canada), 2023. English. NNT : 2023UPASP048 . tel-04162672

HAL Id: tel-04162672
https://theses.hal.science/tel-04162672v1

Submitted on 16 Jul 2023

Addressing individual electronic spins with a microwave superconducting resonator

Adressage de spins électroniques individuels par un résonateur micro-onde supraconducteur

Thèse de doctorat de l'université Paris-Saclay et de l’université de Sherbrooke

École doctorale n◦ 564, physique en Ile-de-France (PIF)
Spécialité de doctorat : physique
Graduate School : physique, Référent : faculté des sciences d’Orsay

Thèse préparée dans l’unité de recherche **Service de Physique de l'État Condensé** (Université Paris-Saclay, CEA, CNRS) et **Institut Quantique** (Université de Sherbrooke), sous la direction de **Denis VION**, directeur de recherche, CEA Saclay, sous la direction de **Michel PIORO-LADRIÈRE**, professeur, Université de Sherbrooke, et sous le co-encadrement de **Patrice BERTET**, directeur de recherche, CEA Saclay

Thèse soutenue à Paris-Saclay, le 09 mai 2023, par

Zhiren WANG

Composition du Jury

Membres du jury avec voix délibérative

Marco APRILI Directeur de recherche, Université Paris-Saclay	Président
Gunnar JESCHKE Professeur, Eidgenössische Technische Hochschule Zurich	Rapporteur & Examinateur
Silvano DE FRANCESCHI Directeur de recherche, CEA Leti	Rapporteur & Examinateur
Audrey BIENFAIT Chargée de recherche, ENS Lyon	Examinatrice
Tim TAMINIAU Directeur de recherche, Technische Universiteit Delft	Examinateur
Patrick FOURNIER Professeur, Université de Sherbrooke	Examinateur

Thèse de doctorat

NNT : 2023UPASP048

Titre : Adressage de spins électroniques individuels par un résonateur micro-onde supraconducteur

Mots clés : circuit quantique, spin, boîte quantique, compteur de photon unique, résonance paramagnétique électronique

Résumé : Les spins uniques dans les solides sont de bons candidats pour la mise en œuvre de bits quantiques pour le traitement de l'information quantique grâce à leurs longs temps de cohérence. Cependant, en tant qu'objets quantiques individuels à l'échelle atomique, ils sont difficiles à traiter et à enchevêtrer les uns avec les autres. Ce travail de thèse explore deux approches distinctes mais liées pour manipuler et détecter des spins uniques ; toutes deux utilisent des circuits quantiques hybrides fonctionnant à des températures de l'ordre du millikelvin. Dans la première approche, la résonance paramagnétique électronique (RPE) de spins individuels est démontrée en détectant leur fluorescence : un compteur de photons micro-onde détecte le photon émis par un spin excité. Les spins utilisés sont des ions paramagnétiques d'erbium dans un cristal de scheelite, et sont couplés magnétiquement à un résonateur planaire supraconducteur de facteur de qualité élevé. Ils sont détectés individuellement avec un rapport signal/bruit de 1,9 en une seconde. Le signal de fluorescence présente de l'antibunching (dégroupement), prouvant ainsi qu'il provient d'émetteurs individuels. Des temps de cohérence allant jusqu'à 3 ms sont mesurés, limités par le temps de vie radiatif du spin. Cette expérience de contrôle quantique d'un spin unique ouvre également la voie à de nouvelles applications de RPE, notamment pour la caractérisation d'objets microscopiques. Dans la seconde approche, la détection des spins est basée sur l'exploitation du degré de liberté de charge des spins de trous et de leur forte interaction spin-orbite intrinsèque. Nous démontrons une nouvelle plateforme compacte composée de boîtes quantiques définis électrostatiquement dans le GaAs, et pré-remplis de spins de trous par illumination dans le domaine optique ; les spins sont couplés électriquement à un résonateur supraconducteur pour sonder leurs états de charge et de spin. En utilisant ce résonateur en régime de lecture dispersive, nous montrons que des sauts de charge unique dans les boîtes quantiques peuvent être détectées après l'illumination. Il s'agit d'une étape cruciale dans l'étude du spin d'un trou unique dans un semi-conducteur. Dans l'ensemble, les deux méthodes présentées dans cette thèse ouvrent de nouvelles voies pour le développement des capteurs quantiques et du traitement quantique de l'information.

Title : Addressing individual electronic spins with a microwave superconducting resonator

Keywords : quantum circuit, spin, quantum dot, single photon counter, electron spin resonance

Abstract: Single spins in solids are good candidates for implementing quantum bits for quantum information processing thanks to their long coherence times. However, being individual atomic-scale quantum objects, they are difficult to address and to entangle with one another. This thesis work explores two distinct but related approaches for manipulating and detecting single spins, both involving comparable hybrid circuit quantum electrodynamics platforms operated at millikelvin temperatures. In the first approach, single electron spin resonance (ESR) is demonstrated by spin fluorescence detection: a microwave photon counter is used to detect the photon emitted by an excited spin. The spins are paramagnetic erbium ions in a scheelite crystal and are coupled magnetically to a high-quality factor planar superconducting resonator. They are detected individually with a signal-to-noise ratio of 1.9 in a one second-integration time. The fluorescence signal shows anti-bunching, proving that it comes from individual emitters. Coherence times up to 3 ms are measured, limited by the engineered spin radiative lifetime. This single-spin quantum control experiment also opens the route to new applications of ESR, in particular for microscopic object characterization. In the second approach, the detection of spins is based on leveraging the charge degree of freedom of hole spins and their strong intrinsic spin-orbit interaction. We demonstrate a compact novel platform made of electrostatically defined quantum dots in AlGaAs/GaAs heterostructure, filled with hole spins by optical illumination. The spins are coupled electrically to a superconducting resonator for probing their charge and spin states. Using this resonator as a dispersive readout, we show that single charge tunneling events in the dots can be detected after illumination. This represents a critical step towards addressing single hole spin in a semiconductor. Overall, the two methods reported in this thesis open new avenues for the development of quantum sensing and quantum computing applications.

À ma famille

Acknowledgements

Going through this co-supervised long journey of thesis in Paris and Sherbrooke has been a challenge and a privilege that I will always cherish. It is a thesis full of enthusiasm, passion, beautiful moments of discoveries, as well as disappointment. I am deeply grateful for the support, guidance, and encouragement I received from so many people along the way.

To begin with, I would like to express my deepest gratitude to my two thesis directors for their invaluable guidance, support, and expertise throughout my thesis journey. Michel, thanks for leading me from electrical engineering into the realm of quantum physics at the beginning of my thesis. Your insights, knowledge, passion, and relentless encouragement enable us to turn our prototype idea into reality. Denis, thanks for always being available for all my scientific and technical questions. Your rigorous approach of doing research has been a great asset to me on this journey.

I owe a great sum of gratitude to a number of colleagues in both the Quantronics (SPEC - Service de Physique de l'Etat Condensé, France) and the group of Michel Pioro-Ladrière at l'Institut Quantique (Sherbrooke, Canada). I am immensely grateful to Patrice and Emmanuel, for your relentless care in the research as my co-directors. The dance of single spin would not be possible without both of you. Patrice, thank you for your scientific advice, fruitful discussions, and guidance throughout the research. Thanks Manu for sharing your physical insights and solving countless issues we encountered in the lab. Thanks Daniel for your scientific support, encouragement, and for spending your time correcting my thesis. Thanks Léo for all the work together and our daily discussions. The setup and experiments of SMPD that you built are critical to the project. Thanks Marianne for getting me in touch with erbium, for helping me understand it better, for the spin echo experiments we conducted together, which set a good start for me being in Quantro, and for the serendipitous and beautiful discovery of microwave atomic frequency comb that we made. Thanks Eric for helping me with the resonator design, simulation and your friendliness. Thanks Milos for building the setup to stablize the current of the magnet coil. Thanks Boris and Yutian for your kind support and availability of helping me with the experiments. Thanks to Pief, Sebastian and Pascal for their technical support. Thanks to other permanent members of Quantro: Cristian, Hélène, Hugues, Marcelo, Çağlar for having been available of discussion and support in the experiment. Thanks to all the new and old fellows in Quantro: Jaime, Louis, Joan, Manas, Emanuele, Alexander, Alexandre, Brian, with whom I had good scientific and casual moments. You are awesome to work with.

Beyond SPEC, I would like to express my gratitude to our collaborators who have contributed to this project. Firstly, Philippe Goldner, Diana Serrano, and Alban Ferrier from ChimieParisTech, who kindly provided the erbium sample. Also, I would like to thank Thierry Chanelière from l'Institut Néel and Sylvain Bertaina from IM2NP for their assistance in characterizing the crystal through CW and pulse EPR measurements.

Next, I would like to deliever my huge gratitude to the other side of the Atlantic. Thanks Dany for your support on the project of hybrid system and to Julien for teaching me how to fabricate quantum dot devices from scratch and answering my numerous questions. Thanks Pierre for our work together and your ongoing pursue on the quantum dot devices. I appreciate your dedication to advancing this project. A huge thanks goes to Ioanna and Marc-Antoine, my office mates and friends, thank you for being part of this great adventure with me in Canada and for your support during tough moments. Thanks also to Sophie and Sara for the helpful discussion on physics. Thanks to Michele, Stéphane for the technical support. Thanks to Alexandre Blais and his group members for helping me understand better circuit QED theory, especially Catherine and Camille. You are absolutely brilliant. To other members at IQ - Clément, Joffrey, Claude, Charles, Laurine - thanks for the scientific sessions and beer sessions from 5 to 8.

Last but not least, a special thanks to my dear friends and my family, for your unwavering support and for always being there to lend an ear or offer a word of encouragement. Your friendship has sustained me through the ups and downs of this process. This journey would have been harder without you. Thanks Elina, our “tea ceremony” is always a highlight and a wonderful break from the physics world. Thanks Aicha, listening to you playing piano is a true pleasure. Thanks Camille for sharing those wonderful moments in Québec and Bretagne with you. Thanks Dangning, Haishi, Xiaohan for the regular barbecue “meetings” and Chinese food journey in Paris. Thanks Jacinta for your encouragement from overseas during the process of writing. Thanks to Chef Zhu and Chef Chensi for feeding me with scrumptious food that kept me going. And to Mabelle, Ala, Gaël, Perinne, Di, Xiliang, Yakun, Yukun, Mayu, Heng, Manqi, Valeria, Nicolas - the time we spent together in Paris and Québec is something I'll always treasure. A special thanks goes to Ruojing, your support, encouragement, words of wisdom, cheering, and inspiration have been a constant source of strength. Finally, I must express my very profound gratitude to my family for providing me with unwavering support and continuous encouragement throughout my years of study and through the process of researching and writing this thesis.

Contents

List of Figures

List of Abbreviations

2DEG	2-dimensional electron gas
2DHG	2-dimensional hole gas
cQED	Circuit quantum electrodynamics
CPW	Coplanar waveguide
EDSR	Electric dipole spin resonance
ESD	Electrostatic discharge
ESR	Electron spin resonance
IPA	isopropanol
NMR	Nuclear spin resonance
QED	Quantum electrodynamics
PCB	Print circuit board
PDD	Periodic Dynamical Decoupling
PMT	Photomultiplier tubes
qubit	Quantum bit
SMPD	Single microwave photon detector
SNSPD	Superconducting nanowire single-photon detectors
SOI	Spin-orbit interaction

Useful physical constants

Constants in SI units [1] :

- vacuum electric permittivity, $\varepsilon_0 = 8.854 \times 10^{-12}$ F/m
- vacuum magnetic permeability, $\mu_0 = 4\pi \times 10^{-7}$ H/m
- Planck constant, $h = 6.63 \times 10^{-34}$ Js
- reduced Planck constant, $\hbar = h/2\pi = 1.05 \times 10^{-34}$ Js
- Bohr magneton, $\mu_B = 9.274 \times 10^{-24}$ J/T, $\mu_B/h = 13.996$ GHz/T
- Boltzmann constant, $k_B = 1.38 \times 10^{-23}$ J/K
- elementary charge, $e = 1.6 \times 10^{-19}$ C

---

[1] Values from NIST (https://physics.nist.gov/cuu/Constants/index.html)

Résumé étendu

Le développement des technologies quantiques vise à utiliser des objets quantiques dans des états superposés ou intriqués pour effectuer des mesures avec une précision améliorée (capteurs quantiques), pour simuler des systèmes quantiques à grand nombre de particules (simulateurs quantiques), ou pour traiter quantiquement de l'information (calcul quantique). Grâce à leurs longs temps de cohérence quantique, les spins uniques dans les solides sont de bons candidats pour l'implémentation de bits quantiques pour le calcul quantique. Cependant, en tant qu'objets quantiques individuels à l'échelle atomique, ils sont difficiles à adresser et à intriquer de façon contrôlée les uns aux autres. Leur intégration dans des dispositifs solides appropriés et plus macroscopiques, tels que les circuits supraconducteurs macroscopiques sont une solution. Ces systèmes hybrides, dits d'électrodynamique quantique sur circuits (cQED) [1, 2], devraient donc ouvrir de nouvelles perspectives pour le contrôle et la lecture de spins uniques.

Dans une plateforme cQED hybride, l'adressage de spins repose sur leur couplage au champ électromagnétique d'un circuit résonant. Deux schémas de couplage sont possibles : les spins étant des dipôles magnétiques intrinsèques, ils sont naturellement couplés à la composante magnétique oscillante du résonateur (schéma I) ; en revanche, ils ne se couplent pas directement à sa composante électrique. Toutefois, si les spins sont portés par des particules mobiles chargées électriquement (comme les électrons et les trous des semi-conducteurs par exemple), et si les spins sont sujets à une interaction spin-orbite intrinsèque dans leur cristal hôte, ils se couplent alors indirectement au champ électrique oscillant du résonateur (schéma II). En pratique, le schéma I correspond le plus souvent à un régime de couplage faible, tandis que le schéma II peut atteindre le régime de couplage fort.

Ce travail de thèse explore deux approches distinctes mais reliées, basées sur les deux schémas de couplage mentionnés, et visant à manipuler et à mesurer l'état quantique de spins individuels ; toutes deux utilisent des circuits quantiques hybrides fonctionnant à des températures de l'ordre de la dizaine de millikelvin. Dans la première approche, la résonance paramagnétique électronique (RPE) de spins individuels est démontrée en détectant leur fluorescence : un compteur de photons micro-ondes détecte le photon émis par un spin initialement excité et relaxant spontanément vers son état fondamental. Les spins utilisés sont des ions paramagnétiques d'erbium dans un cristal de scheelite ($CaWO_4$), et sont couplés magnétiquement à un résonateur planaire supraconducteur de facteur de qualité élevé. Dans la deuxième approche, les spins sont des trous à l'interface d'une hétérostructure GaAs/AlGaAs non dopée, confinés dans des boîtes quantiques définies par des électrodes de grille, où leur degré de liberté de charge et leur forte interaction spin-orbite intrinsèque sont exploités. Nous démontrons une nouvelle plateforme compacte sans contact à des réservoirs de charges, dans laquelle les boîtes quantiques sont pré-remplies en trous générés par illumination dans le domaine optique ; les spins sont ici couplés électriquement à un résonateur supraconducteur pour manipuler et sonder leurs états de charge et de spin. Après illumination, en balayant les tensions de grille et en utilisant le résonateur en régime de lecture dispersive, nous observons des sauts de charge uniques dans ces boîtes quantiques. Ce résultat est un pas important vers l'étude du spin d'un trou unique dans un semi-conducteur.

Partie I : contrôle et mesure du spin électronique de dopants individuels d'un cristal

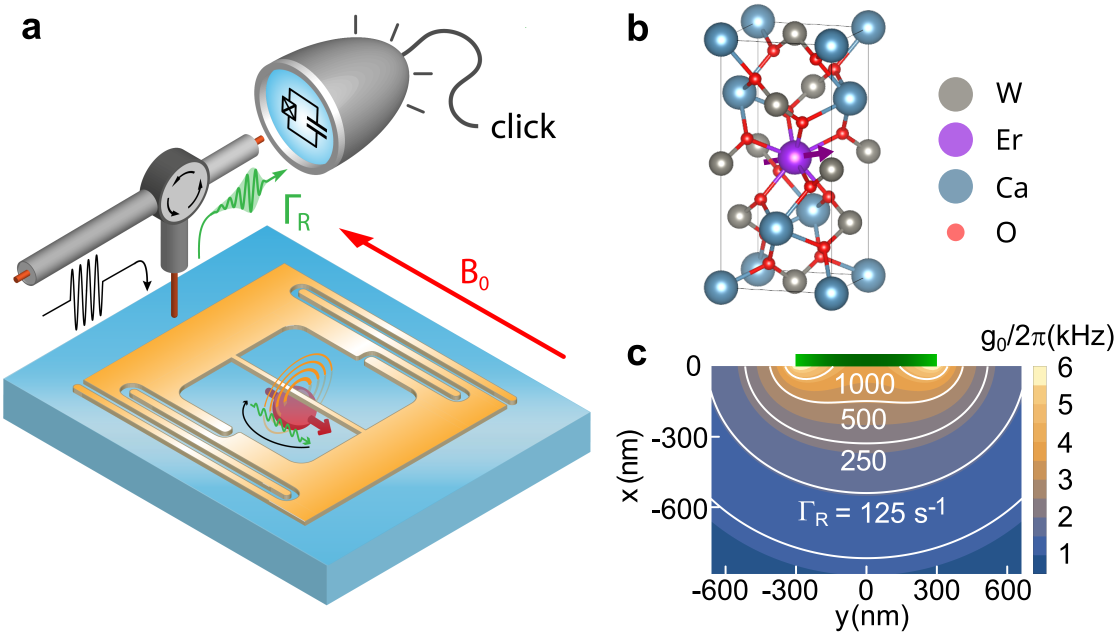

Figure 1: **Plateforme expérimentale de la première expérience de cette thèse**. **(a)** Principe de l'expérience : Un cristal (bleu ciel) contenant des spins électroniques Er^{3+} (un seul spin représenté en rouge) couplés au champ magnétique (cercles oranges) de l'inductance L d'un résonateur LC supraconducteur de fort facteur de qualité (orange) est refroidi à 10 mK. Des impulsions d'excitation (noire, à gauche) sont envoyées au système à la fréquence du résonateur, via une antenne (marron). Lorsqu'un spin est excité, il renvoie avec un taux Γ_R un unique photon micro-onde (vert, à droite) routé par un circulateur vers un compteur de photons (gris et bleu) qui le détecte. La fréquence d'un spin est accordée à la résonance de résonateur par application d'un champ magnétique B_0 parallèle au plan du résonateur. **(b)** Structure cristalline de Er^{3+} : $CaWO_4$. L'ion central Ca^{2+} de la maille tétragonale du cristal est remplacé à hauteur de 3 ppb par un ion Er^{3+}. **(c)** Carte de la constante de couplage $g_0(x, y)$ et du taux de relaxation radiative $\Gamma_R(x, y)$ calculés en fonction de la position du spin (x, y) par rapport au nanofil inductif (rectangle vert).

Le principe de l'expérience de la première partie est présenté dans la Figure 1a. Un spin d'ion erbium Er^{3+} remplaçant un ion calcium Ca^{2+} dans un cristal de $CaWO_4$ (voir Figure 1b) est couplé au champ magnétique oscillant généré par l'inductance d'un résonateur supraconducteur fabriqué au-dessus du cristal. Le

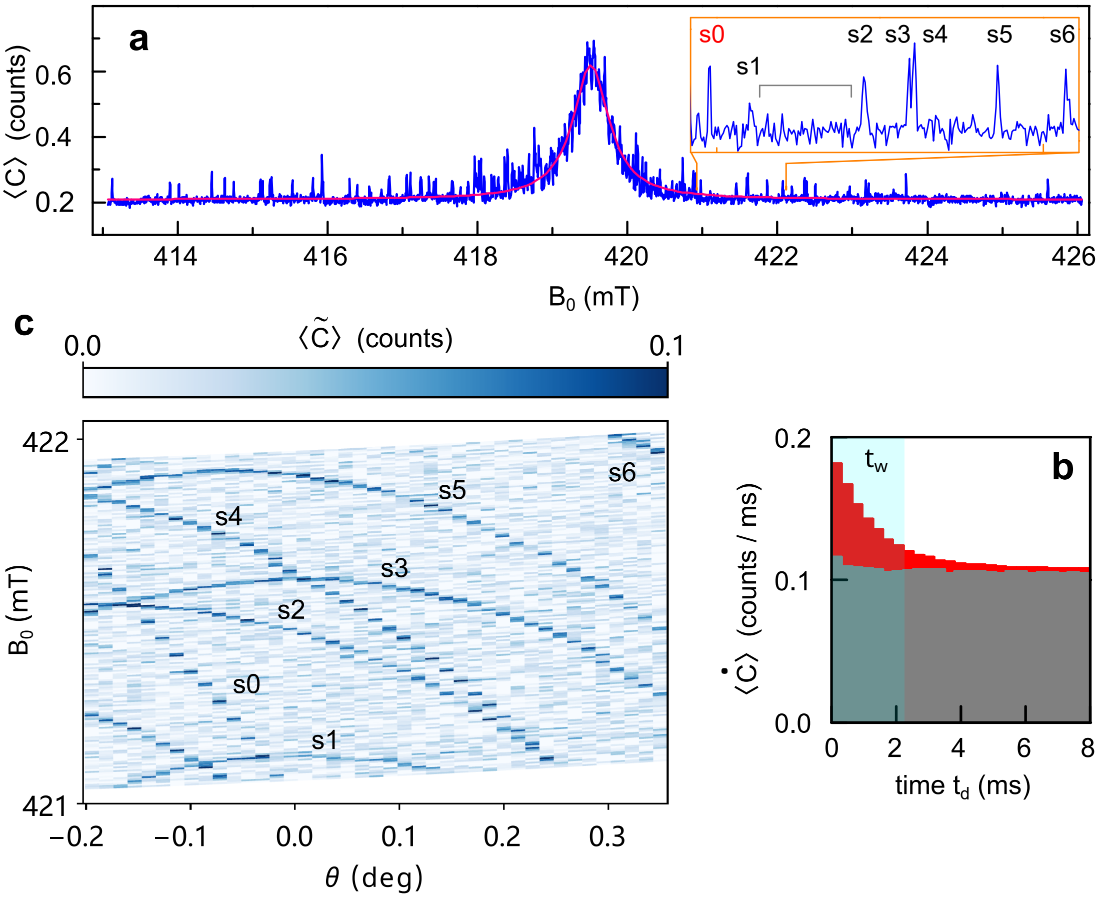

Figure 2: **Spectroscopie de spin à faible excitation** ($\sim -117\,$dBm à l'entrée de l'échantillon). **(a)** Nombre moyen de coups $\langle C \rangle$ (ligne bleue) détectés par le compteur à la suite d'une impulsion d'excitation, en fonction du champ B_0. Le pic large à 419.5 mT (ajusté par un pic lorentzien en rouge) est la résonance RPE de l'ensemble des ions erbium, tandis que les pics étroits proviennent d'ions Er^{3+} individuels. Encadré : vue élargie, montrant 7 pics (nommés de s0 à s6). **(b)** Histogrammes du taux moyen de coups enregistré sur le spin $s0$ (rouge), et sur le bruit de fond (gris) moyennés sur la fenêtre B_0 représentée par une barre grise horizontale dans l'encadré **a**. La fenêtre bleue est la fenêtre d'intégration pour tous les points de données en **a**. **(c)** Nombre moyen de coups excédant le bruit de fond $\langle \widetilde{C} \rangle$, à la suite d'une impulsion d'excitation, en fonction de l'amplitude du champ B_0 et de l'angle θ auquel il est appliqué par rapport à l'axe de symétrie de l'ensemble d'erbium. Les résonances de 7 spins (nommés de s0 à s6) sont visibles.

spin est excité par une impulsion micro-onde et revient à son état fondamental en émettant un photon micro-onde avec un taux d'émission Γ_R augmenté par effet Purcell [3]. Ce photon émis est détecté avec une efficacité globale $\eta \sim 0.42$ par un compteur de photons micro-ondes unique (SMPD : single microwave photon detector) basé sur un qubit supraconducteur pompé dans un schéma de mélange à 4 ondes [4, 5]. Le bas taux de comptage de faux positifs $\alpha \sim 100\ s^{-1}$ de ce SMPD permet de détecter un seul spin avec un rapport signal sur bruit SNR $\sim$ 1.9 en une seconde. La Figure 1c montre le taux de relaxation radiative Γ_R du spin et sa constante du couplage $g_0/2\pi$ au résonateur, calculés en fonction de la position du spin

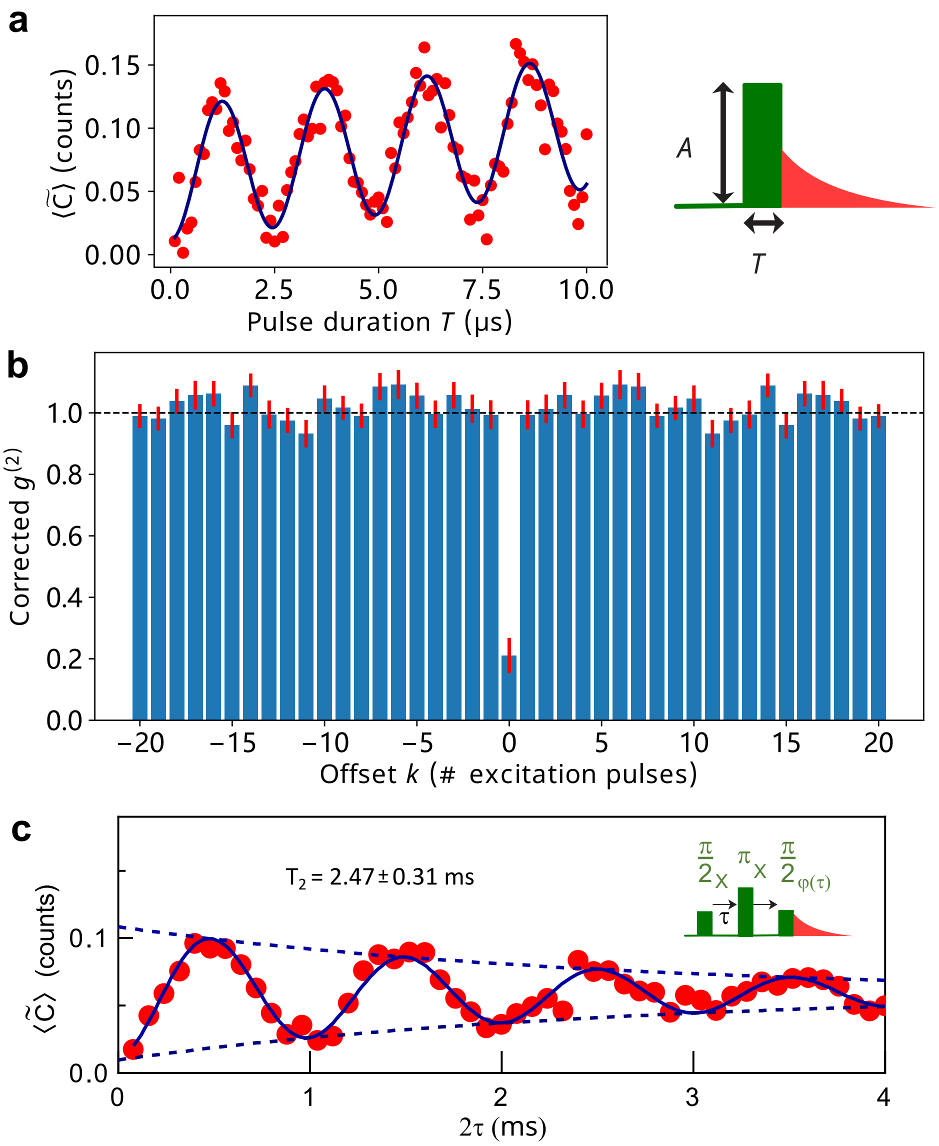

Figure 3: **Mesures temporelles sur spin unique.** **(a)** Nombre de coups $\langle\widetilde{C}\rangle$ (points rouges) mesuré en fonction de la durée T d'une impulsion excitatrice du spin s0, montrant une oscillation de Rabi. La courbe solide bleue est un ajustement sinusoïdal avec un fond croissant linéairement. **(b)** Fonction d'autocorrélation $g^{(2)}$ du spin s0 corrigée du bruit de fond du SMPD, en fonction du nombre k de séquences d'excitation séparant deux mesures. La mesure $g^{(2)}(0) = 0.2 \pm 0.1$ prouve que l'émission provient d'un unique spin. **(c)** Nombre de coups $\langle\widetilde{C}\rangle$ (points rouges) mesuré en fonction du délai 2τ de la séquence d'écho de spin montrée en médaillon ; la phase $\varphi(\tau) = 2\pi\Delta\tau$ de la dernière impulsion augmente linéairement avec $\Delta = 1\,\mathrm{kHz}$. L'ajustement correspondant (ligne solide) et son enveloppe (ligne pointillée) donnent un temps de cohérence $T_2 = 2.47 \pm 0.31\,\mathrm{ms}$ (spin s6).

au voisinage du nanofil inductif. Avec nos paramètres expérimentaux, le couplage atteint quelques kilohertz, conduisant à un taux $\Gamma_\mathrm{R} > 500\ s^{-1}$ pour les spins les plus fortement couplés, situés à moins de 200 nm du nanofil.

Pour mesurer le spectre RPE des spins de notre échantillon, nous enregistrons le nombre moyen de coups $\langle C\rangle$ détectés durant un temps t compris entre 2 et 200 millisecondes après une impulsion d'excitation, en fonction du champ magnétique B_0. À faible excitation et pour $t = 2$ ms, nous observons (voir Figure 2a) non seulement un pic large centré à 419.5 mT qui correspond à la résonance magnétique d'un ensemble d'ions Er^{3+} : CaWO_4 [6], mais aussi de nombreux pics étroits inégalement répartis dans le spectre, qui correspondent chacun à l'émission d'un ion individuel comme le montre la série de mesures suivante. Le taux de comptage $\langle \dot{C} \rangle$ après une impulsion d'excitation sur l'un de ces pics décroît exponentiellement en fonction du temps (voir Figure 2b), comme attendu pour la relaxation d'un unique spin. La position B_0 de chacun de ces pics est stable dans le temps, et dépend de l'angle θ auquel est appliqué B_0 (Figure 2c), comme attendu pour la résonance RPE fortement anisotrope des ions erbium.

Après avoir obtenu le spectre, nous sélectionnons le pic isolé $s0$ pour prouver qu'il provient d'un spin émetteur unique. Lorsque le champ est accordé sur ce pic, le nombre de coups $\langle \widetilde{C} \rangle$ détectés après soustraction du bruit d'obscurité dépend sinusoïdalement de la durée de l'impulsion appliquée (oscillation dite de Rabi - voir Figure 3a), comme attendu pour un spin unique. Le contraste des oscillations est en fait une mesure de l'efficacité totale de détection, $\eta = 0.12$. Nous mesurons ensuite les corrélations des taux de comptages à deux instants différents (Figure 3b). Plus précisément, la fonction $g^{(2)}(k)$ quantifie les coïncidences de coups (normalisé à 1 pour des événements non corrélés) entre deux instants séparées par k séquences d'excitations. Nous mesurons comme attendu $g^{(2)}(k) \sim 1$ lorsque $k \neq 0$; en revanche, la valeur $g^{(2)}(0) = 0.2 \pm 0.1$ montre qu'il est très peu probable d'obtenir 2 photons au cours de la même séquence, et prouve donc que les photons proviennent bien d'un unique émetteur, à savoir ici d'un unique spin de Er^{3+} : CaWO_4. Cet adressage de spins individuels ouvrant la voie à leur utilisation en tant que qubits, il est intéressant de caractériser leur cohérence quantique. Par une séquence d'écho de Hahn, nous mesurons un temps de cohérence T_2 de ces spins individuels de plusieurs millisecondes (voir Figure 3c), principalement limité par le temps de relaxation Purcell.

Dans notre expérience, des dizaines de spins individuels avec des temps de cohérence supérieurs à la milliseconde sont interfacés par le même résonateur microondes. Cela ouvre de nouvelles perspectives à la fois pour l'informatique quantique hybride, et pour une RPE opérationnelle sur des spins individuels : notre méthode est directement applicable à un grand nombre de systèmes spin-matrice et offre un volume de détection relativement grand (10 $\mu\mathrm{m}^3$) ; elle nous permet d'envisager la caractérisation de cellules ou de molécules individuelles.

Partie II : vers l'adressage du spin d'un trou unique dans des boîtes quantiques définies par des grilles électrostatiques et initialisées par illumination

La deuxième expérience vise à contôler et mesurer des spins de trous en exploitant leur degré de liberté de charge et leur forte interaction spin-orbite intrinsèque [7]. Ces trous sont confinés électrostatiquement dans des boîtes quantiques définies par des électrodes de grilles à la surface d'hétérostructure semiconductrices. L'adressage électrique des spins dans ces boîtes quantiques nécessite un contrôle précis et une lecture fiable de leurs états de charge et de spin. Une architecture cQED est particulièrement adaptée à ces deux fonctions, et permet une opération entièrement micro-

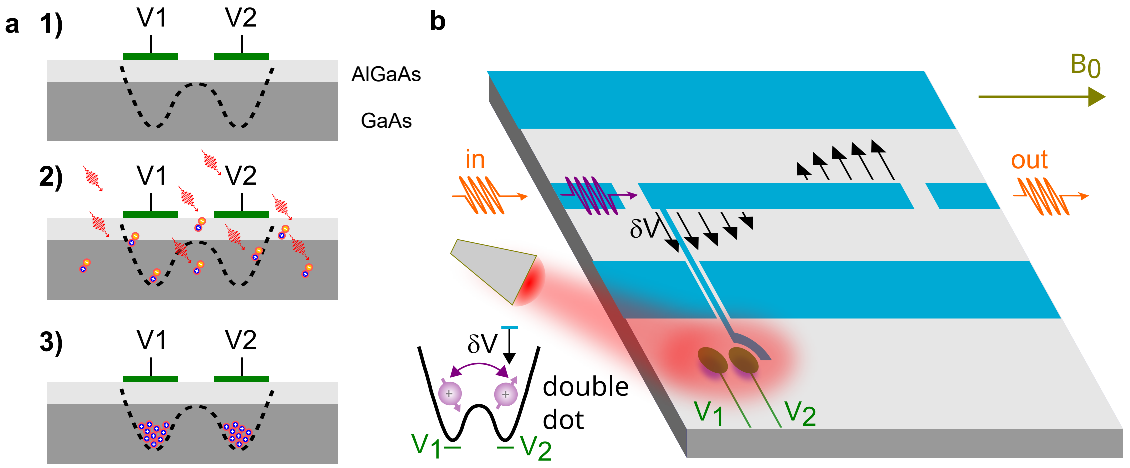

Figure 4: **Principe de la plateforme expérimentale de la deuxième expérience de cette thèse : Des électrodes de grille définissent une double boîte quantique à l'interface d'une hétérostructure semiconductrice. Cette double boîte est destinée à confiner un trou unique et est couplée à un résonateur coplanaire permettant de contrôler et de mesurer l'état quantique du spin du trou.** **(a)** Des tensions appliquées à deux électrodes de grille (vert) créent un double puit de potentiels pour les trous. Une illumination de l'échantillon par de la lumière infrarouge crée des paires électron-trou dans le semiconducteur (gris), les trous étant piégés dans le double puits ; le but est ensuite de vider progressivement le double puits à l'aide des grilles de façon à ne garder qu'un unique trou. **(b)** Le conducteur central du résonateur coplanaire (bleu) constitue une grille additionelle pour les boites. Une première impulsion mico-onde δV (violet) appliquée au résonateur peut donc induire un déplacement du trou dans le double puits et un retournement de son spin par couplage spin-orbite. Le résonateur permet aussi la lecture dispersive des états de charge et de spin à l'aide d'une autre impulsion micro-onde (orange).

onde, plus pratique que les mesures de transport conventionnelles [8]. Comme la Figure 4b le montre, une extrémité du conducteur central d'un résonateur coplanaire (où la tension électrique δV est maximale) sert de grille additionnelle à une double boîte quantique. La tension δV induit le déplacement du trou d'une boîte à l'autre, déplacement qui se couple au spin en raison de la forte interaction spin-orbite intrinsèque du trou. Cette forte interaction entre le spin chargé et le résonateur permet de contrôler l'état du spin et de le lire de manière dispersive avec des impulsions de micro-ondes appliquées au résonateur. La lecture dispersive repose notamment sur le changement de la capacité effective et donc de la fréquence du résonateur, en fonction de la position du trou dans le double puits et de l'état du spin. Cette approche nous a amenés à envisager une nouvelle architecture potentiellement scalable ne reposant pas sur le transport conventionnel de charges. Notre idée clé est la suivante : au lieu de remplir les boîtes en leur transférant des trous à partir d'un réservoir de charges voisin, nous proposons de créer des paires électron-trou par illumination optique dans le substrat GaAs, et d'accumuler les trous créés sous les grilles électrostatiques des boîtes, comme illustré dans la Figure 4a.

Tout d'abord, nous utilisons le résonateur pour surveiller l'effet de l'illumination tout au long du processus d'initialisation de la double boîte quantique. Le spectre

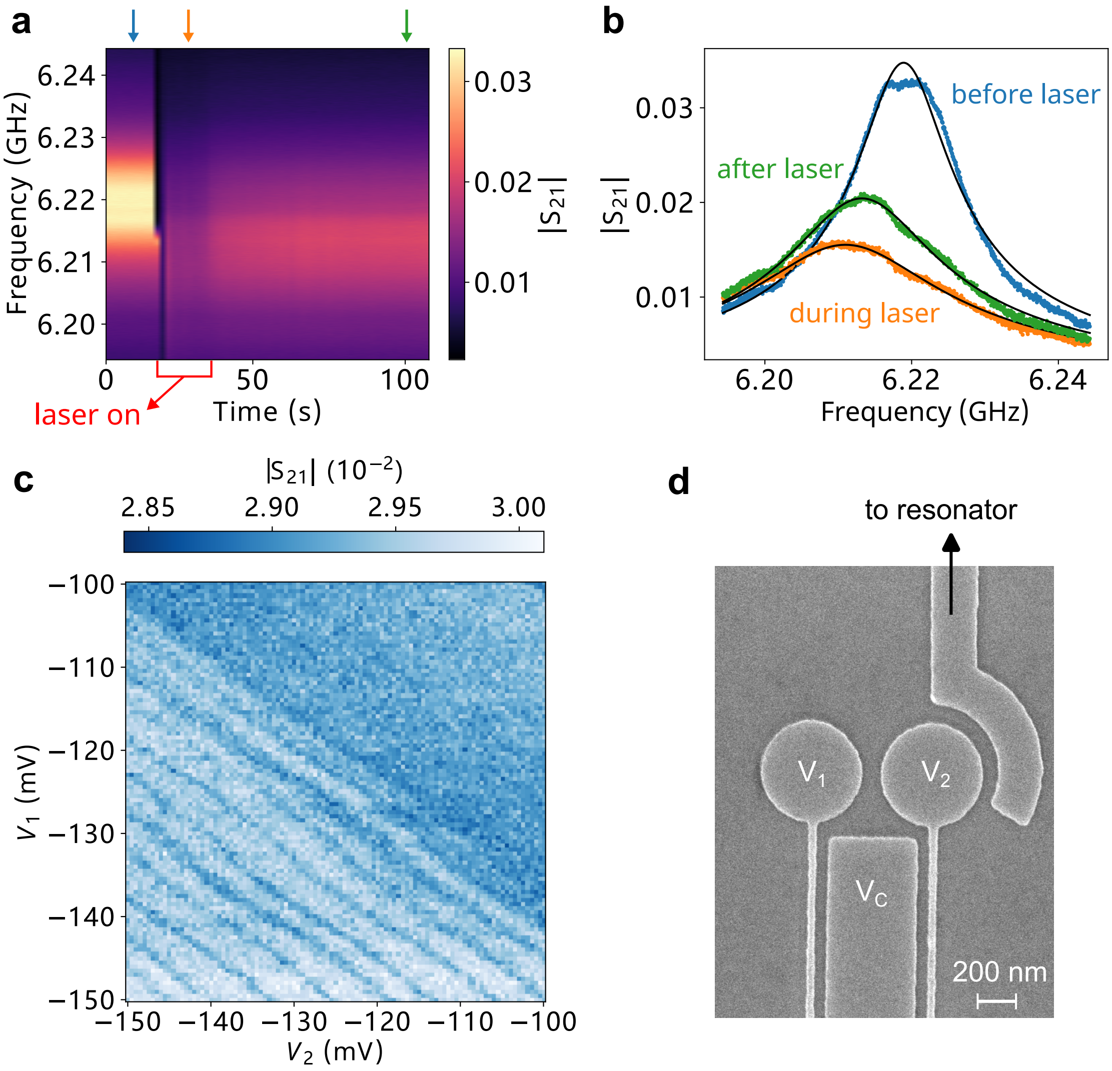

Figure 5: **Approvisionnement optique des charges pour les boîtes quantiques et la détection de charges.** **(a)** Spectre de transmission du résonateur mesuré temporellement, où le laser est allumé entres $t \sim 18\,\mathrm{s}$ et $t \sim 36\,\mathrm{s}$. La carte des couleurs représente l'amplitude du coefficient de transmission $|S_{21}|$. Les flèches en haut indiquent trois régimes : avant (bleu), pendant (orange) et après (vert) l'illumination. **(b)** $|S_{21}|$ en fonction de la fréquence de la sonde pour les trois traces indiquées par des flèches dans le panneau **a**, ajustées par une fonction lorentzienne (lignes pleines noires). **(c)** Diagramme de stabilité de charge. $|S_{21}|$ sondé à la fréquence de résonance du résonateur en fonction de V_1 et V_2 sur les grilles. La tension de la grille centrale est fixée à $V_C = 0.5\,\mathrm{V}$. **(d)** Micrographie électronique à balayage de la région des boîtes quantiques et la configuration des tensions sur les grilles pour mesurer le diagramme de stabilité de charge.

du résonateur, mesuré en transmission toutes les 1.8 seconde, est montré sur la Figure 5a, b. On distingue trois étapes : (i) de $t = 0$ à $t \sim 18$ s, le laser est éteint et le spectre reste inchangé. (ii) le laser est ensuite allumé entre $t \sim 18$ s et $t \sim 36$ s, ce qui entraîne une diminution de la fréquence de résonance et une augmentation de la largeur de sa raie de résonance, et donc de ses pertes. (iii) Le laser est enfin éteint pour $t > 36$ s, la fréquence de résonance et la largeur de raie ne retournant que partiellement vers leurs valeurs initiales. Ces observations résultent d'un changement de la capacité et des pertes résistives du résonateur après illumination. Cela indique que des charges permanentes sont créées dans le substrat non dopé.

Afin de vérifier qu'une partie des charges créées a effectivement été piégé dans les boîtes quantiques après illumination, nous effectuons une mesure du diagramme de stabilité de charge de la double boîte. Pour cela, nous balayons les tensions V_1 et V_2 appliquées sur les grilles et nous mesurons le coefficient de transmission S_{21} du résonateur à sa fréquence de résonance. Au lieu d'un diagramme de double boîte montrant une structure en nid d'abeille, nous observons (voir Figure 5c, d) un diagramme en bandes inclinées à environ -45° ; ces bandes séparées par des chutes de S_{21} traduisant l'effet tunnel d'une unique charge sont caractéristiques d'une unique boîte quantique couplée aux deux grilles. Bien que le régime de double boîte n'ait pas été atteint sur ce premier essai, ces résultats sont une preuve de concept de la nouvelle architecture proposée : des trous ont bien été introduits dans une boîte quantique par illumination, et la boite progressivement vidée par augmentation des tensions de grille. Cette avancée fournit un outil supplémentaire pour l'adressage de spins de trou uniques dans des boîtes quantiques.

Conclusion

Dans l'ensemble, les deux méthodes présentées dans cette thèse ouvrent de nouvelles voies pour le développement de la résonance paramagnétique électronique (RPE) ultime et pour le traitement quantique de l'information à base de spins individuels.

Chapter 1

Introduction

The mysterious but fascinating "reshaped" lights transmitted or reflected from crystals offer a glimpse on the astonishing nature of light-matter interaction in the early age of scientific discoveries, and their spectacular colorfulness foreshadows the vivid and prosperous research subdomains and applications today. The birth of quantum mechanics at the beginning of 20th century brought a new frame for understanding both light and matter. The concept of light quanta or photons, introduced by A. Einstein, describes the minimum indivisible packet of energy contained in the electromagnetic field. Meanwhile, as basic building elements for matter, atoms manifest themselves with discrete or quantized energy levels, and reveal a new non-classical degree of freedom inherent to particles: their spin. To study the quantum interaction between light and matter, a research field called cavity quantum electrodynamics is developed in atomic physics [9], and its derivative, circuit quantum electrodynamics (cQED)[10, 11], expands the same concepts to solid-state systems with artificial atoms and resonators made of electronic circuits. The cQED concepts, applicable to various systems, provide powerful new tool kits for addressing individual quantum objects such as spins and photons, which can then be used for sensing other existing objects or for carrying quantum information to be processed. We present in this introduction the motivation of the experimental Ph.D. work, as well as the general concepts and challenges of quantum sensing and quantum computing. Then among several possible candidates for the physical realization in today's quantum technologies, we focus on specific hybrid spin-photon systems utilizing the cQED platform. Finally, a brief presentation is given about the two different spin-photon coupling schemes and measurement approaches, which compose the two major parts of this thesis work.

1.1 Quantum technologies: sensing and computing

1.1.1 Detecting quantum objects

"What are the non-classical aspects of the objects governed by the principles of quantum mechanics and how can we access them?" are the questions we never cease to ask since the moment when scientists stepped out of the well-established edifice of classical physics. Light and matter belong to these objects which went through a long journey of observation, understanding, and later on, manipulation. They were sort of "entangled" (in a non-quantum manner) in the long history of science, where one is used to study the other or vice versa. There are examples such as iridescent colors converted from white light through a prism demonstrated by I. Newton in 1660s, intriguing fluorescence light generated from special trees or crystals[12], and spontaneous emission of excited atoms. Quantum theory not only gives better understandings and explanations of these phenomena, but also promises a new realm for exploration. The continuous pursuit for the non-classical aspects of light and matter leads to scientific discoveries and drive the development of technologies to conduct measurements in a regime which could not be imagined before. Quantum sensing is a field developed to detect the objects behaving quantum mechanically or to use these quantum objects to perform measurements with improved detection limit or accuracy.

Visible light or microwave radiation, i.e. the electromagnetic field at different frequency, has a wave-like nature which has been exploited and widely developed into a mature domain known as telecommunications. Meanwhile, it also possesses a particle-like nature and its energy is composed of discrete chunks corresponding to the so-called photons. The electromagnetic field containing exactly one photon is probably one of the most typical representatives of a true quantum state, given that no analogy can be found in a classical world. The quantum nature of a single photon also makes it favorable as a probe for acquiring information from other quantum objects. In addition to this discreteness, the quantumness of a single- or few-photon-Fock states lies also in the relentless vacuum fluctuations and quantum field noise predicted by the quantum description of electromagnetic field. In this framework, vacuum is not completely void and half a photon energy in the background always exists for a given mode, whose observable (e.g. electric field or magnetic field) thus appears with zero expectation value but non-zero variance. The intrinsic noise from vacuum fluctuation imposes challenges for the detection of a single photon from its field observables. However, quantum theory allows any change of measurement basis, so that the detection can be switched to the energy or photon-number basis, where the outcome is definite: *one* for single-photon state and *zero* for vacuum. Since the energy of vacuum quantum fluctuation cannot be transferred to any detector and thus does not generate any photon-detection noise, this strategy can lead in principle to an infinite Signal-to-Noise Ratio (SNR), despite the existence of field noise, surprisingly.

There are various approaches for the implementation of optical single-photon detectors [13], such as photomultiplier tubes (PMT) [14], single-photon avalanche photodiodes [15], or superconducting nanowire single-photon detectors (SNSPD) [16]. It is reasonable to expand such detection to the microwave domain, which is usually described by voltages and currents in electronic circuits. However, access to the hidden discreteness of microwave energy sounds much more difficult because of its 5-orders-of-magnitude lower energy scale compared to optical photons. This huge difference makes it less effective to trigger measurable macroscopic effect and indeed imposes particular challenges for the detection of microwave photons. To tackle the challenge, new cQED schemes have been introduced, in which a multi-level artificial atom interacts with the incoming microwave. In particular, one idea is to map an incident microwave photon to the excited state or to the phase of the superposed states of this artificial atom, which can then be read-out easily [4, 17, 18]. This all circuit-based approach provides a large flexibility for engineering the detector.

Apart from photons, another large family of quantum objects are atoms. Indeed, quantum physics was born in the search for the explanation of "why do atoms absorb and emit light only at certain frequencies?" The answer is in the quantized energy levels of the electronic structure of atoms. This concept also applies to macroscopic electronic circuits, which were considered as classical till the demonstration of the quantum behavior and the existence of quantum levels for a current-biased Josephson junction [19]. The quantum control of an electrical circuit, with noticeably the preparation of superpositions of distinguishable states of the circuit, was later demonstrated on the Cooper-pair box circuit [20, 21, 22]. This first artificial atom circuit had a rich legacy in terms of quantum circuits, including the now ubiquitously used transmon qubit. New methods for controlling this new type of quantum systems were needed. They were often inspired from existing quantum control techniques, noticeably magnetic resonance developed for controlling spins.

In the atomic structure, the discovery of *spin* (quantized intrinsic angular momentum) is probably one of the biggest milestones along the establishment of quantum mechanics. Subjected to magnetic field, electrons and certain atomic nuclei reveal extra energy levels or quantized magnetic moments. They can absorb or emit electromagnetic radiation, resulting in the change of magnetic moment from one state to the other. This leads to the birth of magnetic resonance [23, 24], later on evolving into two major subdomains: electron spin resonance (ESR) and nuclear magnetic resonance (NMR). The methodological development of these two domains based on the intrinsic degree of freedom of electrons and nuclei has far-reaching influence until today.

ESR spectroscopy (one of the main methods used in this work), provides means to identify and manipulate paramagnetic impurity species, and to study their interactions with the environment, with applications ranging from chemistry, biology to quantum computing [25, 26]. However, due to its limited signal-to-noise ratio, it gives access only to quantities averaged on ensembles of spins. To better understand the organization of matter at an atomic scale and to manipulate individual spins, single-spin detection sensitivity is required. The detection of single spin has been reached by using spin-dependent photoluminescence [27, 28, 29], transport measurements [30, 31, 32, 33], and scanning-probe techniques [34, 35, 36]. Different from these existing methods, we explore in this thesis two distinct but related approaches for single spin manipulation and detection; these approaches are applied to two different material systems, but involve similar hybrid cQED platforms. In both cases, microwave photons are used to detect a spin, light and matter being entangled in a quantum way.

Once a single spin can be addressed, it can be turned itself into a new detector or a quantum sensor to study its environment with atomic precision. For example, the electron spin of diamond defects can be used to probe remotely the surrounding carbon nuclear spin bath [37, 38, 39], to reach atomic imaging with spatial reconstruction and high spectral resolution for a cluster of nuclear spins [40]. Furthermore, one can imagine obtaining structural information about molecules with such a quantum sensor based on spin probes or labels (stable paramagnetic compounds added or covalently bound to a molecule) [41, 42]. Quantum sensing gives thus access to an unprecedented world, with potential applications in physics, chemistry and even biology.

1.1.2 Quantum information processing

A switch or transistor in either an ON or OFF state for electrical current is known as a "bit" encoding either 1 or 0, and is commonly used to represent *information*. Classical computation processes classical information formed from streams of bits. Today's computer contains billions of transistors integrated on a processor chip and the information processing is realized by manipulating the bits or states of transistors through electronic circuits, resulting in certain logical operations. Since the world is fundamentally governed by quantum mechanics, a natural extensive question to ask is "what is the information contained by a quantum object and what can be done to process this type of information?". The answers to these questions lead to the new realm of quantum information processing or quantum computing.

The simplest quantum object is a two-level quantum system such as an electron spin. One can encode information in its two basis states $|0\rangle$ and $|1\rangle$ and call it a quantum bit or *qubit*. Contrary to a classical bit being either in its 0 or 1 state, quantum mechanics allows the state $|\psi\rangle$ of a qubit to be in any arbitrary superposition $|\psi\rangle = a|0\rangle + b|1\rangle$ of its two basis states, where a and b are complex numbers satisfying $|a|^2+|b|^2 = 1$ and determine the probability of measuring the qubit in state $|0\rangle$ and $|1\rangle$ respectively. The manipulation on a qubit can "parallelly" modify both coefficients. As for two qubits, the whole system state $(a|00\rangle + b|01\rangle + c|10\rangle + d|11\rangle)$ lives in a 4-dimensional Hilbert space. In particular, a state $a|00\rangle + b|11\rangle$ is called an entangled state and shows a strong correlation between the two qubits. In a N qubit system, the state can be any arbitrary superposition of the 2^N basis states, whereas the state of a classical N bit system needs only N booleans to be determined (N dimensions). This exponential increase of space dimension and quantum entanglement are the unique properties of quantum system, and are at the heart of their power to treat information.

For processing quantum information encoded in qubits, new algorithms need to be devised to make use of the quantum properties pointed out above. In 1985, Deutsch and Jozsa firstly proposed a quantum algorithm demonstrating "quantum parallelism" and quantum speed-up in solving a problem more efficiently than a classical computer [43]. The first influential quantum algorithm was proposed by P. Shor in 1994 for factoring integers [44], outperforming the best known classical ones exponentially faster as the number of digits increases. Later on L. Grover proposed a search algorithm showing that searching a target in an unstructured dataset of N elements can be performed with a number of algorithmic steps of order $\sqrt{\mathrm{N}}$ instead of N for a classical search [45].

Though an advantage of quantum computer has been demonstrated theoretically, the fragility of quantum information in real systems subject to decoherence by their environment hinders the physical implementation of a quantum processor in practice. Maintaining the quantum coherence of many physical qubits during a time sufficient for running an algorithm is very difficult. It will require not only qubits with very long intrinsic coherence times, but also error correction schemes based on redundancy of quantum information in several hardware qubits per single logical qubit. Up to today, a fully functional quantum processor with thousands of highly coherent qubits has not been demonstrated yet. But there are many possible candidates for implementing physical qubits. In principle, any two-level quantum systems or multi-level systems with selectively addressable two levels can be used as qubits. The promising platforms nowadays are superconducting circuits [46, 47], solid-state spin qubits [48], trapped-ions [49], neutral atoms [50, 51] and photonic systems [52, 53]. Each system has its own advantages and drawbacks, requiring specific techniques for manipulation as well.

Among these candidates, superconducting qubit circuits and spin qubits are two prominent solid-state platforms. Quantum information encoded in these circuits and processed in cQED architectures offer a high versatility for engineering and controlling many parameters, such as the qubit transition frequency, the type and the strength of qubit-qubit interaction [1], etc. By exploiting conventional lithography and other fabrication techniques in microelectronics industry, scaling up physical qubits to a large number should be much more feasible compared to other systems, as demonstrated by the 433-qubit chip recently announced by IBM [54]. In recent improvements [55, 56], superconducting qubit coherence time has reached an order of magnitude of one milisecond. However, this finite time is still limiting the fidelity and usefulness of noisy intermediate-scale quantum processors (NISQ).

On the contrary, solid-state spin systems have much longer coherence time compared to superconducting circuits. This is the case for electron and nuclear spins of donors in silicon [57, 58], nitrogen-vacancy centers in diamond [59], and rare-earth ions in specific host crystals [60]. They all have reported coherence time of the order of a second. However, spins, being individual atomic-scale quantum objects, are difficult to address and to entangle with each other, though proposals have been made to implement large-scale spin-based architecture for quantum computing [61, 62].

In order to combine the advantages of different systems and platforms, hybrid quantum system have been proposed [63, 64, 2]; these proposals could lead to novel approaches for quantum technologies and to new regimes for exploring physics. Our work is part of this effort on hybrid platforms.

1.2 Hybrid quantum systems

The integration of different solid-state systems, such as macroscopic superconducting circuits and microscopic electrical charges and spins in semiconductor or insulator, will bring new perspectives for both quantum computing and sensing.

For example, one can imagine an architecture where superconducting qubits, as computing unit with fast control, are coupled to spins ensembles, as memory units with long coherence time. A proof-of-concept of such a spin memory was first demonstrated in a spin ensemble of nitrogen-vacancy centers in diamond [65], with the storage, and the subsequent retrieving, of a superposed state of a qubit in the collective excitations of the spin system.

As for sensing, the detection of spins through their emitted microwave photons is a good example of hybrid system. Normally, spontaneous emission of radiation from spins is negligible compared to other non-radiative decay processes (an excited spin in vacuum will emit one photon every 300 million years), due to the weak interaction between the magnetic dipole of spin and electromagnetic field. However, by strongly coupling spins to a superconducting resonant circuit, their radiative emission rate can be drastically enhanced (this is the celebrated Purcell effect discussed further below), and become the dominant spin relaxation mechanism [3]. This thus allows us to control spin relaxation, and opens a new route for spin detection using their microwave fluorescence signal [5].

Here, in this thesis, we use the Purcell effect and microwave fluorescence to address single spins with superconducting circuits. The capability of control and measure single spins will not only allow the detection of individual spins, but also enable the essential qubit-readout process for spin-based quantum computing. The hybrid systems, involving microwave photons in quantum circuits and spins, are built on a cQED framework which will be discussed in this section.

1.2.1 Quantum circuits and spin systems

Superconducting quantum circuits

Superconducting electronic circuits can be arranged in a way resembling an optical resonant cavity, which is a device used to tame electromagnetic radiation in free space into a spatially confined system. The cavity or resonator acts as a box, with walls defined by the mirrors. Photons, reflected back and forth in this box, can be trapped inside with a high energy density and a long lifetime. The residual losses of the walls as well as their transparency determine how long the photons can stay in the cavity before being lost or leaking out. Different from optical cavities, superconducting resonant circuits operate at microwave frequencies. In this frequency range, the simplest "box" for microwave photons is a lumped-element LC resonator circuit made of one capacitor and one inductor (see Figure 1.1a).

But effective LC resonators can also be obtained by distributing their inductance and capacitance along a transmission line. An example is a half-wavelength coplanar waveguide resonator. As shown in Figure 1.1b, this type of circuit is a 2D version of a coaxial cable (transmission line) with a central conductor in the middle and ground plane on both sides. The input and output ports are formed by two small gaps in the central line acting as mirrors with finite transparency for microwave. The microwave entering the circuit is reflected back and forth on both ends and therefore is confined in it. The fundamental resonant mode is a half wavelength between the two gaps, with a maximum of electric field at the gaps.

Both lumped-element and distributed resonators can be modelled by a quantized harmonic oscillator with a resonant angular frequency ω_0, being also the energy of one resonator photon divided by $\hbar$ (reduced Planck constant), as shown in Figure 1.1d. At millikelvin temperatures, the resonator energy-level spacing or photon energy is larger than the thermal fluctuation and quantum effects can prevail. The resonator can absorb and re-emit single photons when coupled to other quantum objects able to emit photons, e.g. spins. In the other limit, when the resonator is addressed by classical signals, its quantum dynamics that follows the correspondence principle is fully classical, and the discrete nature of its energy levels cannot be observed. For observing the quantum behavior of a quantum circuit based on a harmonic resonator, a non-linear element ensuring it does not follow the correspondence principle is thus needed, such as the Josephson junction already used in the first quantum circuit experiments.

A Josephson junction is a tunnel junction with superconducting electrodes separated by a thin insulating layer across which electrons can tunnel, which couples their superconducting phases. From the electrical point of view, this component can often be considered as a non-dissipative non-linear inductor whose inductance depends on the current through it [66]. The smaller the Josephson critical current, the larger the inductance. The most widely used superconducting artificial atom

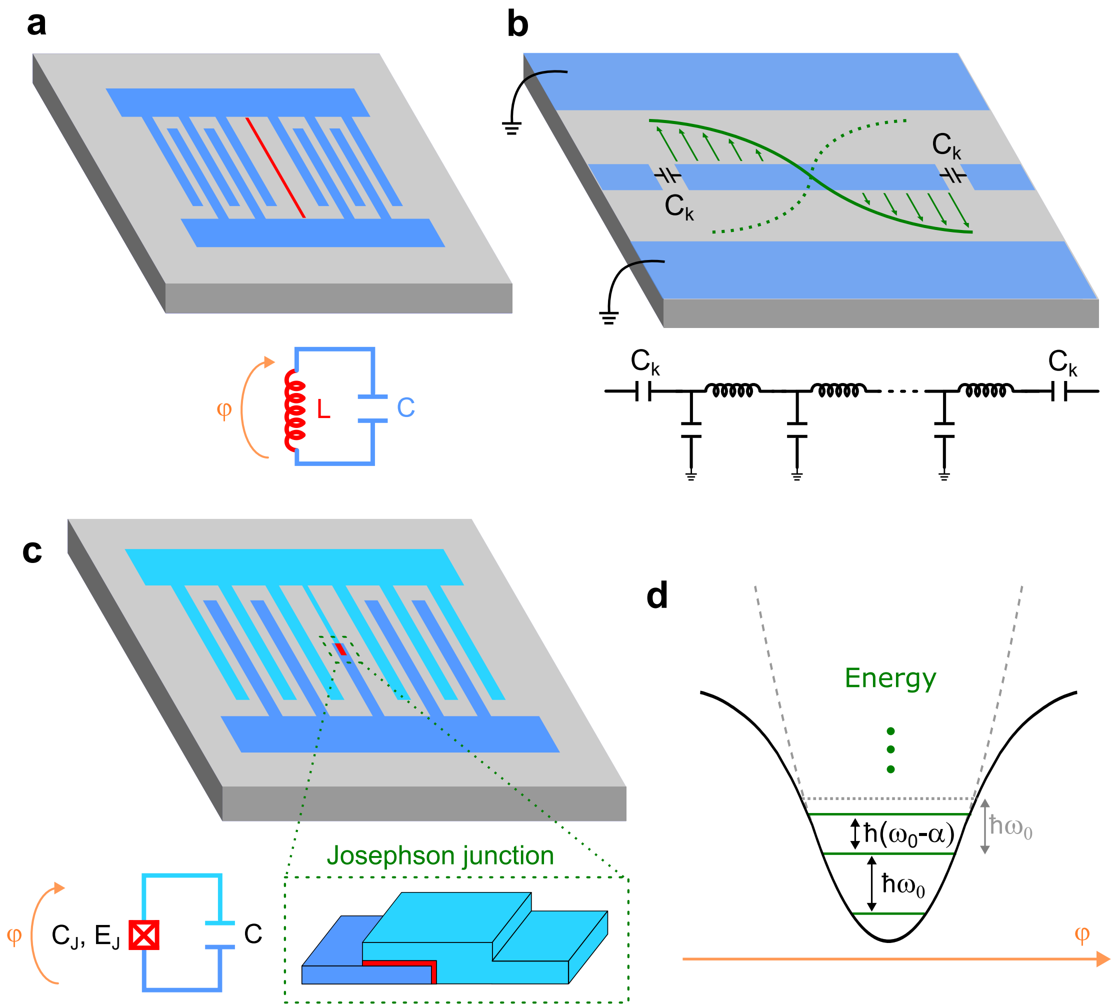

Figure 1.1: **Schematic of different types of quantum circuits.** **(a)** Lumped-element LC resonator formed by an inductor (red) and an interdigitated capacitor (blue). φ is the reduced phase across the inductor. **(b)** Half-wavelength coplanar waveguide (made from a central conductor and ground plane) resonator bounded by two separated gaps of capacitance C_k in the central conductor. The green arrows depict the electric field distribution of the resonator fundamental mode. **(c)** A transmon qubit formed by one capacitor and one Josephson junction (green dash box). The light and dark blue represent the two capacitor pads of the qubit, the red the insulator in the overlap region. φ is the reduced phase across the junction. **(d)** Anharmonic oscillator and unequal energy level spacing of the transmon, resulting from the nonlinearity of Josephson junction. The gray dash line represents the case of a harmonic oscillator with the same resonant frequency ω_0 (simple LC circuit and transmission line resonator).

nowadays, namely the transmon, [67, 68], consists of a small Josephson junction that provides a non-linear inductance connected in parallel to a capacitance. The inductance and the capacitance are adjusted for placing the resonance frequency $(LC)^{-1/2}$ in a convenient frequency range (typically between 5 and 15 GHz). The anharmonicity introduced by the Josephson junction makes the resonator anharmonic, see Figure 1.1c, d. The energy spacing between the ground state and the first excited state being different from the one between the first excited state and the second excited state, one can selectively address the two lowest levels of the system with microwave coherent signals, see Figure 1.1d. The possibility of tuning the circuit parameters by engineering and of manipulating the circuit states as for natural atoms with lasers makes the circuit a true artificial atom.

In this thesis work, lumped-element LC circuit, distributed coplanar waveguide resonator and transmon qubit are all involved, which will be discussed in detail in the corresponding experiments.

Spin systems

Different forms of electronic spins in solid-state systems exist, and the four main ones are shown in Figure 1.2 : (a) spins in quantum dots, (b) spins of rare-earth ions, (c) spins of donors in semiconductors, (d) spins of more complex crystal defects.

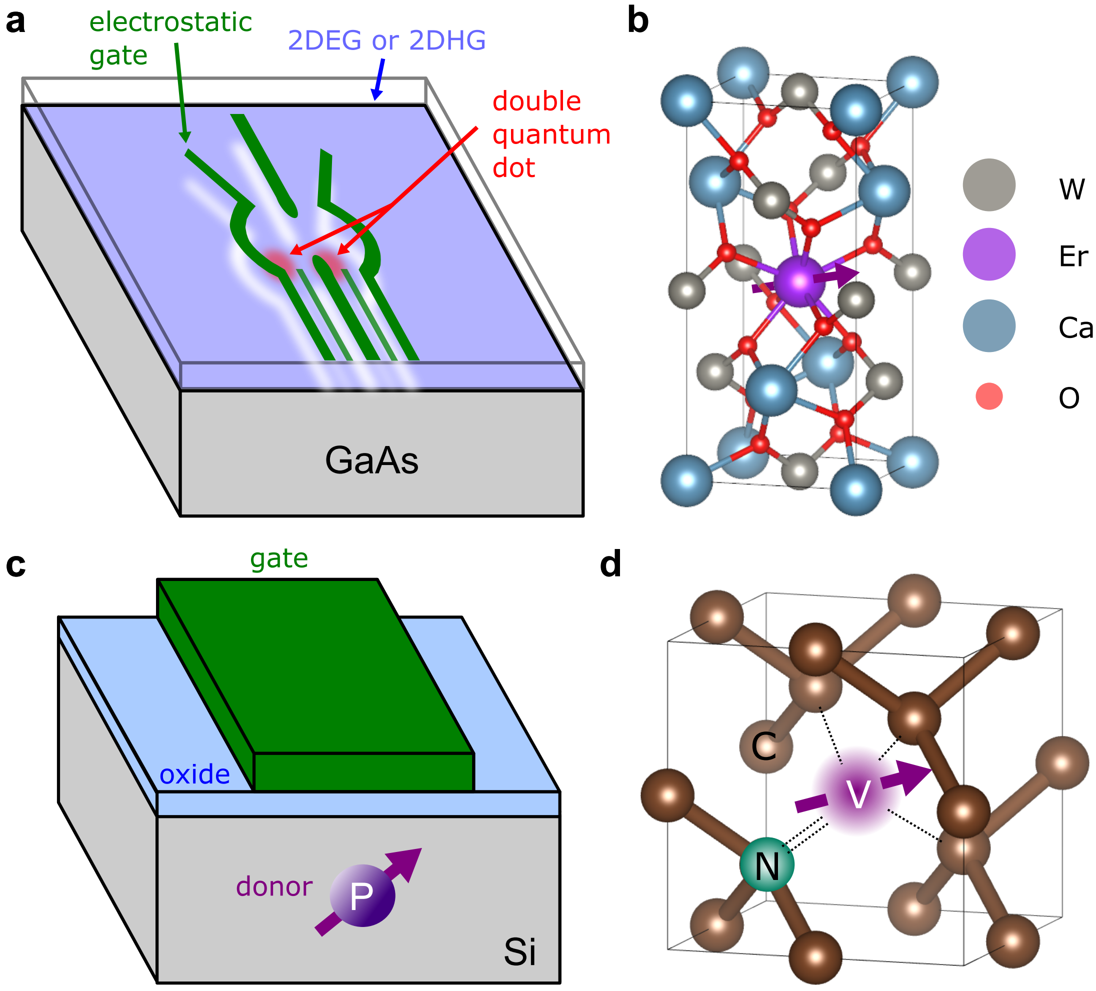

Figure 1.2: **Different types of solid-state spin systems.** **(a)** Electrostatic-gate-defined double quantum dot. **(b)** Rare earth ion in an insulating crystal (e.g. Er^{3+} : CaWO4). **(c)** Donor atom in semiconductor (e.g. phorsphorus in silicon). **(d)** Crystal point defect (e.g. nitrogen-vacancy center in diamond).

The most widely investigated case is that of charge carriers in semiconductors (such as Si and GaAs), either conduction band electrons or valence band holes. Both of these carriers have a spin degree of freedom (1/2 for both electron and light hole, and 3/2 for heavy hole). Since these carriers are free to move in semiconductors, one can trap and control a few of them by creating a box with an electrostatic potential, in which the number of charges is adjustable. A conventional approach is to start with a sheet of electrons or holes confined at a semiconductor interface, namely a 2-dimensional electron gas (2DEG) or hole gas (2DHG), and to deplete the regions where the carriers are not wanted using biased electrostatic metal gates above. The remaining island of carriers contains a finite number of charges, which can in principle be tuned down to one. This type of devices with confinement in all three dimensions is called electrostatic gate-defined quantum dots (see Figure 1.2a).

Two other categories of spins are impurities that keep their spin in a host crystal, including some dopants in semiconductors and rare-earth ions in various crystals (see Figure 1.2b,c). They are both impurities substituting an atom on regular atomic sites in the crystal structure, but the physics is quite different. The unpaired extra electrons of dopants (as phosphorus in silicon for instance) is the origin of measurable spins, whereas rare-earth ions have more complex electronic structure and some transitions under certain conditions can be treated as effective spins detectable by ESR spectroscopy.

The fourth category of spins is the crystal point defects, such as nitrogen-vacancy centers in diamond (see Figure 1.2d).

In this thesis, we will deal with two systems: rare earth ions in insulator (erbium ions in $CaWO_4$) and holes in semiconductor quantum dots.

1.2.2 Circuit quantum electrodynamics with spins

Quantum interactions between light and matter have been investigated in great details in the framework of cavity quantum electrodynamics (cavity-QED). A single-mode electromagnetic field mode with frequency ω_0 that is confined inside a resonant cavity and forms a quantized harmonic oscillator. An atom modeled as a two-level system with a transition frequency of ω_s placed in this cavity is coupled to the electric field on the electromagnetic mode. In addition, the cavity can dissipate energy in its walls and/or be pierced by holes to exchange electromagnetic field with free space outside, as sketched in Figure 1.3a. The full model of cavity-QED describes the interaction between the atom and the field in any regime: at a single photon level, at the level of a macroscopic coherent field, whether both objects are in resonance or not.

Whereas in free space the excited atom would always return spontaneously to its ground state by radiative emission of a single photon propagating away, the situation is different in cavity-QED: The atom can only relax radiatively if it is resonant with the cavity ($\omega_0 = \omega_s$) or, in the opposite case, if the cavity has losses in its walls or can leak outside. In the resonant or nearly resonant case, the spontaneous emission rate can be largely enhanced, as demonstrated by Purcell in 1946 [69]. This effect can be used to control the lifetime of atoms [70] and even make the spontaneous emission become the dominant relaxation mechanism for spins in solid, whose dominant decay mechanism is usually non-radiative [3]. Moreover, in the strong coupling regime [71, 11], that is when the interaction strength g_0 between atom and cavity exceeds both the atom decay rate Γ and the cavity decay rate κ, a single excitation (photon) can coherently oscillate between the atom and cavity, a phenomenon known as vacuum

Rabi oscillation.

On the contrary, when the atom frequency is detuned from the cavity frequency ($\omega_0 \neq \omega_s$), the spontaneous emission of the atom can be greatly suppressed, because the photons to be emitted cannot fit in the cavity. In such situation, the atom keeps its coherence and the remaining interaction between the atom and the cavity has a coherent effect on both components. Specifically, when the atom-cavity frequency detuning $\Delta = \omega_s - \omega_0$ is much greater than their interaction strength g_0, the dispersive regime is reached, and the remaining atom-cavity coupling now makes the cavity frequency dependent on the state of the atom, which provides a method for measuring its state by probing the cavity [10].

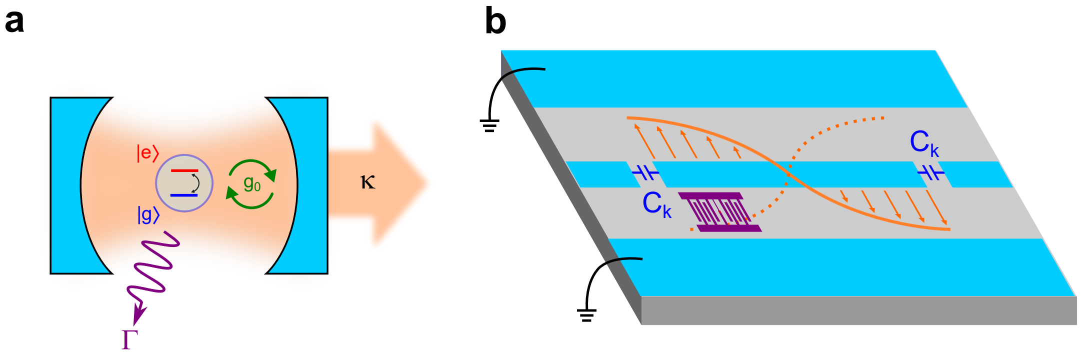

Figure 1.3: **Schematic of cavity-QED (a) and circuit-QED (b) system.** A two-level real atom (a) or transmon artificial atom (b) exchanges energy coherently with a resonant cavity (a) or a resonator circuit (b) at rate $2g_0$. The atom decays through the cavity at rate Γ.

In general, the physics of cavity QED can be used to describe any two-level system interacting with a bosonic system (e.g. photons, phonons, magnons, etc). Its concept can be generalized in a common framework applicable to many systems, such as real atoms in a resonant microwave cavity [72], trapped-ions coupled to their motional degrees of freedom [73], quantum dots coupled to semiconductor optical cavity [74, 75], as well as circuit QED (cQED) systems introduced above [11], for which a circuit-based artificial two-level atom is coupled to an on-chip resonator or a 3D cavity.

Although in 2004 cQED began just as a circuit-based derivative of cavity QED experiment (see Figure 1.3b), nowadays it has largely extended to a powerful platform useful for a big range of solid-state physical systems. Indeed, cQED is particularly favorable for addressing fundamental quantum objects in advanced hybrid quantum systems made thanks to the design versatility offered by lithography fabrication techniques and microwave engineering. Over the previous decade, the cQED toolbox has brought powerful tools for controlling various hybrid quantum systems, e.g. the quantum control of on-chip surface acoustic phonons [76], the detection of quanta of collective spin excitations (magnons) from ferromagnet [77], single-shot detection of a single magnon [78], the coherent manipulation of Andreev states [79], the strong coupling between single microwave photon and charges confined in gate-defined semiconductor quantum dots [75, 80, 81], the all-microwave control and readout of quantum dot charge qubits [82], and also the subject of this thesis work, addressing spins with superconducting circuits, which can be used to perform ESR spectroscopy for spin detection [83, 5, 6] or to create a spin-photon interface for spin-based quantum computing [84, 85, 86].

The essential part in addressing spins with cQED is to couple them to the electromagnetic field confined in a resonant circuit. The two possible coupling schemes are shown in Figure 1.4. Since spins are intrinsic magnetic dipoles, this coupling arises naturally with the oscillating magnetic field in the resonator (scheme I). On the contrary, spins do not couple directly to the electric part of the field. However, if the spin particle also carries a charge and is movable (e.g. electrons and holes in semiconductors), the resonator oscillating electric field can indirectly couple to the spin (scheme II) in two cases: when a dc magnetic field gradient is applied to the system so that the resonator electric field moves the spin in the gradient, thus showing to the spin an apparent variable magnetic field; and when intrinsic spin-orbit interaction exists for the spin in its host crystal. Scheme I is normally in the weak coupling regime, while scheme II can reach strong or barely strong coupling regime. We will discuss these two coupling schemes more in detail in the next sections, which form the two major parts of this thesis.

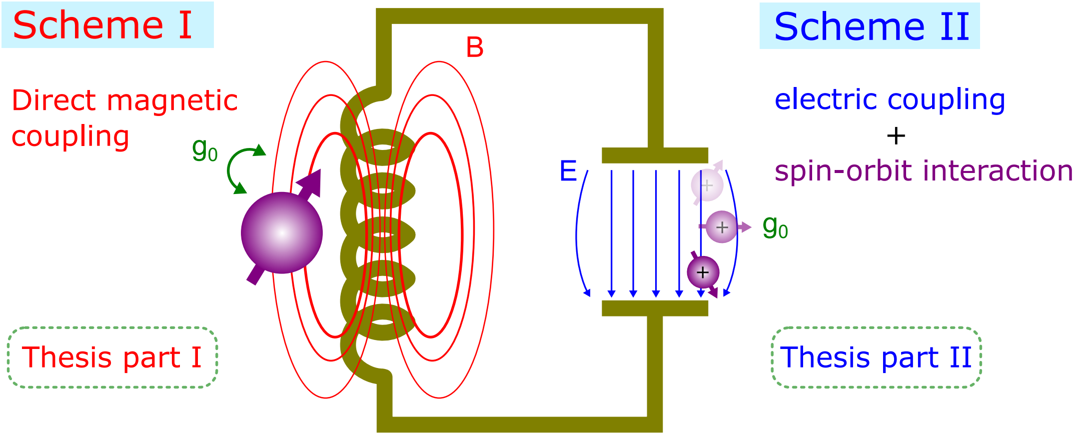

Figure 1.4: **Two coupling schemes between a single spin and the electromagnetic field in a resonator.** (i) Magnetic dipole of spin couples directly to the magnetic field of the resonator. (ii) The spin couples indirectly to the resonator through the motion of its charge under an electric field and spin-orbit interaction.

1.2.3 Addressing spins with magnetic coupling

Magnetic dipole coupling is the most straightforward approach for detecting paramagnetic species in a certain volume since the birth of magnetic resonance. However, due to the extremely small magnetic dipole moment of spin, ESR detection normally relies on collecting the signal of a large spin ensemble. The conventional methods are either using continuous wave to measure absorption or using pulses to excite spins to a superposition of up and down so that the ensemble builds up a transient transverse magnetization and radiates cooperatively a detectable coherent field. Detecting these reflected or re-emitted fields gives the information about the spin ensemble transition. A commercial ESR spectrometer reaches nowadays a sensitivity of $\sim 10^9$ spins for a measurement time of one second. By using high-quality-factor superconducting resonators in a cQED setup operated at millikelvin temperatures and quantum-limited microwave amplifiers, the ESR sensitivity has been pushed to about one hundred spins with an integration time of one second, despite the small coupling strength between spin and field in cavity (55 Hz in the reported geometry of ref. [83]). This sensitivity reaches the fundamental limit determined by quantum fluctuations of the electromagnetic field, beyond the limit of thermal or instrumental noise.

Even if electromagnetic field quantum fluctuations set the ultimate limit of signal-to-noise ratio in field detection, one can still bypass this limit by changing the detection method to energy-based measurement. With the aim of detecting few spins and eventually a single spin, measuring the energy or number of photons emitted by the spins present a winning advantage. Indeed, when a single excited spin emits eventually one photon, the corresponding signal on the field quadratures is spoiled by the 1/2 photon vacuum quantum noise in total. On the contrary, this 1/2 photon noise energy cannot manifest itself in an energy detector. A single photon detector can thus give a definite binary answer about whether a photon arrives or not (with an infinite signal-to-noise ratio in principle), and help reach single spin sensitivity.

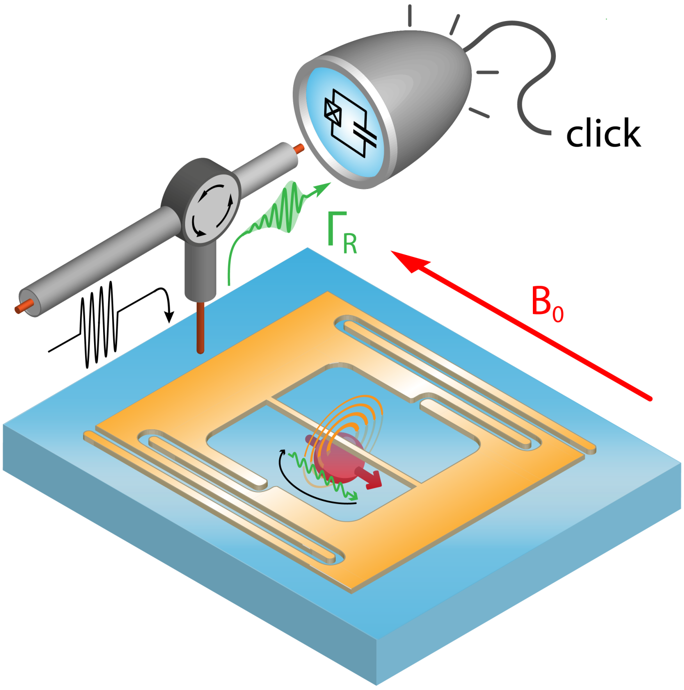

Figure 1.5: **Principle of the first experiment in this thesis: Single spin spectroscopy by microwave photon counting**. An individual electron spin (shown in its ground state as a red arrow) embedded in a crystal is excited by a microwave pulse (black pulse and arrow); it then relaxes back to its ground state by emitting a microwave photon (green wiggly arrow and outgoing green pulse), which is routed via a circulator towards a microwave photon counter based on a superconducting transmon qubit. To enhance its radiative rate Γ_R, the spin is coupled magnetically to the mode (shown as orange concentric circles) of a high-quality-factor superconducting planar microwave LC resonator (in orange). The spin frequency is tuned to the resonator by application of a magnetic field B_0 parallel to the resonator plane.

The photon-counting method for detecting a single Er^{3+} ion has already been demonstrated with optical transition [87, 29]. Performing an ESR experiment using an optical detection has been successfully applied on a hand of spins, noticeably the celebrated NV centers. Performing true ESR spectroscopy experiments in the microwave range using a photon-counting detection scheme requires a practical Single Microwave Photon Detector (SMPD). The demonstration of this new ESR detection scheme with a SMPD counting fluorescence photons was first reported in ref. [5], with a detection sensitivity of about one thousand spins in one second, still far away from single-spin sensitivity.

Setting up an improved version of this pioneering work, including superior cQED resonator design, spin sample, SMPD performance and experimental setup, we finally reach this milestone: **single electron-spin-resonance detection by microwave photon counting**. My personal contribution to this work mainly consisted in designing and making the resonator and the sample, whereas another PhD student, Léo Balembois, mainly worked on the SMPD and on the experimental setup.

The principle of our experiment is shown in Figure 1.5. The spin in a crystal is coupled to the oscillating magnetic field generated by the inductor of a superconducting resonator on top of the crystal. The spin is excited by a microwave pulse and then decays back to its ground state by radiating a microwave photon at a rate enhanced by the Purcell effect. This emitted photon is detected by a superconducting-qubit-based SMPD with low dark count noise, thus enabling single-spin resolution. However, the weak spin-resonator coupling strength and the limited overall SMPD efficiency do not allow us to perform single shot detection of an excited spin (i.e. high fidelity single photon detection after a single spin excitation pulse). The first part of the manuscript is dedicated to this experiment.

1.2.4 Addressing spins with electrical coupling

Spins being quantum magnetic dipoles, they do not couple directly to an electric field by nature. But many particles, carrying a spin, happen to also carry an electric charge. Moving electrically such particles in a magnetic field gradient is thus an indirect way to control their spin. Another case is the intrinsic spin-orbit interaction (SOI) of charge carriers in solids, which couples the spin degree of freedom of the carriers to their momentum. These effects lead to the method of Electric Dipole Spin Resonance (EDSR) for controlling the magnetic moment of spins with electric field.

The first experimental observation of EDSR was performed with the conduction-band electrons in indium antimonide (InSb), a semiconductor with large intrinsic SOI [88]. With the development of technologies in semiconductor industry and nanoscale device fabrication, it becomes feasible to use electrostatic metal gates to isolate and confine a single electron on a tiny island, known as quantum dot, which also gives access to single electron spin. The electrostatic gate-defined quantum dot provides a build-in controllability over the charge in the dot, and is therefore an ideal system to manipulate spins by EDSR. To make it work, two key ingredients are necessary: a structure capable of moving charges in a controllable manner, and SOI with large coupling strength. A typical architecture for implementing the first ingredient is a double quantum dot, where a double potential well is created and the charge is shuffled back and forth between the two wells using an applied oscillating electric field. The second ingredient can be realized either through intrinsic SOI (by choosing a proper material system with large build-in intrinsic SOI) or through synthetic SOI (by applying a permanent magnetic field gradient, with a micromagnet for instance).

Though the SOI of bulk electrons in GaAs or Si is too small to induce spin rotations, some special materials and particular confinement geometries can lead to large SOI strength, as in InAs nanowires [89]. As for introducing synthetic SOI, the integration of a micrometer-size ferromagnet close to a quantum-dot device has been proven to be a practical and efficient method [90]: a static magnetic field difference is created between the two dots of the double-dot, and the spin feels an effective oscillating magnetic field while being shuffled back and forth between the dots.

However, the two methods present drawbacks: relying on intrinsic SOI for controlling electron spin imposes particular constraints on the choice of material systems, and micromagnets for synthetic SOI brings engineering complication for device fabrication. To bypass these drawbacks, we choose to work on a new type of spins: hole spins. Originating from the absence of an electron of the valence band, such a hole is a quasi-particle with positive charge and spin 1/2 or 3/2 (1/2 for light holes and 3/2 for heavy holes). The most noticeable feature of hole spin is its strong intrinsic SOI, even in the materials where SOI is normally negligible for electrons [48]. Therefore hole spin can be manipulated electrically in the most common semiconductor materials, such as Si, Ge and GaAs, without the complication of incorporating micromagnets [91, 92, 93].

Addressing spins electrically in quantum dots requires good control and readout of their charge. cQED is very well suited for both of these functions. Different from conventional transport measurement, it brings an all-microwave approach for manipulating and detecting charges. cQED-based charge detection has already been demonstrated for electron systems [8]. With the integration of micromagnets, single electron spin detection has been reached [84, 85, 86]. Here we will adopt the same detection architecture for holes. As shown in Figure 1.6, one end of a half-wavelength coplanar waveguide resonator (where the electric field is maximum) is extended near one control gate of the double dot. The quantum fluctuations of the resonator electric field (voltage δV) couples to the motion of the hole between the dots, which couples to the spin due to the large intrinsic SOI of the hole. The resulting large spin-resonator interaction strength g_0 (strong or barely strong coupling) makes it possible to control the spin state and to read it out dispersively (possibly in a single shot) with simple microwave pulses applied to the resonator. This dispersive readout [8] relies on the change of the resonator effective capacitance and thus resonator frequency, depending on the charge location in the double-well and its spin state.

This all-microwave readout approach for spins with cQED lead us to envision a novel scalable architecture for hole-spin qubits in quantum dots, which does not rely on conventional charge transport. Our key idea is the following: instead of filling the dots by transferring holes from a charge reservoir, we propose to create electron-hole pairs by optical illumination on the semiconductor, to accumulate the corresponding holes beneath dots' electrostatic gates, and consequently fill them.

In this new proposal, the device complexity is largely reduced. The novelty and advantages can be summarized as follows:

- Quantum dots are initialized by trapping charges from simple illumination.

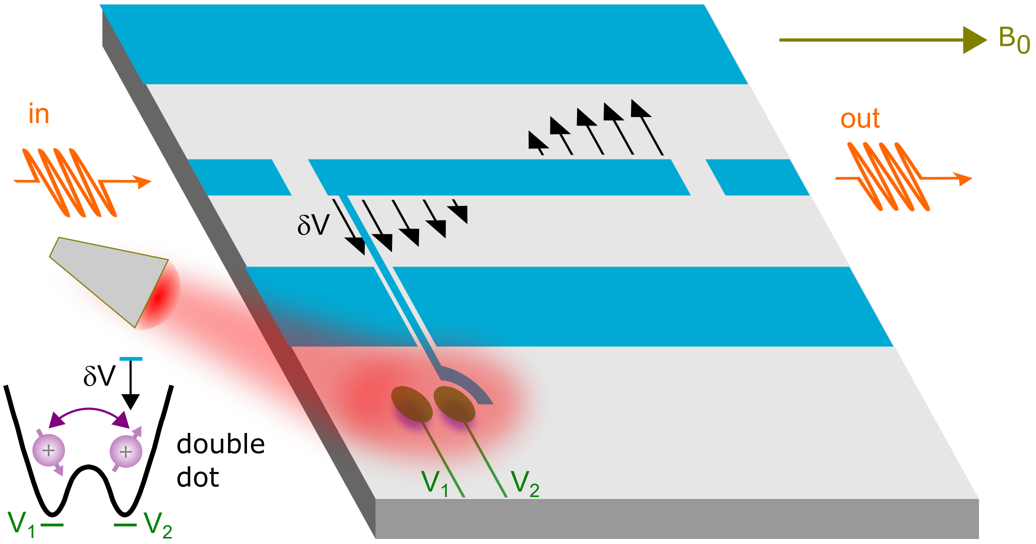

Figure 1.6: **Principle of the second experiment in this thesis: Towards addressing a single hole spin in a double quantum dot initialized by illumination**. Infrared light creates electron-hole pairs in the substrate (gray) and the bias applied to the electrostatic gates (green) traps the holes and forms a double quantum dot beneath. The central conductor of a coplanar waveguide resonator (blue) is extended near one of the quantum dot gates. The voltage fluctuation δV of the resonator is coupled to the charge hopping inside the double potential well. This allows the control and dispersive readout of charge and spin states using microwave pulses (orange). A static magnetic field B_0 is applied in the resonator plane.

- The substrate can be undoped.
- Ohmic contacts (required for transport measurements) are no longer needed.
- Only two accumulation gates are required for creating a double quantum dot.
- Charge detection can be performed by microwave pulses using a cQED architecture.

Figure 1.6 shows this newly proposed spin qubit platform with optical-electrostatic initialization of quantum dots and microwave dispersive readout for charges and spins. Furthermore, this platform can also be used for interfacing solid-state qubits and optics. The second part of the manuscript will be dedicated to a proof-of-concept of charge detection within this new proposal, which is a prerequisite step towards the detection of a single hole spin.

1.3 Outline of the thesis

My thesis work consisting of two distinct experiments, the present manuscript is naturally divided in two parts (with several chapters each). In these two cQED experiments, spins are addressed either magnetically or electrically. The common ground and links between the two experiments have just been presented in this Chapter 1.

In the first part, we expose how we control and detect individual spins of erbium dopants in a host crystal $CaWO_4$ through magnetic coupling to a resonator and single-microwave photon detection and counting. We begin this part in Chapter 2 with theoretical background and necessary conceptual tools for understanding the experiment. In Chapter 3, we describe the implementation of the devices and experimental setup involved in this experiment, as well as basic characterizations of the devices. Chapter 4 then focuses on spin spectroscopy by fluorescence detection, going from spin ensemble to single-spin-resolved measurements. In Chapter 5, time-domain measurements are presented for individual spins.

In the second part, we aim at detecting hole spins in electrostatic gate-defined quantum dots formed in AlGaAs/GaAs heterostructures, by electric coupling to a resonator and dispersive readout. Along this cQED idea, we explore a novel architecture for creating and measuring quantum dot devices. We begin this part in Chapter 6 with theoretical background and necessary conceptual tools for understanding the experiment. In Chapter 7, we describe the experimental setup and the devices involved in this experiment. In Chapter 8 the characterization results regarding resonator under different situation and the experimental results on charge detection of quantum dots are presented. These results are a key step towards single spin detection and manipulation in quantum dots with cQED.

Finally, conclusions and perspectives are given in Chapter 9.

Part I

Control and readout of individual electronic spins of dopants in a host crystal

Chapter 2

Overview and theoretical background of detecting single erbium ions by their fluorescence

This chapter provides the necessary background to understand the experiment performed in the first part of this thesis, in which electron-spin-resonance detection by microwave photon counting is the key method. Three components are involved in this approach: spins of dopants in a host crystal, a superconducting resonator, and a single microwave photon detector (SMPD). We first describe the spins we investigate inside their host crystal. The rest of the chapter is then devoted to the physics of circuit quantum electrodynamics and its application to spins, and to the SMPD.

2.1 Erbium dopants in a calcium tungstate $\mathrm{CaWO_4}$ scheelite crystal

The electronic spins to be controlled and detected in our experiment originate from the erbium ions in a host crystal of scheelite (calcium tungstate $\mathrm{CaWO_4}$). Erbium belongs to a group of heavy metal atoms known as rare-earth elements, also called lanthanides. The electronic configuration of neutral erbium can be described as $\mathrm{[Xe]4f^{12}6s^2}$ based on the xenon structure ($\mathrm{[Xe]= 1s^2 2s^2 2p^6 3s^2 3p^6 4s^2 3d^{10} 4p^6 5s^2 4d^{10} 5p^6}$). The 4f and 6s electrons of the neutral erbium are valence electrons dominating its chemical properties. In a solid, erbium normally loses 3 electrons from the outmost shells and becomes a trivalent ion $\mathrm{Er^{3+}}$. The electronic configuration of this erbium ion is thus $\mathrm{[Xe]4f^{11}}$, where the odd number of 4f electrons determines its behavior under electromagnetic field.

In $\mathrm{Er^{3+}}$, the 4f shell electrons are closer to the nucleus than the 5s and 5p electrons, as shown by the radial density distribution of the different electronic shells displayed in $\mathrm{Er^{3+}}$ in Figure 2.1. These 4f electrons are thus shielded from external field sources and do not contribute to interactions. This feature makes it possible to approximate $\mathrm{Er^{3+}}$ as a "free ion" with coulomb repulsion of electrons and spin-orbit coupling. The interaction of the ions with the "crystal-field" of their host crystal and an externally applied magnetic field can thus be treated as a perturbation of the free ion. Therefore, the Hamiltonian of the system:

$$\hat{H} = \hat{H}_{FI} + \hat{H}_{CF} + \hat{H}_{spin} \tag{2.1}$$

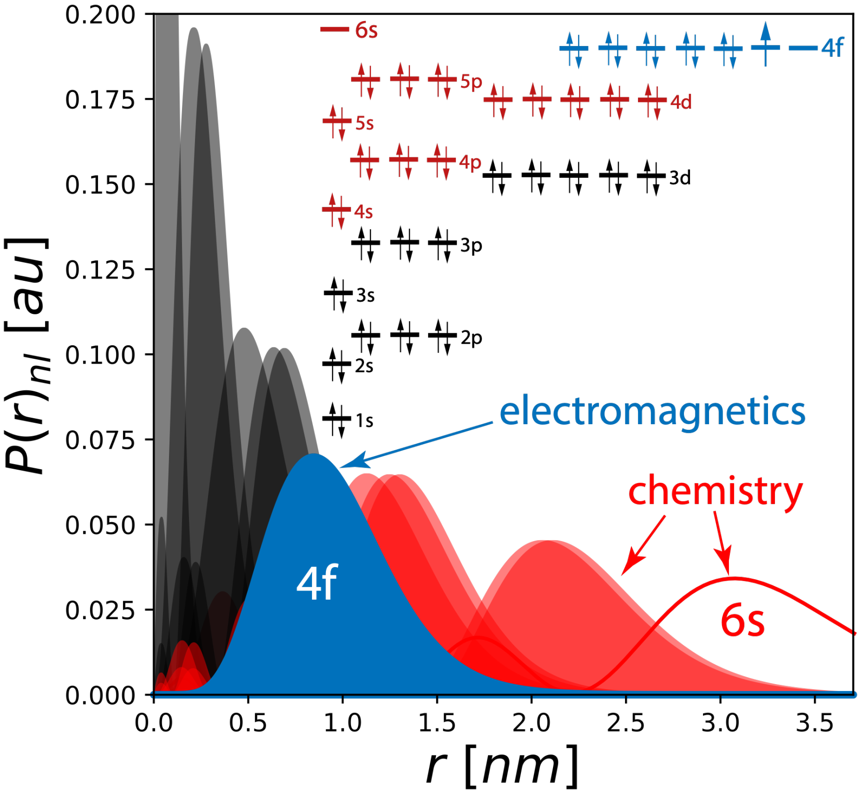

Figure 2.1: **Electronic shell distribution of** $\mathbf{Er^{3+}}$**.** Radial probability distribution of electron orbitals with principle quantum number n and angular quantum number l. For erbium ions, the 6s shell is empty, and the 5s and 5p shells are fully occupied.

contains three parts: the free-ion approximated Hamiltonian $\hat{H}_{FI}$, the interaction with crystal field $\hat{H}_{CF}$ and the spin Hamiltonian under magnetic field $\hat{H}_{spin}$.

As shown in Figure 2.2, the free-ion treatment of Er^{3+} leads to a multiplet ground state $^4I_{15/2}$ and first excited state $^4I_{13/2}$ [94]. The corresponding transition is at 1.5μm. The interaction between the crystal field and the free ion splits the ground state multiplet $^4I_{15/2}$ into eight doubly degenerate Kramers doublets (labelled as Z_1, Z_2 ... Z_8). In the case of a $CaWO_4$ host crystal, the energy difference between Z_1 and Z_2 is 0.57 THz [95], which corresponds to a thermal energy of about 27 K. Given our experiment is performed at millikelvin temperatures (between 10 mK and 20 mK), only the ground state doublet Z_1 is populated. When a non-zero external magnetic field is applied, the ground state Kramers doublet behaves as an effective spin 1/2 system with spin Hamiltonian:

$$\hat{H}_{spin}/\hbar = \mathbf{B_0} \cdot \hat{\gamma} \cdot \hat{\mathbf{S}} = \begin{pmatrix} B_x & B_y & B_z \end{pmatrix} \begin{pmatrix} \gamma_{xx} & \gamma_{xy} & \gamma_{xz} \\ \gamma_{yx} & \gamma_{yy} & \gamma_{yz} \\ \gamma_{zx} & \gamma_{zy} & \gamma_{zz} \end{pmatrix} \begin{pmatrix} \hat{S}_x \\ \hat{S}_y \\ \hat{S}_z \end{pmatrix}, \tag{2.2}$$

where $\hat{\gamma}$ is an anisotropic gyromagnetic tensor and $\hat{\mathbf{S}}$ is the effective spin operator vector defined with Pauli matrices

$$\hat{S}_x = \frac{1}{2}\hat{\sigma}_x = \frac{1}{2}\begin{pmatrix} 0 & 1 \\ 1 & 0 \end{pmatrix}, \quad \hat{S}_y = \frac{1}{2}\hat{\sigma}_y = \frac{1}{2}\begin{pmatrix} 0 & -i \\ i & 0 \end{pmatrix}, \quad \hat{S}_z = \frac{1}{2}\hat{\sigma}_z = \frac{1}{2}\begin{pmatrix} 1 & 0 \\ 0 & -1 \end{pmatrix}. \tag{2.3}$$

Here, we only consider the $I = 0$ isotopes of erbium in our experiment, whereas ^{167}Er for instance contains also a nuclear spin I=7/2, which introduces hyperfine interactions for the electronic spin and thus additional hyperfine levels. The study of other $I \neq 0$ erbium isotopes has not been done in this work.

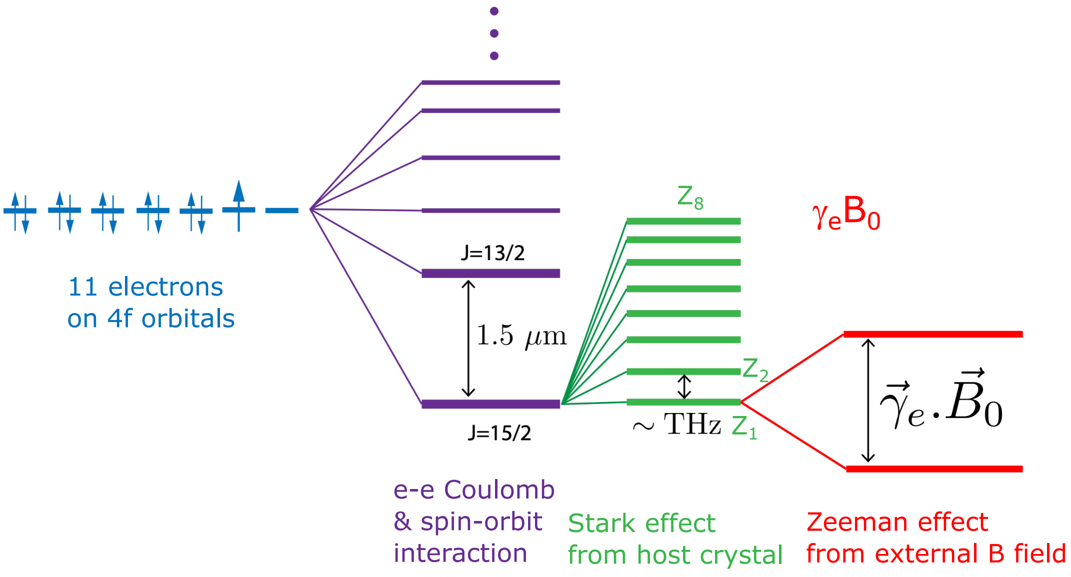

Figure 2.2: **Energy levels** Er^{3+} **in** CaWO$_4$ **crystal under non-zero magnetic field.**

The host crystal used in this work is calcium tungstate (CaWO$_4$), whose structure is tetragonal with unit cell constants $a = b = 5.24$ Å and $c = 11.37$ Å, as shown in Figure 2.3a. The erbium ions Er^{3+} substitute for the calcium ions Ca^{2+} (with long-range charge compensation in the crystal). The sites of Er^{3+} have a rotatory-reflection S_4 symmetry, which means that rotating the crystal by $\pi/4$ around the crystal c-axis and applying a mirror reflection across the (a,b)-plane leaves the site unchanged. This S_4 symmetry leads to a gyromagnetic tensor diagonal in the (a,b,c) frame and isotropic in the (a,b) plane. Defining the component parallel to c as $\gamma_c \equiv \gamma_{||}$ and the perpendicular components in the (a,b) plane as $\gamma_a = \gamma_b \equiv \gamma_\perp$, the gyromagnetic tensor [96] is

$$\hat{\gamma} = \begin{pmatrix} \gamma_\perp & 0 & 0 \\ 0 & \gamma_\perp & 0 \\ 0 & 0 & \gamma_{||} \end{pmatrix}_{a,b,c} = 2\pi \times \begin{pmatrix} 117.3 & 0 & 0 \\ 0 & 117.3 & 0 \\ 0 & 0 & 17.45 \end{pmatrix}_{a,b,c} \text{GHz/T.} \tag{2.4}$$

Compared to the gyromagnetic factor of a free electron $\gamma_e/2\pi = g\mu_B/\hbar = 28$ GHz/T (with a Landé g-factor g=2 and Bohr magneton $\mu_B = 13.996$ GHz/T), the gyromagnetic ratio of Er^{3+} in CaWO$_4$ is 4 times larger in (a,b)-plane. This means that the effective spin of Er^{3+} is 4 times more sensitive to a magnetic field in the (a,b)-plane than a g=2 free electron. This large gyromagnetic factor enhances the coupling between the spins and the electromagnetic field. For example, when the spin quantization axis S_z is defined along the crystal c-axis by applying a magnetic field $B_0 \parallel c$, the transverse magnetic field $B_1 \perp c$ in the (a,b)-plane drives the spin transition more strongly, as described in the next section.

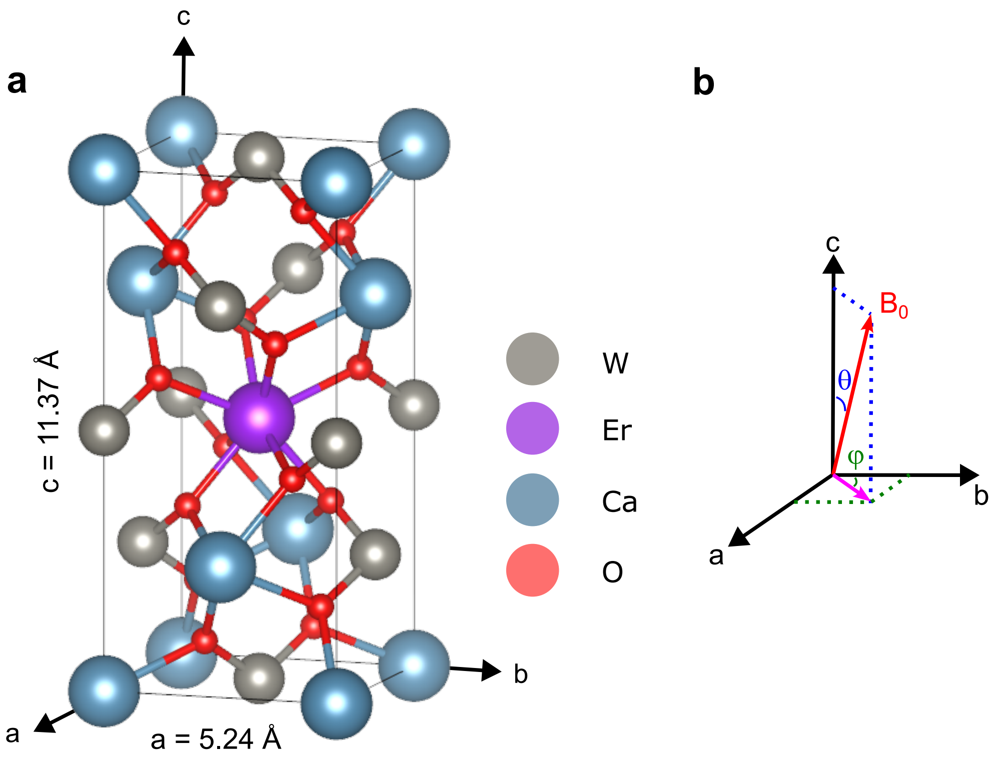

Figure 2.3: **Crystal structure of** $\mathrm{Er}^{3+}:\mathrm{CaWO}_4$. **(a)** Tetragonal unit cell of CaWO$_4$ crystal with central Ca^{2+} replaced by Er^{3+}. This central site has a S_4 symmetry. **(b)** The applied external magnetic field $\mathbf{B_0}$ is expressed in spherical coordinates (B_0, θ, φ), with (a,b,c) being the crystal axes.

Finally, it is useful to write explicitly the spin Hamiltonian using the diagonal elements of the $\hat{\gamma}$ tensor,

$$\hat{H}_{spin}/\hbar = B_x\gamma_\perp\hat{S}_x + B_y\gamma_\perp\hat{S}_y + B_z\gamma_{||}\hat{S}_z, \tag{2.5}$$

where the crystal (a,b,c) axes correspond to (x,y,z) basis of the spin. Expressing the non-zero field B_0 in the spherical coordinates defined in Figure 2.3b, the spin Hamiltonian rewrites

$$\hat{H}_{spin}/\hbar = B_0(\gamma_\perp \sin\theta \sin\varphi \hat{S}_x + \gamma_\perp \sin\theta\cos\varphi\hat{S}_y + \gamma_{||}\cos\theta\hat{S}_z). \tag{2.6}$$

Choosing $\varphi = 0$ without any loss of generality because of the isotropy in the (a,b) plane, the spin Hamiltonian simplifies as

$$\hat{H}_{spin}/\hbar = B_0(\gamma_\perp \sin\theta\hat{S}_y + \gamma_{||}\cos\theta\hat{S}_z). \tag{2.7}$$

We then define an effective gyromagnetic ratio $\gamma_{\text{eff}} \equiv \sqrt{(\gamma_\perp \sin\theta)^2 + (\gamma_{||}\cos\theta)^2}$ and a new angle θ' by $\cos\theta' = \gamma_\perp/\gamma_{\text{eff}}\cos\theta$ and $\sin\theta' = \gamma_{||}/\gamma_{\text{eff}}\sin\theta$, so that

$$\hat{H}_{spin}/\hbar = B_0\gamma_{\text{eff}}(\sin\theta'\hat{S}_y + \cos\theta'\hat{S}_z) = B_0\gamma_{\text{eff}}\hat{S}'_z \tag{2.8}$$

with

$$\begin{pmatrix} \hat{S}'_x \\ \hat{S}'_y \\ \hat{S}'_z \end{pmatrix} = \begin{pmatrix} \hat{S}_x \\ \hat{S}_y\cos\theta' - \hat{S}_z\sin\theta' \\ \hat{S}_y\sin\theta' + \hat{S}_z\cos\theta' \end{pmatrix} \tag{2.9}$$

being the spin vector now expressed in a new orthogonal basis obtained by rotating the axis z by the angle θ' in the (y, z)plane. The energy eigenstates of the spin are thus the eigenstates of $\hat{S}'_z$. Note that angle $\theta' = \theta$ only if $\theta = 0$ or $\pi/2$. This means that, due to the anisotropic character of the $\hat{\gamma}$-tensor, the actual spin quantization axis (or polarization axis) is not aligned with the magnetic field if the latter is not applied along or perpendicular to the crystal c axis.

We now explain how we have coupled the effective Er^{3+} spins in bulk $CaWO_4$ to a superconducting resonator.

2.2 Circuit quantum electrodynamics of a microwave resonator with spins in the substrate

Our experiment operates at millikelvin temperature T and microwave frequency $\omega/2\pi$, so that the energy $\hbar\omega$ of a single photon is much larger than the thermal energy $k_B T$. As a result, the simple resonant circuit that we use to couple to the spins is operated in the quantum regime, with its voltage and current treated as quantum operators. We first introduce this quantum treatment, and take the opportunity to generalize it to a nonlinear resonator, such as the transmon artificial atom, which is at the heart of the single microwave photon detector that we use in our ESR experiment. This will allow us to describe within the cQED theoretical framework the interaction between a single photon in the resonator and a two level system such as a transmon or a spin.

A good review about the quantum treatment of electromagnetic modes in circuits and cQED can be found in ref. [1].

2.2.1 Quantum circuits

Quantization of a simple LC oscillator

The simplest implementation of a resonant circuit is a lumped-element LC resonator, composed of a capacitor C and an inductor L, see Figure 2.4. The electrical variables of this system can be taken as the current I flowing through the inductor and the voltage V built up on the capacitor. These electrical variables obey the following dual relations:

$$I = \frac{\Phi}{L} = -\frac{\mathrm{d}Q}{\mathrm{d}t} = -C\frac{\mathrm{d}V}{\mathrm{d}t}, \tag{2.10}$$

$$V = \frac{Q}{C} = \frac{\mathrm{d}\Phi}{\mathrm{d}t} = L\frac{\mathrm{d}I}{\mathrm{d}t}, \tag{2.11}$$

where Q is the charge on the capacitor and Φ is the magnetic flux in the inductor. The total energy of the resonator:

$$E = \frac{1}{2}LI^2 + \frac{1}{2}CV^2 \tag{2.12}$$

leads to the system Hamiltonian:

$$H = \frac{\Phi^2}{2L} + \frac{Q^2}{2C}. \tag{2.13}$$

One can verify the following Hamilton's equations:

$$\frac{\partial H}{\partial Q} = \frac{Q}{C} = V = \dot{\Phi}, \tag{2.14}$$

$$\frac{\partial H}{\partial \Phi} = \frac{\Phi}{L} = I = -\dot{Q}, \tag{2.15}$$

which confirm that Φ and Q are canonical conjugate variables, as position and momentum in classical Hamiltonian mechanics.

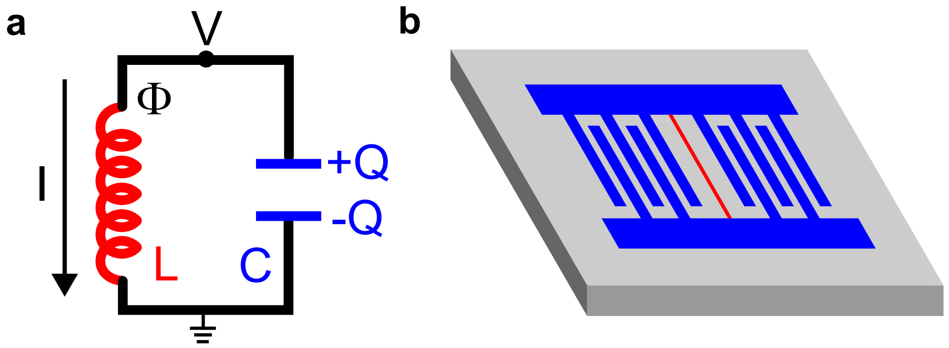

Figure 2.4: **Simple LC resonator.** (a) Lumped-element model of a simple LC resonator. (b) Possible physical implementation of it, on top of a substrate (gray), in which the metal wire (red) in the middle plays the role of the inductor and the interdigitated metal fingers (blue) the role of the capacitor.

The quantization of the system is obtained by replacing the canonical conjugate variables by their corresponding operators ($\Phi \to \hat{\Phi}$, $Q \to \hat{Q}$), which satisfy the commutation relation $[\hat{\Phi}, \hat{Q}] = i\hbar$.

Therefore, the Hamiltonian of the system in the quantum framework is

$$\hat{H} = \frac{\hat{\Phi}^2}{2L} + \frac{\hat{Q}^2}{2C}, \tag{2.16}$$

which in second quantization writes

$$\hat{H} = \hbar\omega_0(\hat{a}^\dagger \hat{a} + \frac{1}{2}), \tag{2.17}$$

The link between operators $(\hat{a}^\dagger, \hat{a})$ and $(\hat{\Phi}, \hat{Q})$ is:

$$\hat{\Phi} = \sqrt{\frac{\hbar Z_0}{2}}(\hat{a}^\dagger + \hat{a}), \tag{2.18}$$

$$\hat{Q} = i\sqrt{\frac{\hbar}{2Z_0}}(\hat{a}^\dagger - \hat{a}), \tag{2.19}$$

where $\omega_0 = 1/\sqrt{LC}$ is the resonant frequency of the resonator and $Z_0 = \sqrt{L/C}$ its characteristic impedance. The creation and annihilation operators $\hat{a}$ and $\hat{a}^\dagger$ satisfy the commutation relation $[\hat{a}, \hat{a}^\dagger] = 1$.

The eigenstates of this quantum harmonic oscillator are the Fock states $|n\rangle$ with eigenenergies

$$E_n = \hbar\omega_0(n + \frac{1}{2}), \tag{2.20}$$

with n the integer number of photons in the resonator, and $\hbar\omega_0$ the energy of a single photon.

In terms of photon creation and annihilation operators, the current and voltage write

$$\hat{I} = \frac{\hat{\Phi}}{L} = \delta I(\hat{a}^\dagger + \hat{a}), \tag{2.21}$$

$$\hat{V} = \frac{\hat{Q}}{C} = i\delta V(\hat{a}^\dagger - \hat{a}), \tag{2.22}$$

where $\delta I = \omega_0\sqrt{\hbar/2Z_0}$ and $\delta V = \omega_0\sqrt{\hbar Z_0/2}$ are the zero-point fluctuations of the quantum field. When no photon is present and the resonator is in its ground state $|0\rangle$ (vacuum), the system has root-mean-square current fluctuations $\langle 0|\hat{I}^2|0\rangle = \delta I^2$ and voltage fluctuations $\langle 0|\hat{V}^2|0\rangle = \delta V^2$.

Current fluctuations generate fluctuations of the magnetic field $\mathbf{B}(\mathbf{r}) = \delta\mathbf{B}(\mathbf{r})(\hat{a}^\dagger + \hat{a})$ at all locations $\mathbf{r}$ around the inductor wire, whereas voltage fluctuations generate fluctuations of the electric field $\mathbf{E}(\mathbf{r}) = i\delta\mathbf{E}(\mathbf{r})(\hat{a}^\dagger - \hat{a})$ between the capacitor electrodes. Consequently, the coupling strength of the resonator electromagnetic field to quantum objects with charge or spin located at $\mathbf{r}$, will be proportional to the electric or magnetic vacuum fluctuations at that location. An example of the lumped-element resonator used in our experiment with spins is sketched in Figure 2.4b. The inductance of the circuit is the superconducting wire in the middle, with the magnetic field concentrated in its neighborhood. On both sides of the wire, the capacitor is mainly formed between the interdigitated fingers. Both the electric field and magnetic field thus have a strong and different spatial dependence.

Quantization of a transmission line resonator

In addition to lumped element LC resonators, a resonant circuit can also be built in a distributed way. Similar to a coaxial cable, a coplanar waveguide transmission line is a common way to transmit microwave within a circuit on chip. The transverse electromagnetic mode, described in Figure 2.5b, propagates along the central conductor. This circuit can be treated as a series of lumped-element LC model, as shown in Figure 2.5a.

A half-wave ($\lambda/2$) resonator is formed by adding two small gaps separated by distance d on the central line, which act as mirrors with finite transparency for microwave (see Figure 2.5c). These two gaps impose zero-current boundary (open) conditions. The microwave entering the circuit is reflected back and forth on both ends and forms a standing wave confined in the circuit, with maximum voltage at the extremities and maximum current in the middle (for the fundamental mode).

The discretization of the transmission line resonator shown in Figure 2.5 into N segments of small length $\delta x = d/N$, small inductance and capacitance to ground $l_0\delta x$ and $c_0\delta x$ respectively (with c_0 and l_0 the capacitance and inductance per unit length), allows us to express the electromagnetic energy. The energy associated with the capacitor at node n is $Q_n^2/2c_0\delta x$ and the energy of the inductor is $[\Phi_{n+1}(x,t) -$

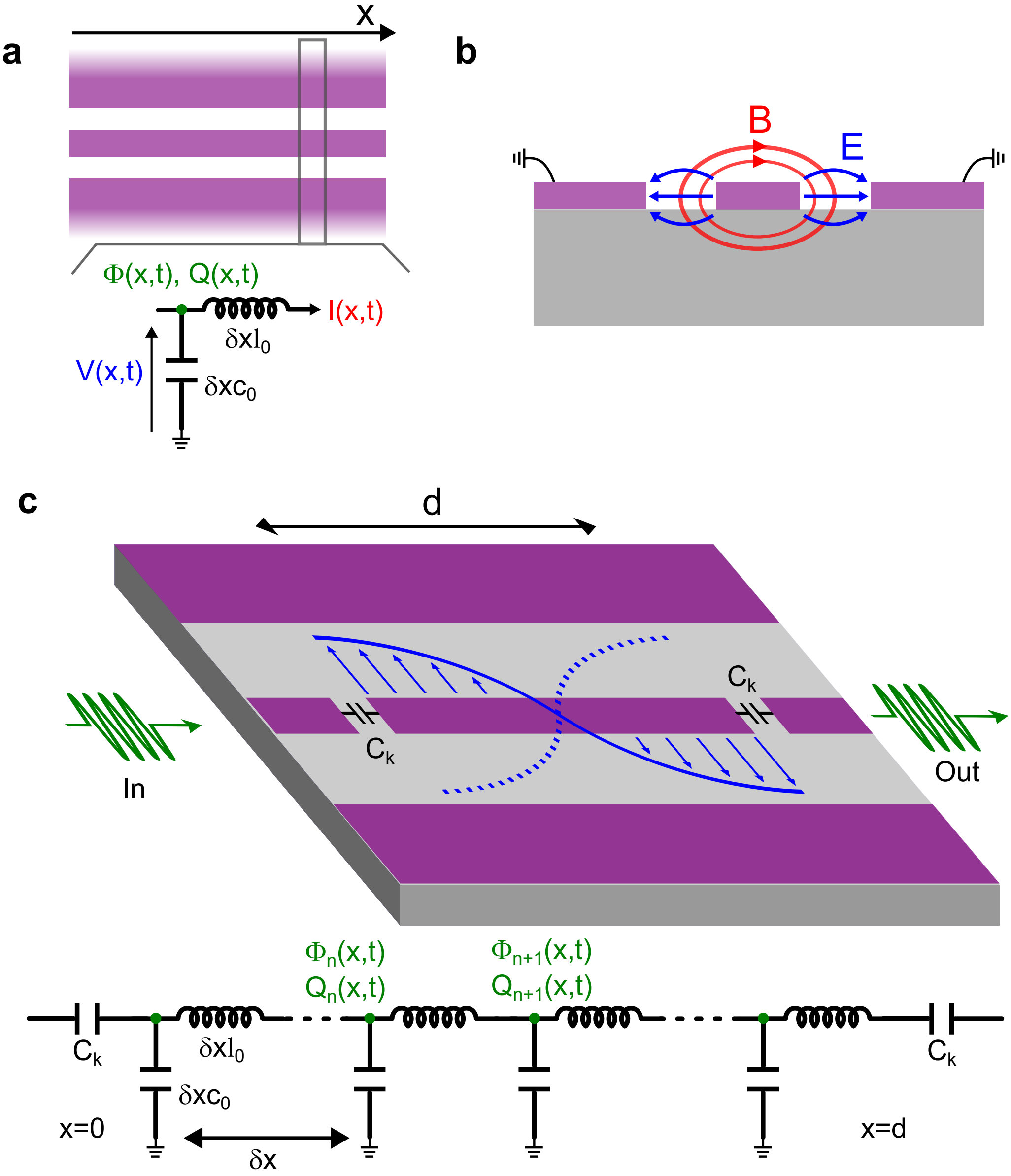

Figure 2.5: **Coplanar waveguide resonator.** (a) Lumped circuit model for a distributed transmission line, with c_0 and l_0 the capacitance and inductance per unit length. (b) Intersection view of the coplanar waveguide, where the spacial distribution of magnetic field (red) and electric field (blue) is indicated in the schematic. The metal on both sides are grounded. (c) A coplanar waveguide resonator formed by adding in the central conductor two open gaps separated by length d. For the fundamental mode, the electric field (blue) is maximized close to the gaps. The coupling capacitance of the resonator to the input and output is C_k.

$\Phi_n(x,t)]^2/2l_0\delta x$. One finds the classical Hamiltonian of the system:

$$H = \sum_{n=0}^{N} \left\{ \frac{Q_n^2}{2\delta x c_0} + \frac{[\Phi_{n+1} - \Phi_n]^2}{2\delta x l_0} \right\}. \tag{2.23}$$

We now consider the continuum limit $N \to \infty$ and $\delta x \to 0$. We define the charge density $Q(x) = Q_n/\delta$ and the continuum flux $\Phi_n = \Phi(x,t)$ and $\Phi_{n+1} = \Phi(x+\delta x, t)$.

By using

$$\lim_{\delta x \to 0} \frac{\Phi_{n+1} - \Phi_n}{\delta x} = \partial_x \Phi(x,t), \tag{2.24}$$

we find the Hamiltonian of the transmission line at a continuum limit

$$H = \int_0^d dx \left(\frac{Q(x,t)^2}{2c_0} + \frac{(\partial_x \Phi(x,t))^2}{2l_0}\right) = \int_0^d dx \mathcal{H}, \tag{2.25}$$

expressed by an integral function of Hamiltonian density $\mathcal{H}$.

The Hamiltonian in Equation 2.25 can be expressed by the sum of an infinite number of normal mode Hamiltonians:

$$H = \sum_{m=0}^{\infty} \hbar\omega_m (\hat{a}_m^\dagger \hat{a}_m + \frac{1}{2}), \tag{2.26}$$

where $\omega_m = (m+1)\omega_0$ (m=0, 1, 2...) is the mode frequency with $\omega_0/2\pi$ the frequency of fundamental mode of open-ended $\lambda/2$ resonator. The detailed mathematical treatment is given in Appendix A.

The non-commuting conjugate observables of each mode are defined as

$$\hat{\phi}_m = \sqrt{\frac{\hbar Z_m}{2}} (\hat{a}_m^\dagger + \hat{a}_m), \tag{2.27}$$

$$\hat{q}_m = i\sqrt{\frac{\hbar}{2Z_m}} (\hat{a}_m^\dagger - \hat{a}_m), \tag{2.28}$$

where $Z_m = \sqrt{L_m/C_T}$ is the characteristic impedance of mode m, with $C_T = dc_0$ the total capacitance of the resonator and $L_m \equiv 1/C_T\omega_m^2$.

It is important to notice that the amplitude of flux or charge has a spatial distribution. The standing wave imposed by open-ended boundary conditions leads to

$$\Phi_m(x) = u_m(x)\hat{\phi}_m = \sqrt{\frac{2}{d}} \cos[\frac{(m+1)\pi}{d} x]\hat{\phi}_m \tag{2.29}$$

For the fundamental mode of the resonator, the amplitude of the flux ($u_{\mathrm{m=0}}$) is the largest at the anti-nodes ($x = 0$ and $x = d$), as well as the voltage $V = \partial\Phi_{\mathrm{m=0}}/\partial t = u_0(x)\partial\hat{\phi}_0/\partial t$.

Here, we have quantized the resonator as a closed system by neglecting the effect of the input-output ports (the capacitors C_k in Figure 2.5c). These ports can shift the mode frequencies and couple the resonator to the outer world, which will be discussed in the section devoted to open quantum system. In the experiment of part two, a $\lambda/2$ resonator is used to perform charge detection in quantum dots.

Transmon artificial atom

The transmon-type artificial atom (or qubit) [67] presently is one of the most simple and widely used superconducting circuits in quantum computing and microwave quantum optics. Although it was derived from the Cooper pair box circuit, it is best described starting from a quantum harmonic LC resonator with the inductor replaced by a Josephson junction, whose non-linearity makes the transition energy

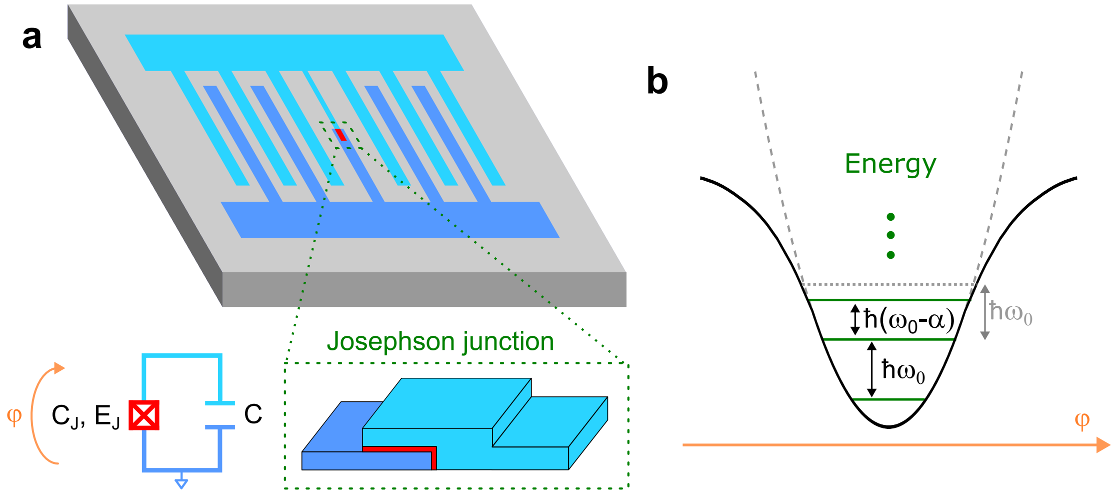

Figure 2.6: **Transmon artificial atom or qubit.** **(a)** A transmon qubit is made of a capacitor (blue) and a Josephson junction (green dash box). The light and dark blue represent the two capacitor pads of the qubit, the red the insulator in the overlap region of the two electrodes. φ is the reduced phase across the junction. **(b)** Anharmonic oscillator and unequal energy level spacing of the transmon, resulting from the Josephson nonlinearity. The gray dashed line represents the case of a harmonic oscillator with the same resonant frequency ω_0.

between subsequent levels smaller and smaller, as sketched in Figure 2.6. Consequently, the transition between the ground and first excited states can be addressed selectively, i.e. without populating higher energy levels.

The Josephson junction is made of two superconducting electrodes separated by a thin insulating barrier. In a classical treatment of the superconducting phase in the electrodes, a phase difference Φ drives a dissipationless supercurrent given by a Josephson relation:

$$I = I_c \sin\varphi = I_c \sin(2\pi\Phi/\Phi_0), \tag{2.30}$$

where the phase difference across the junction is the time integral of the voltage across the junction $\Phi = \int V dt$, $\Phi_0 = h/2e$ the magnetic flux quantum, and I_c the junction's critical current. A Josephson junction has an inductance

$$L_J(\Phi) = \left(\frac{\partial I}{\partial \Phi}\right)^{-1} = \frac{\Phi_0}{2\pi I_c}\frac{1}{\cos(2\pi\Phi/\Phi_0)}. \tag{2.31}$$

This inductance has a nonlinear dependence on the phase Φ or in the current I, in contrast with a geometric inductor. The energy stored in this nonlinear inductor can be calculated from

$$E = \int dt \frac{d\Phi}{dt} I = I_c \int d\Phi \sin(2\pi\frac{\Phi}{\Phi_0}) = -E_J \cos(2\pi\frac{\Phi}{\Phi_0}), \tag{2.32}$$

with $E_J = \Phi_0 I_c/2\pi$ the Josephson energy. The interpretation of the Josephson energy is the residual pairing energy between the electrons on the two sides of the junction induced by the tunneling of electrons across the insulating barrier. A quantized treatment of the transmon circuit shown in Figure 2.6a yields to the following Hamiltonian:

$$\hat{H} = \frac{\hat{Q}^2}{2(C_J + C_S)} - E_J \cos(2\pi\frac{\hat{\Phi}}{\Phi_0}) = E_C \hat{n}^2 - E_J \cos\hat{\varphi}, \tag{2.33}$$

where $E_C = 4e^2/2(C_J+C_S)$ is the charging energy of the total transmon capacitance with one Cooper pair. Here we have defined the reduced phase operator $\hat{\varphi} = 2\pi\hat{\Phi}/\Phi_0$ and the charge number operator as $\hat{n} = \hat{Q}/2e$. Transmon circuits are implemented in the phase regime, i.e. with the Josephson energy E_J much larger than the charging energy E_C ($E_J/E_C \gg 1$) [67]. This allows us to approximate the Hamiltonian of Equation 2.33 by

$$\hat{H}_q = E_C\hat{n}^2 + \frac{1}{2}E_J\hat{\varphi}^2 - \frac{1}{4!}E_J\hat{\varphi}^4, \tag{2.34}$$

separating the linear part of the Josephson inductance from the next order nonlinear term.

Introducing the creation and annihilation operators $\hat{b}$ and $\hat{b}^\dagger$ of one excitation in the transmon as

$$\hat{\varphi} = (\frac{E_C}{2E_J})^{1/4}(\hat{b}^\dagger + \hat{b}),\ \hat{n} = \frac{i}{2}(\frac{2E_J}{E_C})^{1/4}(\hat{b}^\dagger - \hat{b}), \tag{2.35}$$

the Hamiltonian becomes

$$\hat{H}_q = \sqrt{2E_JE_C}\hat{b}^\dagger\hat{b} - \frac{E_C}{48}(\hat{b}^\dagger + \hat{b})^4 \approx \hbar\omega_q\hat{b}^\dagger\hat{b} - \frac{E_C}{8}\hat{b}^\dagger\hat{b}^\dagger\hat{b}\hat{b}, \tag{2.36}$$

where a rotating wave approximation has been made on the right, and $\omega_q = \sqrt{2E_JE_C} - E_C/4$ is the frequency between the ground and first excited states. The second term represents the nonlinearity of the transmon, whose resonance frequency decreases with the number of excitations.

The anharmonicity makes it possible to selectively address the first two levels $\{|g\rangle, |e\rangle\}$ of the transmon, so that the transmon Hamiltonian (Equation 2.36) can be truncated to these two states and the creation and anihilation operators replaced in the following way: $\hat{b} \to \hat{\sigma}_-$, $\hat{b}^\dagger \to \hat{\sigma}_+$, $\hat{b}^\dagger\hat{b} \to \hat{\sigma}_+\hat{\sigma}_- = (\mathbb{1} + \hat{\sigma}_z)/2$. Redefining the reference for energy, the restriction of the trasmon Hamiltonian writes:

$$\hat{H} = \frac{1}{2}\hbar\omega_q\hat{\sigma}_z. \tag{2.37}$$

As any other two-level system or fictitious spin 1/2, the transmon qubit can be pictured on a Bloch sphere (see Figure 2.7). An arbitrary superposition

$$|\psi\rangle = \cos\frac{\theta}{2}|g\rangle + e^{i\varphi}\sin\frac{\theta}{2}|e\rangle, \tag{2.38}$$

of its basis states $\{|g\rangle, |e\rangle\}$ is represented by a vector tilted by an azimuth angle θ and rotated by a meridian angle φ. In this representation, the "north pole" and "south pole" of the sphere correspond to the basis states $|g\rangle$ and $|e\rangle$, whereas equally superposed states $(|g\rangle + e^{i\varphi}|e\rangle)/\sqrt{2}$ fall on the equator.

This Bloch sphere representation is a useful tool for visualizing and understanding the dynamics of any two-level system. The application of a unitary evolution to the system results in a rotation of the corresponding vector on the sphere. In Section 2.4.1, we introduce the physics of electron spin resonance and see how a harmonic microwave drive rotates the spin around certain axes, allowing us to manipulate and control the spin state.

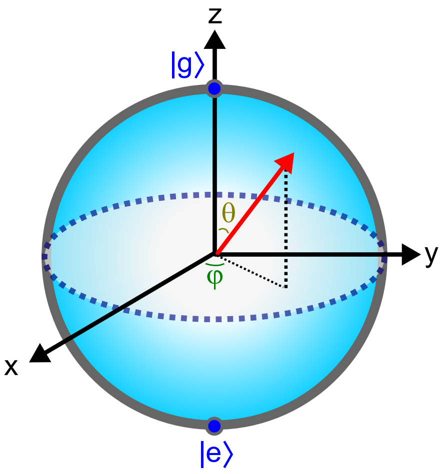

Figure 2.7: **Bloch sphere representation of a qubit.** Any pure state of a quantum two-level system being a superposition of its ground state $|g\rangle$ and excited state $|e\rangle$), it can always be represented by a vector on the sphere (red arrow).

2.2.2 Spins magnetically coupled to a resonator

Spins are intrinsic magnetic dipoles and they couple naturally to the magnetic component of the microwave field in a resonator through magnetic dipole interaction. We use below a fully quantum model to treat the resonator, the spins and their interaction.

Single spin magnetically coupled to a resonator

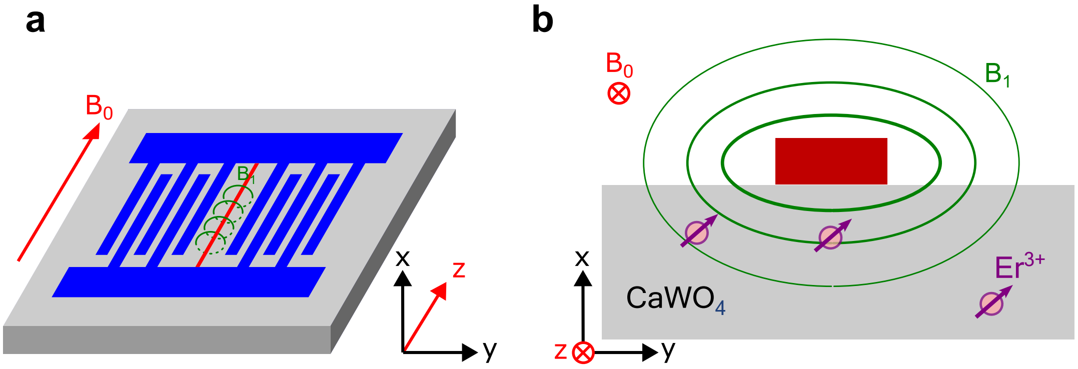

Figure 2.8: **Spins magnetically coupled to a lumped-element LC resonator.** **(a)** Lumped-element resonator implemented by an inductive wire (red) and interdigitated capacitors (blue) on $Er^{3+}:CaWO_4$ crystal (gray). A static field B_0 is applied along the z axis, which is defined by the direction of the wire at the center of the resonator. An oscillating field B_1 (green) is generated around the wire. **(b)** Cross-section of the wire and crystal. The spins of erbium ions (Er^{3+}) in the bulk crystal are magnetically coupled to the oscillating magnetic field B_1 generated by the inductive wire.

We first consider the case of a single spin magnetically coupled to the electromagnetic field $\mathbf{B_1}$ inside a resonator while a non-zero static magnetic field $\mathbf{B_0}$ is applied, as depicted in Figure 2.8. The total Hamiltonian of the system

$$\hat{H} = \hat{H}_0 + \hat{H}_{int} = \hat{H}_r + \hat{H}_s + \hat{H}_{int} \tag{2.39}$$

involves the resonator Hamiltonian $\hat{H}_r$, the spin Hamiltonian $\hat{H}_s$ and the spin-resonator interaction $\hat{H}_{int}$. The first two terms $\hat{H}_0 \equiv \hat{H}_r + \hat{H}_s$ are regarded as the static Hamiltonian of the system, whereas the interaction $\hat{H}_{int}$ is regarded as a perturbation.

The resonator is modeled as the quantized harmonic oscillator of the previous section, with Hamiltonian

$$\hat{H}_r = \hbar\omega_0(\hat{a}^\dagger\hat{a} + \frac{1}{2}). \tag{2.40}$$

The spin Hamiltonian

$$\hat{H}_s = \hbar\gamma_e\mathbf{B_0} \cdot \hat{\mathbf{S}} \tag{2.41}$$

comes from the Zeeman energy of the spin in the applied static field $\mathbf{B_0}$, with $\hat{\mathbf{S}}$ the spin operator. Note that in this experiment we only consider the $I = 0$ erbium isotope and zero field splitting caused by hyperfine interaction between erbium electronic spin and tungsten nuclear spins bath is negligible.

For a spin S=1/2, the Hilbert space of $\hat{H}_s$ is two-dimensional, the spin operator $\hat{\mathbf{S}} \rightarrow \hat{\sigma}/2$ is expressed in terms of the Pauli matrices, and choosing a reference frame in which the magnetic field is along z yields

$$\hat{H}_s = \frac{1}{2}\hbar\omega_s\hat{\sigma}_z, \tag{2.42}$$

with $\omega_s = \gamma_e B_0$ the Larmor angular frequency of the spin in B_0. The two eigen-energies E_g and E_e associated to the ground and excited eigenstates $|g\rangle$ and $|e\rangle$ thus differ by $\hbar\omega_s$.

The resonator field $\hat{\mathbf{B}}_1(\mathbf{r}) = \delta\mathbf{B}(\mathbf{r})(\hat{a}^\dagger + \hat{a})$ at frequency ω_0 also couples to the spin through magnetic dipole interaction, resulting in

$$\hat{H}_{int} = \hbar\gamma_e\hat{\mathbf{B}}_1(\mathbf{r}) \cdot \hat{\mathbf{S}} = \hbar\gamma_e(\hat{a}^\dagger + \hat{a})\delta\mathbf{B}(\mathbf{r}) \cdot \hat{\mathbf{S}}, \tag{2.43}$$

where $\delta\mathbf{B}(\mathbf{r})$ is the zero-point fluctuation of magnetic field at the spin position $\mathbf{r}$.

Expressing the Hamiltonian in the unperturbed $\{|g\rangle, |e\rangle\}$ basis and introducing the ladder operators

$$\hat{\sigma}_+ = |e\rangle\langle g|,\ \hat{\sigma}_- = |g\rangle\langle e|, \tag{2.44}$$

the interaction rewrites

$$\hat{H}_{int} = \hbar(\hat{a}^\dagger + \hat{a})(g_0\hat{\sigma}_+ + g_0^*\hat{\sigma}_- + \alpha_g|g\rangle\langle g| + \alpha_e|e\rangle\langle e|), \tag{2.45}$$

where

$$g_0 = \gamma_e\langle e|\delta\mathbf{B_1} \cdot \hat{\mathbf{S}}|g\rangle \tag{2.46}$$

is the coupling constant describing the strength of the resonator field-induced spin transition, and $\alpha_g = \gamma_e\langle g|\delta\mathbf{B_1} \cdot \hat{\mathbf{S}}|g\rangle$ and $\alpha_e = \gamma_e\langle e|\delta\mathbf{B_1} \cdot \hat{\mathbf{S}}|e\rangle$ are small corrections on the eigen-energies. Note that $\hat{H}_{int}$ being Hermitian ($\hat{H}_{int} = \hat{H}_{int}^\dagger$), it has real off-diagonal element $g_0 = g_0^*$. In Section 3.1.2, we will estimate this coupling constant g_0 using the dimensions in our implementation of the device.

We then treat the total Hamiltonian as a static part $\hat{H}_0 = \hat{H}_r + \hat{H}_s$ perturbed by $\hat{H}_{int}$, using the interaction picture. Applying the unitary transformation

$$\hat{U}_0(t) = e^{i\hat{H}_0 t/\hbar} = e^{i\omega_s \hat{\sigma}_z t/2} e^{i\omega_r (\hat{a}^\dagger \hat{a} + \frac{1}{2})t/2}, \tag{2.47}$$

the Hamiltonian of the system $\hat{H}'(t) = \hat{U}_0(t)\hat{H}\hat{U}_0^\dagger(t) + i\dot{\hat{U}}_0(t)\hat{U}_0^\dagger(t)$ is expressed in a frame rotating at the Larmor frequency for the spin and at the resonator frequency for the resonator field:

$$\begin{aligned} \hat{H}'(t) &= \hat{U}_0(t)\hat{H}_{int}\hat{U}_0^\dagger(t) && (2.48) \\ &= \hbar g_0 \left(\hat{a}\hat{\sigma}_+ e^{i(\omega_s-\omega_0)t} + \hat{a}\hat{\sigma}_- e^{-i(\omega_s+\omega_0)t} + \hat{a}^\dagger\hat{\sigma}_+ e^{i(\omega_s+\omega_0)t} + \hat{a}^\dagger\hat{\sigma}_- e^{-i(\omega_s-\omega_0)t} \right) \\ &\quad + \hbar(\hat{a}e^{-i\omega_0 t} + \hat{a}^\dagger e^{i\omega_0 t})(\alpha_g|g\rangle\langle g| + \alpha_e|e\rangle\langle e|) && (2.49) \\ &\sim \hbar g_0 \left(\hat{a}\hat{\sigma}_+ e^{i(\omega_s-\omega_0)t} + \hat{a}^\dagger\hat{\sigma}_- e^{-i(\omega_s-\omega_0)t} \right). && (2.50) \end{aligned}$$

The simplified Equation 2.50 corresponds to the rotating wave approximation and neglects all the terms that do not conserve the total number of excitations in the spin-resonator system: the fast rotating terms $\pm(\omega_s+\omega_0)$ compared to $\pm(\omega_s-\omega_0)$, and the terms in which the frequency corrections α_g and α_e are much smaller than the resonator frequency ω_0. Note that this rotating wave approximation is valid only if $\omega_s + \omega_0 \gg g_0$, $|\omega_s - \omega_0|$ and $\omega_0 \gg \alpha_g$, α_e.

Returning back to the Schrödinger picture, the interaction Hamiltonian

$$\hat{H}_{int} = \hbar g_0 (\hat{a}^\dagger \hat{\sigma}_- + \hat{a}\hat{\sigma}_+) \tag{2.51}$$

describes the two opposite processes that can occur at the rate g_0: the spin emits one photon ($\hat{a}^\dagger\hat{\sigma}_-$) into the resonator by relaxing from its excited state to its ground state ; or it absorbs one photon from the resonator ($\hat{a}\hat{\sigma}_+$) in the opposite transition.

Finally, the total Hamiltonian of the system

$$\hat{H} = \hbar\omega_0(\hat{a}^\dagger\hat{a} + \frac{1}{2}) + \frac{1}{2}\hbar\omega_s\hat{\sigma}_z + \hbar g_0(\hat{a}^\dagger\hat{\sigma}_- + \hat{a}\hat{\sigma}_+) \tag{2.52}$$

takes the form of the well-known Jaynes-Cummings Hamiltonian [97] that describes the coherent behavior of excitation exchange between a two-level atom and a quantized electromagnetic mode (in our case, a single spin coupled to the resonator field).

2.2.3 Open quantum systems

Modeling the dissipation

The spin-resonator system discussed up to now was a closed system without interactions with the outer world. In this section, we open our quantum system, i.e. we include the effect of the environment surrounding the spins, and we couple the resonator to the outer world as sketched in Figure 2.9: the resonator has internal losses characterized by a rate κ_i, and is capacitively coupled to a transmission line with which it can exchange energy at a rate κ_c. As for the spins, their energy can leak away by exciting phonons in their host crystal (spin-lattice relaxation), or leak to the transmission line through the resonator by a radiative process at a rate Γ_R (as described below). In addition, the fluctuations of the magnetic environment (surrounding nuclear spins and external magnetic field) cause spin decoherence. Here, we model all these processes.

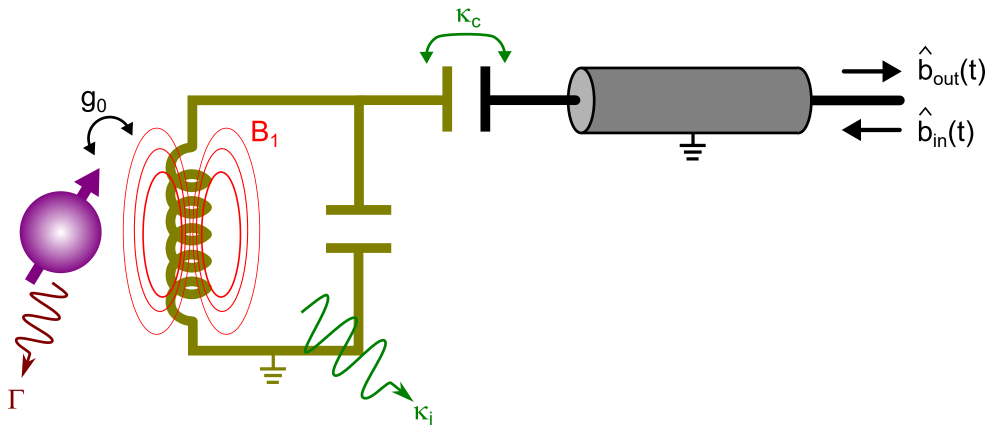

Figure 2.9: **Spin-resonator system interacting with its environment.** A single spin with a decoherence rate Γ is coupled with a coupling strength g_0 to the resonator through the magnetic field B_1. The resonator has an internal decay rate κ_i, and is coupled to a transmission line at a rate κ_c. $\hat{b}_{\text{in}}(t)$ and $\hat{b}_{\text{out}}(t)$ are the input and output field operators on the line at the resonator port.

It is first needed to introduce a more powerful formalism. Whereas unitary transformations describe the quantum coherent evolution of our system when it is isolated, its dynamics becomes non-unitary and irreversible once it is open. The system may evolve into a statistical mixture $\{p_i, \psi_i\}$ of several different states labeled i, where p_i is the probability of finding the system in a pure state $|\psi_i\rangle$. The general state of our open system is fully described by its density operator

$$\hat{\rho} = \sum_i p_i |\psi_i\rangle\langle\psi_i|. \tag{2.53}$$

The open system dynamics is described by a master equation that gives the explicit form of the time derivative of the density matrix $\hat{\rho}$.

In general, the environment takes away quantum information about the system under study, but can also send it back later to the system. When the time after which the environment has completely forgotten previously acquired information is much shorter than the shortest timescale of the system dynamics, the memory of the environment can be neglected. Assuming this Markovian approximation applies, the master equation takes a simple Lindblad form:

$$\frac{\mathrm{d}\hat{\rho}}{\mathrm{d}t} = \frac{1}{i\hbar}[\hat{H}, \hat{\rho}] + \sum_k \left(\hat{L}_k \hat{\rho} \hat{L}_k^\dagger - \frac{1}{2}\{\hat{L}_k^\dagger \hat{L}_k, \hat{\rho}\} \right). \tag{2.54}$$

This equation describes the dynamics in the Schrödinger's picture, and includes the coherent evolution under the system Hamiltonian (the first term) as well as the incoherent evolution due to several different decoherence mechanisms (labeled k) occurring in parallel. The operators $\hat{L}_k$, also called quantum jump operators of channel k, and the $\hat{L}_k \hat{\rho} \hat{L}_k^\dagger$ terms describe the evolution due to quantum jumps along the channel. Each corresponding anti-commutator term $\{\hat{L}_k^\dagger \hat{L}_k, \hat{\rho}\}/2$ describes the evolution when no jump occurs along the channel.

We now discuss in detail the different dissipative channels involved in our system, and give their corresponding Lindblad operators:

- **Spin decoherence:** Spins coupled to the environment suffer from two types of decoherence mechanisms: energy relaxation and pure dephasing. In the first case, the environment takes away the energy from excited spins, which results in a change of the longitudinal polarization $\langle\hat{\sigma_z}\rangle$ of the spins. In the second case, $\langle\hat{\sigma_z}\rangle$ does not change, but the spin transition frequency fluctuates due to the environment, leading to the accumulation of a random relative phase between different spin states.

- **Energy relaxation.** In general, spin relaxation in a solid with rate Γ_1 is dominated by a non-radiative decay channel in which spins exchange energy with the phonons in the crystal. The associated rate Γ_{NR} that characterizes this spin-lattice relaxation process, depends on both the spin-phonon coupling strength and the spin frequency. At finite temperature, the environment contains an average number $\bar{n}_{th} = 1/[\exp(\hbar\omega_s/k_BT) - 1]$ of thermal phonons that lead to relaxation rates $\Gamma_{\mathrm{NR}}(\bar{n}_{th}+1)$ for downward transition $\hat{\sigma}_-$ and $\Gamma_{\mathrm{NR}}\bar{n}_{th}$ for upward transition $\hat{\sigma}_+$. The corresponding Lindblad operators of these processes are

$$\hat{L}_{s-} = \sqrt{\Gamma_{\mathrm{NR}}(\bar{n}_{th}+1)}\hat{\sigma}_-, \tag{2.55}$$

$$\hat{L}_{s+} = \sqrt{\Gamma_{\mathrm{NR}}\bar{n}_{th}}\hat{\sigma}_+. \tag{2.56}$$

- **Pure dephasing.** In the host crystal, the bath of all kinds of nuclear spins undergoing flip-flop transitions is a source of fluctuating magnetic field for electronic spins. In addition, the current in the coil generating the static magnetic field can also fluctuate. As a result, the noisy magnetic environment leads to fluctuations of the spin transition frequency and therefore to dephasing. This can be understood from the time evolution of a spin under its free Hamiltonian $H_0 = \hbar\omega_s\hat{\sigma}_z/2$, in presence of low frequency fluctuations of the frequency. After a time Δt, the spin accumulates a phase difference from the expected one $\Delta\varphi = \omega_s\Delta t$. The rate Γ_φ characterizes the speed at which $\Delta\varphi$ is lost ; the corresponding Lindblad operator is

$$\hat{L}_{s\varphi} = \sqrt{\Gamma_\varphi}\hat{\sigma}_z. \tag{2.57}$$

The total decoherence rate Γ_2 and coherence time T_2 of the spin combine relaxation and pure dephasing in parallel, hence

$$\Gamma_2 = \frac{\Gamma_1}{2} + \Gamma_\varphi,\, T_2 = \frac{1}{2T_1} + \frac{1}{T_\varphi}, \tag{2.58}$$

with T_1 and T_φ the energy relaxation time and the pure dephasing time.

Resonator relaxation The relaxation of the resonator is due to exchanges of photons with its environment, described by $\hat{a}$ and $\hat{a}^\dagger$. Our resonator is made of a metallic thin film fabricated on top of a host crystal. The materials contain many microscopic defects (such as defects in the oxide and at material interface) which can exchange energy with the macroscopic resonator mode. This process is characterized by an internal loss rate κ_i. Meanwhile, the resonator has been coupled on purpose with a coupling rate κ_c to the outside transmission line. Therefore, the total resonator decay rate is $\kappa = \kappa_i + \kappa_c$. At finite temperature, the photon bath of the environment contains an average number $\bar{n}_{th} = 1/[\exp(\hbar\omega_r/k_B T) - 1]$ of thermal photons; it can either give a photon to the resonator ($\hat{a}^\dagger$) or take one away from the resonator ($\hat{a}$). The total rate depends on the thermal photon number $\bar{n}_{th}$ and the decay rate κ. The Lindblad operators describing this process are

$$\hat{L}_{r-} = \sqrt{\kappa(\bar{n}_{th} + 1)}\hat{a}, \tag{2.59}$$

$$\hat{L}_{r+} = \sqrt{\kappa\bar{n}_{th}}\hat{a}^\dagger. \tag{2.60}$$

Purcell effect

Discovered by Purcell in 1946, the spontaneous radiative emission rate of an excited atom can be enhanced when the atom is incorporated in a resonant cavity. This so-called Purcell effect also applies to a cQED system when a superconducting artificial atom or a spin is coupled to an external line through a resonator [98, 3]. One can understand this phenomenon intuitively by considering the leaky resonator as a new environment for the spin with a density of states concentrated at the spin frequency when both systems are on resonance. The resonator decays so quickly compared to the spin that the excitation shared by both objects cannot be kept long. Then the spin gains an effectively faster decay rate than if the resonator was absent. Equipped with the theoretical tool introduced before for describing the spin-resonator system with dissipation, we are now able to give explicitly the resonator-induced spin relaxation rate (Purcell rate), following an approach similar to [99, 100, 9].

We start here with the spin-resonator Hamiltonian of Equation 2.52 in the rotating frame that corresponds to the unitary transformation $\hat{U}_0(t) = \exp(i\hat{H}_0 t/\hbar)$ with $\hat{H}_0 = \hbar\omega_r(\hat{a}^\dagger\hat{a} + 1/2) + \hbar\omega_r\hat{\sigma}_z/2$, so that

$$\hat{H}' = \frac{\hbar\delta}{2}\hat{\sigma}_z + \hbar g_0(\hat{a}^\dagger\hat{\sigma}_- + \hat{a}\hat{\sigma}_+) \tag{2.61}$$

with $\delta = \omega_s - \omega_r$ the spin-resonator frequency detuning.

Under our experimental conditions (spin in a solid at 10 mK measured with microwave, where $\hbar\omega_s \gg k_B T$), the spontaneous emission rate of the spin is negligible compared to the resonator decay rate. In addition, the average number of thermal photons $\bar{n}_{th} \sim 0$ is also negligible. This situation leads to a single jump operator $\hat{L} = \sqrt{\kappa}\hat{a}$ which describes the decay of the system by emitting one photon into the environment. The Equation 2.54 is written as

$$\frac{\mathrm{d}\hat{\rho}}{\mathrm{d}t} = \frac{1}{i\hbar}[\hat{H}', \hat{\rho}] + \kappa(\hat{a}\hat{\rho}\hat{a}^\dagger - \frac{1}{2}\hat{a}^\dagger\hat{a}\hat{\rho} - \frac{1}{2}\hat{\rho}\hat{a}^\dagger\hat{a}). \tag{2.62}$$

Given that the system has at most one excitation, the density operator can be restricted to a 3-dimensional subspace defined by the states $|e, 0\rangle$, $|g, 1\rangle$ and $|g, 0\rangle$ such that

$$\begin{pmatrix} \dot{\rho}_{e0,e0} \\ \dot{\rho}_{g1,g1} \\ \dot{\rho}_{e0,g1} - \dot{\rho}_{g1,e0} \\ \dot{\rho}_{e0,g1} + \dot{\rho}_{g1,e0} \end{pmatrix} = \begin{pmatrix} 0 & 0 & ig & 0 \\ 0 & -\kappa & -ig & 0 \\ 2ig & -2ig & -\kappa/2 & -i\delta \\ 0 & 0 & -i\delta & -\kappa/2 \end{pmatrix} \begin{pmatrix} \rho_{e0,e0} \\ \rho_{g1,g1} \\ \rho_{e0,g1} - \rho_{g1,e0} \\ \rho_{e0,g1} + \rho_{g1,e0} \end{pmatrix}. \tag{2.63}$$

The population of ground state $|g,0\rangle$ increases at a rate κ as $\dot{\rho}_{g0,g0} = \kappa\rho_{g1,g1}$.

In the weak-coupling regime ($\kappa \gg g_0$), the cavity decays faster than the time for the spin and resonator to exchange a photon, so that the cavity remains empty at all times and the probability of finding the system in state $|g,1\rangle$ is negligible (i.e. $\rho_{g1,g1} \sim 0$). We also assume the coherence of the system $\rho_{e0,g1}$ and $\rho_{g1,e0}$ follows adiabatically the change of the excited state population [9], resulting in $\dot{\rho}_{e0,g1} = 0$ and $\dot{\rho}_{g1,e0} = 0$.

Finally, we obtain the equation of evolution for the population of state $|e,0\rangle$:

$$\dot{\rho}_{e0,e0} = -\Gamma_R\,\rho_{e0,e0}, \tag{2.64}$$

with

$$\Gamma_R = \frac{\kappa g_0^2}{\frac{\kappa^2}{4} + \delta^2} \tag{2.65}$$

the Purcell-enhanced radiative emission rate. When the spin and the resonator are in resonance ($\delta = 0$), the Purcell rate reaches its maximum

$$\Gamma_R = \frac{4g_0^2}{\kappa}. \tag{2.66}$$

This formula shows that increasing the spin-resonator coupling constant g_0 and the quality factor $Q = \omega_0/\kappa$ (i.e. decreasing the resonator loss rate κ) yields a larger radiative emission rate. Bismuth donors spins in silicon coupled to a high-Q resonator with small mode volume have for instance been used to demonstrate the control of $\Gamma_R(\delta)$ over 3 orders of magnitude [3]. Below a certain δ, spontaneous emission of photons to the coupled resonator becomes the dominant relaxation mechanism for spins in the solid, such that $\Gamma_1 = \Gamma_R + \Gamma_{\mathrm{NR}} \sim \Gamma_R$. In our experiment, we will work in the Purcell regime where radiative decay dominates.

Input-output theory

The master equation of an open quantum system describes the time-evolution of its state $\hat{\rho}$, but not what leaks out of it. In our case, given the radiated field leaking in the transmission line attached to the resonator precisely provides the signal that we measure experimentally, its knowledge is needed. To obtain its dynamics in Heisenberg's picture, a quantum Langevin equation is needed [101, 102]. In our case, this equation is derived within the input-output formalism that keeps track on the input and output fields on the transmission line.

As indicated in Figure 2.9, we introduce the input and output fields in the transmission line, $\hat{b}_{\mathrm{in}}(t)$ and $\hat{b}_{\mathrm{out}}(t)$, that are coupled to the resonator with coupling constant κ_c. The input field is usually either vacuum noise or a coherent drive. In addition, we can also model the internal loss channel κ_i of the resonator as another fictitious transmission line with $\hat{b}_{\mathrm{in,int}}$ and $\hat{b}_{\mathrm{out,int}}$ input and output fields.

Using these definitions and $\kappa = \kappa_i + \kappa_c$, the dynamics of the intra-resonator field $\hat{a}(t)$ follows the quantum Langevin equation and input-output relation

$$\dot{\hat{a}}(t) = \frac{1}{i\hbar}[\hat{a}(t), \hat{H}] - \frac{\kappa}{2}\hat{a}(t) + \sqrt{\kappa_c}\hat{b}_{\mathrm{in}}(t) + \sqrt{\kappa_i}\hat{b}_{\mathrm{in,int}}(t), \tag{2.67}$$

$$\hat{b}_{\mathrm{out}}(t) + \hat{b}_{\mathrm{in}}(t) = \sqrt{\kappa}\hat{a}(t). \tag{2.68}$$

In Equation 2.67, the first term is the equation of motion of $\hat{a}(t)$ in the Heisenberg's picture under the sole system Hamiltonian $\hat{H}$. The second term describes the damping of intra-resonator field, whereas the third and fourth terms are the input fields penetrating the resonator. Equation 2.68 simply expresses that the sum of the incoming and outgoing fields is equal to the resonator field loss. If there are several ports j coupled to the system, one has simply to sum the damping terms $\sum \kappa_{c,j}\hat{a}(t)/2$ and the inputs terms $\sqrt{\kappa_{c,j}}\hat{b}_{\mathrm{in,j}}(t)$ in Equation 2.67, and use one Equation 2.68 (with a j index) per port.

2.2.4 Measurements

To obtain the absorption spectrum of a given system, the standard technique is to apply to it a coherent drive with certain frequency and to monitor the transmitted or reflected signal, or scattering coefficient $S = S_{\mathrm{in\,out}}$. The frequency-dependent S contains spectroscopic information about the system under study. This method is used throughout the thesis in both experiments to measure the resonant frequency of resonators. We now use the introduced input-output formalism to quantify the coherent drive and scattering matrix.

Coherent drive

The microwave drive used in our experiment is considered as classical (i.e. a coherent drive with an average number of photons so large that its relative fluctuations are negligible). A continuous propagating microwave with frequency ω_d and phase ϕ_d is represented by a complex field amplitude $\beta(t) = A(t)\exp(-i\omega_d t - i\phi_d)$, having the dimension of square root of photons per second. Applying this incoming classical drive field to the input of the resonator replaces $\hat{b}_{\mathrm{in}}(t)$ with $\hat{b}_{\mathrm{in}}(t) + \beta(t)$ in the Langevin Equation 2.67.

As a result, this equation gains an extra term $\sqrt{\kappa_c}\beta(t)$ that can be absorbed in the system Hamiltonian by replacing $\hat{H}$ as $\hat{H} \to \hat{H} + \hat{H}_d$, where

$$\hat{H}_d = \hbar[\varepsilon(t)\hat{a}^\dagger e^{-i\omega_d t - i\phi_d} + \varepsilon(t)^* \hat{a} e^{i\omega_d t + i\phi_d}] \tag{2.69}$$

is the driven Hamiltonian with $\varepsilon(t) = i\sqrt{\kappa}A(t)$ the effective complex amplitude of the drive seen by the resonator. In fact, this way of including a coherent drive can be generalized to multiple drives, each drive bringing one extra term of the form Equation 2.69 in the total Hamiltonian. By definition, the power of the drive is $P_{\mathrm{in}} = \hbar\omega_0\langle\hat{b}_{\mathrm{in}}^\dagger\hat{b}_{\mathrm{in}}\rangle = \hbar\omega_0|\beta(t)|^2$. Under the coherent drive, the time-evolution unitary $\exp(i\hat{H}_d t/\hbar)$ is equivalent to a displacement operator. If the resonator mode begins with a vacuum, the external drive will lead to a coherent state $|\alpha\rangle$ for the intra-resonator mode.

We now consider the case of only the resonator with a simple harmonic oscillator Hamiltonian $\hat{H} = \hbar\omega_0\hat{a}^\dagger\hat{a}$ and study the response of the steady state of the system in driven-damped situation. We use the mean value of the intra-resonator field $\langle\hat{a}\rangle(t) = \alpha(t)$ and the complex amplitude of the drive in Equation 2.67:

$$\dot{\alpha}(t) = -i\omega_0\alpha(t) - \frac{\kappa_i + \kappa_c}{2}\alpha(t) + \sqrt{\kappa_c}\beta(t). \tag{2.70}$$

After a Fourier transform, the spectral relation between the incoming field and intra-resonator field can be easily obtained as follows

$$\alpha(\omega) = \frac{\sqrt{\kappa_c}}{(\kappa_i + \kappa_c)/2 - i(\omega - \omega_0)}\beta(\omega) \tag{2.71}$$

The mean photon number $\bar{n}$ inside the resonator at steady-state equals to $|\alpha|^2$, which is determined by the intra-resonator field amplitude and drive amplitude as well. At resonance ($\omega = \omega_0$), we have

$$\bar{n} = \frac{4\kappa_c|\beta|^2}{(\kappa_i + \kappa_c)^2} = \frac{4\kappa_c P_{\text{in}}}{\hbar\omega_0(\kappa_i + \kappa_c)^2} \tag{2.72}$$

In our experiment, where spins are magnetically coupled to the fluctuating magnetic field around the inductor, it is also interesting to know the strength of the oscillating current and magnetic field given by an incident power. With the mean photon number, they can be easily obtained as

$$\langle\hat{I}\rangle(t) = 2\delta I\sqrt{\bar{n}}\cos\omega_0 t, \tag{2.73}$$

$$\langle\hat{\mathbf{B}}(\mathbf{r})\rangle(t) = 2\delta\mathbf{B}(\mathbf{r})\sqrt{\bar{n}}\cos\omega_0 t. \tag{2.74}$$

Scattering matrix

In an experiment, the spectroscopic measurements on a resonator is usually performed with a one- or two-port network, as shown in Figure 2.10. The measured transmission and reflection coefficients are contained in a scattering matrix. An instrument called Vector Network Analyser (VNA) gives access to the S-matrix as a function of probe frequency. For a two-port network, the transmission coefficients are recorded in S_{12} (transmission from 2 to 1) and S_{21} (transmission from 1 to 2) components of the S-matrix. The reflection coefficients are recorded in S_{11} (reflection on port 1) and S_{22} (reflection on port 2). Classically, these coefficients can be obtained from the ratio of input and output voltages (or currents) on the designated ports while keeping the unrelated ports undriven. Here we will use the framework of coherent drive introduced in the previous section to quantify the S-matrix.

At steady state, the components of the S-matrix are the ratios between the output signal $\beta_{\text{out,j}}$ on port j and the applied input coherent drive $\beta_{\text{in,i}}$ on port i, while $\beta_{\text{in,k}}$ is kept at 0 for any $k \neq i$. The full matrix is as follows:

$$S(\omega) = \begin{bmatrix} S_{11}(\omega) & S_{12}(\omega) \\ S_{21}(\omega) & S_{22}(\omega) \end{bmatrix} = \begin{bmatrix} \beta_{\text{out},1}(\omega)/\beta_{\text{in},1}(\omega) & \beta_{\text{out},1}(\omega)/\beta_{\text{in},2}(\omega) \\ \beta_{\text{out},2}(\omega)/\beta_{\text{in},1}(\omega) & \beta_{\text{out},2}(\omega)/\beta_{\text{in},2}(\omega) \end{bmatrix}. \tag{2.75}$$

Note that all the matrix elements are frequency dependent.

The input-output relations in Equation 2.68 can also be adapted for coherent signal, such as $\beta_{\text{in,j}}(\omega) + \beta_{\text{out,j}}(\omega) = \sqrt{\kappa_{c,j}}\beta(\omega)$ for port j. Therefore, we can write explicitly the expression for the complex components of the S-matrix:

- **Reflection:**

$$S_{11}(\omega) = \frac{\sqrt{\kappa_{\text{c},1}}\beta(\omega) - \beta_{\text{in},1}}{\beta_{\text{in},1}} = \frac{(\kappa_{\text{c},1} - \kappa_{\text{i}})/2 + i(\omega - \omega_0)}{(\kappa_{\text{c},1} + \kappa_{\text{i}})/2 - i(\omega - \omega_0)}. \tag{2.76}$$

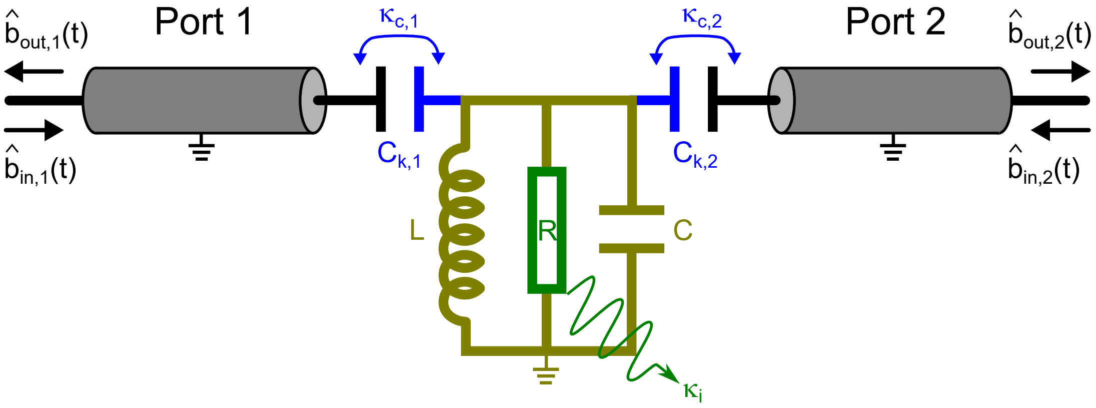

Figure 2.10: **Two-port input-output network for probing a resonator.** An RLC resonator is coupled to the outside through two ports with coupling capacitances $C_{k,1}$ and $C_{k,2}$ (corresponding coupling rates are $\kappa_{c,1}$ and $\kappa_{c,2}$ respectively). The resonator has an internal loss κ_i modelled by a resistor (green). $\hat{b}_{\mathrm{in,j}}(t)$ and $\hat{b}_{\mathrm{out,j}}(t)$ are the input and respective output fields at the port j.

Note that for the case of one port measurement, only the S_{11} parameter is accessible and in this case we can use κ_c to represent $\kappa_{c,1}$.

As shown in Figure 2.11, the amplitude of the reflection coefficient is a negative Lorentzian function. When probing on resonance ($\omega = \omega_0$), the reflection amplitude equals to $|\kappa_c - \kappa_i|/(\kappa_c + \kappa_i)$. Depending on the relation between the external coupling rate κ_c and internal damping rate κ_i, it is interesting to distinguish three different regimes:

- **Under-coupling** ($\kappa_i \gg \kappa_c$): Only a small portion of the incoming signal can enter the resonator, resulting in a small dip in the reflection amplitude and a small phase shift, while the most part of the signal is reflected back.
- **Critical coupling** ($\kappa_i = \kappa_c$): The resonator has perfect absorption at resonance and the reflection amplitude drops to 0, together with a π-shift on phase.
- **Over-coupling** ($\kappa_i \ll \kappa_c$): Big part of the signal is reflected back with a 2π phase shift across the resonance and a small part of the signal can be absorbed by the resonator. On resonance, the amplitude has a small dip.

When probing far from resonance ($\omega \gg \kappa_c + \kappa_i$), the reflection amplitude is approaching one, $|S_{11}| \to 1$, which means perfect reflection and the signal cannot enter the resonator. This makes a reflection measurement “self-calibrated” such that fitting the $S_{11}(\omega)$ can give directly both internal and external rates [103]. Since the reflection measurement requires only one line, it can also bring some inconvenience in practice. For measurements at low temperature (our case), the input line is usually heavily attenuated to remove the radiation

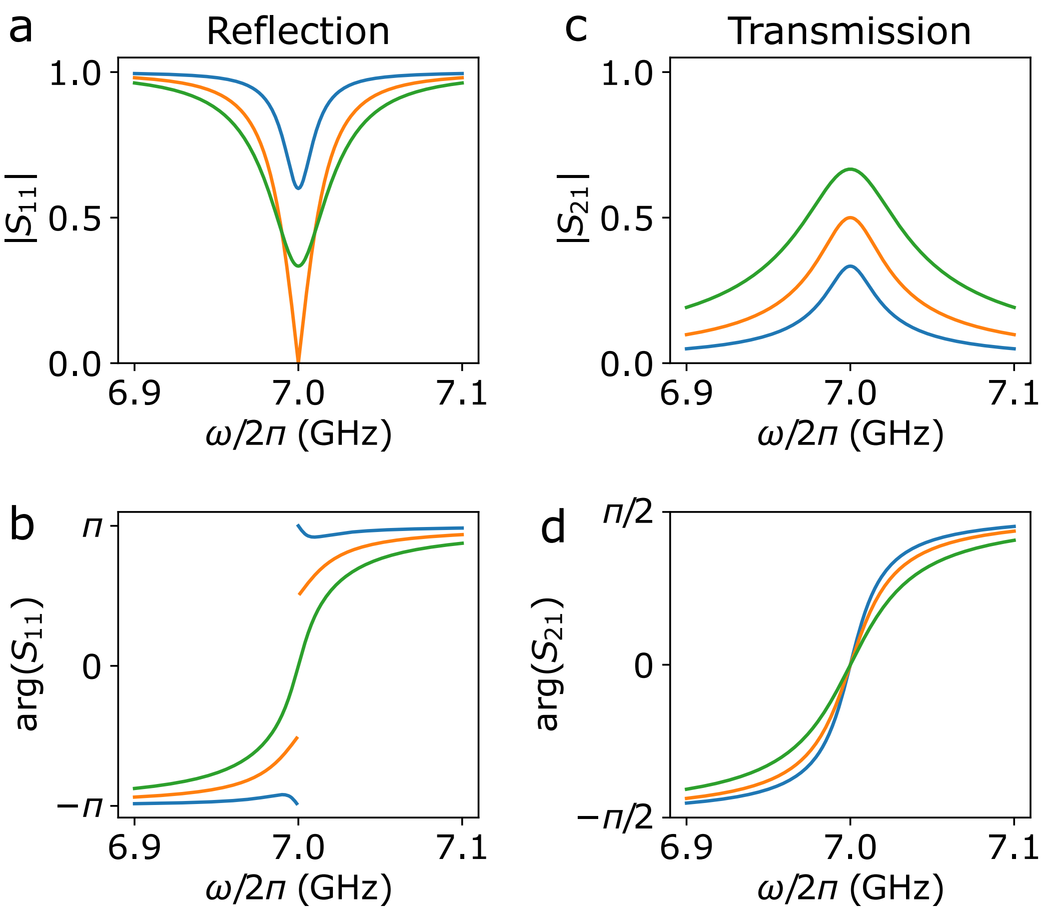

Figure 2.11: **Calculated reflection and transmission spectrum.** For reflection measurements, amplitude (a) and phase (b) of reflection coefficient are plotted S_{11} as function of probe frequency ω. The resonator has a resonant frequency $\omega_0/2\pi = 7$ GHz and internal loss rate $\kappa_i/2\pi = 20$ MHz. The external coupling rates are chosen to be $\kappa_c = \kappa_i/4$ (blue), κ_i (orange), $2\kappa_i$ (green). For transmission measurements, amplitude (c) and phase (d) of reflection coefficient are plotted S_{21} as function of probe frequency ω. We consider the case of symmetric coupling $\kappa_{c,1} = \kappa_{c,2}$ and $\kappa_{c,1} + \kappa_{c,2} = \kappa_i/2$ (blue), κ_i (orange), $2\kappa_i$ (green).

coming from high temperature stage, therefore we need to separate the input and output lines with a circulator to avoid the signal being attenuated twice when going out. This increases the complexity of the measurement setup. In the first experiment of this thesis, we measure reflection of the system.

- **Transmission:**

$$S_{21}(\omega) = \frac{\sqrt{\kappa_{c,2}}\beta(\omega) - \beta_{\text{in},1}}{\beta_{\text{in},1}} = \frac{\sqrt{\kappa_{c,1}\kappa_{c,2}}}{(\kappa_{c,1} + \kappa_{c,2} + \kappa_{\text{i}})/2 - i(\omega - \omega_0)}. \tag{2.77}$$

As shown in Figure 2.11, the amplitude of transmission coefficient is a positive Lorentzian function and reaches its maximum $4\sqrt{\kappa_{c,1}\kappa_{c,2}}/(\kappa_{c,1} + \kappa_{c,2} + \kappa_i)$ at resonance ($\omega = \omega_0$). In the region far from resonance ($\omega \gg \kappa_{c,1} + \kappa_{c,2} + \kappa_i$), the amplitude is approaching zero $|S_{21}| \to 0$. We notice that it is impossible to independently distinguish the coupling rates at port 1 and port 2 by only measuring the $|S_{21}|$. In addition, when the resonator is under-coupled ($\kappa_i \gg \kappa_{\mathrm{c},1}, \kappa_{\mathrm{c},2}$), the total linewidth is determined by the internal loss rate $\kappa_{c,1} + \kappa_{c,2} + \kappa_i \sim \kappa_i$.

In the second experiment of the thesis, we work on transmission measurement. The resonator is designed to have an asymmetric coupling $\kappa_{c,2} \gg \kappa_{c,1}$, such that most of the signal will go out through the port with larger coupling rate (port 2 in this case), which is used as output port. The port with small coupling is used as input port to avoid signal flowing backwards to the input.

2.3 Single microwave photon detector (SMPD)

In this section, we discuss briefly another important component which makes our experiment possible: the single microwave photon detector (SMPD) that we have used, developed in the group during two other PhD theses. An ideal SMPD is a device capable of detecting a single incoming microwave photon and gives a binary answer 1 or 0 (click or no click) when a photon arrives or not. Ours is not ideal but sufficiently good for our purposes. As said before, each of the excited spins will emit radiatively a microwave photon when its relaxation is dominated by Purcell effect. This microwave fluorescence signal of the spins will be detected by the SMPD with a finite efficiency.

Detecting microwave photons is challenging, due to their 5-orders-of-magnitude lower energy compared to optical photons, which makes it less effective to trigger measurable macroscopic effect. Developing SMPD devices for microwave photonics is thus a subject of intense research since about a decade [4, 17, 18, 104, 105, 106, 107]. Our SMPD device is based on a cQED architecture : An incoming single photon state is mapped onto the excited state of a well-controlled two-level system (qubit) initialized in its ground state. Measuring the state of the qubit then reveal whether a photon arrived or not. The proof-of-principle demonstration on this type of SMPD device can be found in [4]. Emanuele Albertinale and Leo Balembois have improved the device for spin detection [5]. In this experiment, we use the improved version of the SMPD. We present here only the indispensable background regarding the working principle of the device, and more details can be found in the thesis [108].

2.3.1 Working principle of SMPD

In our SMPD device, a transmon-type superconducting qubit [67] is used, its state being a marker indicating whether a microwave photon arrived or not. The essential and clever process enabling the qubit excitation upon single photon arrival is a pumped parametric process called four-wave mixing, which converts an incoming photon at a given frequency into a qubit excitation at a different frequency, moreover in an irreversible way. This process is depicted in Figure 2.12 in three steps that we detail below.

The transmon qubit is coupled to two different modes at the same time, namely a “buffer mode” with frequency ω_b and a “waste mode” with frequency ω_w (buffer resonator and waste resonator), see Figure 2.12a. The buffer resonator is used as a “buffer” to receive the incoming photon to be processed. A continuous pump tone

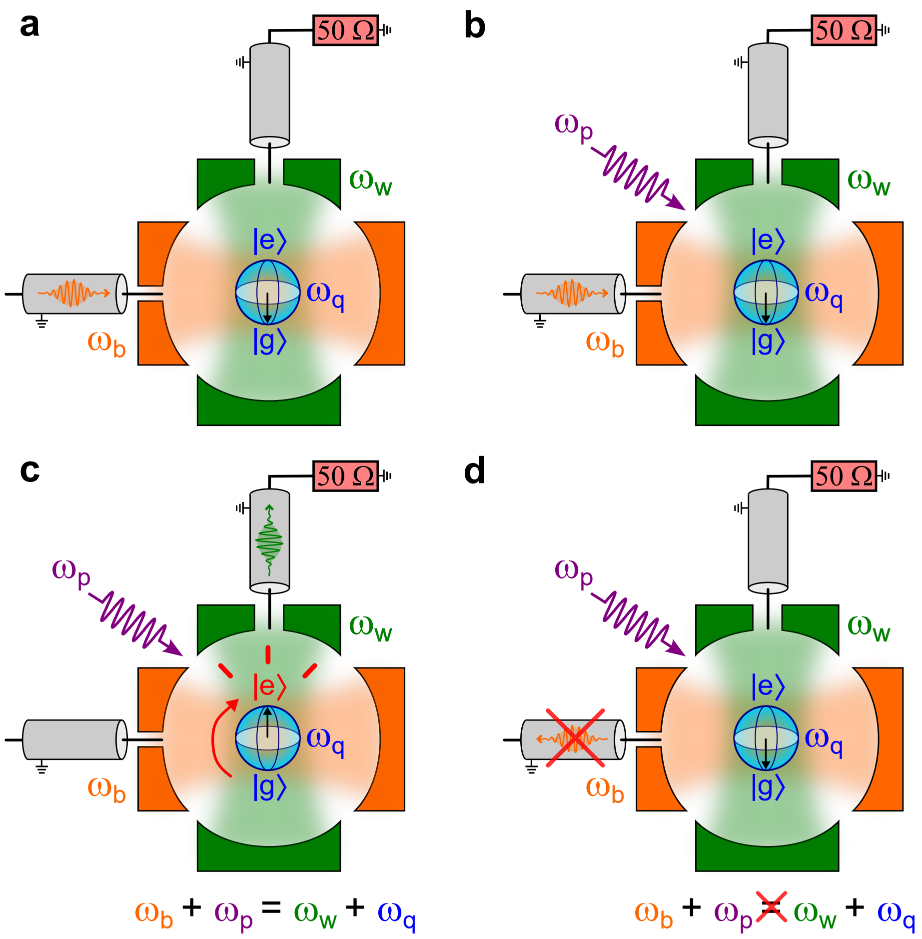

Figure 2.12: **Working principle of the SMPD used in this work.** **(a)** A qubit represented by its Bloch sphere in blue at the center, with a transition frequency ω_q between its ground and excited states $|g\rangle$ and $|e\rangle$, is coupled permanently to two electromagnetic modes represented here as cavities: a buffer mode with frequency ω_b (orange) and a waste mode ω_w (green). An incoming photon enters the buffer resonator through a transmission line. The waster resonator is connected to a transmission line terminated by a 50 Ω dissipative element (pink). **(b)** A continuous pump tone (purple) is applied at frequency ω_p such that $\omega_p + \omega_b = \omega_q + \omega_w$ to enable the four-wave mixing parametric process. **(c)** This process converts the incoming photon into a qubit excitation (red arrow) plus a photon in the waste resonator (green). **(d)** This photon in the waste resonator is rapidly dissipated in the dissipative element, which prevents the inverse parametric process that would generate a photon in the buffer from the qubit excitation and photon in the waste.

with frequency ω_p is used as a parametric drive for a four-wave mixing non-linear process, see Figure 2.12b. The frequency of the drive is well-chosen to satisfy the relation $\omega_p + \omega_b = \omega_q + \omega_w$ such that the incoming photon in the buffer resonator is converted into an excitation of the qubit and another photon ω_w in the waste mode. The waste resonator is designed with a large external coupling rate and its output line is terminated with a 50 Ω resistor. As a result, the photon generated in the waste mode leaks out easily and gets eventually dissipated on the terminator (hence its “waste resonator“ name), see Figure 2.12c. Then the absence of the photon in the waste resonator prohibits the inverse process through which the excitation of the qubit and the waste photon could be converted into a photon in the buffer resonator, see Figure 2.12d. Then the qubit is reset to its ground state, and the system is ready for the detection of a new photon. This irreversible process with a controllable detection time window (the pump duration) allows us to detect single photons within the bandwidth of the buffer resonator, in a cyclic manner.

The SMPD device used in this work is implemented as a superconducting circuit fabricated on top of a sapphire substrate. Figure 2.13a and b show both its circuit model and its corresponding chip layout. The important components of the circuit are:

- **the qubit:** it is of the transmon type, with a single Al/AlO$_\mathrm{x}$/Al Josephson junction and a shunted capacitor. The transmon behaves as a non-linear resonator with non-equally spaced adjacent energy levels, the qubit being formed by the two lowest ones. The transition frequency between these two levels is fixed.

- **the buffer resonator and its Purcell filter:** it is formed by a half-wave coplanar waveguide (CPW) transmission line with two open ends, one of them being capacitively coupled to the transmon. This resonator embeds a SQUID device whose inductance can be varied by passing a current through a grounded line generating a local flux in the SQUID loop ; this inductance variation makes it possible to tune the buffer frequency in-situ with the current bias. The middle of the buffer resonator is capacitively coupled to an auxiliary half-wave CPW resonator with a frequency centered on that of the buffer. This auxiliary resonator plays the role of a Purcell filter that prevents the transmon from relaxing through the buffer. At its center is the input for collecting the incoming photons to be detected.

- **the waste resonator and its Purcell filter:** They are implemented similarly to the buffer resonator and its Purcell filter. A line at the center of the waste's Purcell filter is used both for dissipating the waste photons and for reading the qubit out dispersively.

- **the pump and qubit drive line:** It is implemented as a simple CPW line capacitively coupled to the qubit.

2.3.2 SMPD operation

The SMPD device is operated in a cyclic manner that we describe below and then we introduce its different figures of merit.

SMPD detection cycle

The SMPD detection is performed cyclically, with a total duration T_C of the cycle. Figure 2.14 shows the complete detection cycle, which is composed of 3 steps:

Detection (D): During the detection step, a continuous pump tone at frequency ω_p is switched on and waits for the incoming photons. The duration of the pump drive defines the length of the detection window T_D. When a photon impinges on

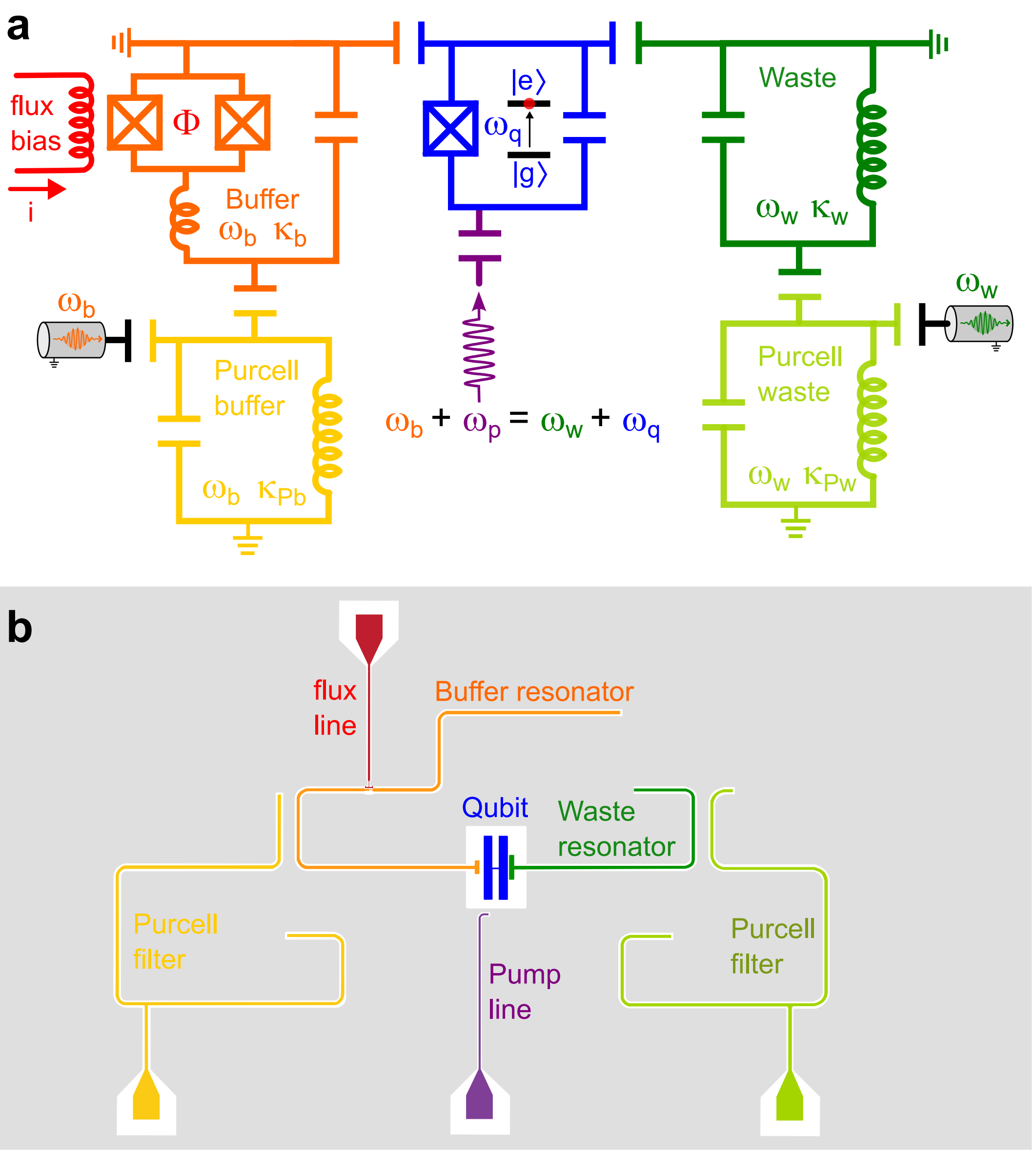

Figure 2.13: **Circuit implementation of the SMPD device used in this work.** **(a)** Circuit model of the device: a transmon qubit (blue) is capacitively coupled to a buffer CPW resonator (orange) and a waste CPW resonator (dark green). A tunable inductor inserted in the middle of the buffer resonator makes it possible to tune the buffer frequency ω_b (detection band center) to the targeted photon frequency. This tunable inductor is actually a SQUID biased by a local magnetic flux Φ induced by a current bias line (red) to ground. Two Purcell filters are included on both buffer (yellow) and waste (light green) resonators in order to limit relaxation of the transmon through the resonators, and thus increase its relaxation time T_1. A pump drive matching the relation $\omega_p + \omega_b = \omega_q + \omega_w$ is applied to switch on the four-wave mixing, thanks to the non-linearity of the transmon's Josephson junction. **(b)** Chip layout of the SMPD design. More details about the design can be found in the thesis of Leo Balembois.

the system during this step, the qubit reaches its excited state while another photon is generated in the waste and dissipated.

Measurement (M): The qubit state is then measured by dispersive readout of the waste resonator. The outcome of the measurement is a binary answer: a "click" (resp. no click) for the transmon being measured in its excited state $|e\rangle$ (resp. ground state $|g\rangle$).

Reset (R): A conditional reset is performed after the measurement step to ensure the qubit is in its ground state $|g\rangle$ before starting the next detection cycle. A π-pulse bringing back the qubit from its excited state to its ground state is applied only if the qubit is measured excited. No reset operation is performed if the qubit is found in its ground state.

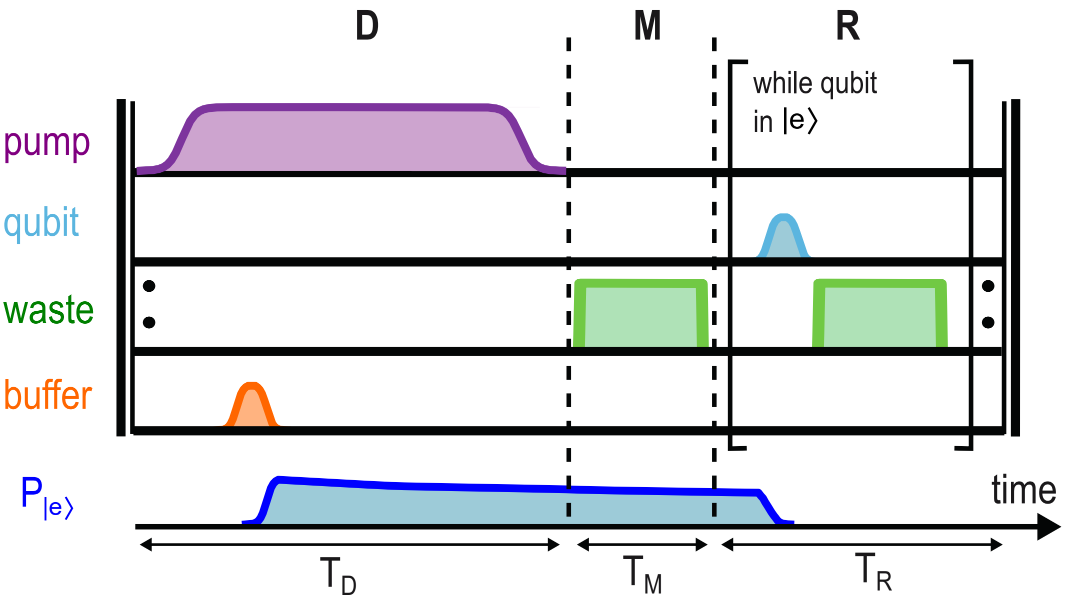

Figure 2.14: **SMPD detection cycle.** A cycle consists of three parts: the detection (D) during which the pump tone (purple long pulse) is switched on, the measurement (M) during which a readout pulse (green) is sent to the waste, and a conditional reset (R) during which de-excitation π pulses (light blue) are sent to the transmon until it is read out in its ground state (second green pulse). An incoming photon (orange) in the buffer is rapidly converted into an excitation of the transmon, whose probability P_e (dark blue on bottom row) decays slowly at the transmon relaxation rate, until the transmon is reset abruptly.

SMPD figures of merits

The figures of merits of the SMPD are its dark count rate, its detection efficiency, and its detection bandwidth. They have tight relations with experimental parameters and will eventually determine the performance of the detector, such as its signal-to-noise ratio.

- **Dark count rate:** The dark count rate α is the rate of false-positive clicks reported by the detector. Here specifically, we define the dark counts as the counts in absence of input signal. After the qubit is reset to its ground state, a false click can have three origins: measurement infidelity, thermal excitation of the qubit and spurious photons in the lines.

  - **Measurement infidelity.** Even if the qubit is in its ground state, the readout can still give a false result as if the qubit was in its excited state. The measurement infidelity is negligible in our case.
  - **Thermal excitation of qubit.** In equilibrium, the qubit has a finite probability of being excited, depending on the electromagnetic temperature of its environment [109] and on possible rare high-energy excitation events [110]. These qubit excitations not due to incoming photons lead to unwanted clicks.
  - **Spurious photons in the buffer lines.** In reality, even if the thermometer reports a base temperature of 10 mK, the objects around the SMPD can still be warmer than that due to imperfect thermalization of the electronic components and lines. This leads to out-of-equilibrium photons, usually broadband, in the lines. Those in the buffer line and having a frequency inside the buffer detection band are detected. Although the resulting clicks are not strictly speaking dark counts since they correspond to real photons, we still call them "dark counts" because they are spurious signal in the absence of the controllable photon source to be detected, such as spins.

  The typical dark count rate of the SMPD used in this work is $\alpha \sim 100\text{s}^{-1}$. We have observed slow dark count rate fluctuations over week time scales ranging typically from 130 s^{-1} to 90 s^{-1} mainly due to variation in qubit T_1 and a slow cooling down of the line and of the qubit.

- **Efficiency:** The SMPD efficiency is the average probability of detecting a click when a photon is entering the buffer input. It can be determined from the detected number of counts divided by the total number of incoming photons (when the detector is far below saturation). This SMPD efficiency is the product of three contributions:
  - **Duty cycle:** The photons arriving outside the detection time window are of course lost, which lowers the efficiency down to about $\eta_{\text{duty}} = T_D/T_C$.
  - **Conversion efficiency:** The fact that not all photons arriving during the detection window can be converted to a qubit excitation, leads to a finite efficiency η_{conv}. Note that when the detector is saturated by a large input photon flux, the conversion efficiency obviously drops drastically.
  - **False negative:** The measurement of an excited qubit can also give a result interpreted as non-excited qubit due to the measurement infidelity. Besides, an excited qubit can also relax before or during readout. The first case is negligible in our experiment, and the second one leads to a finite efficiency η_{T_1} if the qubit T_1 is too short.
- **Detection bandwidth:** The bandwidth gives the frequency range of photons that can be detected by the SMPD. The chosen linewidth of the buffer resonator and the four-wave mixing process determine together the bandwidth of the detector.

2.4 Electron-spin-resonance detection by microwave photon counting

2.4.1 Electron spin resonance (ESR)

The Zeeman interaction between the electronic spin and external magnetic field B_0 splits the degenerate spin states existing at zero field, as shown in Figure 2.15a. The spin physics is then described by the spin 1/2 Hamiltonian introduced in Section 2.1,

$$\hat{H}_s = \frac{1}{2}\hbar\omega_s(B_0)\hat{\sigma}_z, \tag{2.78}$$

with a frequency $\omega_s(B_0)$ that usually falls in the microwave domain for fields not exceeding one Tesla.

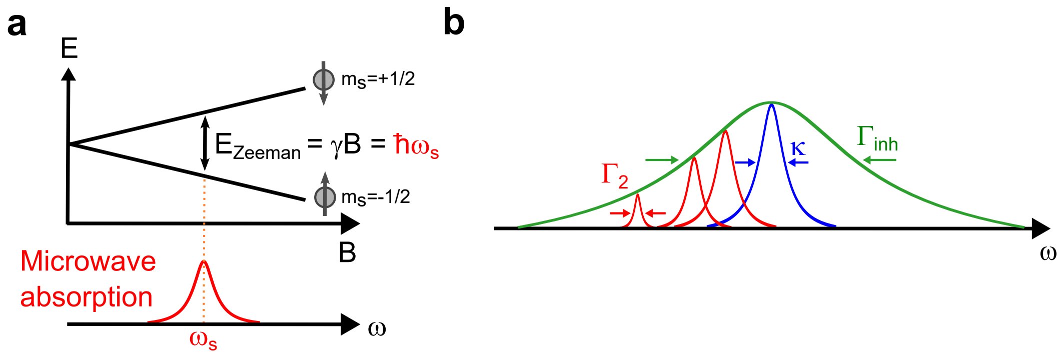

Figure 2.15: **Electron spin resonance and typical linewidths in our experiment. (a)** Electron spin resonance. The degenerate eigenstates of a spin 1/2 system are split under non-zero magnetic field by an energy difference $E_{\text{Zeeman}} = \gamma B$ (we neglect the zero-field splitting that can exist for particular impurities in particular crystals). An applied microwave close to the spin Larmor frequency $\omega_s = E_{\text{Zeeman}}/\hbar$ can be absorbed coherently within a certain linewidth, leading to an evolution of the spin state. **(b)** Typical resonant lines in our experiments: Resonator (blue) with linewidth $\kappa/2\pi = 470$ kHz, single spin (red) with homogeneous linewidth $\Gamma_2/2\pi \sim 2$ kHz and spin ensemble (green) with inhomogeneous linewidth $\Gamma_{\text{inh}}/2\pi \sim 8$ MHz.

The spin can absorb (and then reemit) electromagnetic radiation at microwave frequencies close to its Larmor frequency ω_s, which results in an evolution of its quantum state. This process is called electron spin resonance (ESR) [24]. In the absorption spectrum, see Figure 2.15b, the intrinsic single spin linewidth is called homogeneous linewidth Γ_2. For a spin ensemble in a solid, each spin has its local electrical and magnetic environment, so that the spin transition frequencies are different and spread out to form a collective absorption line with an inhomogeneous linewidth Γ_{inh}. Note that in our experiment with erbium ions in CaWO$_4$, the typical homogeneous linewidth is about $\Gamma_2 \sim 2$ kHz, whereas the inhomogeneous linewidth is about $\Gamma_{\text{inh}} \sim 8$ MHz (along the crystal c-axis), which is around 15 times larger than the linewidth $\kappa/2\pi = 470$ kHz of the resonator that we will use.

We now model the ESR process assuming a static external field $\mathbf{B_0} = B_0\,\hat{z}$ defining the spin quantization axis (longitudinal direction) and a classical transverse harmonic drive $\mathbf{B_1} = B_1 \cos(\omega_d t + \varphi)\,\hat{x}$. The drive Hamiltonian is thus

$$\hat{H}_{\text{int}} = \frac{1}{2}\hbar\gamma_e \mathbf{B_1} \cdot \hat{\sigma} = \frac{1}{2}\hbar\gamma_e B_1 \cos\omega_d t\, \hat{\sigma}_x, \tag{2.79}$$

where we assume $\varphi = 0$ for simplicity. Moving to a frame rotating at the spin Larmor frequency with the unitary operator $\hat{U}_0(t) = \exp(i\hat{H}_s t/\hbar)$ and using the relation $\hat{\sigma}_x = \hat{\sigma}_+ + \hat{\sigma}_-$ lead to the new Hamiltonian

$$\begin{aligned}\hat{H}' &= \frac{1}{2}\hbar\gamma_e B_1 \cos\omega_d t(\hat{\sigma}_+ e^{i\omega_s t} + \hat{\sigma}_- e^{i\omega_s t}) & (2.80)\\ &= \frac{1}{4}\hbar\gamma_e B_1(\hat{\sigma}_+ e^{i(\omega_s+\omega_d)t} + \hat{\sigma}_+ e^{i(\omega_s-\omega_d)t} + \hat{\sigma}_- e^{i(\omega_s+\omega_d)t} + \hat{\sigma}_- e^{i(\omega_s-\omega_d)t}), & (2.81)\end{aligned}$$

where the relation $\cos\omega_d t = [\exp(i\omega_d t) + \exp(-i\omega_d t)]/2$ has been used. Performing then the rotating wave approximation, i.e. eliminating the fast terms in $\omega_s + \omega_d$ that average to zero for the spin dynamics, we are left with

$$\hat{H}' = \frac{1}{4}\hbar\gamma_e B_1[\hat{\sigma}_+ e^{i(\omega_s-\omega_d)t} + \hat{\sigma}_- e^{i(\omega_s-\omega_d)t}] \tag{2.82}$$

If the applied oscillating field has exactly the Larmor frequency ω_s, the Hamiltonian is reduced to

$$\hat{H}' = \frac{1}{4}\hbar\gamma_e B_1(\hat{\sigma}_+ + \hat{\sigma}_-) = \frac{1}{4}\hbar\gamma_e B_1 \hat{\sigma}_x, \tag{2.83}$$

which causes a Rabi rotation around $\hat{x}$ at the Rabi frequency $\Omega = \gamma_e B_1/4$.

In the Bloch's sphere representation, the spin rotates by a Rabi angle proportional to the drive amplitude B_1 and to the microwave pulse duration, a complete Rabi period corresponding to a 2π rotation of the spin. One can also define π- and $\pi/2$- pulses, which bring for instance the spin from its ground state $|g\rangle$ to its excited state $|e\rangle$ and to an equal superposition of two states $(|g\rangle + |e\rangle/)\sqrt{2}$ (on the Bloch's sphere equator), respectively, see Figure 2.16. In a real experiment like ours, the spatial distribution of the driving field can be very large ; the spins of a spatially distributed ensemble thus experience very different B_1 and very different Rabi angles at the end of a microwave pulse, which will be discussed in detail in the next chapter. Moreover, the phase φ in the classical drive $\mathbf{B_1} = B_1 \cos(\omega_d t + \varphi)\,\hat{x}$ determines the axis along which the spin will rotate under the drive (in the frame rotating at the spin Larmor frequency).

2.4.2 Detection methods for microwave

Excited spins with Purcell-enhanced decay rate can spontaneously emit incoherent photons into the resonator and relax back to their ground states. Photons, being quanta of electromagnetic field with wave-particle duality, can be detected by two different methods: field quadrature detection and energy detection.

Field quadrature detection

Classically, the electromagnetic mode with frequency ω_0 can be described by the complex amplitude $A = |A|e^{i(\omega_0 t+\phi)}$. In the time frame rotating at ω_0, the mode now expressed as $A = |A|e^{i\phi}$ can also be decomposed in its in-phase $X = \mathrm{Re}(A)$ and out-of-phase $Y = \mathrm{Im}(A)$ quadratures, as shown in Figure 2.17a. These two

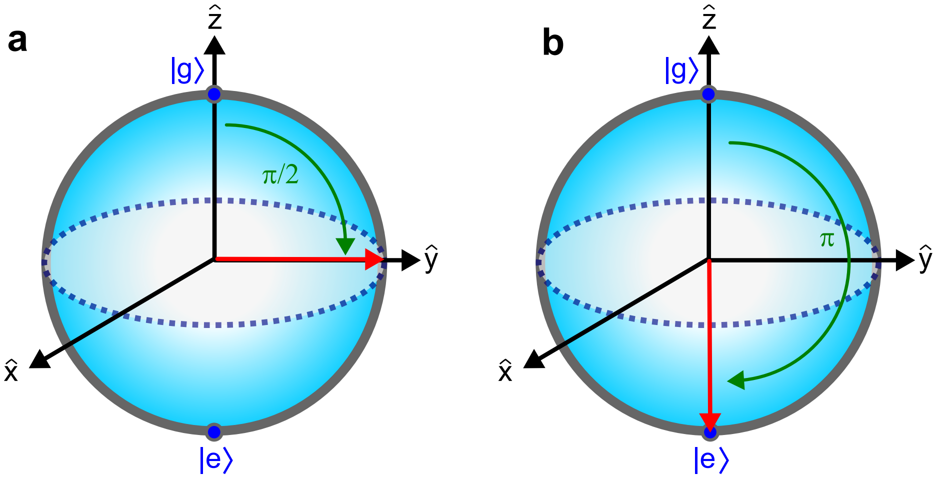

Figure 2.16: **Spin rotation around $\hat{x}$ by a $\pi/2$-pulse (a) and by a π-pulse (b) in the Bloch's sphere representation.**

quadratures X and Y of the electromagnetic field are canonical conjugate variables that give a phase-space representation of the field. In the quantum description, they are promoted to operators satisfying the commutation relation $[\hat{X}, \hat{Y}] = i/2$[1], and their variance $\langle \Delta\hat{X}^2 \rangle = \langle \hat{X} \rangle^2 - \langle \hat{X}^2 \rangle$ and $\langle \Delta\hat{Y}^2 \rangle$ satisfy Heisenberg uncertainty relation $\langle \Delta\hat{X}^2 \rangle \langle \Delta\hat{Y}^2 \rangle \geq 1/16$.

Note that quadrature variables were already presented in an indirect way in Section 2.2.1, where the field inside a simple LC oscillator has been quantized by introducing operators for charge and flux observables, obeying commutation relation $[\hat{\Phi}, \hat{Q}] = i\hbar$. Here the charge represents the electric part of the field and flux the magnetic part. Actually they can be regarded as the "quadratures" of the resonator mode since they are proportional to the field quadrature observables. In general, the choice of a pair of orthogonal variables X and Y defines one set of quadratures, which is relative to a chosen phase reference. This can be understood intuitively in the relative phase introduced by rotating the (X, Y) frame in Figure 2.17a.

The photon creation $\hat{a}^\dagger$ and annihilation $\hat{a}$ operators

$$\hat{a} = \hat{X} + i\hat{Y} \tag{2.84}$$

$$\hat{a}^\dagger = \hat{X} - i\hat{Y} \tag{2.85}$$

can also be defined from the quadrature operators, and obey the commutation relation $[\hat{a}, \hat{a}^\dagger] = 1$.

The eigenstates of the photon number operator $\hat{n} = \hat{a}^\dagger\hat{a}$ are the Fock states $|n\rangle$. The lowest-energy state of the mode (zero photon state) is defined as the vacuum state $|0\rangle$. As shown in Figure 2.17b, this vacuum state has a Gaussian probability distribution of its quadratures around the phase space origin (presented as a blurry disk with radius of 1/2). Note that even if the mean values of its field quadratures are zero $\langle \hat{X} \rangle = \langle \hat{Y} \rangle = 0$, they have a non-zero variance satisfying the minimal Heisenberg uncertainty relation:

$$\langle \Delta\hat{X}^2 \rangle = \langle \Delta\hat{Y}^2 \rangle = \frac{1}{4}. \tag{2.86}$$

---

[1] Here we use dimensionless quantities for simplicity.

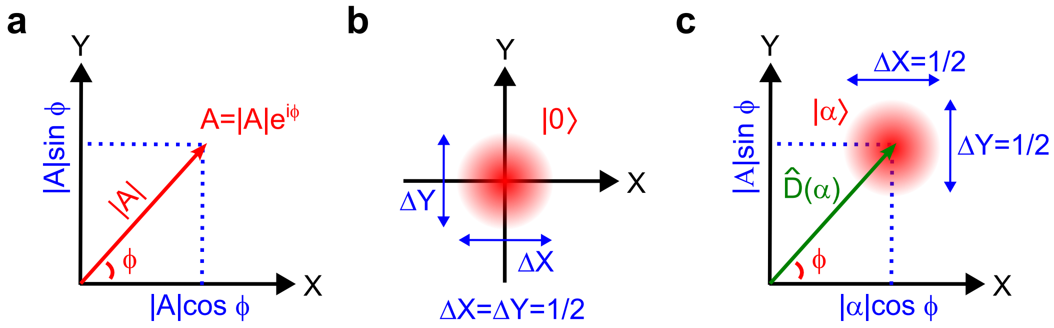

Figure 2.17: **Electromagnetic field in phase-space representation.** **(a)** Classical picture. **(b)** Vacuum state shown as the 2D density of probability of the two quadratures. The distribution is a Gaussian of revolution with standard deviation of half a square-root of photon (schematically represented). **(c)** Coherent state obtained by a displacement $\hat{D}(\alpha)$ of the vacuum, with the same quantum fluctuations.

Moreover, a classical harmonic drive applied to a certain mode ω_0 results in a displacement in the phase space of the vacuum state of this mode by a complex quantity $\alpha = |\alpha|e^{i\phi}$, the corresponding displacement operator being $\hat{D}(\alpha) = \exp(\alpha\hat{a}^\dagger + \alpha^*\hat{a})$ (see Figure 2.17c). This drive or displacement of vacuum state leads to a "coherent state"

$$\hat{D}(\alpha)|0\rangle = |\alpha\rangle, \tag{2.87}$$

which is the eigenstate of the annihilation operator

$$\hat{a}|\alpha\rangle = \alpha|\alpha\rangle, \tag{2.88}$$

with a mean photon number $\langle\alpha|\hat{a}^\dagger\hat{a}|\alpha\rangle = |\alpha|^2$.

In the lab time frame for the mode ω_0, the coherent state is rotating in the phase space at an angular frequency ω_0, as shown in Figure 2.18a. Therefore, the mean quadrature values are time-dependent and write

$$\langle\hat{X}\rangle = |\alpha|\cos\omega_0 t \tag{2.89}$$

$$\langle\hat{Y}\rangle = |\alpha|\sin\omega_0 t \tag{2.90}$$

(see Figure 2.18b). As the vacuum state, coherent states also satisfy the minimal Heisenberg uncertainty relation $\langle\Delta\hat{X}^2\rangle = \langle\Delta\hat{Y}^2\rangle = 1/4$.

We can notice that, when the signal to be detected is rather small (such as a single photon emitted from a single spin), the vacuum noise of 1/2 a square root of photon spoils the signal on the field quadratures and leads to poor signal-to-noise ratio (SNR) in conventional induction-mode ESR detection [111]. On the contrary, this overall 1/2 photon noise energy does not manifest itself in an energy detector (energy cannot be absorbed permanently from vacuum). Therefore the measurement of a Fock state through its energy can bypass the fundamental quantum limit that exists on quadratures, which greatly helps reach single spin sensitivity.

Despite the fundamental quantum limit, quadrature detection remains the most widely used small field detection method up to today, because it does not require a

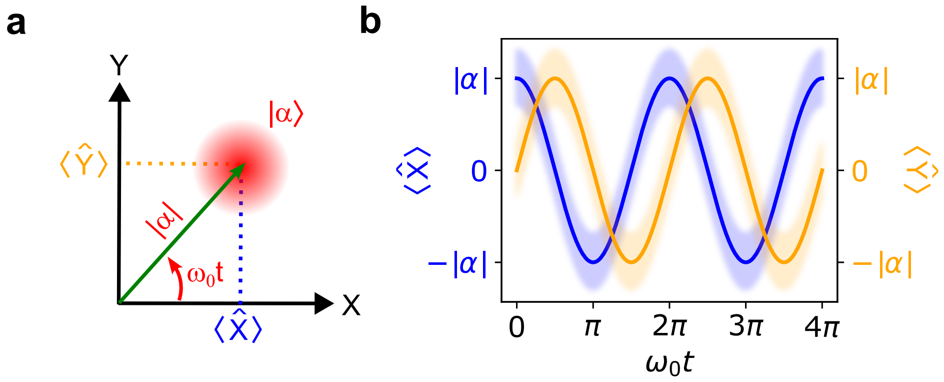

Figure 2.18: **Coherent state in phase-space representation and time evolution.** **(a)** Coherent state in phase-space representation in the laboratory frame. **(b)** Time evolution of its mean quadrature values.

complicated experimental setup (it needs only amplifiers) or special devices (photon detection needs SMPD). With the help of quantum-limited amplifier [112, 113], quadrature detection can reach reasonable SNR in many situations, especially when the signal does not involve a too small number of photons, such as dispersive readout for qubits in cQED (for measuring the state of transmon qubit in SMPD) [10]. Field quadrature detection is also used in the second experiment of this thesis, in which microwave pulses are sent to the system under study to probe the change of its transmission. We discuss this in detail in the second part of the thesis manuscript.

Photon detection

As already said, the detection can also be performed in energy, in the photon number basis (Fock basis). The observable in this case is the photon number operator $\hat{n} = \hat{a}^\dagger \hat{a}$ and the measurement on Fock state $|n\rangle$ yields

$$\langle n|\hat{a}^\dagger \hat{a}|n\rangle = \langle n-1|\sqrt{n}\sqrt{n}|n-1\rangle = n, \tag{2.91}$$

where the relation $a|n\rangle = \sqrt{n}|n-1\rangle$ is used.

The variance of the observable $\hat{n}$

$$\langle \Delta \hat{n}^2 \rangle = \langle n|(\hat{a}^\dagger \hat{a})^2|n\rangle - \langle n|(\hat{a}^\dagger \hat{a})|n\rangle^2 = 0 \tag{2.92}$$

showing no noise on photon number measurements by ideal energy detectors. In particular, the vacuum state $|0\rangle$ is measured with a definite outcome of zero photon.

The SMPD is an energy detector working in the microwave domain. However, it is designed for detecting only one photon at each cycle and is saturated after the first received photon. It is thus not able to characterize Fock states with photon numbers larger than one, and its actual observable is not $\hat{n}$ but

$$\hat{P} = \mathbb{1} - |0\rangle\langle 0|. \tag{2.93}$$

Therefore the measurement with the SMPD yields a definite binary number: $\langle 0|\hat{P}|0\rangle = 0$ for the vacuum state and $\langle n|\hat{P}|n\rangle = 1$ for any Fock states with $n >= 1$, including Fock state $|1\rangle$. As for a generic photon number detector, there is no noise on the observable and there is no fundamental limit to the SNR in detecting single photons with a SMPD.

In the first experiment of this thesis, we perform photon detection of the spin microwave fluorescence signal with an SMPD.

2.4.3 ESR detection with photon counting and signal-to-noise ratio

Detecting spins by microwave photon counting

In practice, having a large Purcell-enhanced relaxation rate Γ_R for spins compared to their non-radiative decay rate is the prerequisite for detecting spins by their fluorescence signal. In the Purcell-limited regime, the excited state population P_e of an excited spin $\hat{\rho}_s = |e\rangle\langle e|$ decays exponentially as

$$P_\mathrm{e} = e^{-\Gamma_R t}, \tag{2.94}$$

whereas the ground state population evolves as

$$P_\mathrm{g} = 1 - e^{-\Gamma_R t}, \tag{2.95}$$

which also describes the single photon emission rate as a function of time.

The SMPD device introduced in the Section 2.3 allows us to detect the arrival of a single photon during the spin relaxation, with a finite efficiency due to the finite duty cycle of the cyclic operation, and with a temporal resolution equal to the duration T_C of a cycle.

Figure 2.19 shows the complete protocol used for ESR detection with our SMPD. A particular sequence j starts with a π-pulse to bring a spin from its ground state to its excited state. The moment after the pulse is defined as $t = 0$. Then the excited state probability decays exponentially as Equation 2.94, while the SMPD starts its iterated detection cycles detailed in Figure 2.14. The outcome of each cycle is a boolean variable $c_j(t)$ of either 1 or 0 representing the count number at the central time t of the cycle. The measurement cycles do not stop until the spin is most likely to be found in its ground state: the total measurement process lasts for a time t_m (several T_1 times of spin), after which the probability of having one photon already emitted from the spin is nearly 1. In practice, we add up all the single count $c_j(t)$ in a time window between $t = 0$ and $t_w < t_m$, in order to get an integrated count signal $C_j(t_w)$ for the sequence j. We repeat N times the same sequence to get an averaged number of counts

$$\langle C \rangle = \frac{1}{N}\sum_{j=1}^{N} C_j(t_w) = \frac{1}{N}\sum_{j=1}^{N}\sum_{t=0}^{t_w} c_j(t). \tag{2.96}$$

Since t_m is much longer than the length of the spin excitation pulse, the total experiment time is roughly $t_\mathrm{exp} \sim N t_m$.

Signal-to-noise ratio

In general, a measurement yields a signal s with a certain statistical distribution described by its mean value $\langle s \rangle$ and variance $\langle \Delta s^2 \rangle$. The signal-to-noise ratio (SNR)

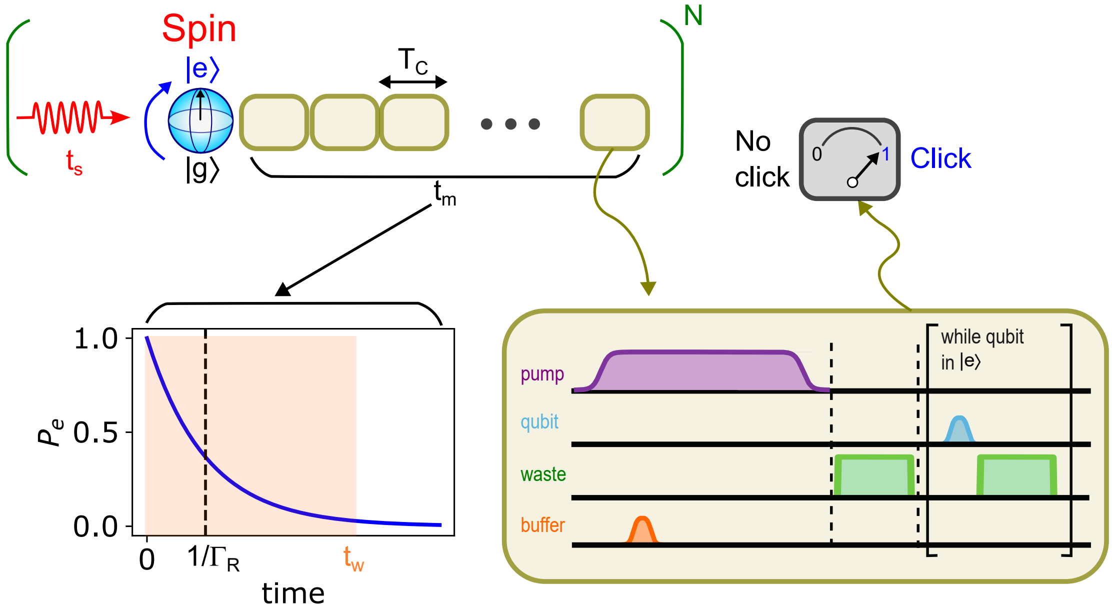

Figure 2.19: **ESR detection with photon counting.** After an excitation pulse (red) applied to the spin (presented in its Bloch's sphere), the detection with the SMPD starts in a cyclic manner with a cycle time T_C. The iteration of the SMPD cycles lasts for a total time t_m covering the whole relaxation of the spin, described by the exponential decay (blue curve) of its excited state probability P_e (the t_w-long orange box represents the chosen integration window). The measurement result of each cycle yields a "click" or "no click". The full sequence is repeated N times during a total measuring time $t_{\mathrm{exp}} \sim N t_m$ (if $t_m \gg t_s$).

of the measurement is defined as

$$\mathrm{SNR} = \frac{\langle s \rangle}{\sqrt{\langle \Delta s^2 \rangle}}. \tag{2.97}$$

The SNR tells us how significant the measurement is, associated with its duration. In practice, a measurement considered as an elementary measurement or single-shot measurement can be repeated and averaged over the repetitions in order to lower the variance and reach a higher SNR corresponding now to the total measurement time over which the averaging has been performed.

We now derive an analytical formula for the SNR of a single spin detection with our SMPD. For spin in the Purcell-limited regime, the radiative relaxation is the dominant decay $\Gamma_1 \sim \Gamma_R$. The emission from a single spin is eventually one photon in the coupled resonator. However, due to the limited detection efficiency η ($0 < \eta < 1$) and finite integration window t_w, one photon signal will not be converted perfectly to one SMPD count. Based on the single photon emission rate in Equation 2.95, the averaged emitted photon number per sequence is $1 - e^{-\Gamma_R t_w}$ and the averaged number of counts $\langle C \rangle$ per sequence and average total number of counts $\langle C_S \rangle$ coming from the spins are

$$\langle C \rangle = \eta(1 - e^{-\Gamma_R t_w}) = \eta' \tag{2.98}$$

$$\langle C_S \rangle = N \langle C \rangle, \tag{2.99}$$

where we have absorbed the non-unity emission in an effective total efficiency η'.

Due to the dark counts detected by the SMPD at a rate α, an average total number of dark counts $\langle C_{DC}\rangle = \alpha t_{\mathrm{exp}}$ are also detected during the full time t_{exp} of the experiment. However, α can be pre-calibrated once for all before any spin measurement by a long averaging for a good precision. Consequently, the dark count signal C_{DC} can always be subtracted precisely from the total number of registered counts to obtain the real spin signal C_S.

The detected noise has two origins:

- **Partition noise:** The finite probability η' ($0 < \eta' < 1$) of detecting "one click" results in a binomial distribution of C_S with variance $\langle \Delta C^2_{\eta'}\rangle = \eta'(1-\eta')N$ for N repetitions.
- **Dark counts:** Given that dark count events are independent of each other and occur at a constant rate α, they follow a Poissonian distribution with a variance equal to the mean. The variance on C_{DC} is thus $\langle \Delta C^2_{DC}\rangle = \alpha t_{\mathrm{exp}}$.

The SNR of the measurement writes

$$\mathrm{SNR} = \frac{\langle C_S\rangle}{\sqrt{\langle \Delta C^2_{\mathrm{DC}}\rangle + \langle \Delta C^2_{\eta'}\rangle}} = \frac{\eta' N}{\sqrt{\alpha t_{\mathrm{exp}} + \eta'(1-\eta')N}} = \frac{\eta'\sqrt{N}}{\sqrt{\alpha t_m + \eta'(1-\eta')}}, \tag{2.100}$$

where $t_{\mathrm{exp}} \sim N t_m$ is used and where we have chosen an integration time equal to the measurement time ($t_w = t_m$) for simplicity.

On can remark that:

- The measurement SNR scales with the square root of the number of repetitions $\sqrt{N}$.
- If the integration window is too large ($t_w \gg 1/\Gamma_R$), $\eta' \to \eta$ and the dark count noise buries the spin signal, resulting in a low SNR.
- If the integration window is too short $t_w \ll 1/\Gamma_R$, the spin does not have enough time to emit its photon, and $\eta' \to 0$ and SNR$\to 0$.

For a fixed dark count rate α, the optimal SNR is obtained by repeating the sequence at the Purcell rate such that $t_m = T_R = 1/\Gamma_R$. Choosing a one second-long experiment ($t_{\mathrm{exp}} = 1$ s) and using $N = t_{\mathrm{exp}}\Gamma_R$, the SNR takes the simple form

$$\mathrm{SNR}_{\mathrm{opt}} = \frac{\eta\Gamma_R}{\sqrt{\alpha + \eta(1-\eta)\Gamma_R}}. \tag{2.101}$$

In chapter 4, We will compute the single spin sensitivity of our experiment from the measured SNR with one second of total measurement time.

Chapter 3

Device and experimental setup implementation

In this chapter, we explain how we have designed and fabricated or setup the different units and components of our experiment. This includes the crystal with the spins, the resonator fabricated on it, the single microwave photon detector (SMPD), and the experimental setup used to perform the measurements. In a first part, we focus on the crystal-resonator device, discussing its design, simulation, and fabrication. The detailed design considerations, fabrication, and pre-characterization of the SMPD are the subject of Leo Balembois' thesis book [108]. We thus give here only a summary with the minimum information required to understand our work. In a second part, we introduce the complete setup used in the experiment (built up using different technologies such as microwave engineering, superconducting magnets, cryogenic physics, electronics, etc). After that, we present basic characterization results on the resonator and the SMPD. Meanwhile, we explain how measurements on the resonator could be used to align the magnetic field in the sample plane, which happened to be crucial for the experiment.

3.1 Spin-resonator sample

3.1.1 Host crystal sample for spins

The $CaWO_4$ crystal used in our experiment originates from a boule grown by the Czochralski method from $CaCO_3$ (99.95% purity) and WO_3 (99.9 % purity). The boule was characterized by continuous-wave ESR spectroscopy [114]: the residual doping concentration in erbium was found to be 3.1 ± 0.2 ppb, which corresponds to an average distance between the closest erbium ions of about 300 nm. Specifically, only the $I = 0$ erbium isotope with 77 % natural abundance is of interest for our work, the remaining 23 % abundant ^{167}Er isotope with nuclear spin $I = 7/2$ [115] having not been measured.

Other nuclear spins are certain calcium (Ca) and oxygen (O) isotopes, whose concentrations are negligible, as well as the 14 % abundant ^{183}W tungsten having a nuclear spin $I = 1/2$ [115]. At 10 mK, these are unpolarized and form a nuclear spin bath which is responsible for part of the decoherence of the erbium electronic spins.

The sample that we have used was cut from the boule in a rectangular slab shape

(7 mm × 4 mm), with the surface approximately in the (ac) crystallographic plane, and the c-axis parallel to its 4mm-long edge. To allow an easy micro-fabrication of the resonator on this slab, one of its big faces was then optically polished. The final thickness is reduced from 2 mm down to 0.5 mm using the service from the company SurfaceNet GmbH.

3.1.2 Superconducting resonator for addressing spins

Design

The superconducting resonator used to address spins was designed as a lumped-element LC resonator, as discussed in Section 2.2.1. The goal is to have a resonator with a simple planar geometry easy to fabricate, and with a small inductor L well coupled to a hundred of spins and a maximum capacitor C to lower the resonator impedance $Z = \sqrt{L/C}$ and maximize the zero point current fluctuations and spin-resonator coupling g_0, according to Equation 2.21 and Equation 2.46.

In our design, the resonator is formed from an inductive wire in the middle (94 μm length and 600 nm width) and two symmetric interdigitated capacitors on the left and right sides (see dimensions in Figure 3.1b. The top and bottom capacitor pads are designed as a vertical dipole antenna to be coupled to a vertical electrical field (see Section 3.1.2 and Section 3.2.1)

The capacitor pads are shaped as 20 μm wide strips separated by 10 μm in order to increase the pad (and thus resonator) resilience to magnetic field penetration.

Figure 3.1c shows a schematic of the 600 nm-wide and 94 μm-long inductive wire at the center of the resonator. Compared to a previous experiment of the group [6], these dimensions are reduced for the purpose of addressing fewer spins in the magnetic volume immediately below the wire, where the spins have a stronger coupling strength g_0 to the resonator and consequently a larger Purcell decay rate Γ_R. A rough estimation of the number of addressable spins in the yellow dashed cuboid of Figure 3.1c, yields approximately ~ 200 spins. Given the inhomogeneous linewidth $\Gamma_{\text{inh}}/2\pi \sim 8$ MHz of the spin ensemble, known from a previous experiment [114], targeting a resonator decay rate κ such that $\Gamma_{\text{inh}}/\kappa \sim 10$ (see Figure 2.15b) should lead to 20 addressable spins within the resonator linewidth. With such a small number, we expect to address individual spins on the foot of the spin frequency distribution.

As our crystal chip was large enough, we have decided to place on it 3 resonators with slightly different resonant frequencies. The crystal is then to be stuck on a silicon chip, itself hold in a 3D copper cavity equipped with a pin antenna soldered to a SMA connector (see this mounting in Figure 3.7).

The 3 resonators are made of identical inductive wires but different capacitors, obtained by varying the length of the outermost capacitor fingers on both left and right sides. This allows us to vary the frequency of the resonator (around 7 GHz) by 7% to be in the tunable range of the buffer resonator of SMPD. Defining the ratio $0 < R < 1$ of the actual length of these extreme fingers to their maximum length, we summarize the design parameters in Table 3.1.

Electromagnetic simulations

To precisely find the frequencies ω_0 of our three resonators, their characteristic impedances Z_0, as well as their energy decay rates κ, we use a 3D finite-element

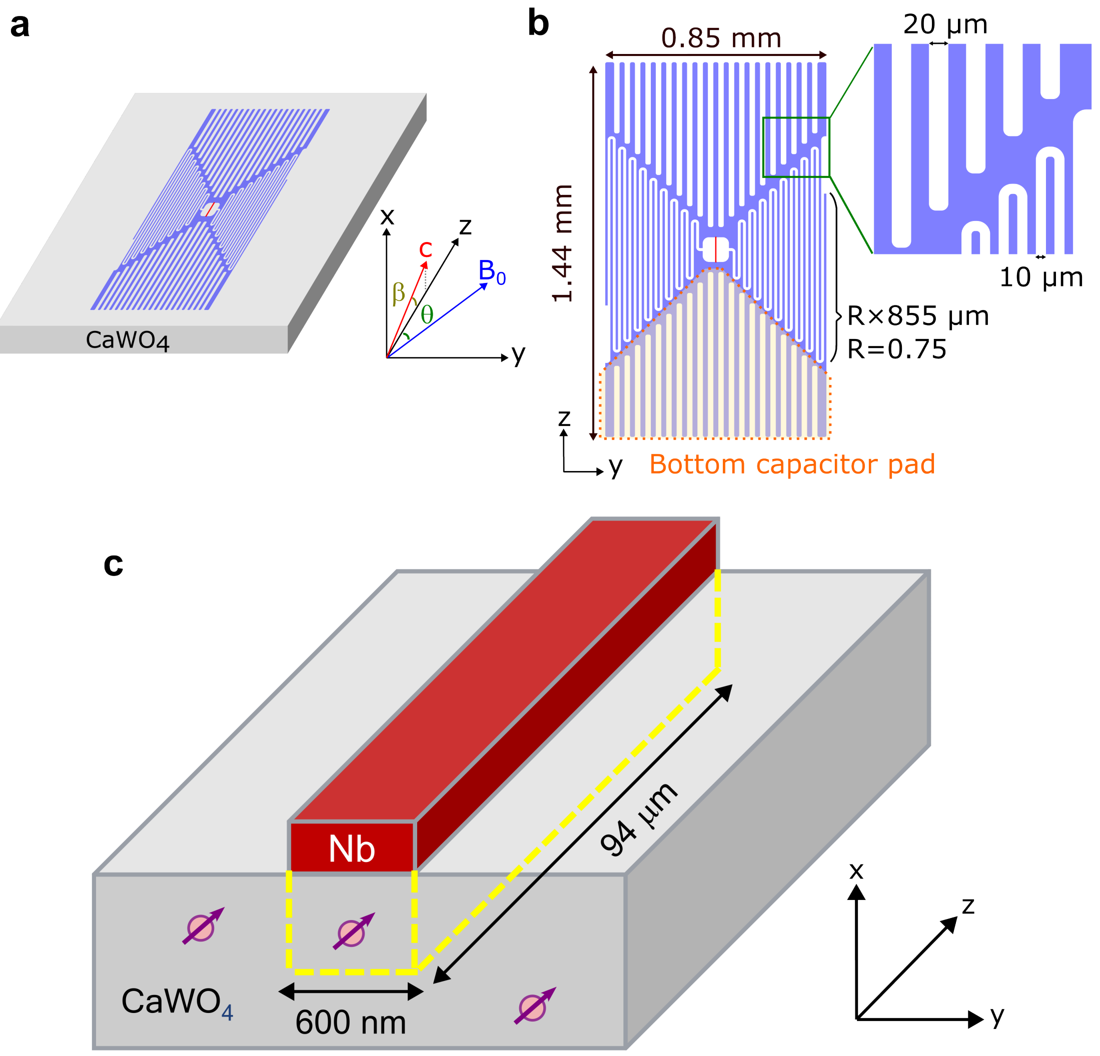

Figure 3.1: **Spin-resonator design.** **(a)** Schematic of the sample. A niobium resonator (blue) is fabricated on top of the $CaWO_4$ crystal (gray). The inductive wire (red) at the center of the resonator defines the z-axis. The $x-y$ plane perpendicular to z, has its y axis in the sample plane and the x axis orthogonal to it. β is the angle between the crystal c-axis and the sample plane. θ is the angle between the projection of c-axis in the $y-z$ plane and the magnetic field B_0 (also applied in the $y-z$ plane). **(b)** Design of our "bow-tie"-shaped resonator, with striped top and bottom (orange dashed box) pads, left and right interdigitated capacitors with 10 μm-wide fingers and gaps, and central inductive wire (red). Pad strips are 20 μm wide. To adjust the resonator frequency, the length of the outermost fingers on both sides is varied (fraction $0 < R < 1$ of the 855 μm maximum length). In this example $R = 0.75$. **(c)** Schematic of the 94 μm-long and 600 nm-wide inductive wire (red), with a cuboid (yellow dashed) of most strongly coupled spins (see also Figure 3.4 for more quantitative information about coupling).

microwave simulator called HFSS from ANSYS Inc, operated in the so-called eigensolver mode. Our full model is shown in Figure 3.2a, where the following 5 elements are included:

resonator design	reso 1	reso 2	reso 3
outermost finger fraction R	0.5	0.75	1
outermost finger length 855R (μm)	427.5	641.25	855

Table 3.1: **Resonator geometric properties.** Three resonators are pattern on the $CaWO_4$ sample.

- A perfectly conducting metallic box ($33 \times 9 \times 16$ mm^3) representing the 3D copper cavity mentioned above.
- A silicon chip ($5.9 \times 3 \times 0.3$ mm^3) fitting in the box, used for holding the $CaWO_4$ crystal.
- The $CaWO_4$ crystal ($7 \times 4 \times 0.5$mm^3) stacked on the silicon chip.
- The resonator on top of the crystal, modeled with zero thickness and 2D impedance models: 0 resistance and 8.67 m$\Omega/\square$ reactance (resulting from 0.2 pH/$\square$ at 6.9 GHz).
- a metallic pin plunging in the copper cavity through a hole in its top wall, used as an antenna to excite the system.

We point out here that the dielectric tensor of $CaWO_4$ is anisotropic, so that the resonator frequencies depend on the orientation of the crystal. Note in this respect that the HFSS (X,Y,Z)-coordinate system shown in Figure 3.2 is different from the convention (x, y, z) used throughout this manuscript, the crystal c-axis being aligned with the HFSS X-axis.

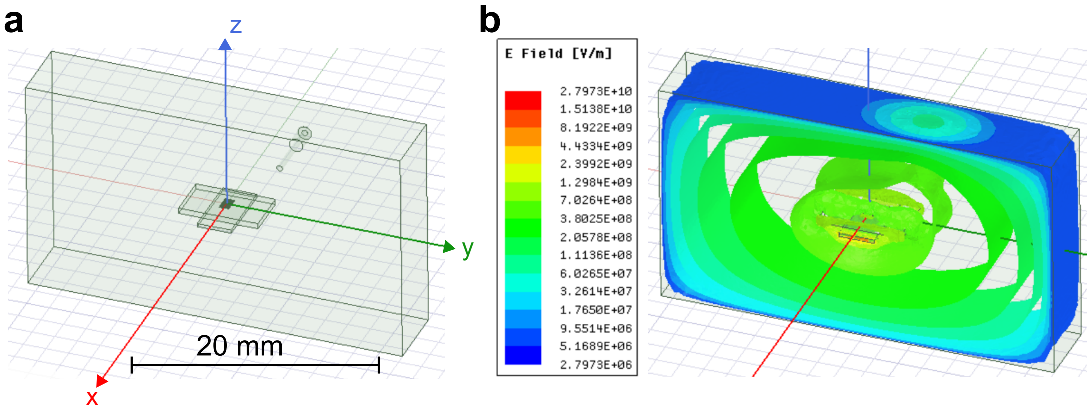

Figure 3.2: **HFSS simulated geometry and results for the copper box mode. (a)** HFSS geometric model of the metallic box ($33 \times 9 \times 16$ mm^3), the metallic pin in a box wall hole, and the silicon chip ($5.9 \times 3 \times 0.3$ mm^3) supporting the $CaWO_4$ crystal ($7 \times 4 \times 0.5$ mm^3). The resonator model created with zero thickness on top of the $CaWO_4$ chip is shown on Figure 3.3. **(b)** Simulated electric field amplitude of the box fundamental mode in logarithmic scale (1 Joule in the mode).

The dielectric constants of $CaWO_4$ are $\epsilon_{a,b} = 11.7 \pm 0.1$ and $\epsilon_c = 9.5 \pm 0.2$; they are known from measurements at room temperature at 1.6 kHz [116] and 1 MHz

[117]. Since no measurements were reported for cryogenic temperatures, we first use the room temperature values in our simulations. Then we fabricate a device with the simulated geometry and measure it at cryogenic temperature. The discrepancy between simulated and measured resonant frequencies gives a correction factor for the dielectric constants. We finally use the corrected $\epsilon_{a,b} = 10.65$ and $\epsilon_c = 8.96$ to perform the simulations on the geometry of interest.

We had also to face a technical problem: simulating submicron geometric dimensions ($600\,nm$-wide wire) together with large dimensions in the millimeter range causes meshing issue for the software. To solve this issue, we had to model our $600\,nm$-wide wire by a fictitious $2\,\mu m$-wide one, with however corrected values of its geometric and kinetic inductances in order to match those of the narrow wire (kinetic inductance of $0.2\,\mathrm{pH}/\square$ and geometric inductance of x + $0.24\,\mathrm{pH}/\mu m$ instead of x $\mathrm{pH}/\mu m$ for a $2\,\mu m$ wire).

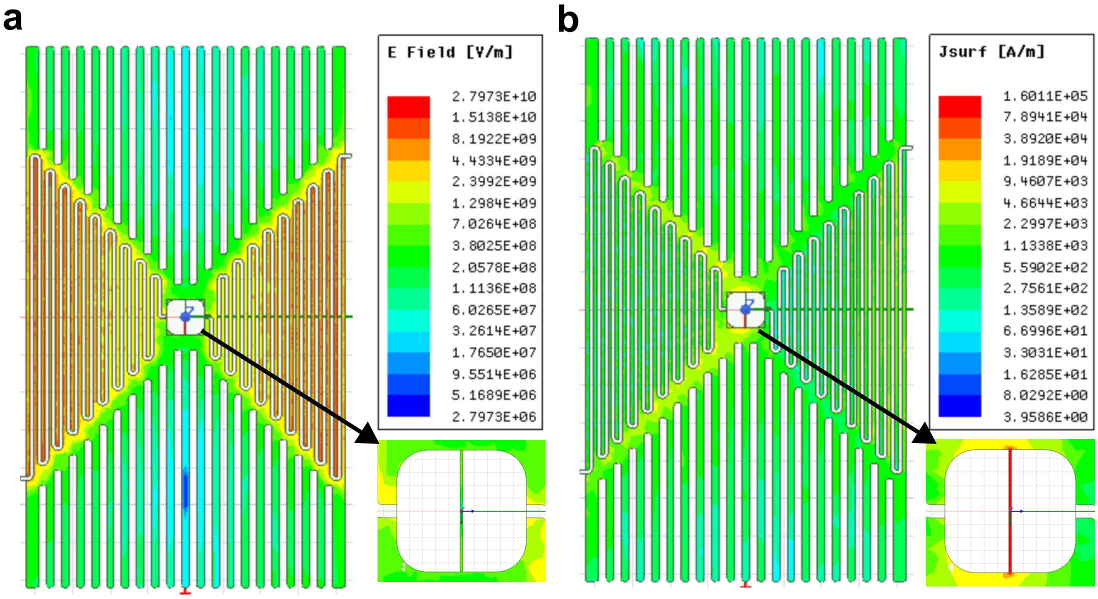

Figure 3.3: **HFSS simulation on resonator 2.** **(a)** Simulated electric field distribution in logarithmic scale of resonator mode with 1 Joule energy applied. **(b)** Simulated surface current distribution in logarithmic scale of resonator mode with 1 Joule energy applied.

We then use HFSS to solve the eigenmodes of the system. This eigensolver performs "undriven" analysis by assuming a certain amount of energy stored in the system, and finds the eigenmodes with complex eigenfrequencies (real frequency and damping of the system) and field distribution by solving Maxwell equations. The analysis continues iteratively with refined meshing of the geometric object until the relative change of eigenfrequencies $\Delta\omega_0/\omega_0$ is below a preset threshold (0.1% in our case). Then it computes the field in the dielectric volume and currents or charges on the metal. Here we have simulated three resonator geometries independently. The fundamental mode of the copper box (TE011 mode) is shown in Figure 3.2b. The magnitude of its electric field is plotted in logarithmic scale for 1 Joule of energy in the mode. The simulated electric field and surface current distribution on resonator 2 can be seen in Figure 3.3, with 1 Joule of energy in the resonator mode. From the eigenmode study in HFSS, we can also obtain the eigenfrequency and coupling rate (or quality factor) for each mode found by the simulator. Table 3.2 summarizes the simulation results obtained for the fundamental mode of the box and the resonator mode of each design. The 3 resonators are separated by 100 MHz and around the targeting 7 GHz as expected.

resonator property	reso 1	reso 2	reso 3	box
$\omega_0/2\pi$ (GHz)	7.247	7.118	6.961	8.364
$\kappa_c/2\pi$ (MHz)	0.13	0.087	0.054	61
quality factor (Q)	56000	82000	130000	137

Table 3.2: **Simulated resonator properties.**

To enhance the magnetic coupling constant between spin and resonator field, a low-impedance resonator ($Z_0 < 50\,\Omega$) is favored to ensure a larger vacuum fluctuation of current Section 2.2.1. Here in the simulation, the resonator impedance Z_0 can be extracted by adding and varying a small inductance δL (typically 1 pH) in the middle of the wire and performing a linear expansion of $\omega_0 = 1/\sqrt{LC}$, which gives

$$\frac{\delta\omega_0}{\omega_0} = -\frac{\delta L}{2L}. \tag{3.1}$$

Adding for instance 1 pH to the wire of resonator 2, induces a variation $\delta\omega_0/2\pi = 10\,\text{MHz}$ of the simulated resonant frequency. The total resonator inductance is therefore

$$L = -\frac{\delta L\omega}{2\delta\omega} = 356\,\text{pH}, \tag{3.2}$$

and the resonator impedance

$$Z_0 = \omega_0 L = 16\,\Omega. \tag{3.3}$$

The sole wire inductance can be estimated from the 0.2 pH/□ kinetic inductance and 1 pH/μm geometric inductance. Thus $L_{\text{wire}} \sim 132\,\text{pH}$ accounts for about 37% of the total inductance in the resonator.

Spatial distribution of spin-resonator coupling constant

As shown in the cross-section of the resonator in Figure 2.8, a magnetic field $\mathbf{B_1}$ generated by the inductive wire current couples to spins beneath. We now estimate quantitatively the magnetic coupling constant g_0 between the resonator and a single spin close to the inductive wire, the former being aligned along z and modeled as infinitely long, with width $w = 600\,\text{nm}$ and thickness $t = 50\,\text{nm}$. The current is along z and all quantities such as the current density $j_z(x, y)$, the current induced magnetic field $\mathbf{B_1}(x, y) = [B_{1,x}(x, y), B_{1,y}(x, y), 0]$ or the coupling strength $g_0(x, y)$ depend on the x and y coordinates only. Moreover, we take the origin on the crystal surface in the middle of the wire (see Figure 3.4), so that $j_z(x, y)$ is even in y. Consequently, as a function of y, $B_{1,x}(x, y)$ is odd, $B_{1,y}(x, y)$ even and $g_0(x, y)$ even. According to Equation 2.46, we have in our geometry with $\mathbf{B_1} \perp \mathbf{B_0}$

$$\frac{g_0(x, y)}{2\pi} = \frac{\gamma_\perp}{2h}||\delta\mathbf{B_1}(x, y)||, \tag{3.4}$$

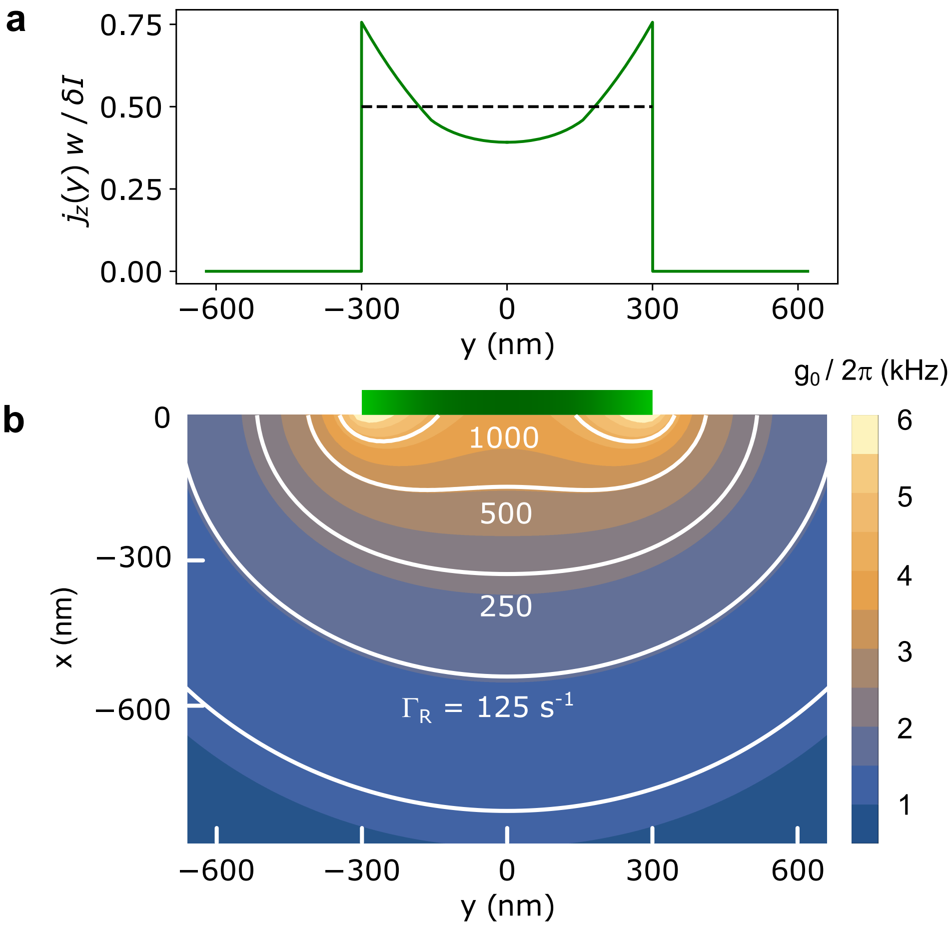

Figure 3.4: Simulation of spin-resonator wire current **(a)** and coupling constant $g_0(x, y)$ and radiative relaxation rate $\Gamma_R(x, y)$ **(b)** as a function of the spin position (x, y) with respect to the wire (shown as a green rectangle). The theoretical current density in the wire is shown as shades of green. (The dashed line in panel **a** corresponds to a constant current density at the same total current)

with $\delta\mathbf{B_1}$ the $\mathbf{B_1}$ vacuum fluctuations that correspond to the current vacuum fluctuations δI (see Section 2.2.1) in the resonator wire. Then

$$\delta\mathbf{B_1}(\mathbf{r}) = \frac{\mu_0}{2\pi}\int_{x'=0}^{t}\int_{y'=-w/2}^{w/2} j_z(\mathbf{r}')dx'dy'\frac{\mathbf{k}\times(\mathbf{r}-\mathbf{r}')}{||\mathbf{r}-\mathbf{r}'||} \tag{3.5}$$

is simply obtained by integrating the Ampere's law over all current lines $j_z(\mathbf{r}')dx'dy'$ with $\mathbf{r} = [x, y, 0]$, $\mathbf{r}' = [x', y', 0]$, and $\mathbf{k} = [0, 0, 1]$ the unit vector along z. For the current distribution $j_z(x, y)$ in our Nb superconducting wire, we use an approximation by Van Duzer (ref. [118]) assuming a constant distribution along x (wire thinner than the effective penetration depth λ of the magnetic field in the superconductor) and a wide wire satisfying $2wt/\lambda^2 > 1$:

$$\begin{aligned} j_z(y) = j_0/\sqrt{1-(2y/w)^2} \text{ if } & \quad |y| < |w/2 - \lambda^2/2t|, \\ j_z(y) = 1.165 j_0\sqrt{wt}/\lambda e^{-(w/2-|y|)t/\lambda^2} \text{ if } & \quad |w/2-\lambda^2/2t| < |y| < w/2, \end{aligned} \tag{3.6}$$

with j_0 such that $\int_{y=-w/2}^{w/2} j_z(y) = \delta I$. Given the measured values $\lambda = 120$ nm for Nb, $2wt/\lambda^2 \sim 4$, and the computed $j_z(y)$ is that of Figure 3.4a. Then taking the frequency and impedence of resonator 2, the integration of Equation 3.5 leads to the field map and to the $g_0(x, y)$ map of figure Figure 3.4b. As indicated by Equation 2.65, the iso-B_1 and iso-g_0 are also iso-Purcell rate Γ_R lines. A few of these lines are also shown on the figure.

Fabrication

The resonator was directly fabricated on the polished face of the $CaWO_4$ crystal (see schematic in Figure 3.1a) by sputtering 50 nm of niobium and patterning the film by electron-beam lithography and reactive ion etching. The complete fabrication process is summarized in Figure 3.5.

The process includes only one patterning of the Nb film, by e-beam lithography and reactive ion etching (RIE). However, instead of patterning negatively the resonator geometry in the e-beam resist and using it as the mask for Nb etching, we pattern positively the e-beam resist and evaporate and lift-off aluminum to build a hard protective mask. After etching Nb through this hard Al mask, the latter is removed by wet etching. The optical microscope image of the sample after complete fabrication is shown in Figure 3.6.

3.2 Experimental setup

In this section, we describe the experimental setup that we have used for addressing individual spins and detecting them by fluorescence. This setup includes the spin-resonator mounted in its copper box and a single microwave photon detector (SMPD), both placed in a dilution refrigerator and embedded in a microwave circuit extending up to room temperature.

3.2.1 Spin-resonator and SMPD assembly

Spin-resonator sample

After fabrication of the three resonators on the crystal, the latter is mounted in a 3D copper cavity. Due to the mismatch of dimensions between the crystal and the copper box holder, an extra silicon chip is added to support the crystal, as shown in Figure 3.7. A pin antenna soldered to an SMA connector attached to the top wall of the copper cavity is used as the single input-output port, both for exciting the spins and collecting their signal.

SMPD sample

The SMPD chip is glued on a microwave printed-circuit board (PCB) and bonded to its circuit using aluminum wires. This PCB is then mounted into a dedicated microwave sample-holder (called JAWS). Low-pass (Eccosorb) filters suppressing infrared radiation and higher frequencies are attached to all sample-holder ports (see Figure 3.8). The holder is then shielded from electromagnetic radiations and low-frequency magnetic noise using 3 nested metallic cans (see Figure 3.9). More details can be found in the thesis of Leo Balembois.

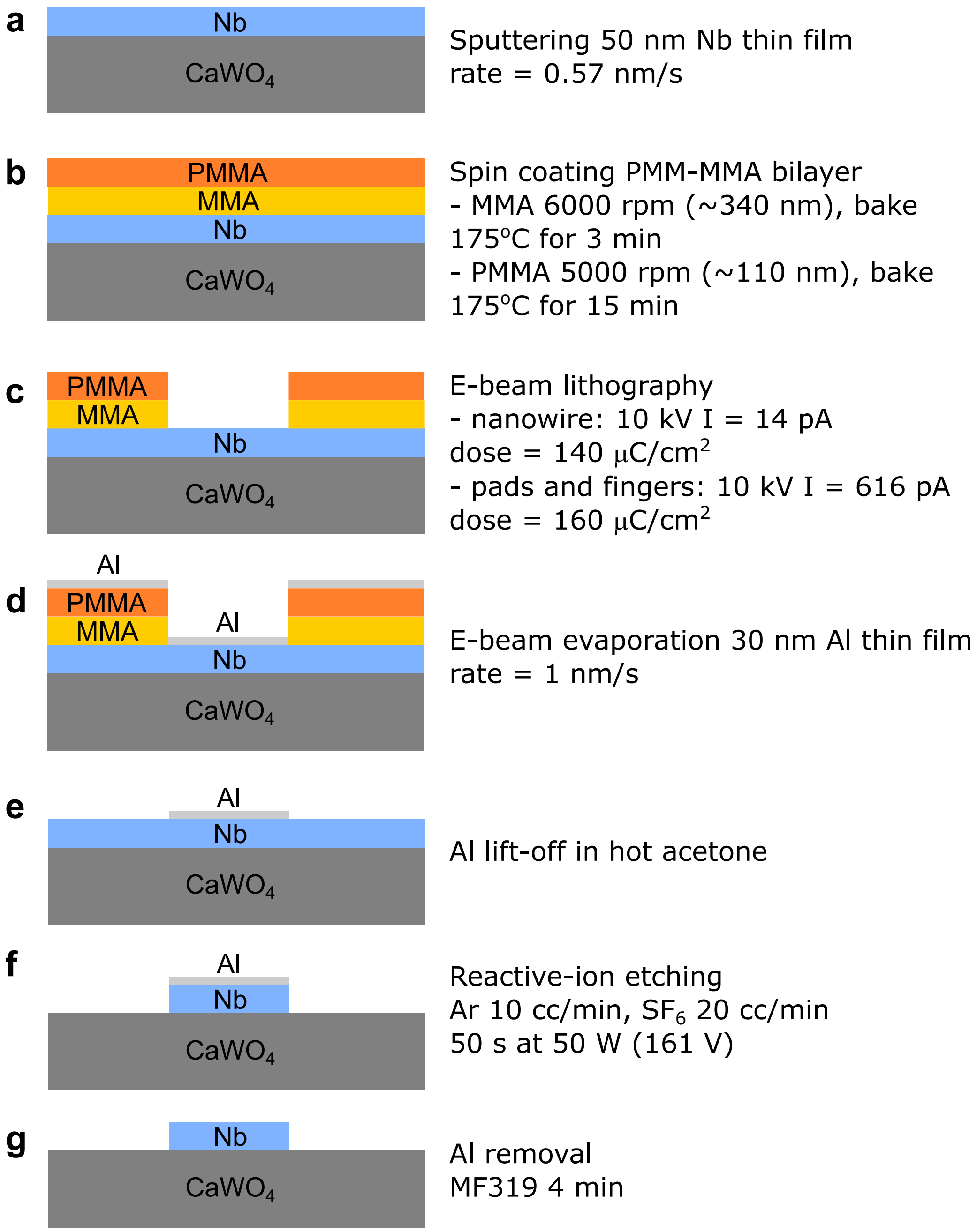

Figure 3.5: **Fabrication process flow of Nb resonator on** CaWO$_4$**.** **(a)** Depositing 50 nm Nb thin film by sputtering. **(b)** Spin coating PMMA-MMA e-beam resist bilayer. **(c)** E-beam lithography for patterning **(d)** Depositing 30 nm Al hard mask by evaporation. **(e)** Lift-off of resist bilayer and Al thin film. **(f)** Reactive-ion etching for Nb. **(g)** Removing Al hard mask.

3.2.2 Low-temperature setup

The schematics of the complete experimental setup is shown in Figure 3.10. The bottom half is located inside a dilution refrigerator with 4 stages at different temperatures. We first discuss this part of the setup inside the refrigerator.

The spin-resonator sample and the SMPD device are attached to the mixing chamber plate of the dilution refrigerator, which is to be cooled down to the base

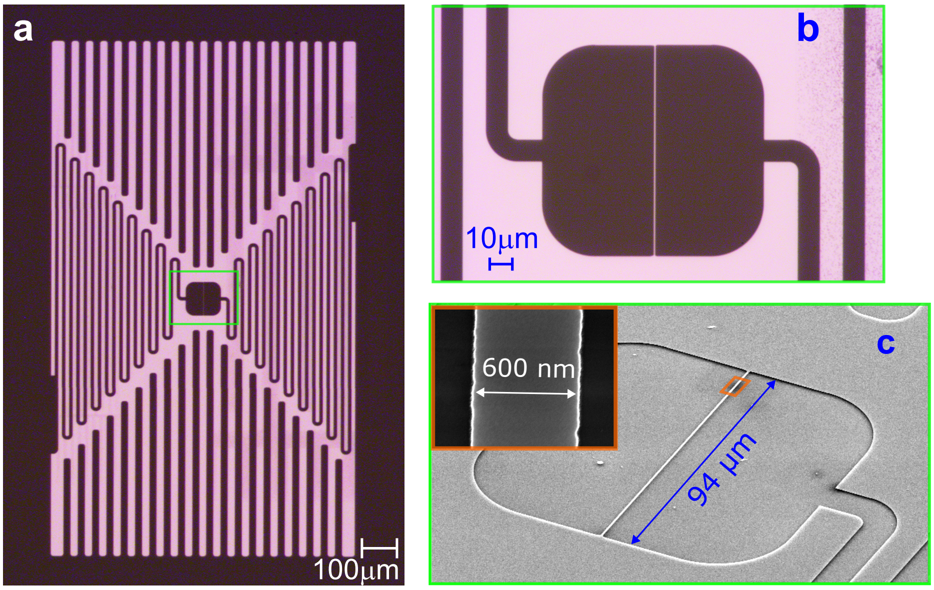

Figure 3.6: **Images of one of the spin-resonators fabricated on the crystal.** **(a)** Optical micrograph of the whole Nb resonator. **(b)** Zoom-in on the central part, showing the inductor wire and the 10 μm gap between the 10 μm wide capacitor fingers. **(c)** Scanning electron micrograph of the center, on a nominally identical sample. The inductive wire has a length of 94 μm and a width of 600 nm (see inset).

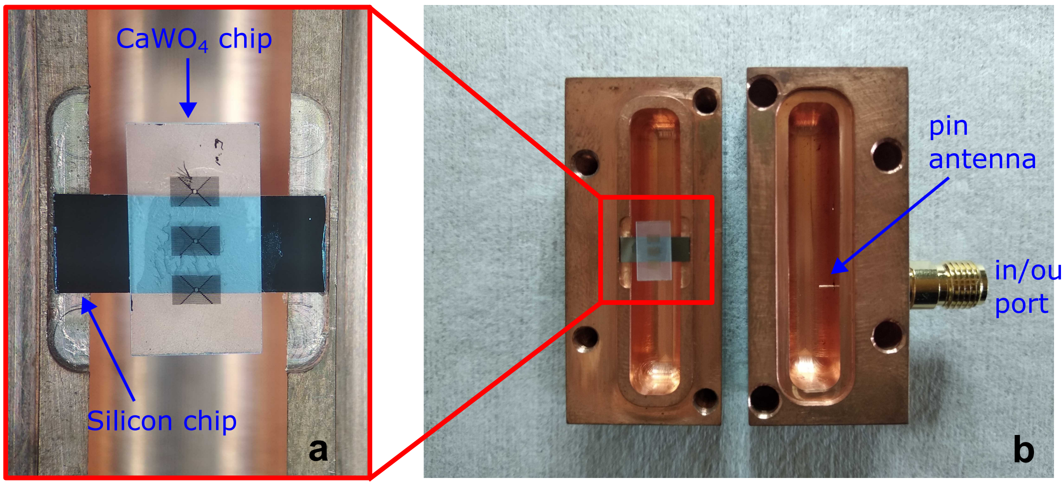

Figure 3.7: **Spin-resonator assembly**. **(a)** Image of zoomed-in view of the center of 3D copper cavity, where the spin-resonator sample (one-side polished 4 × 7 mm $CaWO_4$ chip with 3 resonators fabricated on top) is mounted at the center of the cavity with a supporting silicon chip (dark rectangle). **(b)** Two separate parts of the 3D copper cavity. Spin-resonator sample is mounted in one part and a pin antenna soldered to an SMA connector used as input/output port is installed to the other part.

temperature of 10 mK. More precisely, the spin-resonator holder is mounted at the bottom of a long copper arm (“cold finger”) that locates it at the center of a 3D coil magnet, far away from the SMPD that is thus not perturbed by the magnetic

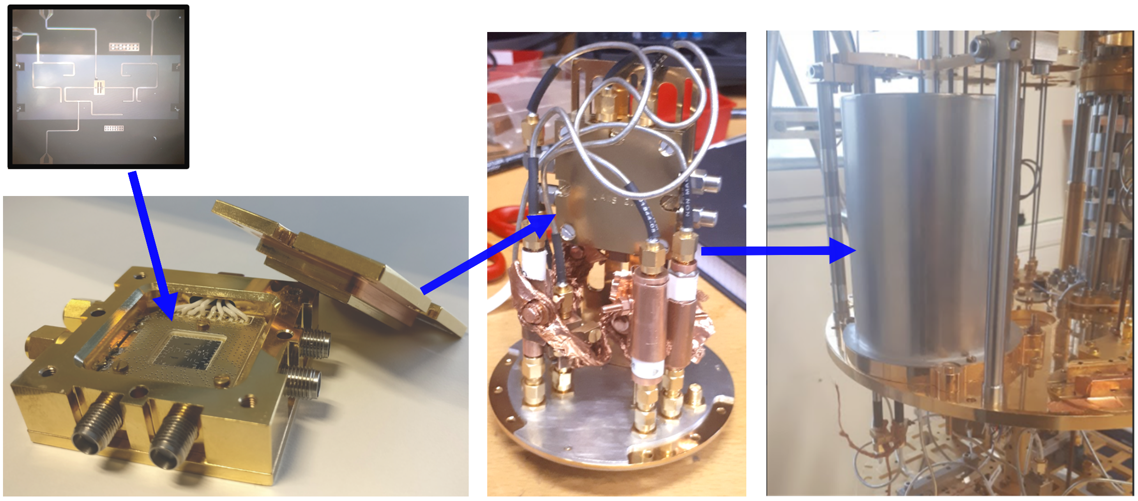

Figure 3.8: **SMPD packaging.** The SMPD chip is glued and wire-bonded in an RF-sample holder (called JAWS). The JAWS is screwed on a copper frame and then mounted with a 3-screen shielding (cooper, μ-metal, aluminium). The figure is taken from [108].

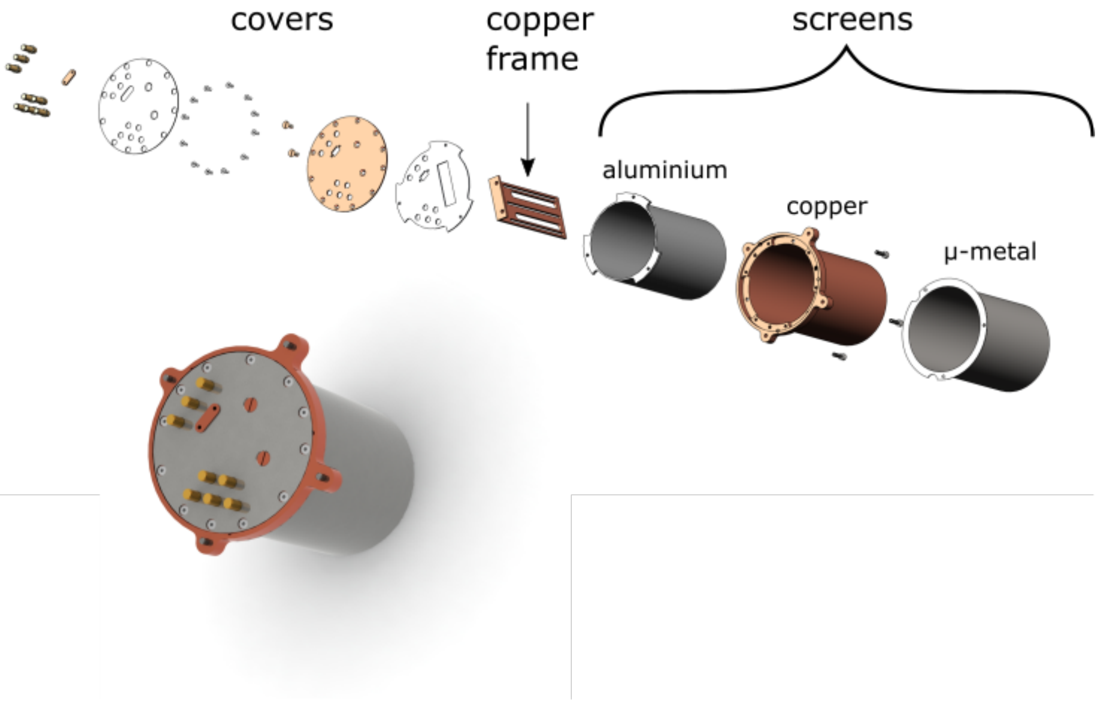

Figure 3.9: **Electromagnetic shielding for SMPD.** Exploded views of the microwave shields used in this experiment. The sample holder of SMPD is screwed on the copper frame. The figure is taken from [108].

field (see Figure 3.11).

The spin excitation pulses are sent through line number 2 in the figure. This line is heavily attenuated ($\sim 110\,\mathrm{dB}$) to optimize its thermalization and thus minimize the number of out-of-equilibrium photons able to produce dark counts in the SMPD. The pulses are directed, through a double- and a single-junction circulator, to the

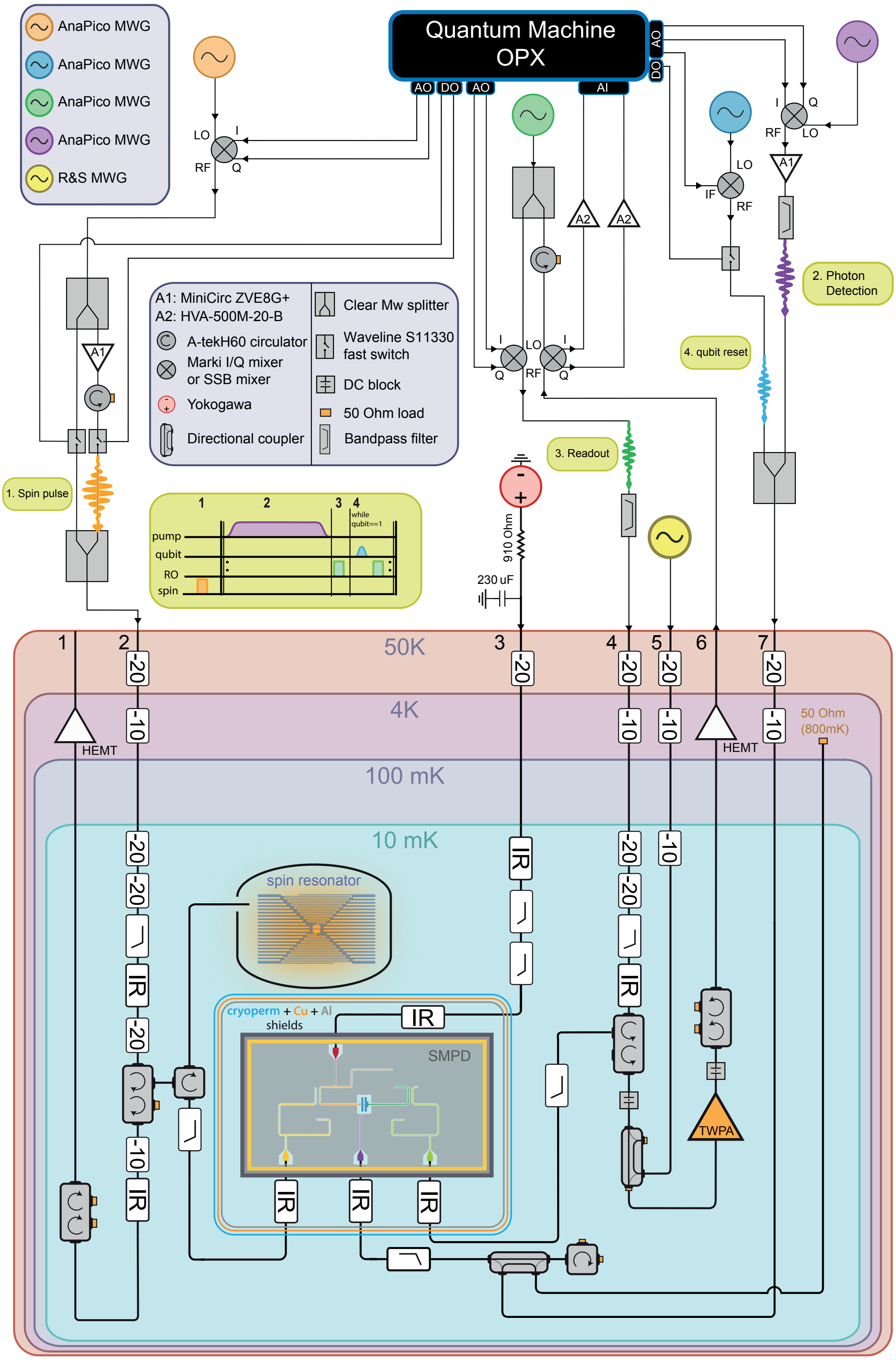

Figure 3.10: **Schematic of the setup**. Wiring and all the components used at room temperature and cryogenic temperature.

antenna of the cavity containing the spin resonator. The pulses partly reflected

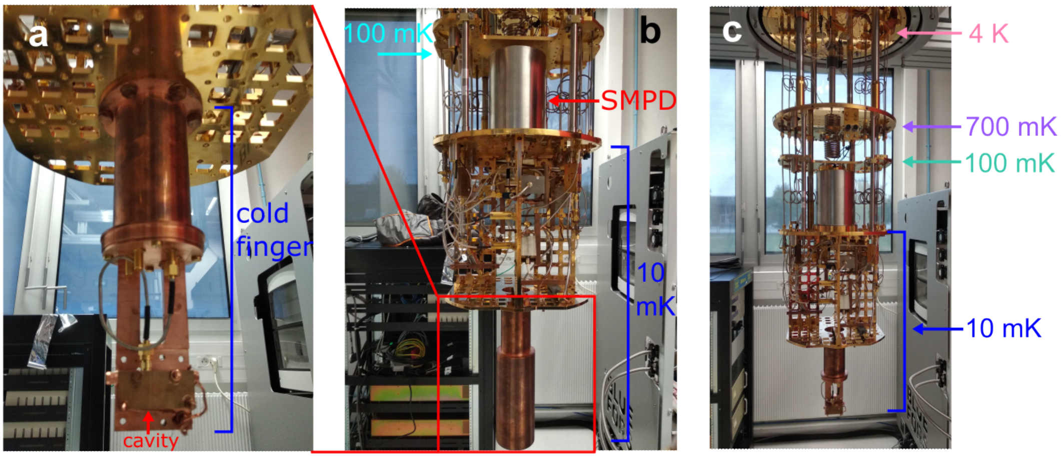

Figure 3.11: **Low temperature setup**. **(a)** The 3D copper cavity hosting spin-resonator sample is mounted to the bottom of the long copper arm (cold finger) and then closed with a cylindrical copper shield (see **b**). The cold finger is attached to the 10 mK plate. **(b)** Image of the entire 10 mK stage in the dilution refrigerator. SMPD box is mounted on the upper 10 mK plate, and all the electronic components are installed between upper and lower 10 mK plates. **(c)** Plates associated with different temperatures when the refrigerator is cold.

on the antenna as well as the output signal coming from inside the copper box are routed to the input of the SMPD device through a single-junction circulator. To pre-characterize the spin resonator as well as the SMPD (next two sections of the present chapter), the signal reflected on the SMPD input is routed to room-temperature via the same single- and double-junction circulators and via output line 1 and its HEMT amplifier; isolation of the experiment from this HEMT is provided by an extra 10 dB attenuation followed by a double-junction isolator. Note that in all the measurements reported in the Chapter 4 and Chapter 5, this line 1 was left open and its HEMT switched off.

In normal operation, the SMPD pump tone and qubit reset pulses are applied via line 7 and its -20 dB directional coupler. The other 2 ports of the coupler are connected to a 50 Ω load at 800 mK and a 50 Ω-loaded circulator at 10 mK, in order to minimize the noise induced by the dissipation of these signals. The SMPD qubit readout pulses are sent via the attenuated line 4 and a double circulator. The reflected signal is routed by this double circulator to a Josephson Traveling Wave Parametric Amplifier (TWPA) [119] pumped from line 5 through a directional coupler; the signal propagates to a second HEMT at 4 K, isolated by a double-junction isolator.

3.2.3 Room-temperature setup

The room-temperature part of the setup (above the 50 K dilution refrigerator frame in Figure 3.10) uses five microwave sources and one FPGA-based instrument (OPX platform from Quantum Machine) in charge of arbitrary waveform generation, digitization, and real time feedback. The OPX instrument provides 10 analog outputs (AO), 10 digital outputs (DO) and 2 analog inputs (AI) for digitization.

The pulses used to drive the spins are generated by I/Q mixing a pair of in-phase

(I) and quadrature (Q) intermediate frequency (IF) signals from the OPX with a local oscillator (LO - orange) at the spin-resonator frequency ω_0. The upconverted microwave signal is then split over 2 branches, one of them including an about 40 dB amplifier, which are then recombined. Only one of the two branches is selected to propagate the signal, using two fast switches controlled by digital lines from the OPX. All the measurements related to spins art performed using the branch with the amplifier. The other branch is used only for pre-characterizing the SMPD, i.e. calibrating the input microwave photon flux and measuring the SMPD efficiency. As already mentioned, the spin excitation pulses enter the dilution refrigerator through line 2.

The SMPD operation (see Section 2.3.2 for details) involves one dc-current and three microwave sources playing the following roles:

- A Yokogawa current source (red) provides the necessary magnetic flux bias to bring the ω_b frequency of the SQUID-tunable buffer resonator of the SMPD in resonance with the frequency ω_0 of the spin resonator, so that the fluorescence photons emitted by the spins are at the center of the SMPD detection band.

- A first microwave source (purple) provides the pump tone at frequency ω_p that enables the four-wave mixing process converting an incoming photon in the buffer into an excitation in the superconducting transmon qubit at ω_q and a photon in the waste resonator at ω_w, according to $\omega_p + \omega_b = \omega_q + \omega_w$.

- A second microwave source (green) reads the SMPD qubit state out by microwave reflectometry and homodyne detection: it actually measures the qubit-state dependent dispersive shift of the readout (waste) resonator.

- A third microwave generator (blue) is used as a local oscillator (LO) for generating the qubits control pulses by sideband mixing the LO with one OPX IF output. The line conveying these pulses is combined with the pump line and connected to line 7 of the refrigerator.

Besides, a Rohde & Schwarz SMR20 microwave source (yellow) at the input of line 5 provides the pump power for the TWPA placed at 10 mK.

3.2.4 3-axis vector magnet

The magnetic field $\mathbf{B_0}$ is generated by a 1T/1T/1T 3-coil superconducting vector magnet, producing independent fields along 3 orthogonal directions X, Y and Z. Each coil is supplied by a commercial current source (Four-Quadrant Power Supply Model 4Q06125PS from AMI) and includes a parallel shunt that can be switched between a superconducting state and a normal state. A coil can thus be operated in one of two possible modes:

- **Current supplied mode:** The shunt is normal and the source delivers the current continuously to the coil. This mode is used for sweeping the magnetic field in a certain range, in order to perform spectroscopy measurement (bringing the spin transition frequency in and out of resonance with the resonator), or to align the total magnetic field in a targeted direction.

- **Persistent mode:** once the coil is loaded with a current, the switch is made superconducting, and the current in the coil becomes persistent. In this mode, the field is constant and very stable compared to the current supplied mode. This mode is used for measurements requiring highly stable field, such as the coherent manipulation of a spin.

Time-domain measurements of Chapter 5 require tuning precisely the spin-resonator frequency detuning δ and to keep it stable (less than 10kHz variation) over long periods of time. To achieve this goal, we take benefit of our Z coil being nearly aligned with the z axis (the axis along the inductive wire of the resonator), thus providing the major part of B_0 field; we thus minimize the noise by placing this coil in persistent mode. Then, the other coil closest to the y axis (the in-plane axis perpendicular to the inductive wire of the resonator) is used to fine-tune δ. The (much smaller) current through that coil is moreover further stabilized using a custom-made feedback loop based on an additional current meter (Keithley 2700 model) and a voltage source (TTi), see Figure 3.12.

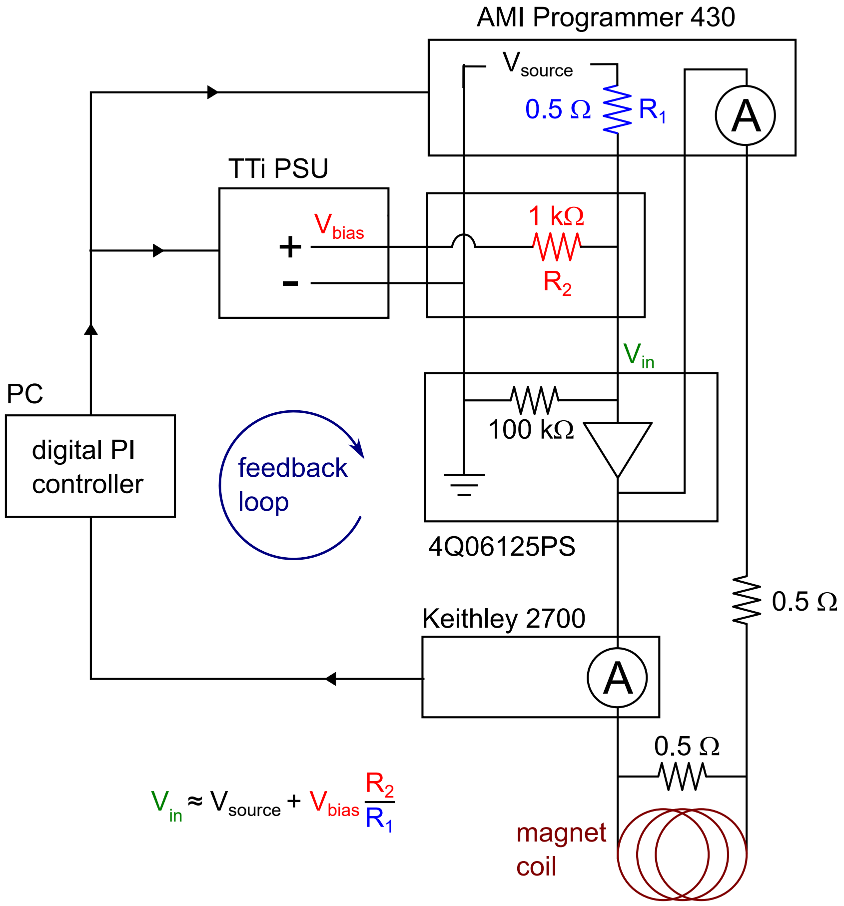

Figure 3.12: Setup for stablizing the current through the coil.

The voltage V_{in} (composed of two parts: V_{source} and V_{bias}) at the input of AMI power supply (4Q06125PS) determines the current in the coil. V_{source} from AMI programmer sets the target current and V_{bias} generated from a power supply unit (TTi) is used for small correction. The current measured in real time by the Keithley 2700 is used by the feedback controller to determine the correction voltage V_{bias} to be applied in TTi. The sensitivity of V_{bias} can be adjusted by the resistance ratio

R_2/R_1 if it is necessary. Since the Keithley 2700 has higher resolution than the internal current meter of AMI programmer, this setup provides better stablization compared to using AMI only.

3.3 Resonator characterization at 10 mK

3.3.1 Reflection measurement at zero magnetic field

We first measure with a vectorial network analyzer (VNA) the reflection coefficient of the three spin-resonators at base temperature 10 mK and zero magnetic field. The power at the input of the copper cavity is around −120 dBm, which corresponds to an average photon number of about 100 in the resonator at steady state. Because the signal is reflected on the single cavity port, we call this type of measurement reflection and the corresponding coefficient S_{11}, although the input and output lines (line 1 and line 2 in Figure 3.10) are separated using a circulator. Figure 3.13a, b shows S_{11} of resonator 2: the resonator has a resonant frequency $\omega_0/2\pi = 7.349\,\text{GHz}$, and is over-coupled with an external coupling rate $\kappa_c/2\pi = 270\,\text{kHz}$ and an internal loss rate $\kappa_i/2\pi = 120\,\text{kHz}$. The latter is limited by the CaWO$_4$ substrate interface and the presence of residual metal on the chip edges. The same measurements performed on resonator 3 are shown in Figure 3.13c, d. All the results are summarized in Table 3.3 and compared with simulations. Note that the measurement data of resonator 1 is not available due to the fabrication issue.

resonator properties	reso 1	reso 2	reso 3
simulated $\omega_0/2\pi$ (GHz)	7.247	7.118	6.961
measured $\omega_0/2\pi$ (GHz)	N.A.	7.349	7.217
measured $\kappa_i/2\pi$ (kHz)	N.A.	120	92
measured $\kappa_c/2\pi$ (kHz)	N.A.	270	114
measured Q_i	N.A.	61000	79000
measured Q_c	N.A.	27000	63000

Table 3.3: **Comparison between simulated and measured resonator properties.**

3.3.2 Magnetic field alignment

We now describe the procedure to bring precisely the external magnetic field B_0 in the resonator plane, following an approach very similar to ref. [114]. Our high-Q thin-film superconducting resonators are sensitive to magnetic field, especially its component perpendicular to the resonator plane [120]. A small out-of-plane field can lead to a drastic reduction of the resonator frequency and an increase of the internal losses. We therefore use the resonator as a "probe" to maximize the frequency and bring the field generated by the 3-axis coils (see Section 3.2.4) in the resonator plane. Note that we use the coil coordinate system (X,Y,Z) in the explanation below.

The goal of the alignment is to find the rotation angle φ_0 around Z transforming (X,Y,Z) into (X′,Y′,Z′ = Z), and then the rotation angle ψ_0 around Y′ transforming

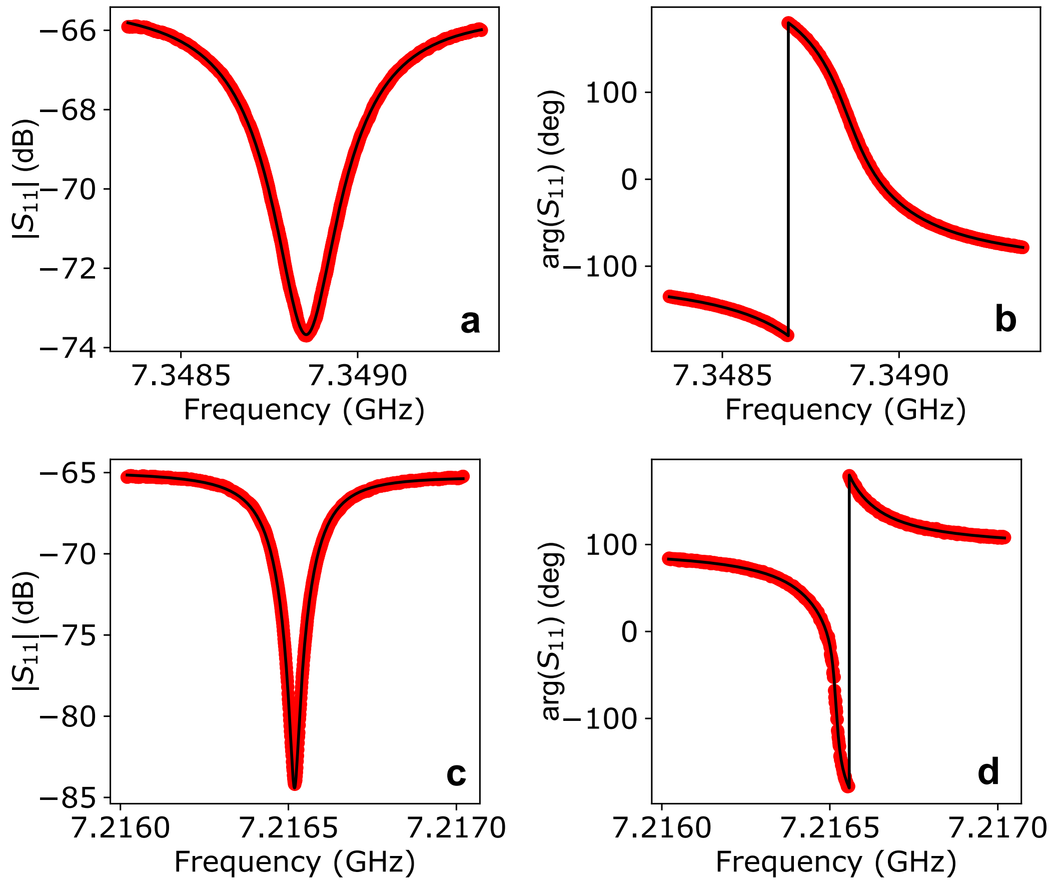

Figure 3.13: **Reflection measurement of the resonators at zero magnetic field.** Amplitude and phase of the reflection coefficient S_{11} as a function of the probe frequency, for resonators 2 **(a,b)** and 3 **(c,d)**. The fits (solid line) to the data (red dots) yield the resonant frequencies ω_0, coupling rates κ_c, and internal loss rates κ_i shown in Table 3.3.

(X′,Y′,Z′) into (X″,Y″ = Y′,Z″) so that the axes Y″-Z″ lay in the resonator plane. The full protocol consists of 4 steps:

1. Apply $B_0 = 50\,\mathrm{mT}$ along the Y-axis with the Y magnet.

2. Measure the resonator frequency while rotating B_0 around Z (in the X-Y plane) by a small angle φ of typically ±1°, using the X and Y magnet. This step is illustrated in Figure 3.14a. The field B_0 is aligned with the resonator plane when the frequency of the resonator reaches its maximum, which corresponds to the small correction angle $\varphi_0 = \arctan(B_X/B_Y)$. Figure 3.14d shows the shift of resonator frequency as a function of rotation angle φ. When φ_0 is found, the field is set back to zero.

3. Apply $B_0 = 50\,\mathrm{mT}$ along Z-axis by the Z magnet.

4. Measure the resonator frequency while rotating B_0 around Y′ in the X′-Z’ plane by a small angle ψ of about ±1° using all the magnets. During this

rotation, the fields needed in magnet X,Y,Z are

$$B_X = -B_0 \sin\varphi_0 \sin\psi \tag{3.7}$$

$$B_Y = B_0 \cos\varphi_0 \sin\psi \tag{3.8}$$

$$B_Z = B_0 \cos\psi \tag{3.9}$$

This step is illustrated in Figure 3.14b. The field B_0 is in the resonator plane when the frequency of the resonator reaches its maximum at $\psi = \psi_0$. Figure 3.14e shows the shift of resonator frequency as a function of ψ. When ψ_0 is found, the field is set back to zero.

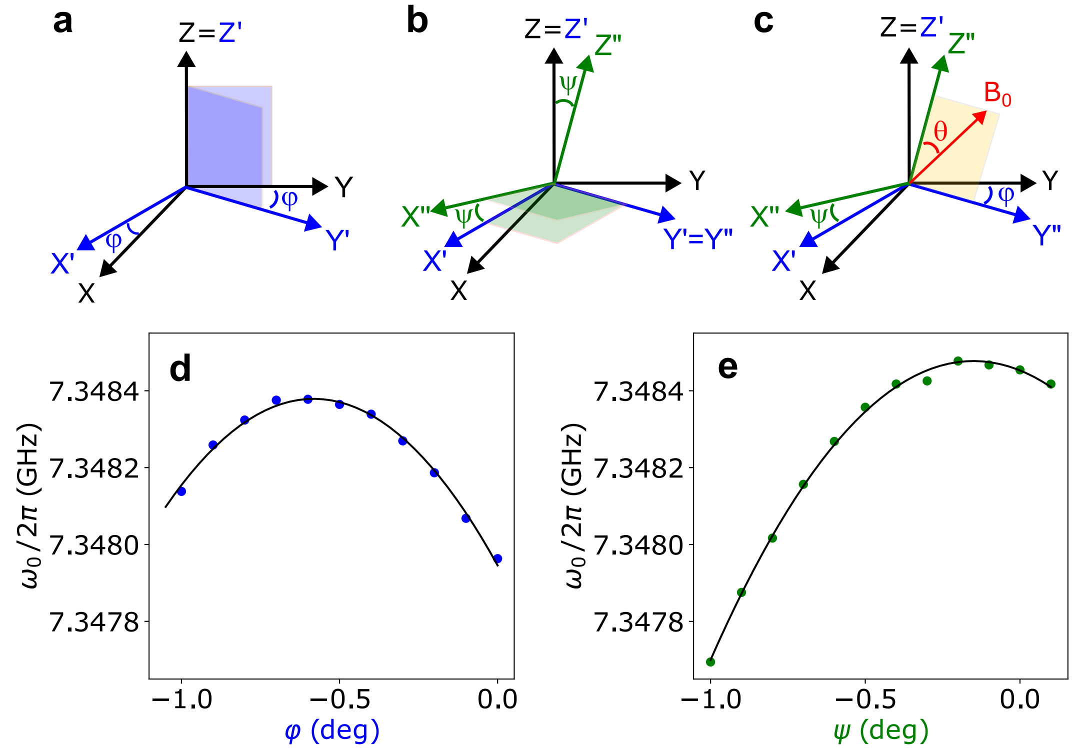

Figure 3.14: **Magnetic field alignment into the plane of resonator 2**. **(a)** A first rotation of an angle φ around Z brings Y to Y' in the resonator plane. **(b)** A second rotation of an angle ψ around Y'=Y" brings Z'=Z to Z" in the resonator plane. **(c)** B_0 field applied in the resonator plane (Y", Z") and making an angle θ with Z". **(d)** Resonator frequency at $B_0 = 50\,\mathrm{mT}$ as a function of angle φ. **(e)** Resonator frequency at $B_0 = 50\,\mathrm{mT}$ as a function of angle ψ.

Now with the known correction angles φ_0 and ψ_0, an arbitrary field B_0 in the Y″-Z″ resonator plane, with an angle θ with respect to Z″ (see Figure 3.14c) is obtained by setting the (X,Y,Z) magnets as

$$\mathbf{B_0} = \begin{pmatrix} B_X \\ B_Y \\ B_Z \end{pmatrix} = B_0 \begin{pmatrix} \sin\theta\sin\varphi_0 - \cos\theta\sin\psi_0\sin\varphi_0 \\ \sin\theta\cos\varphi_0 + \sin\theta\sin\psi_0\cos\varphi_0 \\ \cos\theta\cos\psi_0 \end{pmatrix}. \tag{3.10}$$

3.3.3 Reflection measurement at non-zero magnetic field

To perform ESR detection, we need to apply a magnetic field of about 0.4 T to bring erbium spins in resonance with the resonator at about 7 GHz. It is therefore interesting to characterize the resonator in a magnetic field of this magnitude. We do it here with resonator 2 because its frequency ($\omega_0/2\pi = 7.348$ GHz) is in the tunable frequency range of the SMPD buffer resonator.

Figure 3.15 shows the measured amplitude and phase of the reflection coefficient of resonator 2 at 420 mT. The internal loss rate has increased by nearly a factor of 2 compared to zero field. The still slightly over-coupled resonator is now approaching the critical coupling.

In addition, we have also studied the dependence of the internal loss rate on the input power, equivalently on the average number of photons in the resonator (see Figure 3.16). We clearly see an increase of internal losses by a factor 1.5 between the lower and higher power. We attribute this to parasitic two-level systems creating dielectric losses at low power but being saturated at high power. The total linewidth $\kappa/2\pi = 470\,\mathrm{kHz}$ at single photon level is close to the real situation of a single spin experiment; this narrow linewidth is responsible for the Purcell-enhanced spin relaxation rate (recall Equation 2.65).

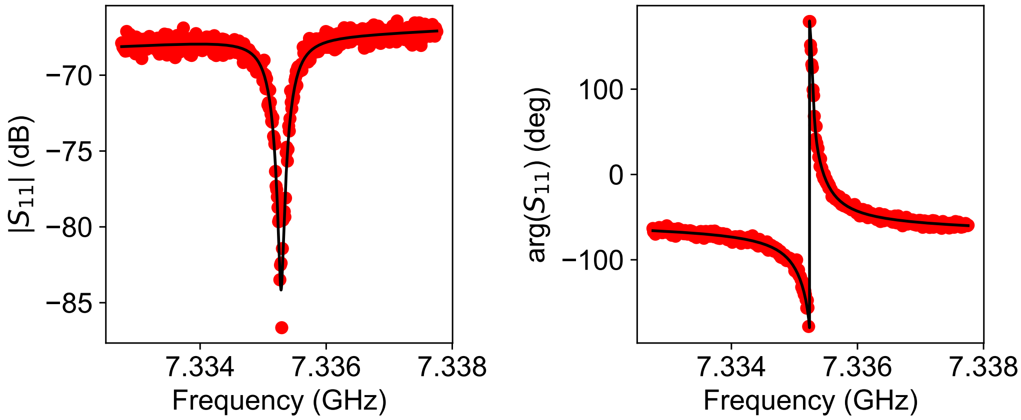

Figure 3.15: **Reflection measurement of resonator 2 at non-zero magnetic field**. Measured amplitude (a) and phase (b) of reflection coefficient S_{11} on resonator 2 as a function of probe frequency (probe power is close to single photon level). The fit (solid line) to the data (red dots) yields a resonant frequency $\omega_0/2\pi = 7.335\,\mathrm{GHz}$, an internal loss rate $\kappa_i/2\pi = 200\,\mathrm{kHz}$ ($Q_i = 37000$) and a coupling rate $\kappa_c/2\pi = 270\,\mathrm{kHz}$ ($Q_c = 27000$).

3.4 SMPD characterization

3.4.1 Figures of merits

The SMPD is operated cyclically. The cycles do not have the same duration but last 12.7 μs on average. Each cycle is composed of three steps: (i) the pumped conversion of an incoming photon into a qubit excitation during 10 μs, (ii) the qubit dispersive readout lasting 2 μs, and (iii) the conditional reset of the qubit to its ground state

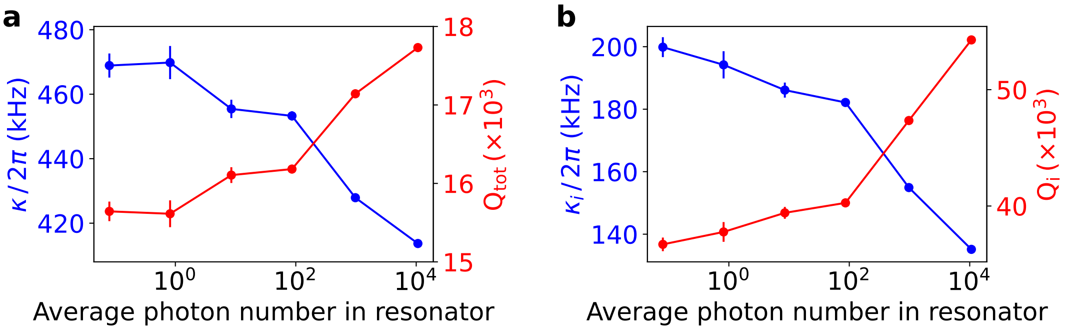

Figure 3.16: **Power-dependent resonator linewidth**. Total resonator linewidth $\kappa/2\pi$ (blue) and total quality factor $\mathrm{Q_{tot}}$ (red) **(a)** and Internal resonator linewidth $\kappa_i/2\pi$ (blue) and internal quality factor $\mathrm{Q_i}$ (red) **(b)**, as a function of average photon number in the resonator.

if it was detected excited. This reset consists of one or several π-pulse(s) applied to the qubit until it is measured in its ground state. The conditional reset time is thus non-deterministic, and lasts from 0.7 μs (feedback time with the OPX) to $0.7 + (2 + 0.7)k$ μs, with k the number of π pulses applied.

At each cycle, a count $C = 1$ is detected if the qubit is found in its excited state (before the reset), and the count time is recorded with sub-microsecond accuracy.

The SMPD is characterized independently, in absence of spin signal, by measuring its key figures of merit in terms of efficiency, dark count rate and detection bandwidth.

Efficiency

The detector efficiency is measured by shining a microwave tone of known power at the detector input. The average input photon flux for a given applied power is calibrated in-situ by measuring the transmon qubit a.c. Stark shift (i.e. the qubit frequency shifted due to the buffer resonator field) and dephasing rate [121]. We have measured the received counts over 1 s as a function of the input photon flux. We show in Figure 3.17 two examples at zero photon flux (dark count) and a flux of 540 photon/s.

The SMPD efficiency is then simply taken as the ratio between the excess count rate above background (dark counts) averaged over 1 s and the applied photon flux. Figure 3.18 shows this excess count rate as a function of the input photon flux up to above 200 thousands photons/s. At hundreds of input photons per second, the efficiency is $\eta_{\mathrm{SMPD}} = 0.32$. Then above 10^4 photons/s, the detector saturates and the efficiency drops. Further optimizing the lifetime of the transmon qubit as well as the readout and pump power for four-wave mixing, would probably yield a better efficiency.

Dark count rate

We define dark counts as the counts that are not due to the spins, that is those originating from spurious excitation of the transmon qubit in absence of incoming photons, and those due to unwanted photons present at the SMPD input [5]. For

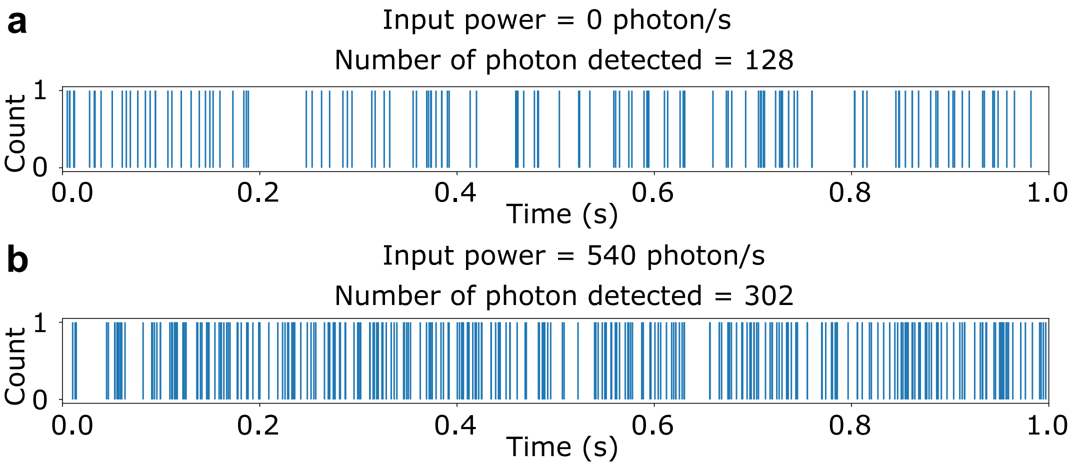

Figure 3.17: **Detected counts shown at their recorded arrival time for input photon fluxes of zero (a) and 540 photon/s (b)**.

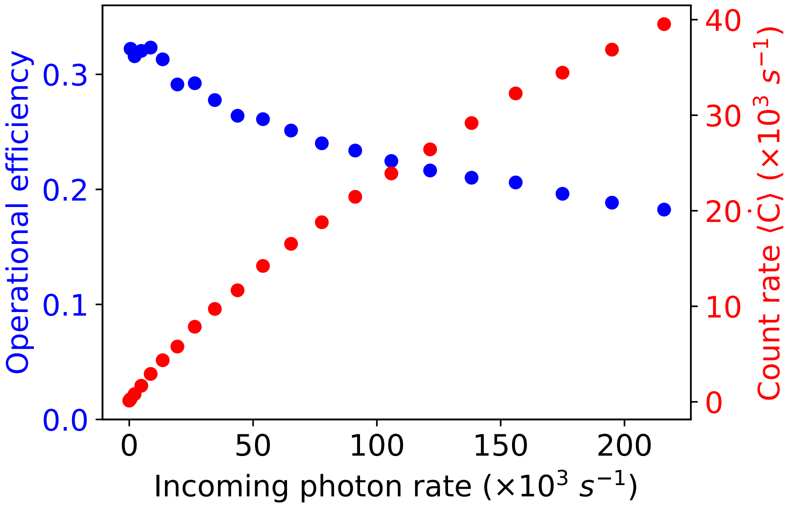

Figure 3.18: **SMPD efficiency.** Excess count rate (red) above background and efficiency (blue) as a function of the applied input photon flux. Below 10^4 photons/s (linear regime), an efficiency of 0.32 is obtained.

this detector, a dark count rate of $106 \pm 3\ s^{-1}$ has been measured over 24 hours. We observed slow dark count rate fluctuation over week time scales ranging typically from $130\,s^{-1}$ to $90\,s^{-1}$ mainly due to variation in qubit T_1 and a slow cooling down of the transmission lines and of the qubit. Figure 3.17a shows an example of a real time trace corresponding to a dark count rate $\alpha = 128\ s^{-1}$.

It is interesting to determine the sources of dark counts in our experiment, in order to lower them in the future. We can discriminate contributions from thermal photons present in the SMPD microwave input line, from the qubit non-zero temperature, and from the heating of the SMPD by the pump, by switching off or detuning the pump tone from the frequency used for proper four-wave mixing. Switching off the pump gives the contribution of spurious qubit excitations and yields a dark count rate of $9\ s^{-1}$. Switching on the pump but detuning it by 10 MHz yields a dark count rate of 11 s^{-1}, which is the joint contribution of qubit spurious excitations and heating by the pump. The pump heating contribution is thus $\sim 2s^{-1}$. Overall, we conclude that the main contribution (92%) to the measured dark counts comes from thermal microwave photons reaching the SMPD via its input line. This corresponds to a thermal population of $\sim 2.4 \times 10^{-4}$ photons in the line, and to an effective temperature of $\sim 42\,\mathrm{mK}$, to be compared to the measured 10 mK base temperature of the refrigerator.

Bandwidth

The detector bandwidth is extracted by measuring the average number $\langle C \rangle$ of detected counts as a function of the frequency of the applied input tone, for a pump frequency fixed at the optimal value for four-wave mixing. In order to mimic the signal from a single spin, we use a $\sim 10\mu s$-long input microwave pulse containing 0.5 photon on average. As shown in Figure 3.19, the full width at half maximum (FWHM) of a Lorentzian fit to the data gives a SMPD bandwidth of 0.9 MHz. For comparison, the dark counts are also plotted.

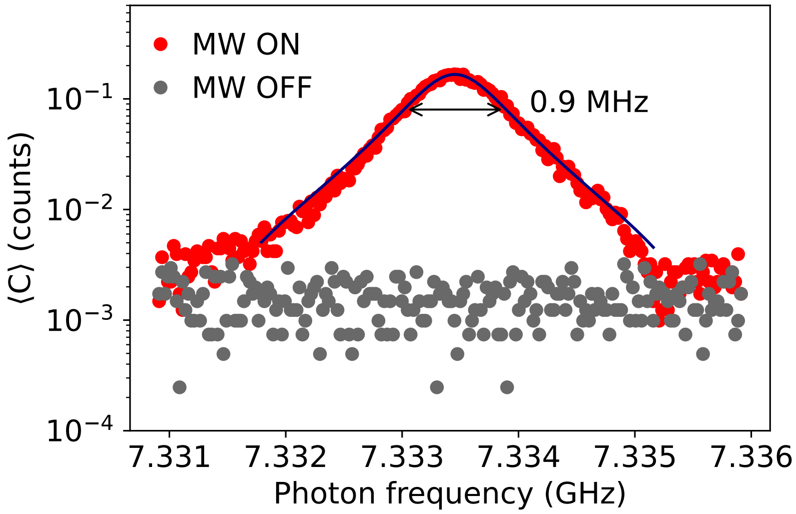

Figure 3.19: **SMPD bandwidth.** SMPD bandwidth. Average number of detected counts as a function of input microwave frequency with microwave on (red dots) and off (gray dots). The solid line is a Lorentzian fit to the data yielding a FWHM bandwidth of 0.9 MHz.

3.4.2 Tuning the SMPD for spin detection

So far the SMPD characterization results that we have presented have been obtained in absence of photons coming from the spins or the spin-resonator. In order to detect the signal from the spin-resonator, the SMPD buffer frequency has to be tuned in resonance with it (using the buffer magnetic flux line), such that $\omega_b = \omega_0$. Figure 3.20a shows a VNA measurement of the reflection coefficient S_{11}, when the SMPD buffer resonator is approaching the spin-resonator. When both resonator lines are overlapping, the fine-tuning can be done by measuring the SMPD counts as done for the bandwidth measurement of Figure 3.19 (i.e. measuring the counts as a function of the frequency of an applied input tone). The results presented in Figure 3.20b show a strong reduction in the counts at the center of SMPD buffer resonance line due to microwave absorption by the spin-resonator.

With all this pre-characterization done, the configuration of the whole setup is now well-prepared for spin detection.

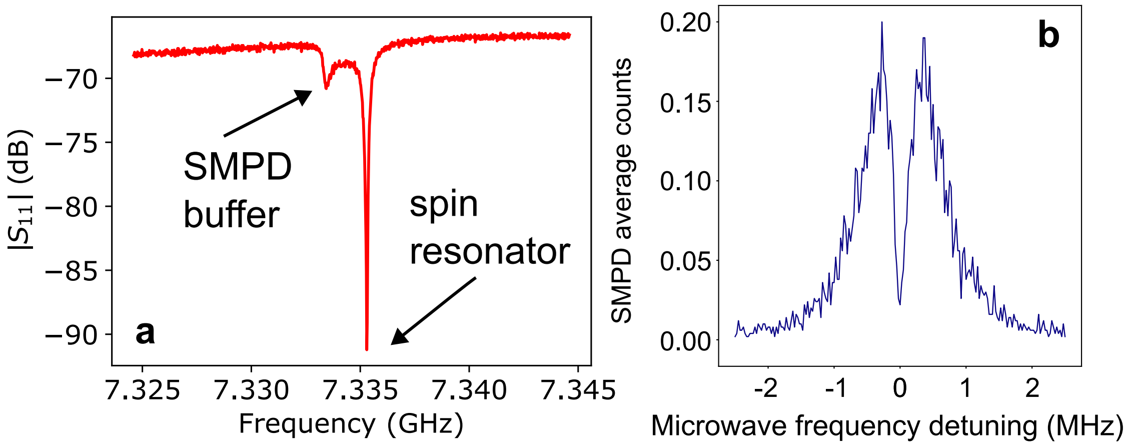

Figure 3.20: **Tuning the SMPD buffer in resonance with the spin-resonator**. **(a)** Amplitude of the reflection coefficient S_{11} as a function of the probe frequency. **(b)** Average SMPD counts as a function of input microwave frequency. Due to absorption by the spin-resonator, a reduction of counts is visible at the center of the SMPD detection band.

Chapter 4

Spin spectroscopy measurements

This chapter focuses on measuring the erbium spectroscopic line of our spin sample (see Section 3.1), with a particularly high resolution at low power. Using our approach of photon counting with the SMPD device discussed in the previous chapter, we reach the hallmark of this experiment: Resolving many individual spin lines inside the spin ensemble spectroscopic line. We begin the chapter by presenting the spin fluorescence signal measured by counting emitted microwave photons. The outcome of this measurement provides a physical quantity, the number of counts C integrated over a certain time, which is recorded when changing the spin transition frequency by sweeping the applied magnetic field, leading to spectroscopy measurements. Then we determine the ensemble-averaged gyromagnetic tensor and crystal symmetry axis by studying the dependence of the spectroscopic line maximum on the magnetic field angle in the crystal plane. As a result, we are able to further align the field B_0 along the projection of the crystal c-axis in the resonator plane. We then show our measurement of the erbium line at high and low spin excitation power, resolving individual spins in the latter case. The final section shows how several individual spin frequencies vary when sweeping both the field amplitude B_0 and its angle θ with respect to the projection of crystal c-axis in the resonator plane, demonstrating that each single spin has a slightly different gyromagnetic tensor.

4.1 Spin fluorescence detection by photon counting

Each measurement corresponding to a particular excitation pulse is repeated in a series of N sequences lasting a sufficiently long time T to let the spins relax to the same initial state. In addition, as discussed in Section 2.4.3, the SMPD device is run cyclically after each excitation pulse, and yields a count $c_j(t_k) \in \{0, 1\}$ at time t_k of cycle k after the excitation of sequence j. Thus the raw data of one complete measurement consists of N arrays of 0s and 1s with their recorded times t_k (actually, only the 1s and their times t_k are really saved in files). Based on this dataset, we define the following quantities of interest to report the results:

- **the average number of counts**

$$\langle C \rangle = \frac{1}{N} \sum_{j=1}^{N} \sum_{t_k=0}^{t_w} c_j(t_k), \tag{4.1}$$

calculated by summing up the counts from $t_k = 0$ to t_w, and averaging over N sequences.

- **the average count rate**

$$\langle \dot{C}(t_d) \rangle = \frac{1}{N} \sum_{j=1}^{N} \left[\frac{1}{\Delta t} \sum_{t=t_d}^{t_d+\Delta t} c_j(t) \right] \tag{4.2}$$

at time t_d, obtained by coarse-graining the counts into bins of duration Δt, and averaging over N sequences.

- **a background-corrected average number of counts**

$$\langle \tilde{C} \rangle = \frac{1}{N} \sum_{j=1}^{N} \left[\sum_{t=0}^{T/2} c_j(t) - \sum_{t=T/2}^{T} c_j(t) \right]. \tag{4.3}$$

Note that in the case of an exponential signal $s(t) = s_1/T_1 \exp(-t/T_1) + s_0$ with an area s_1 on top of a background s_0, Equation 4.3 approximates to

$$\int_0^{T/2} s(t)dt - \int_{T/2}^{T} s(t)dt = s_1(1 + \mathrm{e}^{-T/T_1} - \mathrm{e}^{-T/2T_1}), \tag{4.4}$$

which is independent of the background and proportional to the area s_1 whatever is T. Moreover, it is even equal to s_1 with a relative error of about e^{-T/T_1} when $T \gg T_1$. In the case of a fluorescence signal measured up to $\sim 5T_1$, this relative error is $\mathrm{e}^{-5} < 1\%$; the second half of the signal is in this case very close to the background, which is consequently well subtracted from the first half.

We first measure the background signal alone by not applying any excitation pulse. This measurement also serves as an example to present the raw data and its corresponding analysis. Here the SMPD is tuned in resonance with the spin resonator. The measurement protocol and sequence are nearly identical to the ones used for real spin detection (except for the absence of excitation pulse before SMPD cycles).

The beginning of each sequence is defined as $t = 0$ and the SMPD keeps running for 825 cycles lasting about 10 ms. Then we repeat the same detection sequence. The SMPD outcomes of the first 30 sequences are shown in Figure 4.1a, each red bar representing a count signal $c_j(t) = 1$ in the jth sequence, with recorded click arrival time t. The accumulated total counts of a sequence is obtained from a simple sum, as shown in Figure 4.1b. Repeating the sequence a sufficiently large number of times, we get the average total counts $\langle C \rangle$.

To obtain the average count rate, we choose a coarse-graining time bin size and divide the average number of counts inside a bin by this size. In the example shown in Figure 4.2, the bin size is 0.5 ms and the average count rate of $0.106\,\mathrm{ms}^{-1}$ is the dark count rate α.

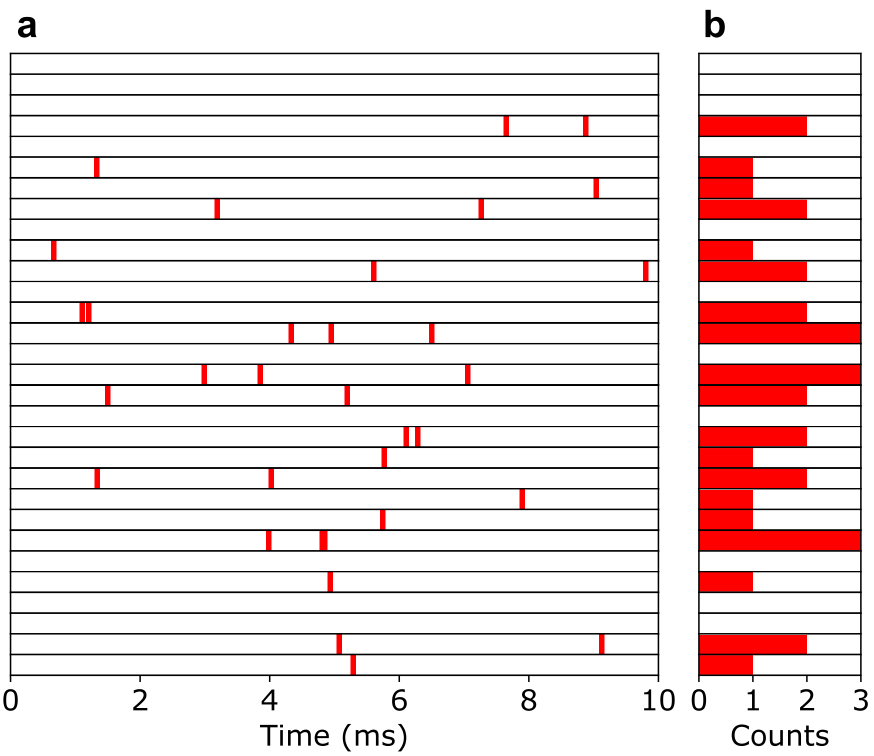

Figure 4.1: **Detection of photon background in presence of the spin sample but in absence of excitation pulses. (a)** SMPD detected events (red bars) with recorded arrival time between $t = 0$ and 10 ms during the first 30 sequences (one row/sequence). **(b)** Accumulated total counts C_j in jth sequence.

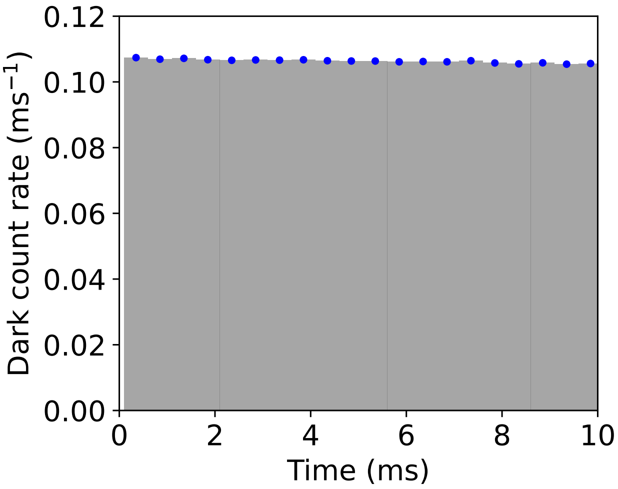

Figure 4.2: **Measured average dark count rate.** Each bar represents a coarse-graining time bin with a width of 0.5 ms and a height of the count rate. The bin center times are indicated with blue dots.

4.2 High-power spin spectroscopy

To excite and detect the spins, we repeatedly apply an excitation pulse followed by photon counting cycles, as described in Figure 2.19. The fluorescence signal, which is the sum of the contributions of all the spins excited by the pulse, strongly depends on the excitation power.

When the spins of interest are out of resonance with the resonator, the excitation pulse cannot excite them directly. However, it can heat up the microwave lines and possibly the spins and increase the dark count rate above its base level. The stronger the applied excitation power, the larger the measured background level. On the contrary, when the spins are in resonance with the resonator, they are directly excited by the pulse and re-emit a microwave fluorescence signal. The SMPD then detects these emitted photons and shows excess counts above the background level.

These excess counts are observables when the spin transition frequency is tuned by the magnetic field into the bandwidth of the spin-resonator, provided that the spins have a large radiative relaxation rate. This result holds for all kinds of paramagnetic species. By sweeping the magnetic field in order to bring different types of spins in and out of resonance with the resonator, we obtain the ESR spectrum of the system under study from the detected counts signal, and identify the different spin species present in the spectrum from their known gyromagnetic ratios. Although this ESR detection by photon counting is a universal method applicable to any types of spins, we use it specifically on erbium spins in our experiment as an example to demonstrate its potential.

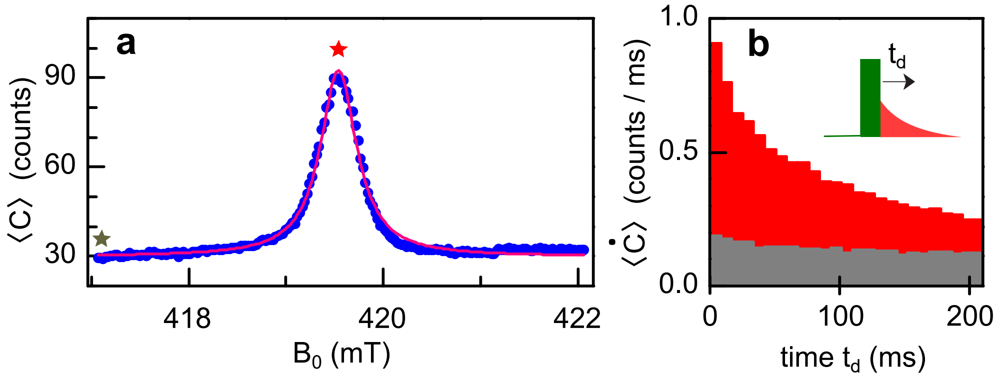

Figure 4.3: **Fluorescence-detected** $\mathrm{Er}^{3+}:\mathrm{CaWO}_4$ **ESR line (a) at high excitation power (**~ -97 **dBm at sample input) and typical microwave fluorescence signal (b).** At each magnetic field B_0, the average number of counts $\langle C \rangle$ is integrated over a $\sim$ 200 ms duration following the excitation pulse (whole t_d range in panel b). Blue dots are data, red line is a Lorentzian fit with FWHM 0.45 mT. Note that the angle θ varies linearly between $-0.006°$ and $0.006°$ over the scan. Fluorescence histograms of average count rate $\langle \dot{C} \rangle$ are shown at the center (red) and tail (grey) of the spin ensemble line (see stars in panel a).

We first record the spectrum of the $\mathrm{Er}^{3+}:\mathrm{CaWO}_4$ resonance with a high input power (~ -97 dBm at sample input), thus exciting many weakly coupled ions that have low Γ_R. The average count rate $\langle \dot{C} \rangle$ as a function of time following the pulse shows an excess compared to the background level (see Figure 4.3b) and decays non-exponentially over a timescale of $\sim$ 100 ms. We plot the average number of counts integrated over the first 200 ms $\langle C \rangle$ as a function of the magnetic field B_0 applied along the z direction, see Figure 4.3a. A smooth, approximately Lorentzian, peak is observed at $B_0 = 419.5\,\mathrm{mT}$, close to $\omega_0/\gamma_{||}$, proving it is the Er^{3+} spin resonance. Its 0.5 mT inhomogeneous Full-Width-Half-Maximum (FWHM) linewidth corresponds to a $\sim 8\,\mathrm{MHz}$-wide distribution.

4.3 Crystal symmetry of spin ensemble

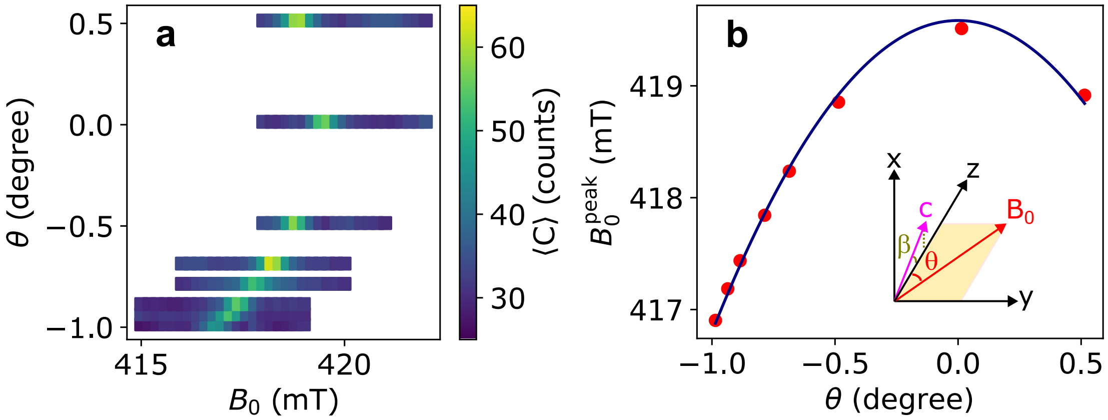

Figure 4.4: **Rotation pattern of the erbium spin ensemble ESR line. (a)** Spectrum of the $\mathrm{Er}^{3+}:\mathrm{CaWO}_4$ resonance as a function of the angle θ between B_0 and the z axis (direction of inductive wire). The color represents integrated counts. **(b)** Measured magnetic field B_0^{peak} (dots) at which the center of the spin ensemble line is found, as a function of the angle θ between B_0 and the c axis projection onto the sample plane. The fit of eq. 4.5 (line) to the data yields the $\theta = 0$ origin as well as the angle $\beta = 0.5°$ between the c axis and the sample plane.

The magnetic field B_0 generated by the 1T/1T/1T 3-axis superconducting vector magnet allows us to measure angular dependence of the ESR spectrum and thus to characterize the gyromagnetic tensor anisotropy. In that aim, we first bring a small 50 mT field in the $(y{-}z)$ sample plane to minimize the resonator losses and frequency shifts with respect to the zero-field values [114], as discussed in Section 3.3.2. We then rotate the field within this $(y - z)$ plane by various angles θ and record the erbium ensemble ESR line (as shown in Figure 4.3 and Figure 4.4a). Plotting the ESR line center as a function of θ gives the rotation pattern shown in Figure 4.4. This pattern is a direct consequence of the anisotropic gyromagnetic tensor $\hat{\gamma}_0$ of CaWO_4. The line center is maximum in magnetic field (and minimum in effective gyromagnetic ratio) at an angle defined as $\theta = 0°$ when B_0 is aligned with the projection of the crystallographic c-axis onto the crystal plane. The small angle β between this c-axis projection and the actual c-axis can be determined as explained just below. Note however that we have no way to determine the other small residual angle (possibly of order 1°) between this c-axis projection and the z-axis parallel to the spin-resonator wire. Because it has a negligible effect on any quantity we could determine, we take this latter angle to be 0 for simplicity.

Now, the B_0 value of the ESR line writes

$$B_0^{\text{peak}} = \hbar\omega_0 / \sqrt{\gamma_{\parallel}^2 \cos^2\theta \cos^2\beta + \gamma_{\perp}^2 (1 - \cos^2\theta \cos^2\beta)}, \tag{4.5}$$

and a fit of Equation 4.5 to the data (see Figure 4.4b) yields the zero of θ and $|\beta| = 0.5°$.

To measure the spectrum of Figure 4.3, we scan the current in the main coil while keeping the other two at fixed values. By doing so, we vary mostly the B_0 amplitude, but also slightly the angle θ. Based on the values set in the persistent coils X and Y, ramping B_Z from 417 to 422 mT causes a linear variation of θ between $-0.006°$ and $0.006°$. Such a small variation has obviously a negligible impact on the results.

4.4 Low-power spin spectroscopy

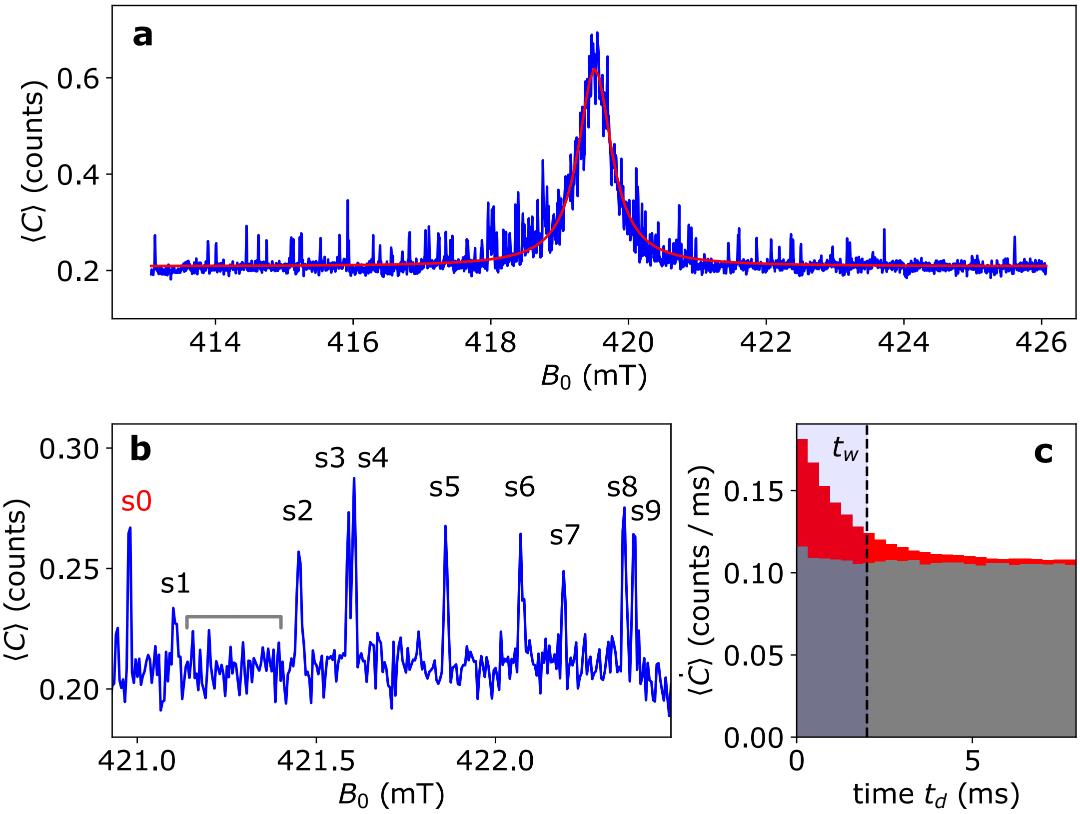

Figure 4.5: **Spin spectroscopy at low excitation power and typical microwave fluorescence signal.** **(a)** Fluorescence-detected $Er^{3+} : CaWO_4$ ESR line (blue) at low power (~ −117 dBm at sample input), measured with an integration window of $t_w = 2\,\text{ms}$ and fitted by a Lorentzian peak (red). Note that the angle θ varies linearly between $-0.016°$ and $0.016°$ over the scan. **(b)** Expanded view of panel **a**, showing 10 peaks (labelled $s0$ to $s9$). **(c)** Histograms of the average count rate on spin $s0$ (red), and on the background (grey) averaged over the B_0 window shown as a horizontal grey bar in panel **b**. The blue window is the integration window for all data points in (a).

We then record the line with $\sim 20\,\mathrm{dB}$ lower excitation power ($\sim -117\,\mathrm{dBm}$ at sample input) while simultaneously reducing the integration time to 2 ms, thus exciting and detecting only the most strongly coupled and fastest relaxing spins. The integrated count $\langle C\rangle(B_0)$ now shows qualitatively different behavior and appears as a sum of narrow, unevenly distributed peaks, with typical amplitude ~ 0.1 excess count over the noise floor (see Figure 4.5a). The fluorescence curve when tuned to one of these peaks shows an exponential decay (see Figure 4.5b), with a time constant of $\sim 2\,\mathrm{ms}$. These features suggest that each peak corresponds to the microwave fluorescence signal originating from a single Er^{3+} ion spin located ~ 200 nm away from the inductive wire of the resonator, analogous to the optical fluorescence spectrum of a collection of individual solid-state emitters [122, 123, 87]. Note that while we observe a large fluorescence signal at the center of the inhomogeneous absorption line, some individual peaks are still found far from the center; a common observation in low-density spectra of optical emitters, and a natural consequence of the random nature of inhomogeneous broadening. This is also possibly supplemented in our particular device by the strain imparted by the thermal contractions of the metallic wire on the substrate just below [124, 125].

4.5 Single-spin-resolved rotation pattern

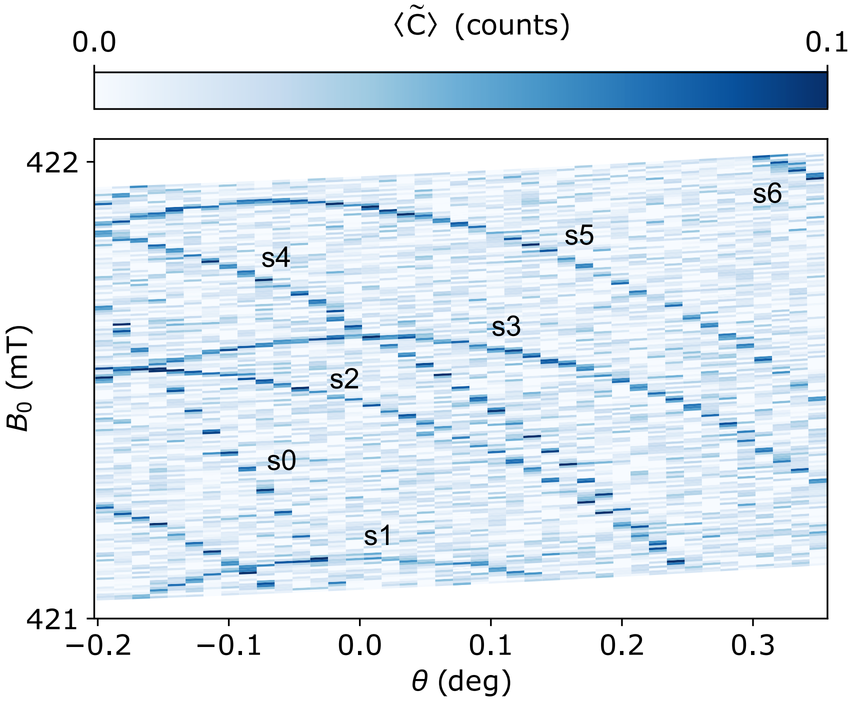

Figure 4.6: **Single-spin-resolved rotation pattern.** Average number of excess count $\langle\widetilde{C}\rangle$ as a function of the magnetic field amplitude B_0 and its angle θ with respect to the projection of the crystal c axis on the sample surface. The range is the same as in the inset of Figure 4.5a, and the same labeling of the spin lines is used. The total data acquisition time was approximately one week.

To demonstrate the stability and reproducibility of the individual spin ESR lines, we perform a two-dimensional magnetic field scan and plot in Figure 4.6 the background-corrected average number of counts $\langle\widetilde{C}\rangle$ (see Equation 4.3) as a function of B_0 and θ. Eight different spin peaks are resolved, and their spectrum is readily followed as a function of θ. It appears that each ion has its own gyromagnetic tensor $\hat{\gamma}$, close to $\hat{\gamma}_0$ but with slightly different values for the principal axes and also a symmetry axis that slightly deviates from the c-axis. This vividly illustrates what inhomogeneous broadening is really, which is usually hidden in a broad and smooth line such the one in Figure 4.3. The individual spin lines are so narrow that the gyromagnetic tensor $\hat{\gamma}$ of each ion could in principle be determined with an accuracy better than 10^{-6} (using a suitably calibrated magnetic field). Because the deviation $\delta\hat{\gamma}$ of the gyromagnetic tensor from the ensemble-averaged one, $\hat{\gamma}_0$, is due to the local electrostatic and strain environment, its accurate measurement can also be turned into a sensitive way to probe this environment (as done with NV centers in diamond [126]). Note that our measurements also call for a better modeling of the response of rare-earth ion spins to applied electric or strain fields.

4.6 Microwave-induced heating and corresponding spurious detected signal

We now discuss heating effects observed after a microwave pulse has been applied to the spin resonator, as observed in [5], and as already mentioned the background counts increase with excitation power (compare for instance dark count rates in Figure 4.3b and Figure 4.5b).

To evidence and clarify this point, we measure the transient signal recorded after an excitation pulse resonant with the SMPD buffer resonator, in three different cases:

1. normal operation on a single spin: the spin, spin-resonator and buffer are all in resonance.
2. normal operation in absence of spins: All spins are far off-resonance, but spin-resonator and buffer are on resonance.
3. all spins, spin resonator and buffer are detuned from each other.

In all cases, a 6 μs-long excitation pulse is applied at the time $t = 0$; the photon counting cycles starts 1 ms before the pulse, is interrupted (SMPD switched off) during the pulse duration, and is restarted during several milliseconds. The corresponding count rates are shown in Figure 4.7).

In normal operation (case 1 and 2 red and blue in Figure 4.7), a count rate spike is observed in the bin immediately after the excitation pulse; this spike corresponds to the decay (at rate κ) of the microwave energy stored by the pulse in the spin resonator. It is not present when the spin resonator is detuned from the signal (case 3), as expected. After the spike, even when no spin signal is present (case 2 - blue), extra counts above the background (grey) are however observed over a time window of about 0.3 ms after the excitation, with a decay time of $\sim$ 100 μs. This extra signal is reminiscent of the one observed over $\sim$ 10 ms in [5], possibly shorter in the present work due to lower excitation pulse powers. For comparison, when detuning the spin resonator from the excitation (case 3 - orange in Figure 4.7), this extra count rate is lower and reaches the background steady-state much faster. All these measurements with no spins indicate that the spurious extra counts decaying over $\sim 100\ \mu$s in normal operation originate from the excitation and subsequent radiative decay of systems that are resonantly coupled to the spin resonator and send photons to the SMPD. It is tempting to identify them with the two-level-system bath that causes field decay and phase noise in superconducting circuits. In normal operation with a spin (case 1 - red in Figure 4.7), these spurious extra counts of course adds to the relevant signal coming from the spin. To lower the impact of this transient heating effect on the results of the next chapter, we choose to discard the counts detected in the first 50 μs (or 100 μs for some measurements) after the excitation.

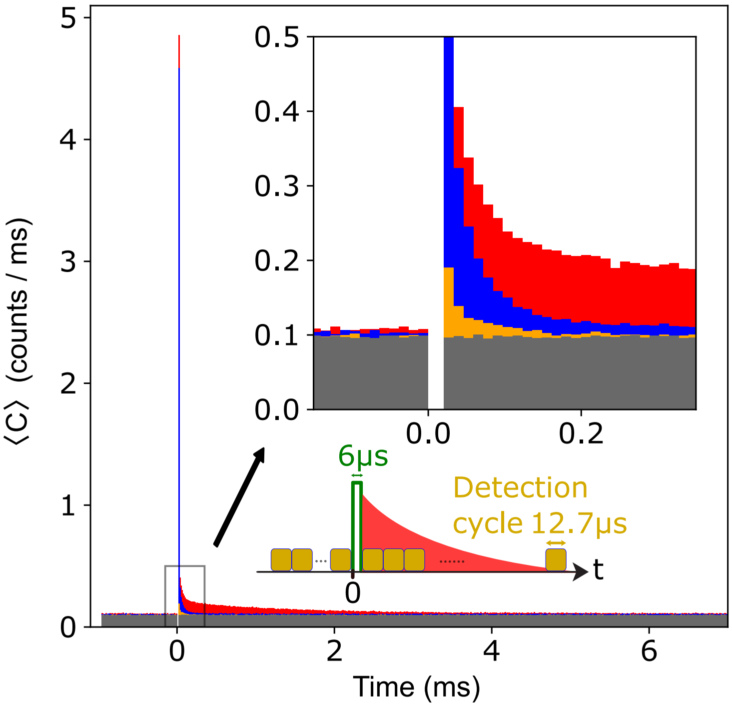

Figure 4.7: **Transient response of the system after microwave excitation.** Measured average click rate versus time before and after a 6 μs-long microwave excitation pulse applied at time 0, for cases 1 (red), 2 (blue) and 3 (orange) - see text. SMPD is switched off during excitation. Dark count background is indicated in grey. Inset is a zoomed-in view around time 0.

We finally study the dependence of this heating effect on the excitation pulse duration and amplitude, in absence of resonant spins. For that we repeat the sequence every 8 ms and integrate the number of counts $\langle C\rangle$ over its duration. The results in Figure 4.8 show an increase of $\langle C\rangle$ as a function of pulse duration and amplitude. This increase with pulse duration is faster as excitation amplitude increases. We also verified that this increase of $\langle C\rangle$ is not due to microwave heating of the line attenuators: by repeating the same measurements as above but with the spin resonator detuned from the SMPD buffer, a much smaller effect is observed, indicating that the excess counts do come from the spin resonator.

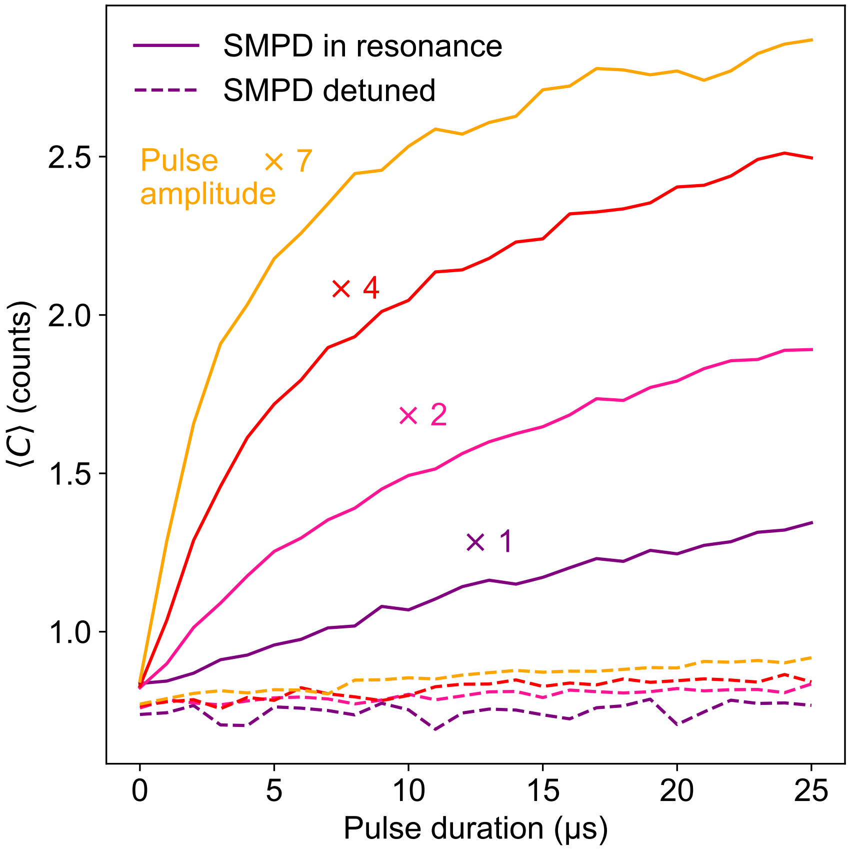

Figure 4.8: **Heating effect versus excitation pulse duration and amplitude.** Measured average counts integrated over a 8 ms-long window after an excitation pulse of varying duration and amplitude, when the spin resonator is detuned from (dash line) or in resonance with (solid line) the SMPD buffer. The excitation pulse frequency is always tuned to the SMPD buffer one.

Chapter 5

Single spin time-resolved measurements

This chapter presents experimental results obtained from time-domain measurements on individual spins chosen randomly on one side of the $Er^{3+} : CaWO_4$ line of Figure 4.5. These results complement the spectroscopic (i.e. frequency-domain) measurements presented in the previous chapter, and give a more direct insight on how a spin is driven by a classical field, and on how long quantum information can persist in the spin. More precisely, we present different spin coherence times, which can be used to understand the microscopic local environment of a spin in an ESR perspective, but are also key figures of merit when the spin is to be used as a quantum bit for quantum information processing. To begin with, we demonstrate the coherent Rabi oscillations of the excited state population of a spin. Then we present intensity-intensity correlation measurements that prove directly that the individual peaks of Figure 4.5 do correspond to single emitters, i.e. individual erbium spins. We then present and discuss the relaxation time T_1 of a spin, its Ramsey coherence time T_2^*, Hahn echo time T_2, and coherence time T_2^{DD} obtained by dynamical decoupling. Finally, the analysis of the data allows us to determine the spin detection efficiency and the signal-to-noise-ratio of our complete setup. All these measurements are obtained by

- choosing a particular sequence of excitation pulses characterized by a set of parameters (pulse amplitudes, pulse durations, delays between pulses, etc.)
- repeating the sequence and measuring one of the already introduced quantities: the average count rate $\langle \dot{C} \rangle$, total counts C, or average excess counts $\langle \widetilde{C} \rangle$
- ramping one of the parameters and plotting the chosen quantity as a function of this parameter.

5.1 Rabi oscillation

After getting the spectrum of Figure 4.6, we select an isolated peak $s0$ and try to bring further evidence of its single-spin origin by observing Rabi oscillations. The applied Rabi sequence is a single microwave excitation pulse with amplitude A and duration T, followed by the cyclic SMPD recording. The extracted excess counts $\langle \widetilde{C} \rangle$

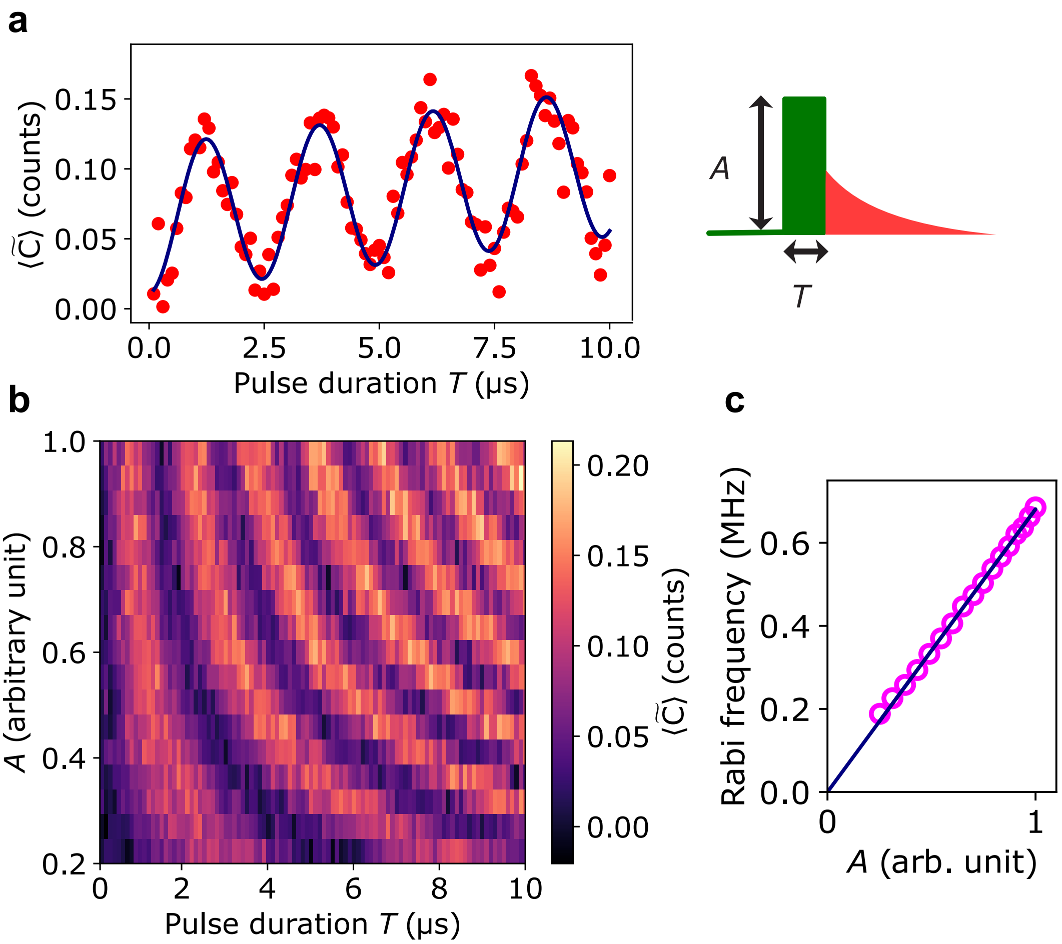

Figure 5.1: **Rabi oscillation of spin s0.** **(a)** Measured average excess count $\langle\widetilde{C}\rangle$ (red dots) as a function of the excitation pulse duration T (see the sequence pictogram) at fixed amplitude A, and corresponding fit (solid line) by a sinusoidal function with linearly increasing offset. **(b)** Measured average excess count $\langle\widetilde{C}\rangle$ (color scale as functions of excitation pulse duration T and amplitude A. **(c)** Rabi frequency (magenta dots) extracted from (b) as a function of amplitude A, and corresponding linear fit through origin (solid line).

oscillates sinusoidally as a function of the pulse duration (see Figure 5.1a). The frequency of this oscillation depends linearly on the pulse amplitude (see Figure 5.1c), as expected for the Rabi oscillation of a single spin. Superposed on these oscillations is a gradual increase of $\langle\widetilde{C}\rangle$, which we attribute to heating of the bath of defects that are responsible for the resonator internal microwave losses, as observed in [5] (see also Section 4.6).

Despite this linear increase of the baseline, the contrast of the signal (peak-to-peak amplitude of the oscillations) is rather stable during the 10 μs-long time window explored. This stability is in contrast with the fast damping observed for Rabi oscillations of an erbium spin ensemble in a similar experiment [127]. This fast damping was very likely due to the overlapping of many Rabi signals such as the one we measure, but with different frequencies and amplitudes due to the distribution in spin frequencies and couplings within the ensemble.

Note that this Rabi experiment allows us to determine the couple (A, T) that corresponds to any targeted Rabi angle θ to be applied to the spin. This is very useful both for electron spin resonance (ESR) and quantum information processing (QIP), for which $\pi/2$ and π pulses are used in many ESR sequences and belong to the QIP universal set of gates.

Note also that the contrast of the Rabi signal will be used to determine the overall collection efficiency of the fluorescence photon from the spin, as explained in Section 5.4.1

5.2 Intensity-intensity correlation function

To ultimately prove the single-spin nature of isolated peaks in the erbium ESR line, we select one of them ($s0$ in Figure 4.6) and use the SMPD to measure the photon statistics of the fluorescence signal and therefore obtain the intensity-intensity time correlation function $g^{(2)}$. The goal of this measurement is to demonstrate whether or not the detected fluorescence photons come from a single microwave photon emitter, then identified as an individual Er^{3+} electronic spin.

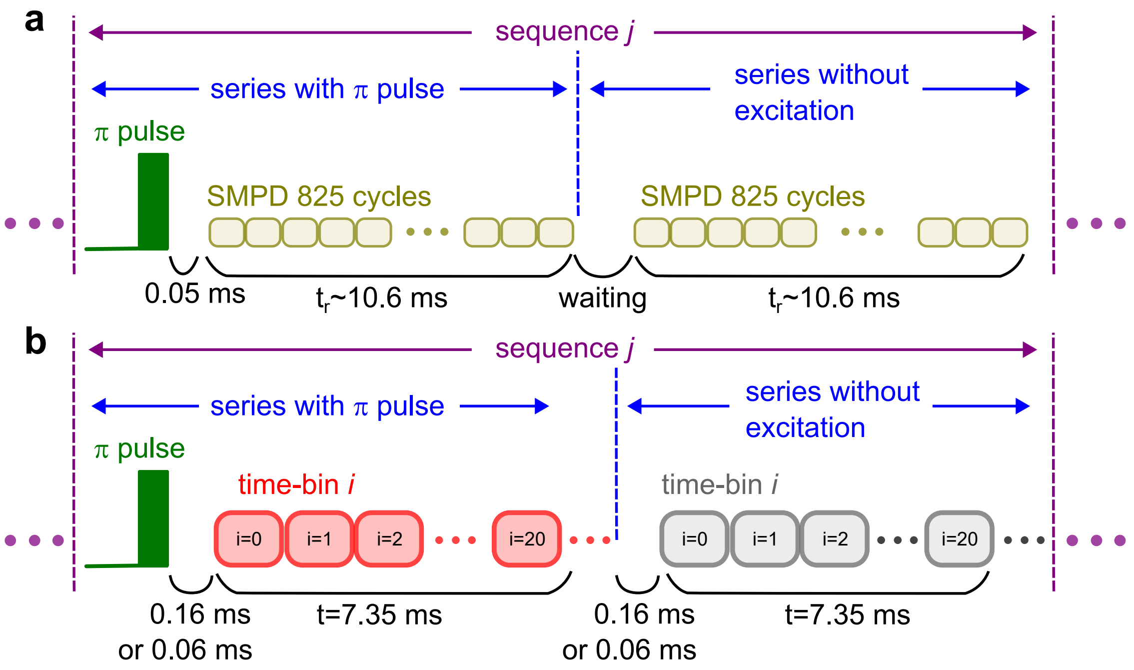

Figure 5.2: **Protocol and sequences for measuring $g^{(2)}$ and SNR. (a)** Schematic of protocol for measuring $g^{(2)}$ function with a single detector by applying repeatedly two interleaved series of sequences (one with spin excitation ~ 4 μs-long π pulse and the other one without). The waiting time in the series without excitation corresponds to one excitation pulse duration plus 50 μs. **(b)** Same schematics emphasizing the chosen time-bins for grouping the count data and analyzing them (see text). A 0.16 ms-long (resp. 0.06 ms-long) window is excluded from the analysis of $g^{(2)}$ (resp. SNR).

To obtain the photon statistics, we measure the SMPD counts when applying two interleaved series of 4363635 sequences labeled from j=0 to j=4363634, repeated every $t_r = 10.6$ ms, as shown in Figure 5.2a. The first series includes π pulses at times $t = 0$ whereas the other one has no excitation pulse. The whole measurement takes about 26 hours. In each sequence, time $t = 0$ is followed by 825 SMPD cycles. As explained in the Heating Section 4.6, a 160 μs-long time window after the excitation pulse is excluded from the analysis in order to minimize the impact of the heating effect (60 μs-long window is chosen for obtaining SNR). The count data in the rest of the sequence are then grouped in subsequent 350 μs-long time-bins indexed by i (with i running from 0 to 20), and centered at time $\tau_i = 100 + (2i + 1) \times 350/2\ \mu$s, see Figure 5.2b. The corresponding number of counts in the bin i of sequence j is denoted as $n_i^{(j)}$. From this dataset, we define two $g^{(2)}$ functions: one inside a sequence, and another one between two separated sequences.

5.2.1 Intra-pulse $g^{(2)}$

We first provide in Figure 5.3a a direct visualization of the anti-bunching observed within a sequence. The count rate $\langle \dot{C} \rangle(t)$ is plotted as a function of time, first, averaged over all recorded sequences, and second, averaged over sequences with a count 1 in the first bin (conditioned curve). When measured on the background (second series), the two curves are identical, as expected from independent events obeying a Poisson statistics. On the contrary, when measured with excitation (first series), the conditioned fluorescence rate is reduced at short times after the first count, compared to the average unconditioned one. This count rate reduction after the π-pulse indicates photon anti-bunching.

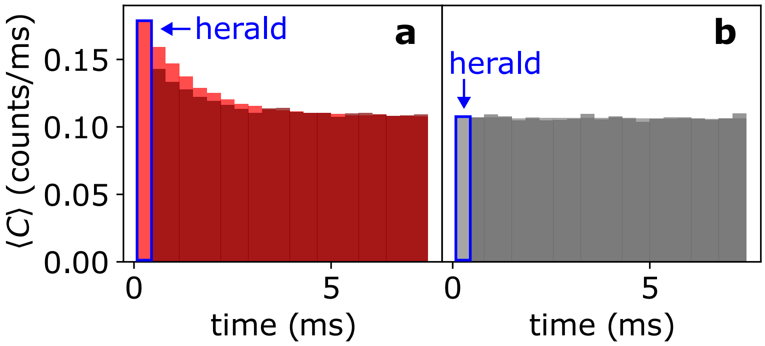

Figure 5.3: **Heralded count rate for spin fluorescence and background. (a)** Average count rate $\langle \dot{C} \rangle$ as a function of delay time after a π excitation pulse, for all recorded traces (bright red) and for traces with a first click detected in the first time-bin (dark red). The bin used for heralding is indicated with a blue box. The reduction of $\langle \dot{C} \rangle$ in the second case indicates the anti-bunching of single spin fluorescence photons. **(b)** Same quantity and same presentation for all recorded background traces (light gray) and for background traces with a click detected in the first time-bin (dark gray). The unchanged $\langle \dot{C} \rangle$ indicates a Poissonian background made of independent dark count events.

In order to quantify this anti-bunching, we define the intensity-intensity correlation function

$$g^{(2)}(\tau = \tau_{i>0}) = \frac{\langle n_0^{(j)} n_i^{(j)} \rangle_j}{\langle n_0^{(j)} \rangle_j \langle n_i^{(j)} \rangle_j} \tag{5.1}$$

inside a sequence. Note that $g^{(2)}(\tau_1)$ plays in our experiment with a single detector the same role as $g^{(2)}(0)$ in an experiment with a beam splitter and two detectors. We then compute $g^{(2)}(\tau)$ for the two series with and without excitation pulses (see Figure 5.4). Without excitation, $g^{(2)}(\tau) = 1$, showing again that dark counts obey a Poissonian statistics. With excitation on the other hand, $g^{(2)}(\tau)$ is below 1 at short time, starting from $g_{\tau}^{(2)}(0) \equiv g^{(2)}(\tau = \tau_1) = 0.90 \pm 0.005$ and exponentially increasing towards 1 at a rate $\Gamma_R = 700\,\mathrm{s}^{-1}$ equal to the fluorescence decay rate. We also show on the figure the calculated

$$g_{\mathrm{se}}^{(2)}(\tau = \tau_i) = \frac{\langle n_0^{(j)} \rangle_j \langle d \rangle + \langle n_i^{(j)} \rangle_j \langle d \rangle - \langle d \rangle^2}{\langle n_0^{(j)} \rangle_j \langle n_i^{(j)} \rangle_j}. \tag{5.2}$$

curve (red solid line) expected from an ideal single-photon emitter with damping rate Γ_R in the presence of dark counts at the measured rate α, where $\langle n_j^{(i)} \rangle$ is the measured average counts in time-bin i and $\langle d \rangle$ is the measured average dark counts in the 350μs-long time-bin. The curve agrees quantitatively with the experimental results, yielding the background-corrected $g_{\tau}^{(2)}(0) = 0.23 \pm 0.06$. We discuss in detail the method used for background correction and the derivation of $g_{\mathrm{se}}^{(2)}(\tau = \tau_i)$ for ideal single emitter in Section 5.2.3. These results demonstrate conclusively that the spectral peak under study ($s0$) is a single microwave photon emitter, which we take as an individual Er^{3+} electron-spin.

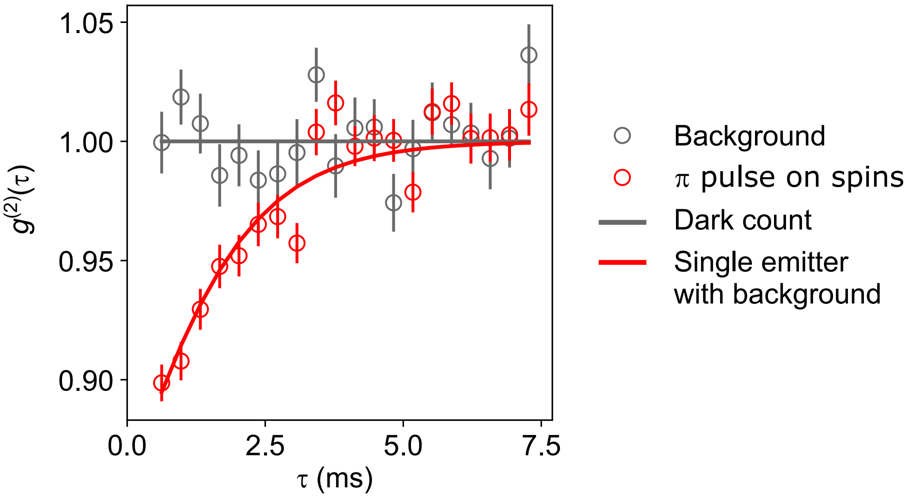

Figure 5.4: **Intra-pulse $g^{(2)}$.** Extracted $g^{(2)}$ function for dark counts only (gray dots) and spin fluorescence signal and dark counts (red dots) as a function of delay time τ. Expected $g^{(2)}$ functions for a Poissonnian background (grey solid line) and for an ideal single emitter in the presence of the same background (red solid line), fitting well the experimental data.

5.2.2 Inter-pulse $g^{(2)}$

From the same dataset, we can also compute an intensity-intensity correlation function $g^{(2)}(k)$ between two sequences separated by k excitation pulses,

$$g^{(2)}(k) = \frac{\langle n_0^{(j)} n_1^{(j+k)} + n_1^{(j)} n_0^{(j+k)} \rangle_j / 2}{\langle n_0^{(j)} \rangle_j \langle n_1^{(j+k)} \rangle_j}, \tag{5.3}$$

where we keep only the first and second bin of the two sequences, symmetrize the function about k=0, and average over all pairs of sequences with the same separation $k \in \mathbb{Z}$. Note that with this definition, the inter-pulse $g^{(2)}(k=0)$ is equal to the intra-pulse $g_{\tau}^{(2)}(0) \equiv g^{(2)}(\tau=\tau_1)$. Figure 5.5 illustrates graphically the meaning of Equation 5.3 and shows the measured function. We observe $g^{(2)}(k \neq 0) = 1$ as expected for uncorrelated events, as well as a small but clear reduction of $g^{(2)}(k = 0)$ below 1. Given that uncorrelated dark count events can only spoil the anti-correlated signal from a single photon source (individual spin), a method to obtain a background-corrected $g^{(2)}$ characterizing the single emitter alone is needed.

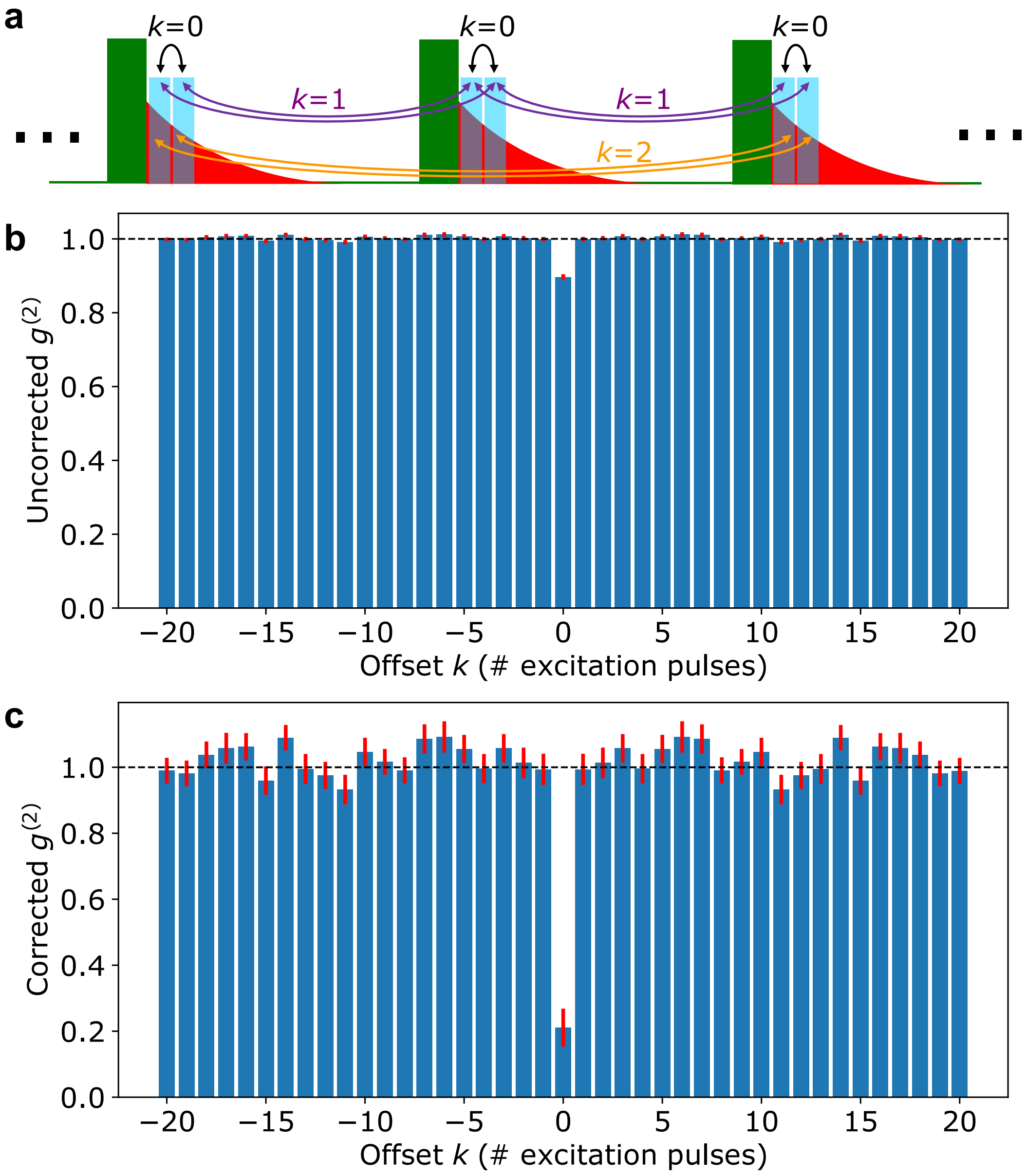

Figure 5.5: **Inter-pulse $g^{(2)}$. (a)** Schematics indicating the bins (blue) chosen after the excitation pulse (green) to compute the inter-pulse $g^{(2)}(k)$ averaged over all pairs separated by the same number k of sequences. **(b, c)** Measured $g^{(2)}(k)$ (blue bars) and corresponding ±1-standard deviation error bars (red) as a function of separation k without (b) and with (c) background correction. Note that the function is exactly symmetric around 0 by definition.

5.2.3 Background correction of $g^{(2)}$

We now describe how we subtract from $g^{(2)}$ the dark count rate contribution, in order to obtain a background-corrected correlation function. We take a similar approach from [87].

We assume that the total click counts n_i measured by the detector has two independent origins: the emission s_i of interest, and a Poissonian background noise d_i made of independent dark count events. We have thus $n_i = s_i + d_i$, $\langle n_i \rangle = \langle s_i \rangle + \langle d_i \rangle$, and $\langle s_i d_i \rangle = \langle s_i \rangle \langle d_i \rangle$. In addition, we assume that the instruments are stable enough during the measurement time so that the dark count rate is time-invariant: $\langle d_i \rangle = \langle d \rangle$.

These assumptions lead to

$$\begin{aligned} \langle n_0^{(j)} n_1^{(j+k)} \rangle_j &= \langle [s_0^{(j)} + d_0^{(j)}][s_1^{(j+k)} + d_1^{(j+k)}] \rangle_j && (5.4) \\ &= \langle s_0^{(j)} s_1^{(j+k)} \rangle_j + \langle s_0^{(j)} \rangle_j \langle d \rangle + \langle s_1^{(j+k)} \rangle_j \langle d \rangle + \langle d \rangle^2 && (5.5) \end{aligned}$$

Similar to the definition of $g^{(2)}(k)$ in Equation 5.3 but considering only the spin signal part, the background-corrected autocorrelation function can be defined as

$$g^{(2)}_{\text{corr}}(k) = \frac{\langle s_0^{(j)} s_1^{(j+k)} + s_1^{(j)} s_0^{(j+k)} \rangle_j / 2}{\langle s_0^{(j)} \rangle_j \langle s_1^{(j+k)} \rangle_j}, \tag{5.6}$$

and we now express it explicitly as a function of the uncorrected $g^{(2)}(k)$ and measurement outcomes: $\langle n_i^{(j)} \rangle_j$, $\langle d \rangle$ and $A_i \equiv [\langle n_i^{(j)} \rangle_j - \langle d \rangle]/\langle d \rangle = \langle s_i^{(j)} \rangle_j / \langle d \rangle$.

With the help of Equation 5.5, we can rewrite Equation 5.3 as

$$g^{(2)}(k) = \frac{\langle s_0^{(j)} s_1^{(j+k)} \rangle_j + \langle s_0^{(j+k)} s_1^{(j)} \rangle_j + [\langle s_0^{(j)} \rangle_j + \langle s_1^{(j+k)} \rangle_j + \langle s_0^{(j+k)} \rangle_j + \langle s_1^{(j)} \rangle_j] \langle d \rangle + 2\langle d \rangle^2}{2[\langle s_0^{(j)} \rangle_j + \langle d \rangle][\langle s_1^{(j+k)} \rangle_j + \langle d \rangle]} \tag{5.7}$$

$$\begin{aligned} &\approx \frac{\langle s_0^{(j)} s_1^{(j+k)} \rangle_j + \langle s_0^{(j+k)} s_1^{(j)} \rangle_j + 2(\langle s_0^{(j)} \rangle_j + \langle s_1^{(j+k)} \rangle_j) \langle d \rangle + 2\langle d \rangle^2}{2[\langle s_0^{(j)} \rangle_j + \langle d \rangle][\langle s_1^{(j+k)} \rangle_j + \langle d \rangle]} && (5.8) \\ &= \frac{\dfrac{\langle s_0^{(j)} s_1^{(j+k)} \rangle_j + \langle s_0^{(j+k)} s_1^{(j)} \rangle_j}{2\langle s_0^{(j)} \rangle_j \langle s_1^{(j+k)} \rangle_j} + \dfrac{1}{A_0} + \dfrac{1}{A_1} + \dfrac{1}{A_0 A_1}}{(1 + \dfrac{1}{A_0})(1 + \dfrac{1}{A_1})} && (5.9) \\ &= \frac{A_0 A_1 g^{(2)}_{\text{corr}}(k) + A_0 + A_1 + 1}{(1 + A_0)(1 + A_1)}, && (5.10) \end{aligned}$$

where we use $A_i = \langle s_i^{(j)} \rangle_j / \langle d \rangle$ and the approximation $\langle s_i^{(j)} \rangle_j \approx \langle s_i^{(j+k)} \rangle_j$.

The inverse of Equation 5.10 gives the background-corrected correlation function

$$g^{(2)}_{\text{corr}}(k) = \frac{(1 + A_0)(1 + A_1) g^{(2)}(k) - A_0 - A_1 - 1}{A_0 A_1}, \tag{5.11}$$

which yields the results in Figure 5.5c.

For N emitters, $g^{(2)}(0)$ should be equal to $(N-1)/N$; in particular, $g^{(2)}(0)$ should be equal to 0 for a single-emitter since it can emit only one photon per sequence. We measure corrected $g^{(2)}(0) = 0.23 \pm 0.06$, and $g^{(2)}(k \neq 0) = 1 \pm 0.04$ (see Figure 5.5c), thus showing clear anti-bunching in each sequence, whereas the emission from different sequences is uncorrelated. The non-zero value of $g^{(2)}(0)$ may be due to heating by the excitation pulse (see Section 4.6); in any case, the fact that its value is well below 0.5 further suggests that the spectral peak under study is a single microwave photon emitter, in the form of an individual Er^{3+} electron-spin.

In addition, it is interesting to compare the measured $g^{(2)}(\tau)$ inside a sequence with the expected $g^{(2)}_{se}(\tau)$ that an ideal single emitter would give in the presence of background noise. In this case, all terms $s_0^{(j)} s_i^{(j)}$ of Equation 5.5 are 0 due to the single emitter character, and writing Equation 5.1 leads to

$$g^{(2)}_{se}(\tau = \tau_i) = \frac{\langle n_0^{(j)} \rangle_j \langle d \rangle + \langle n_i^{(j)} \rangle_j \langle d \rangle - \langle d \rangle^2}{\langle n_0^{(j)} \rangle_j \langle n_i^{(j)} \rangle_j}. \tag{5.12}$$

This is the function that was plotted as a red solid line in Figure 5.4c, showing a good match with the measured $g^{(2)}(\tau)$.

5.3 Coherence properties of individual spins

The ability to address individual spins with microwaves opens the way to use them as spin qubits for quantum computing, and it is thus interesting to characterize their coherence properties. We select a spin from the spectrum (s6 in Figure 4.6) and measure four quantities: the longitudinal relaxation time T_1, the free-induction-decay time T_2^*, the Hahn-echo coherence time, and the dynamical decoupling coherence time. For the results presented in this section, the first 50 μs window after the excitation pulse is excluded from the analysis to minimize the impact of the heating effect, as explained in Section 4.6.

5.3.1 Energy relaxation time

As discussed in Section 2.2.3, the energy relaxation of a spin is due to radiative and non-radiative decay channels: $\Gamma_1 = \Gamma_\mathrm{R} + \Gamma_\mathrm{NR}$. We now report the measurement of these two quantities.

Spin-lattice relaxation

Our ESR detection method by fluorescence photon counting relies on the fast radiative decay of the spins. In our setup, we cannot switch off temporarily this radiative decay and thus make the non radiative relaxation dominant, by detuning temporarily the resonator or spin frequency for instance. It was thus impossible to measure Γ_NR with our setup. But this measurement was done in the thesis work of Marianne Le Dantec on a sample taken from the same batch of $\mathrm{Er}^{3+}:\mathrm{CaWO}_4$ samples as ours. Marianne used coherent-field-ESR and a spin-echo technique with an inversion-recovery sequence to measure the spin relaxation time [114]. In her experiment, the Er^{3+} ions couple inductively to a micro-sized superconducting resonator as in the present work. The measurement pulse sequence with relatively high power probes spins deep in the bulk, which are weakly coupled to the resonator and decay mainly by spin-lattice relaxation. The measured non-radiative relaxation time for B_0 along the crystal c-axis was $T_1 = \Gamma_\mathrm{NR}^{-1} = 213 \pm 1\,\mathrm{ms}$, as shown in Figure 5.6.

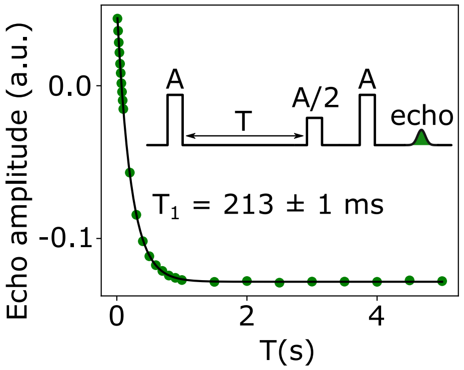

Figure 5.6: **Spin-lattice relaxation measurement of** Er^{3+} **in** CaWO_4**.** Measured echo amplitude at the end of an inversion-recovery sequence (inset) as a function of delay T at 10 mK, with B_0 along the crystal c axis, and $\omega_0/2\pi = 7.853\,\mathrm{GHz}$. Green dots are data, solid line is a fit yielding $T_1 = 213 \pm 1\,\mathrm{ms}$ (figure adapted from [114]).

Radiative relaxation and Purcell effect

As shown in Figure 4.5b, the measured average count rate decays exponentially after an excitation pulse. This decay occurs at a rate much faster than the non-radiative decay rate mentioned above, and is thus the radiative decay rate. We now perform the same measurement on spin s6 and obtain a relaxation time $T_1 = 1.42 \pm 0.07\,\mathrm{ms}$ (see Figure 5.7a) at resonance ($\delta = 0$).

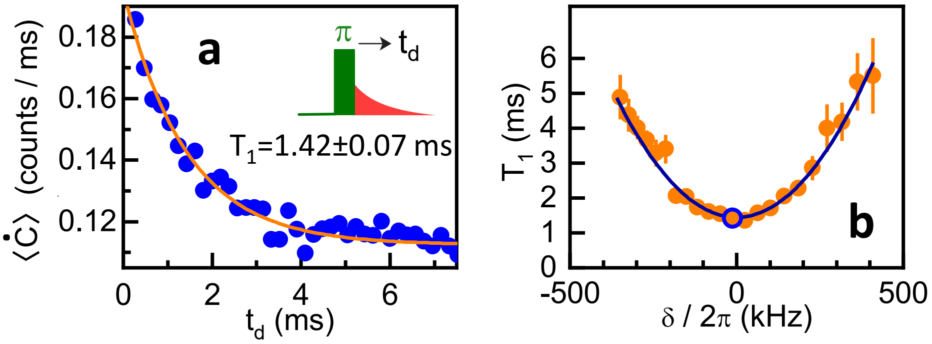

Figure 5.7: **Energy relaxation time and Purcell effect.** **(a)** Energy relaxation: measured average count rate $\langle \dot{C} \rangle$ (blue dots) as a function of delay t_d after a resonant π excitation pulse. Exponential fit (solid orange line) yields the energy relaxation time T_1. **(b)** Purcell effect: measured T_1 as a function of spin-resonator frequency detuning δ (orange dots). A fit by Equation 2.65 for $\Gamma_R^{-1}(\delta)$ (solid black line) yields the spin-resonator coupling constant $g_0/2\pi = 3.54 \pm 0.15$ kHz.

We use a Ramsey sequence (see next subsection) to accurately measure the spin-resonator detuning δ, which allows us to determine the dependence of the spin longitudinal relaxation time T_1 on δ, as shown in Figure 5.7. T_1 is seen to increase quadratically with δ, in agreement with the expected Γ_R^{-1} dependence [3] (see Equation 2.65); a fit yields a coupling constant $g_0/2\pi = 3.59 \pm 0.15\,\mathrm{kHz}$ (see Figure 5.7b). This confirms that non-radiative relaxation is negligible in our measurements, and that $T_1 \simeq \Gamma_R^{-1}$ for the most strongly coupled spins. According to the calculated

g_0 map in Figure 3.4, the measured spin is located 100∼200 nm away from the resonator inductive wire.

5.3.2 Free-induction-decay time

The free-induction-decay time of individual spins was measured by a $\pi/2_X - \tau - \pi/2_\varphi$ Ramsey sequence, with a relative inter-pulse phase $\varphi = 2\pi\Delta\tau$ with $\Delta = 0.025\,\mathrm{MHz}$. The excess count $\langle\widetilde{C}\rangle$ shows oscillations at frequency $\Delta + \delta$, damped with an approximately Gaussian shape and an effective decay time $T_2^* = 170 \pm 33\,\mu\mathrm{s}$ (time for a decay by $1/e$), corresponding to a $\sim 2\,\mathrm{kHz}$ single-spin linewidth (see Figure 5.8).

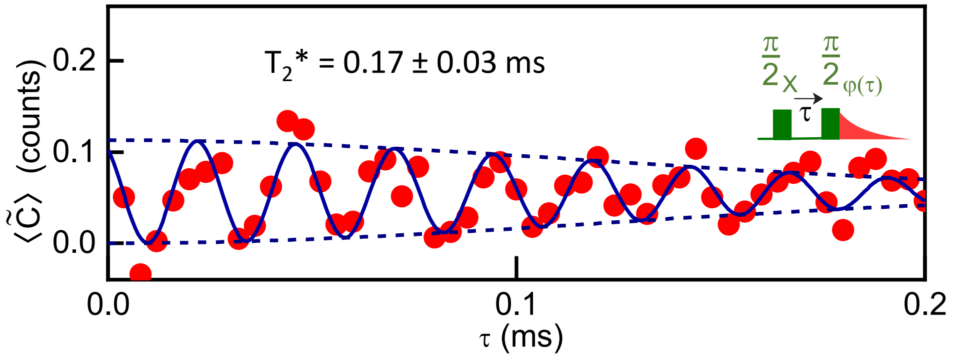

Figure 5.8: **Ramsey sequence on spin s6.** Measured excess counts $\langle\widetilde{C}\rangle$ (dots) versus delay time τ between two resonant $\pi/2$ pulses with relative phase $\varphi(\tau) = 2\pi\Delta\tau$ and $\Delta = 0.025\,\mathrm{MHz}$ (see inset). The corresponding fit (solid line) by a sine function with a Gaussian-decaying envelope (dash lines) yields an effective coherence time $T_2^* = 0.17 \pm 0.03\,\mathrm{ms}$.

In addition to T_2^*, this Ramsey experiment accurately provides the spin-resonator frequency detuning δ from the fitted oscillation frequency $\Delta + \delta$. In practice, we keep the X and Z coils in persistent mode and use the Y coil (stabilized with a custom-made feedback loop) to fine-tune δ (see Section 3.2.4). The measured δ is then used for the Purcell effect measurement mentioned above.

5.3.3 Hahn-echo and dynamical decoupling coherence time

The Hahn-echo coherence time was measured by applying a $\pi/2_X - \tau - \pi_X - \tau - \pi/2_\varphi$ sequence [111] with $\Delta = 1\,\mathrm{kHz}$. An oscillation at frequency Δ is observed in $\langle\widetilde{C}\rangle$, exponentially relaxing with a characteristic time $T_2 = 2.47 \pm 0.31\,\mathrm{ms}$. This is close to the radiative decay limit $2T_1$, indicating that the pure dephasing contribution is $T_\phi = [T_2^{-1} - (2T_1)^{-1}]^{-1} \sim 16 \pm 5\,\mathrm{ms}$, in line with measurements on ensembles of $\mathrm{Er}^{3+} : \mathrm{CaWO}_4$ electron spins in similar samples [6]. This pure dephasing can be suppressed further by a 3-π-pulse Periodic Dynamical Decoupling (PDD) sequence, yielding a decoherence time $T_2^{\mathrm{PDD}} = 2.99 \pm 0.33\,\mathrm{ms}$, which is now equal to $2T_1$ to the accuracy of the measurement.

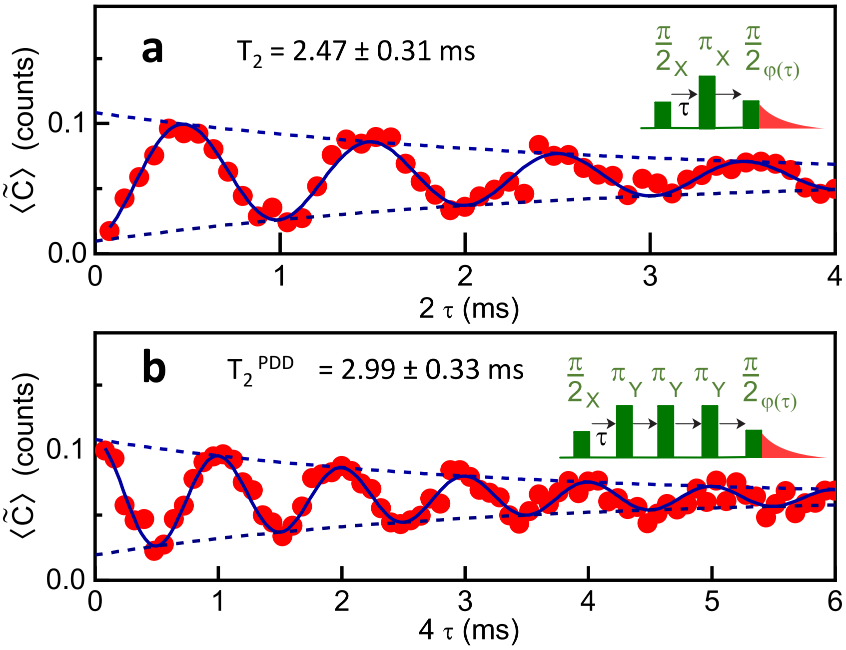

Figure 5.9: **Coherence time measurements of spin $s6$ with a Hahn-echo sequence [panel (a) - see inset] and a Periodic Dynamical Decoupling sequence [panel (b) - see inset].** Measured excess counts $\langle \widetilde{C} \rangle$ (red dots) versus delay τ, with a linearly increasing phase $\varphi(\tau) = 2\pi\Delta\tau$ on the last pulse and $\Delta = 1\,\text{kHz}$. The corresponding fits and their envelope (solid and dash lines) yield coherence times $T_2 = 2.47 \pm 0.31\,\text{ms}$ and $T_2^{\text{PDD}} = 2.99 \pm 0.03\,\text{ms}$. Data taken at $B_0 = 422.085$ mT and $\theta = -0.003°$.

5.3.4 Summary of coherence properties of different spins

The coherence times were also measured on a few other Er^{3+} electron spins, like s7 and s8, which are not indicated on the spectrum of Figure 4.6. In total four ions were measured and their coherence properties are summarized in the table below.

Spin	T$_1$(ms)	T$_2^*$(μs)	T$_2^{\text{echo}}$(ms)
s0	1.26	79	1.38
s6	1.42	170	2.47
s9	1.36	315	1.53
s10	2.21	7.5	2.1

Table 5.1: **Measured spin coherence times.** Spin s0, s6, s9 are the ones indicated in the spectroscopy of fig. 4.5b, and s10 is measured at $B_0 = 422.39\,\text{mT}$ and $\theta = 0.014°$.

T_2^* varies strongly among these ions (between 5 μs and 300 μs), whereas T_2^{echo} are all between T_1 and $2T_1$. The variation of coherence time among different spins can be explained by their different nuclear spin or paramagnetic environment, and also possibly their degree of exposure to surface magnetic noise given their approximate depth of $\sim 100 - 150\,\text{nm}$ according to Figure 3.4 [128, 125]. It is also noteworthy that the coherence times measured here are on par with the longest reported for individual electron spins in solid-state [58], in a platform which gives access to several tens of these spin qubits by simply tuning a dc magnetic field.

5.4 Detection efficiency and signal-to-noise ratio

In the final section of this chapter, we will discuss the overall efficiency of the detection and quantify the single-spin SNR for a certain measurement time t_m by using the same dataset for $g^{(2)}$ measurements.

5.4.1 Overall detection efficiency

The overall efficiency of our setup is found to be equal to $\eta = 0.12 \pm 0.01$ by integrating the fluorescence signal with subtracted background after a π excitation pulse. Losses of counts can occur due to non-radiative spin relaxation, internal losses of the spin resonator, microwave losses between the spin device and the SMPD η_{loss}, and finite SMPD efficiency η_{SMPD}, so that

$$\eta = \frac{\Gamma_{\mathrm{R}}}{\Gamma_{\mathrm{R}} + \Gamma_{\mathrm{NR}}} \frac{\kappa_c}{\kappa} \eta_{\mathrm{loss}} \eta_{\mathrm{SMPD}}. \tag{5.13}$$

Given the measured $\eta_{\mathrm{SMPD}} = 0.32$, $\kappa_c/\kappa = 0.57$, and $\Gamma_R/(\Gamma_R + \Gamma_{NR}) = 0.995$, we deduce $\eta_{\mathrm{loss}} = 0.66$, which is a reasonable value for the microwave losses encountered upon propagation along a 50-cm-long coaxial cable, a circulator, and the filters at the SMPD input.

5.4.2 Signal-to-noise ratio of the measurement

To obtain the signal-to-noise ratio (SNR) of our measurement, we operate as follows: identical sequences with a π excitation pulse are repeated every t_r time during a total measurement time t_m. We then compute the sum C of the counts integrated over the first 2 ms following the excitation pulse, and summed over all the sequences. The same measurement is then made but without any excitation pulse. Figure 5.10a shows the count probability histograms $p(C)$ for $t_m = 1\,\mathrm{s}$, with and without applied excitation pulses. This yields a single-spin SNR $C_{spin}/\delta C_\pi = 1.91$, with C_{spin} and δC_π the distance between the two histograms and the standard deviation of the histogram with excitation, respectively. We also verify that the SNR scales as the square root of the measurement time t_m up to at least 1 minute (see Figure 5.10b), indicative of good measurement stability.

We now use a very simple model and the measured overall efficiency $\eta = 0.12$ to calculate a theoretical maximal expected SNR, to be compared with the measured one.

For the measurement series with a π excitation pulse repeated every t_r, a t_d-long integration time, and a spin relaxation rate Γ_R, the steady-state spin polarization at the beginning of each sequence is $S_{z0} = -1/2 \tanh(\Gamma_R t_r/2)$, yielding an average number of counts per sequence $-2\eta S_{z0}(1 - \mathrm{e}^{-\Gamma_R t_d})$; summed over t_m, the average total number of counts

$$C_{spin} = \eta \frac{t_m}{t_r} \tanh(\frac{\Gamma_R t_r}{2})(1 - \mathrm{e}^{-\Gamma_R t_d}). \tag{5.14}$$

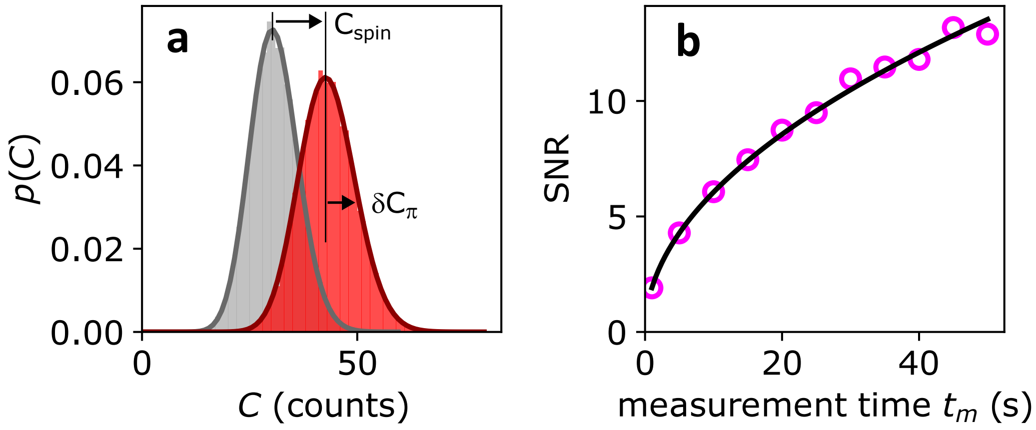

Figure 5.10: **Signal-to-noise ratio of the measurement.** **(a)** Measured probability distribution $p(C)$ of the total count C integrated over the first 2 ms of $t_r = 7.5$ ms long, either with no excitation pulse applied (grey) or with a π excitation pulse (red). Sequences are repeated and counts are summed during a measurement time $t_m = 1\,\text{s}$. Solid lines are Poissonian fits, yielding the spin signal $C_{spin} = 12.4$ (difference between the mean values of the two distributions) and the standard deviations $\delta C_0 = 5.5$ and $\delta C_\pi = 6.5$. **(b)** Measured signal-to noise ratio $C_{spin}/\delta C_\pi$ (magenta dots) as a function of measurement time t_m, and fit by a function $A\sqrt{t_m}$ (solid line). Data taken at $B_0 = 421.042$ mT and $\theta = -0.024°$.

The noise has two contributions: one from the dark count fluctuations (Poissonian distribution), whose variance is $\alpha t_d t_m/t_r$, and one from the partition noise of the detected photons (binomial distribution), with variance $(1-\eta)C_{spin}$. Therefore, the width of the histogram with excitation is $\delta C_\pi = \sqrt{\alpha t_d t_m/t_r + (1-\eta)C_{spin}}$. The signal-to-noise ratio is finally

$$\text{SNR} = \frac{C_{spin}}{\delta C_\pi} = \frac{C_{spin}}{\sqrt{\alpha t_d t_m/t_r + (1-\eta)C_{spin}}}. \tag{5.15}$$

For the parameters of our experiment ($T_1 = \Gamma_R^{-1} = 1/(700\text{s}^{-1}) = 1.43\,\text{ms}$, $\alpha = 10^2\text{s}^{-1}$, $\eta = 0.12$), a numerical optimization indicates a maximum SNR of 2.5 for $t_d = 2\,\text{ms} = 1.4T_1$ and $t_r = 3\,\text{ms} = 2.1T_1$. In the experiment, we use a larger repetition time to minimize the effect of heating; for the parameters used ($t_d = 2\,\text{ms}$ and $t_r = 7.5\,\text{ms} = 5.2T_1$), the formula yields a SNR of 1.95, in agreement with the measured value of 1.91.

5.5 Impact of the work

In this section, we discuss the significance of our results for practical single electron spin resonance spectroscopy. A stringent constraint of our method is that the operation temperature should satisfy $T \ll \hbar\omega_0/k$ to keep the dark count rate low; millikelvin temperatures seem therefore unavoidable for measurements at X band. On the other hand, one particularly interesting aspect is its applicability to a broad range of paramagnetic species, irrespective of their coherence time, provided their radiative relaxation rate Γ_R can be enhanced up to $\sim 10^3\text{s}^{-1}$ or higher by the Purcell effect and their non-radiative relaxation rate is smaller than Γ_R. Many paramagnetic impurities have indeed non-radiative relaxation rates in the range of $10^{-3} - 10^3\,\mathrm{s}^{-1}$ at $\sim 1 - 4\,\mathrm{K}$ [129, 130, 131], and thus also likely at millikelvin temperatures. Although reaching the desired radiative relaxation rate of $\Gamma_R > 10^3\mathrm{s}^{-1}$ was made easier in this work by the large transverse g-factor of 8.3 in $\mathrm{Er}^{3+} : \mathrm{CaWO}_4$, this large relaxation rate was also demonstrated for donor spins in silicon with g-factors of only 2, using a similar resonator geometry but with a narrower and shorter wire [132]. Whereas in our experiment the spins are located in the sample supporting the resonator, it is also possible to deposit a small volume of a spin-containing insulating material, such as a powder or micro-crystal, onto a pre-fabricated resonator device. Such an approach could be suitable for measuring individual rare-earth-ion-containing molecules [31], nanocrystals [133], or proteins whose active center contains a transition-metal-ion [134, 135]. Based on the $10\,\mu\mathrm{m}^3$ detection volume demonstrated here using $\mathrm{Er}^{3+} : \mathrm{CaWO}_4$, we extrapolate that a $0.5\,\mu\mathrm{m}^3$ detection volume would be achievable for an electron-spin with a g-factor of two, under the same experimental conditions. All these metrics could be improved with better SMPD performance, in particular reduced dark count rates, highlighting a strong motivation for the continued development of SMPD devices.

Part II

Towards addressing single hole spin in gate-defined semiconductor quantum dots initialized by illumination

Chapter 6

Overview and theoretical background

This chapter provides the necessary background to understand the experiment in the second part, in which single electron or hole isolated in semiconductor quantum dots is detected through dispersive measurement of microwave photons using the platform of circuit quantum electrodynamics. The chapter begins with electrostatic gate-defined quantum dots, an architecture to isolate charges electrically. Next, we recall the distributed coplanar waveguide resonator introduced in Section 2.2.1 and then discuss the detection mechanism of charge states in quantum dots through microwave photons in the resonator. Furthermore, mediated by charge, spin can be coupled to the resonator and probed in a similar way by microwave. Finally, based on the detection schemes described before, a new architecture is proposed for scalable quantum computing in semiconductor qubit system, where optics is introduced for the first time as an initialization method for electrostatic gate-defined quantum dots.

6.1 Charge box: quantum dots in semiconductor

A quantum dot is an artificially structured nanoscale "box" that can isolate and keep a certain number of electrons or holes inside. To physically implement a quantum dot device, there are various approaches and material systems, such as single-atom dots [32], self-assembled dots [136], semiconductor lateral [137] or vertical dots [138], carbon nanotubes [84], etc. In the experiment presented in the part II of the thesis, we will focus on semiconductor lateral quantum dots electrostatically defined by the electric potential generated from nearby electrodes called "gates". The charge carriers (electrons or holes) trapped inside the dots have interesting properties concerning their charge and spin degrees of freedom, which can be exploited as building blocks for electron- or hole-based quantum information processor [139, 140, 141, 142, 142, 143]. Reviews on this subject can be found in [48, 144, 145, 146].

6.1.1 Single quantum dot

Coulomb blockade

A quantum dot is usually regarded as a "0D" device due to the confinement from all three directions (either by electric potential, geometry of the material system or a combination of both). We treat this system as a mesoscopic island that can host a small number of charges and its specific confinement configuration leads to the discrete energy spectrum of the charges on it. As shown in Figure 6.1a, the quantum dot is represented by a gray disk and the charges (electrons or holes) in the dot come from the nearby reservoir by quantum tunneling thanks to the small distance and narrow barrier. The confinement of the dot results in discrete electrochemical potential levels inside the dot (see Figure 6.1b), which can be adjusted by the voltage applied on the gate electrode nearby.

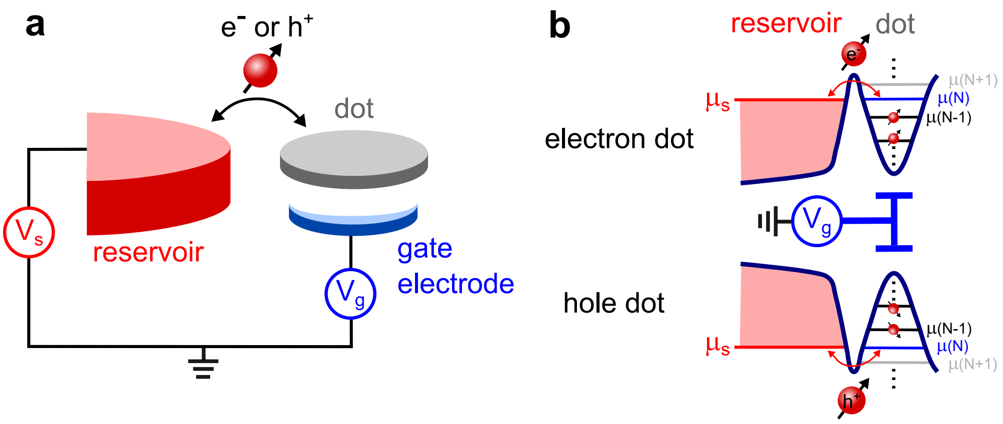

Figure 6.1: **Single quantum dot.** **(a)** Schematic picture of a single quantum dot in lateral geometry. The quantum dot (gray disk) is connected to a source reservoir of electrons or holes through a narrow tunnel barrier. The electrochemical potentials of the reservoir and dot are controlled by voltage bias V_s on the source side and V_g on the gate electrode, respectively. **(b)** Schematic diagrams of electrochemical potential levels in the reservoir and quantum dot for the cases of electrons and holes. The height of the levels in the quantum dot can be tuned by gate bias V_g.

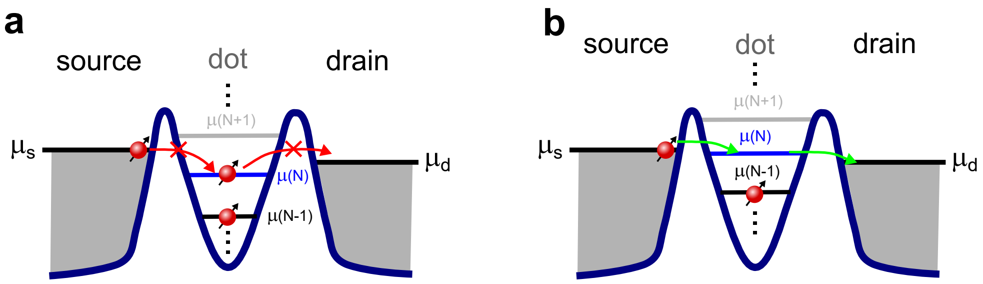

Figure 6.2: **Coulomb blockade and transport regime.** **(a)** Schematic of Coulomb blockade for a single dot containing N electrons. The dot is connected to the source (left) and the drain (right) reservoir with tunnel barriers. The chemical potentials of both reservoirs (μ_s and μ_d) are between the highest occupied level $\mu(N)$ and the lowest empty level $\mu(N+1)$. The entry of new electrons or the exit of electrons in the dot is prohibited. **(b)** Transport regime. The lowest empty level $\mu(N)$ is between μ_s and μ_d, which allows the electron transport from one side to the other.

In addition, the electronic properties of charges in quantum dots are also determined by their non-negligible mutual Coulomb interaction. An extra energy, called charging energy E_c, is at the cost every time when adding one charge onto the island due to Coulomb repulsion. Given $E_c \gg k_B T$ at low temperature and larger energy spacing in the dot, the tunneling of charges from or to the reservoir can be largely suppressed and the number of charges in the dot is in a blocked status. This phenomenon known as Coulomb blockade is depicted in Figure 6.2. In this case, the electrochemical potential of the reservoir is between the highest occupied level and the lowest empty level, so that the charge transport is blocked by the occupied level while its energy is not high enough to reach the next level.

In the following analysis, we will determine the electrostatic energy associated with electrons confined in a single quantum dot, where the number of charges is N. A gate electrode with bias V_g is coupled to the dot by a capacitor C_g. The dot can exchange particles with the reservoir through quantum tunneling, represented by a component with resistance R_t and capacitance C_t in Figure 6.3a. The tunnel rate at temperature T is given by

$$t = \frac{\Delta E}{e^2 R_t[\exp(\Delta E/k_B T) - 1]}, \tag{6.1}$$

where ΔE is the energy difference between the reservoir and the empty level of the dot, and e is the electric charge.

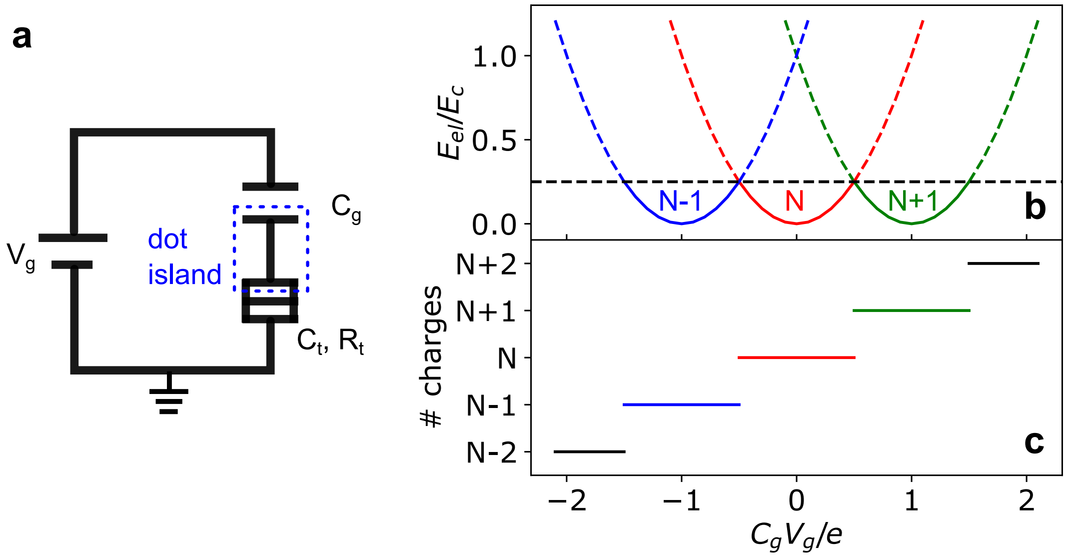

Figure 6.3: **Energy and charge number of single quantum dot.** **(a)** Circuit diagram of a single dot coupled to a reservoir by quantum tunneling and coupled to a gate electrode through capacitor C_g. **(b)** Electrostatic energy of the single dot as a function of number of charges in the dot and gate bias V_g. The solid lines indicate the energy of the ground state with corresponding number of charges in the dot. **(c)** Number of charges in the dot as a function of gate bias V_g.

The electrostatic energy of the dot is then expressed as

$$E_{\text{el}} = E_c(N - \frac{C_g V_g}{e})^2 - \frac{1}{2}C_g V_g^2, \tag{6.2}$$

where $E_c = e^2/[2(C_g + C_t)]$ is the charging energy. Given that the second term $C_g V_g^2/2$ does not contain the charge number variable N, we neglect it for simplicity while analysing the charge stability of the dot. Figure 6.2b shows the energy of the system as a function of external bias V_g in terms of different charge number N inside the dot. $E_{\mathbf{el}}$ depends quadratically on V_g, and each time when V_g crosses the charge degeneracy point, N changes in order to minimize the energy of the system. As shown in Figure 6.3c, the number of charges inside the dot shows step-dependence on the V_g and in the Coulomb blockade regime, the N is fixed regardless of the change of the V_g.

Charge stability diagram

Due to Coulomb blockade, the number of charges inside the quantum dot is fixed, and the transition occurs to minimize the total electrostatic energy of the system. From an energy diagram perspective, transitions correspond to the alignment of the reservoir levels and empty levels in the dot, which can be adjusted using voltage bias on the gates. The map of stable charge configurations in the system as a function of external bias is called charge stability diagram.

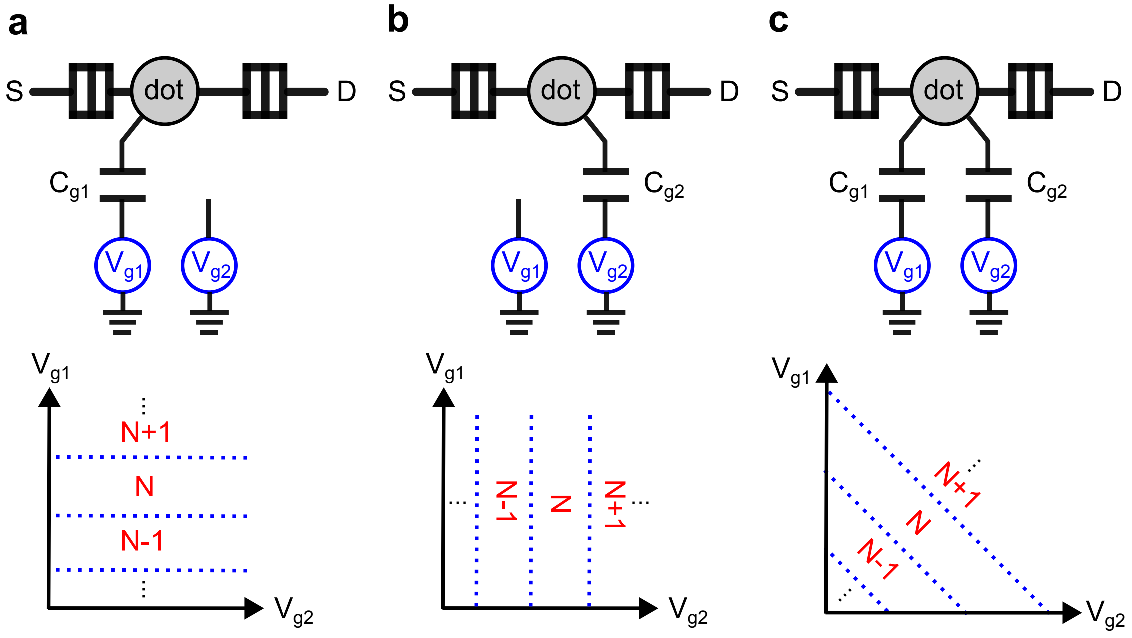

Figure 6.4: **Charge stability diagram of a single quantum dot.** Map of charge transitions (dash line) as a function of voltage bias on the gates and corresponding circuit diagram representations for the cases of only gate 1 connected (a), only gate 2 connected (b) and both gates connected (c). Away from the dash lines, the dot is in Coulomb blockade regime and the charge numbers associated to the dot are fixed.

To begin with, we consider a single quantum dot of electrons controlled by two identical gate electrodes, and the levels of source and drain reservoirs are aligned($V_S = V_D$). When only one gate is connected and the other is left open, the transport region takes the form of either vertical or horizontal lines. The number of charges inside the dot is fully dependent on only one control gate and the region between two transition lines is in Coulomb blockade (see Figure 6.4a and b). The capacitance C_{g1} (or C_{g2}) determines how much the chemical potential of the dot changes in response to changes in the gate voltage, and therefore affects the spacing of the horizontal (or vertical) transition lines.

When two gates are involved in controlling the chemical potential of the dot, the charge transition lines have a slope depending on the ratio of coupling capacitance C_{g1}/C_{g2} (see Figure 6.4c). This ratio affects the relative strength of the coupling between the dot and the two gates.

As for the hole quantum dot, the control gates need opposite polarity compared to electron system to increase the number of holes confined in the dot, in which the decrease of the gate bias (more negative) leads to larger number of holes.

6.1.2 Double quantum dot

A double-quantum-dot device consists of two coupled islands, enabling the manipulation of the orbital degrees of freedom within each dot and their mutual tunnel coupling as an artificial molecule. For planar quantum-dot-based quantum information processing, double quantum dots can isolate a single electron or hole, allowing for the control of the charge or spin degree of freedom of the carriers. Figure 6.5a depicts a schematic of the double quantum dot, where the coupled two islands enable the inter-dot tunneling of the carriers isolated in the dots. The double dot is also coupled to the reservoirs called source and drain on both sides. Each dot has one control gate to adjust the chemical potential within the dot.

In the Coulomb blockade regime, as shown in Figure 6.5c, the total number of charges inside the double dot is fixed. At the lowest unoccupied level, one charge can be shared by both dots, resulting in a non-localized wavefunction and electric dipole.

Effective Hamiltonian

We now consider the simple case of only one electron in the double quantum dot with tunnel coupling t. The localized orbital degrees of freedom in the left and right dot can be treated as two basis states of the system, namely $|L\rangle$ and $|R\rangle$, as shown in Figure 6.6a. We can thus express the state of the electron within the subspace of $\{|L\rangle, |R\rangle\}$ and corresponding Pauli matrices are

$$\hat{\tau}_z = |L\rangle\langle L| - |R\rangle\langle R|, \tag{6.3}$$

$$\hat{\tau}_x = |L\rangle\langle R| + |R\rangle\langle L|. \tag{6.4}$$

Therefore, the effective Hamiltonian of the system takes the form

$$\hat{H} = \frac{1}{2}\delta\hat{\tau}_z + t\hat{\tau}_x, \tag{6.5}$$

where δ is the inter-dot energy detuning.

After diagonalizing the Hamiltonian, the eigenenergies of the double quantum dot are obtained as

$$E_{\pm} = \pm\frac{1}{2}\sqrt{4t^2 + \delta^2}. \tag{6.6}$$

Figure 6.6b shows the energy spectrum of Equation 6.6.

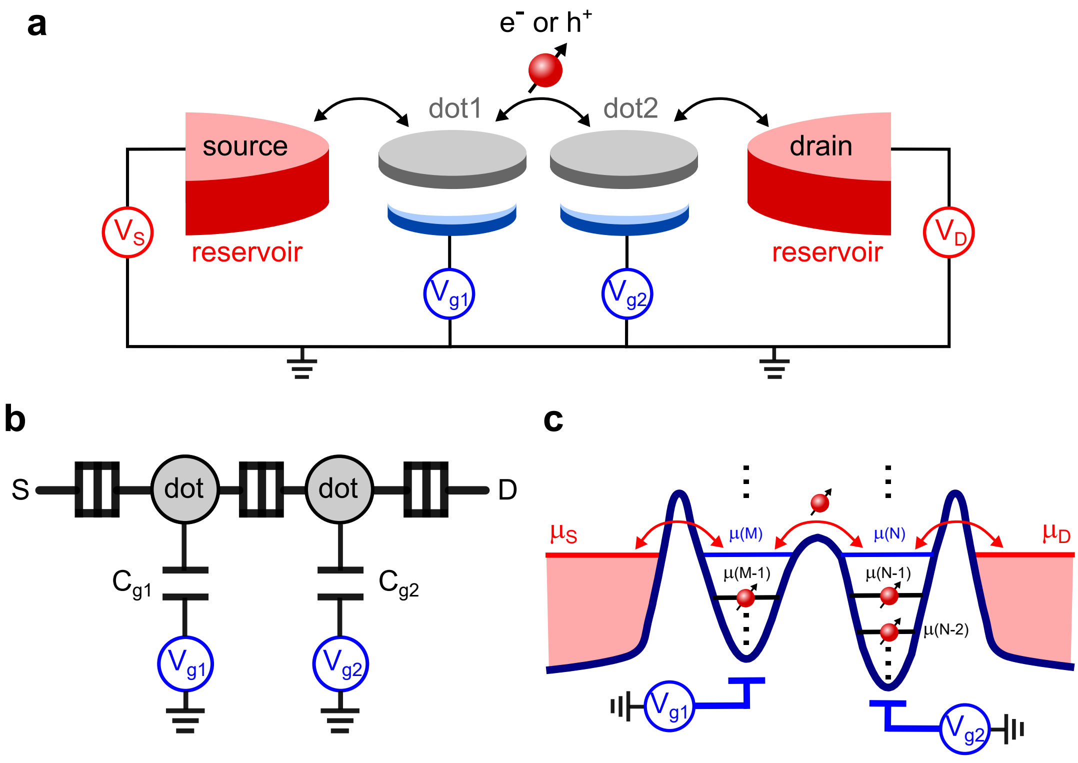

Figure 6.5: **Double quantum dot.** **(a)** Schematic of two coupled mesoscopic islands forming a double quantum dot, where electron or hole can hop between the islands by quantum tunneling. **(b)** Circuit model of the double quantum dot. The links of source-dot1, dot1-dot2, dot2-drain are tunnel barriers. Voltage V_1 (resp. V_2) is used to adjust the chemical potential within the dot through capacitor C_{g1} (resp. C_{g2}). **(c)** Schematic of quantum well and chemical potential level configuration formed by voltage bias on source, drain, gate 1 and gate 2. The occupied number of levels inside dot 1 and dot 2 are noted as M and N respectively.

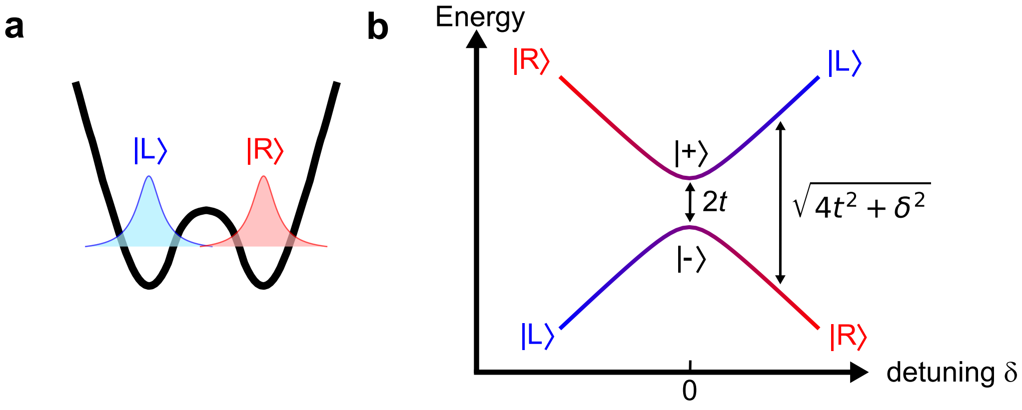

Figure 6.6: **Wavefunction and energy spectrum of double quantum dot.** **(a)** Schematic of electron wavefunctions in the double well of double quantum dot defined as $|L\rangle$ and $|R\rangle$ for left and right dot respectively. **(b)** Spectrum of system eigenenergies with a tunnel coupling t and energy detuning δ between left and right dot.

At zero inter-dot detuning (levels at left and right are aligned), the electron is delocalized due to tunnel coupling and the eigenstates of the systems are $|\pm\rangle = (|L\rangle \pm |R\rangle)/\sqrt{2}$. The Hamiltonian $\hat{H} = t\hat{\tau}_x$ in the basis $\{|+\rangle, |-\rangle\}$ has the form

$$\hat{H}' = t\hat{\tau}'_z, \tag{6.7}$$

with $\hat{\tau}'_z = |+\rangle\langle+| - |-\rangle\langle-| = |R\rangle\langle L| + |L\rangle\langle R| = \hat{\tau}_x$.

At large detuning ($|\delta| \gg 2t$), the electron is either localized in the left or right dot and the energy separation is approximately $|\delta|$. At intermediate detuning ($|\delta| \sim t$), the eigenstates of the system are $\cos\frac{\theta}{2}|L\rangle + \sin\frac{\theta}{2}|R\rangle$ and $-\sin\frac{\theta}{2}|L\rangle + \cos\frac{\theta}{2}|R\rangle$ with a mixing angle θ defined by $\tan\theta = 2t/\delta$ [147]. This effective Hamiltonian of a charge in double quantum dot describes a simple two-level system and also the realization of a charge qubit with quantum dots.

6.1.3 Physical implementation for a double quantum dot

The most common platform for implementing a lateral semiconductor quantum dot device is a 2-dimensional electron gas (2DEG) or a 2-dimensional hole gas (2DHG) defined with electrostatic gates. As shown in Figure 6.7, 2DEG or 2DHG can be formed at the interface of semiconductor stacks, such as $\mathrm{Al_xGa_{1-x}As/GaAs}$, which provides the confinement of carriers on the vertical direction (z). The carriers capable of moving freely in the 2D interface are then restricted by the potential generated from the metal gate electrodes above, leading to lateral confinement (x and y). In this case, a combination of material system and electrostatic potential provides confinement for carriers in 3 directions.

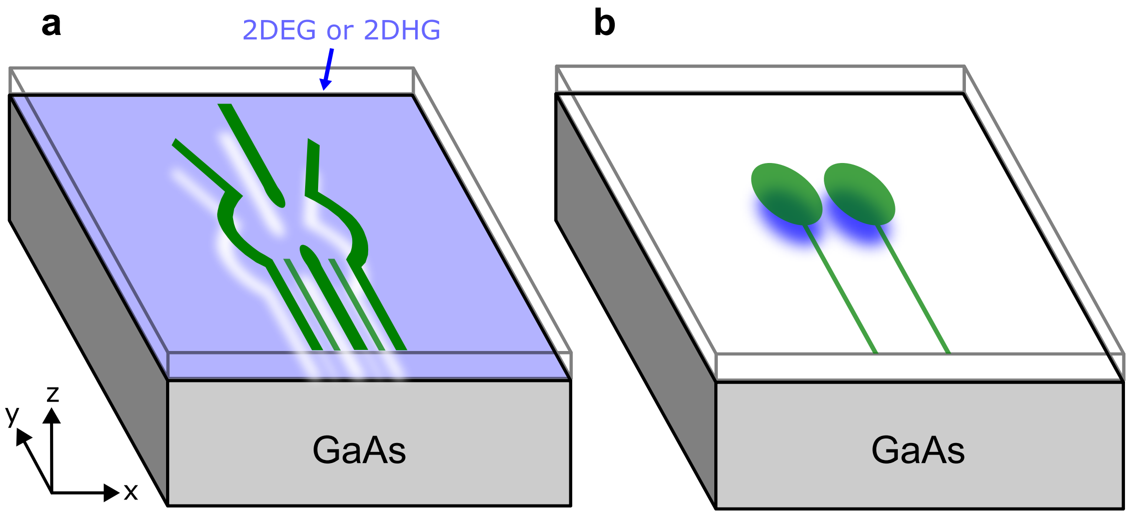

Figure 6.7: **Physical platform for implementing quantum dot device. (a)** Depletion approach. Electrostatic gates (green) are biased with repulsive voltages to deplete the 2DEG or 2DHG (blue) in the unwanted regions (white) to form quantum dots. **(b)** Accumulation approach. Quantum dots are formed by accumulating charges (blue) beneath the gates (green) with attractive biases. Note that if the leads are narrow enough, charges cannot be accumulated below.

In general, the creation of quantum dots have two possible approaches:

- **Depletion:** Starting from a sheet of charges (2DEG or 2DHG) that originates from dopants in the substrate or global gate's attraction, one can apply repulsive voltages on the local gates (negative for electrons and positive for holes) to deplete the charges in the unwanted regions. The remaining small clusters of charges constitute quantum dots.

- **Accumulation:** Quantum dots are formed by applying attractive voltages on the gates to accumulate charges beneath. Typically, the substrate is undoped and the charges in the quantum dots are introduced from nearby reservoir (ohmic contact).

6.2 Circuit quantum electrodynamics with quantum dots

The concepts of cQED introduced in Section 2.2 shows the use of an oscillating magnetic field in a superconducting resonator to couple spins magnetically. In this section, we will use the electric field part of the resonator to couple directly to the charges and indirectly to spins. Recall the introduced half-wavelength coplanar waveguide resonator (see Section 2.2.1), and the electric field of its mode has a spatial distribution, as shown in Figure 6.8. The fundamental mode of the resonator is described by the Hamiltonian

$$\hat{H}_r = \hbar\omega_0(\hat{a}^\dagger\hat{a} + \frac{1}{2}), \tag{6.8}$$

where the electric field is maximized at anti-nodes near the two gaps of input and output, which will be utilized to couple the charge dipoles in the quantum dots.

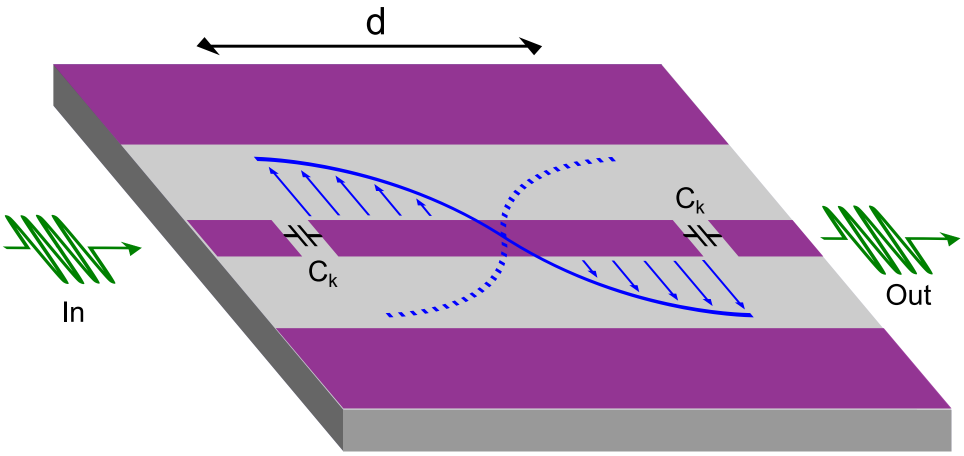

Figure 6.8: Coplanar waveguide resonator formed by two gaps (with coupling capacitance C_k) separated by distance d in the central conductor of the transmission line. The electric field (blue) of fundamental mode is maximized at two ends next to the gaps.

6.2.1 Charge-resonator coupling

In order to couple to the charge dipole in the double quantum dot with the electric field inside the resonator, the central conductor of the resonator is extended near one of the electrostatic gates of the double dot (near the right dot in the case of Figure 6.9). The voltage (electric field) from microwave with vacuum fluctuation amplitude δV given by $\hat{V}_1 = \delta V(\hat{a} + \hat{a})$ will change the energy of the right dot and thus create an inter-dot energy detuning

$$\hat{\delta} = e\alpha\delta V(\hat{a}^\dagger + \hat{a}), \tag{6.9}$$

where α is the lever arm describing the proportion of the field from the resonator resulting in actual change of the energy in the dot.

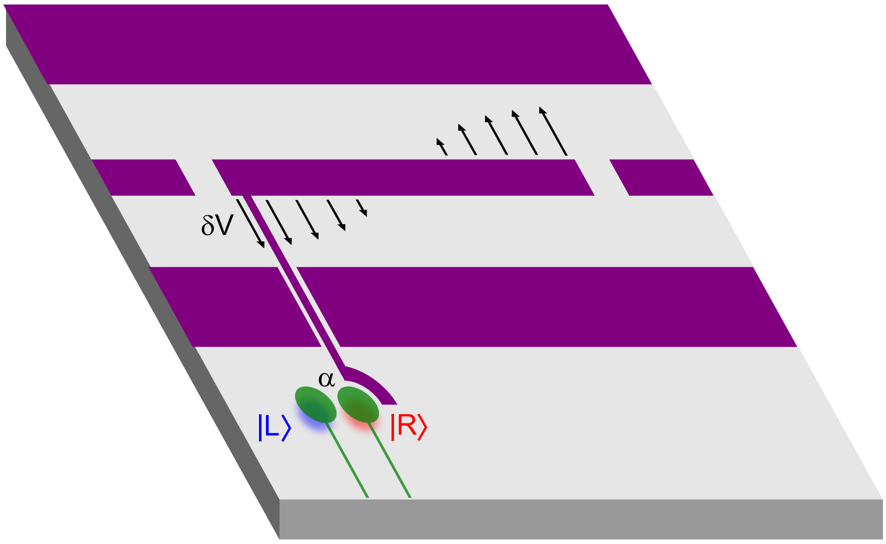

Figure 6.9: **Coplanar waveguide resonator coupled to the charge dipole inside a double quantum dot**. The central conductor of the resonator (purple), with an amplitude of vacuum fluctuation of voltage δV indicated by arrows, is extended near one of the electrostatic gates (green) of the double quantum dot and applies an effective inter-dot detuning with a lever arm α, resulting in an electric dipole coupling.

Therefore, the charge-resonator interaction Hamiltonian is

$$\hat{H}_{\text{int}} = \hat{\delta}|R\rangle\langle R| = \hbar g_0(\hat{a}^\dagger + \hat{a})(\mathbb{1} - \hat{\tau}_z), \tag{6.10}$$

using $|R\rangle\langle R| = (1 - \hat{\tau}_z)/2$. The coupling constant is

$$\hbar g_0 = \frac{1}{2}e\alpha\delta V. \tag{6.11}$$

The total Hamiltonian is

$$\hat{H} = \hbar\omega_0(\hat{a}^\dagger + \hat{a}) + \frac{1}{2}\delta\hat{\tau}_z + t\hat{\tau}_x + \hbar g_0(\hat{a}^\dagger + \hat{a})(\mathbb{1} - \hat{\tau}_z) \tag{6.12}$$

We can rewrite the total Hamiltonian in the $\{|+\rangle, |-\rangle\}$ basis for the case of zero inter-dot detuning ($\delta = 0$), such that

$$\hat{H}' = \hbar(\omega_0 + g_0)(\hat{a}^\dagger + \hat{a}) + t\hat{\tau}'_z + \hbar g_0(\hat{a} + \hat{a})\hat{\tau}'_x \tag{6.13}$$

$$\sim \hbar\omega_0(\hat{a}^\dagger + \hat{a}) + \frac{1}{2}\hbar\omega_c\hat{\tau}'_z + \hbar g_0(\hat{a}^\dagger\hat{\tau}'_- + \hat{a}\hat{\tau}'_+), \tag{6.14}$$

by using $\omega_0 + g_0 \sim \omega_0$ and the rotating wave approximation. The ladder operators are defined as

$$\hat{\tau}'_- = |-\rangle\langle+|,\ \hat{\tau}'_+ = |+\rangle\langle-|, \tag{6.15}$$

and the charge-qubit frequency writes $\omega_c = 2t/\hbar$. The Hamiltonian of the coupled charge-resonator system has the form of Jaynes-Cummings model. The theory and experimental demonstration of a double quantum dot coupled to a microwave resonator are reported in references [148, 8].

6.2.2 Charge detection

Dispersive charge readout

The Jaynes-Cummings type of interaction between a two-level system and a resonator provides a method to read out the charge state when the system is in the dispersive regime, in which the charge-resonator detuning $\Delta = \omega_c - \omega_0$ is much larger than the coupling constant: $|\Delta| \gg g_0$ [10].

At zero inter-dot detuning, the energy separation of states $|+\rangle$ and $|-\rangle$ ($\hbar\omega_c = 2t$) is only determined by the charge tunnel coupling rate (depending on the tunnel barrier height and the inter-dot distance). The system is in the dispersive regime when the relation $|2t/\hbar - \omega_0| \gg g_0$ is satisfied and the charge-resonator Hamiltonian can be well approximated by

$$\hat{H}_{\text{disp}} \approx \hbar(\omega_0 + \chi\hat{\tau}'_z)\hat{a}^\dagger\hat{a} + \hbar t\hat{\tau}'_z, \tag{6.16}$$

where $\chi = g_0^2/\Delta$ is known as the dispersive shift (we neglect the vacuum Lamb shift for simplicity) [10]. Here the resonator frequency depends on the charge state in the double dot. If the charge is in $|-\rangle$ state, $\langle\hat{\tau}'_z\rangle = -1$ and the resonator frequency is $\omega_0 - \chi$; while the charge is in $|+\rangle$ state, $\langle\hat{\tau}'_z\rangle = +1$ and the resonator frequency is $\omega_0 + \chi$, see Figure 6.10.

The fact of charge-state-dependent resonator dispersive shift offers a method to detect charge transition with microwave while changing the gate bias. By probing the resonator at ω_0, the transmitted amplitude or phase will tell whether the transition occurs or not. Note that this detection is possible only if the tunnel splitting and resonator frequency are in the same order of magnitude ($2t \sim \omega_0$), otherwise the large charge-resonator detuning $\Delta = 2t/\hbar - \omega_0$ will lead to zero dispersive shift $\chi = g_0^2/\Delta \sim 0$. By varying the voltage bias on the gate, the inter-dot detuning δ can be changed, and here we consider two cases:

- **Zero inter-dot detuning** ($\delta = 0$). The levels in the left and right dot are aligned. The ground state of non-localized charge ($|-\rangle$) in the double dot can be probed from the resonator dispersive shift $\omega_0 - \chi$.
- **Large inter-dot detuning** ($\delta \gg 2t$). The charge is localized in one of the dots. The energy difference between the levels in the left and right dot are too large to cause measurable dispersive shift.

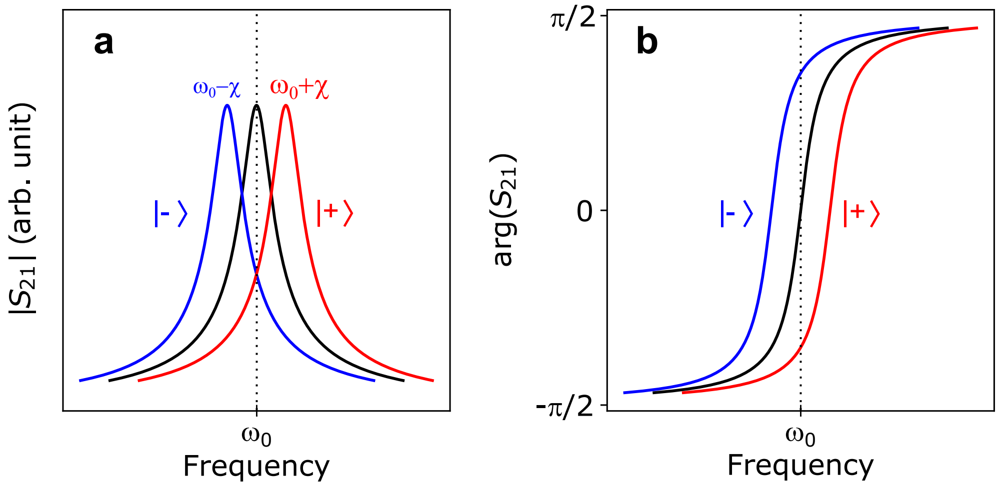

Figure 6.10: **Resonator charge-state-dependent dispersive shift.** The amplitude (a) and phase (b) of resonator transmission for the 3 cases: charge-resonator uncoupled (black), charge-resonator coupled with charge in $|-\rangle$ state (blue) and in $|+\rangle$ state (red). The corresponding resonator frequency shifts are $\omega_0 \pm \chi$ for $|\pm\rangle$.

Therefore each time when the levels of double dot are aligned, one transition line can be obtained.

Quantum capacitance

In addition to the framework of cQED, the shift of resonator frequency can be seen in a perspective of quantum capacitance [149, 150]. When a single electron tunnels between two single-particle levels in weakly coupled quantum dots, the differential capacitance $C_q = \partial Q/\partial V_g$ changes, and this change depends on the charge tunnel coupling and the gate bias (inter-dot detuning). If the electron is localized within the dot, the capacitance is zero, whereas in the case of zero inter-dot detuning and large tunneling, the differential capacitance arises. This change of capacitance thus leads to a change in resonator frequency:

$$\delta\omega = \frac{1}{\sqrt{LC}} - \frac{1}{\sqrt{L(C+C_q)}}. \tag{6.17}$$

Furthermore, quantum capacitance can arise not only from the charge tunneling between two quantum dots, but also from the tunneling between a quantum dot and a reservoir. Whenever single electrons tunnel into or out of discrete levels, this event can be detected by probing the coupled resonator.

6.3 New architecture for scalable quantum computing

The control and readout of charge states by microwave enabled by cQED [8] provides an alternative approach other than conventional transport-based charge detection. The cQED architecture leads us to envision a novel scalable hybrid platform without introducing charge reservoirs or dopants which are necessary in the formation of quantum dots in conventional approaches.

In this new method, instead of filling the dots by transferring charges from reservoirs to the potential wells created by electrostatic gates, we propose to use optical illumination as a source of charge carriers, where the optically generated electron-hole pairs are split by electric field of the gates and holes can therefore be accumulated beneath. Figure 6.11a shows a simple example of creating a double quantum dot with only two accumulation gates. The protocol, as shown in Figure 6.11b, consists of 3 steps:

1. Positive or negative bias is applied to the electrostatic gates in order to create electric field and form a double potential well in the substrate.
2. The illumination is switched on for a short amount of time and the electron-hole pairs generated by light are split by the existing electric field.
3. The charges are then trapped by gates biased with opposite polarity (negative bias for holes and positive bias for electrons).

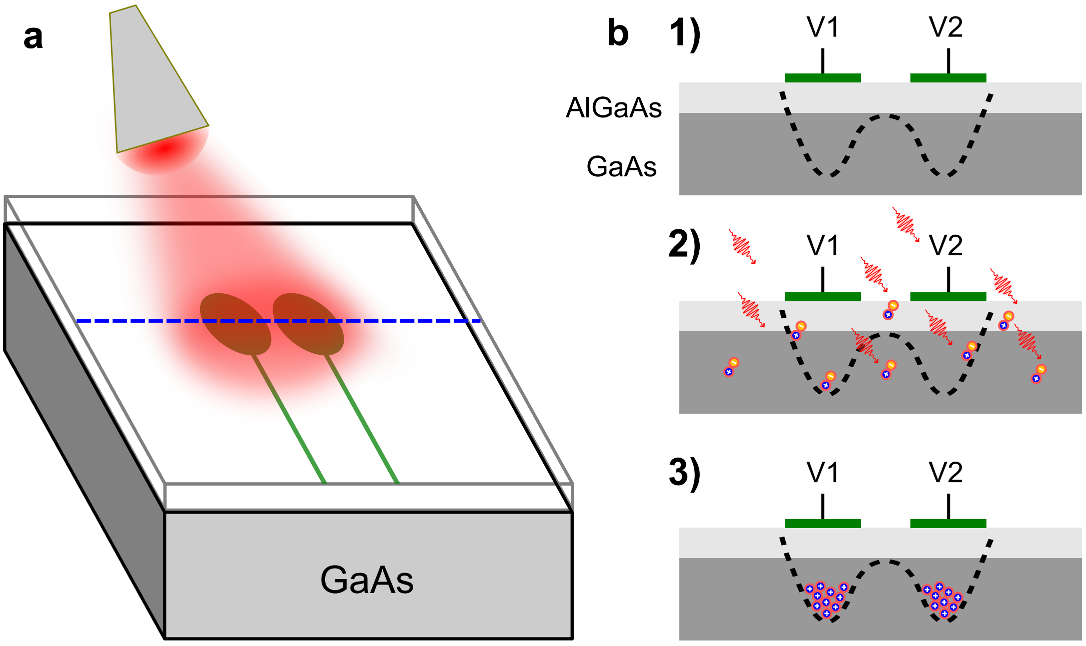

Figure 6.11: **Optical initialization of quantum dots.** **(a)** Infrared light is shining on the surface of AlGaAs/GaAs substrate with two accumulation gates (green). **(b)** Protocol for optical initialization of quantum dots, with the schematics showing the cross-section indicated by blue dash line in **a**: (1) Negative bias is applied to both accumulation gates. (2) Incoming photons from infrared light generate electron-hole pairs in the semiconductor substrate. (3) The electric field generated from gates splits the electron-hole pairs and accumulate holes beneath the negatively biased gates.

In this new proposal, the illumination and accumulation gates help to reduce the complexity of conventional device in depletion mode, which requires normally ohmic contact or dopants for creating 2DEG and complicated gate layout to create quantum dots (as discussed in Section 6.1.3). We can build quantum dots on a undoped substrate without introducing ohmic contact, which also simplifies the fabrication process. In addition, the superconducting resonator in cQED architecture can perform charge readout by microwave, but also acts as a quantum bus to couple distant qubits to create long-range entanglement [10, 151, 152, 153], which will help scale up quantum-dot-based computing architecture.

Chapter 7

Devices and experimental setup

In this chapter we explain how we have designed and fabricated or setup the different units and components of our experiment. This includes resonator-quantum-dot hybrid device and the experimental setup used to perform the measurements. In a first part, we focus on the resonator-quantum-dot device, discussing its design, simulation, and fabrication. In a second part, we introduce the complete setup used in the experiment, including room-temperature part, cryogenic-temperature part and optical setup. Finally, we present basic characterization results on the optics and the test resonator sample.

7.1 Design of hybrid device of quantum dot and resonator

7.1.1 Semiconductor quantum dot

Substrate

The substrate used for hosting the quantum dot device in our experiment has a AlGaAs/GaAs heterostrucutre grown by molecular beam epitaxy (MBE) technique. The growths were performed on a 76 mm-diameter, single-side polished semi-insulating GaAs (100) wafer in National Research Council of Canada. Figure 7.1 shows the substrate structure after MBE growth. No dopants were introduced during the growth.

Design of electrostatic gates

The electrostatic gates involved in the operations of quantum dot devices can be categorized in three types according to their functions:

- **Accumulation gates:** create certain potential profile under bias to trap the charges of interest beneath and tune the number of charges in the dots.
- **Depletion gates:** deplete the charges in the unwanted regions, usually biased with opposite polarity compared to accumulation gates.
- **Barrier gates:** realize local fine-tuning of inter-dot or dot-reservoir barrier height.

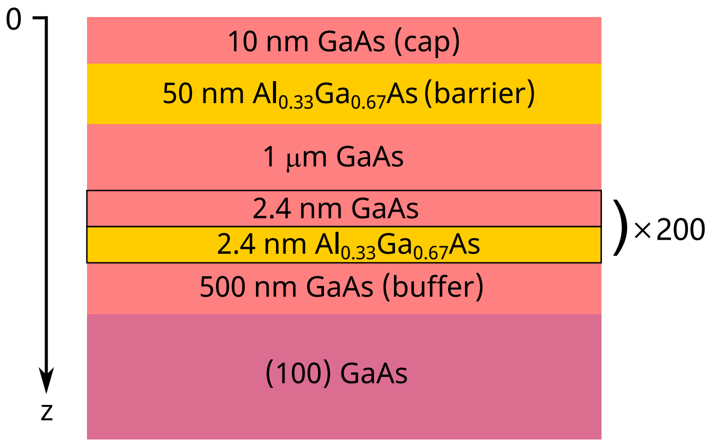

Figure 7.1: **Substrate structure for quantum dot device.** Above the (100) GaAs wafer (purple) are epitaxial $Al_{0.33}Ga_{0.67}As$ (yellow) and GaAs (red) layers grown by MBE.

In practice, one gate can influence another due to the spatially extended electric fields and their mutual coupling. Therefore the operation of quantum dots is a synergy of all the gates. For example, the accumulation gates can also change the barrier height while tuning the number of trapped charges. Adding barrier gates gain more degrees of freedom for control, but also introduces more constraints and device complexity for design and fabrication.

In order to implement the idea elaborated in Section 6.3, we have made two designs of three-gate double dot device, as shown in Figure 7.2. Both designs use two identical accumulation gates, formed by disks with a diameter d = 500 nm and narrow leads with width w_L for electrical connection. Note that the leads are represented by zero-width lines in the design to be created by line exposure in e-beam lithography (see fabrication Section 7.2) and their actual width w will be determined after the fabrication. The goal of this design is to maximize the ratio d/w_L so that charges are mainly accumulated below the disk and few charges or no charges are trapped below the leads. With the help of industrial process, vertical connection could be built to remove planar leads as an ultimate solution.

The two disks of accumulation gates are separated by a 100 nm gap whose distance determines the inter-dot barrier height at zero-bias. Between the two accumulation gates, we have made two possible choices of gate design. In design 1, a rectangular depletion gate is added in order to deplete the charges below the adjacent leads. In design 2, a barrier gate, with the same width of the leads of accumulation gates, is added to tune the inter-dot tunnel barrier height.

These designs allow us to work in the many-electron or many-hole regime (compared to reaching a single charge in the dot), which should be sufficient to demonstrate a proof-of-concept for detecting the charges generated from illumination.

Simulation

In order to obtain the potential profile generated by the designed gate layout, we performed simulation with electrostatic module in the finite-element analysis tool COMSOL Multiphysics. The software solves for the electrostatics of the geometric

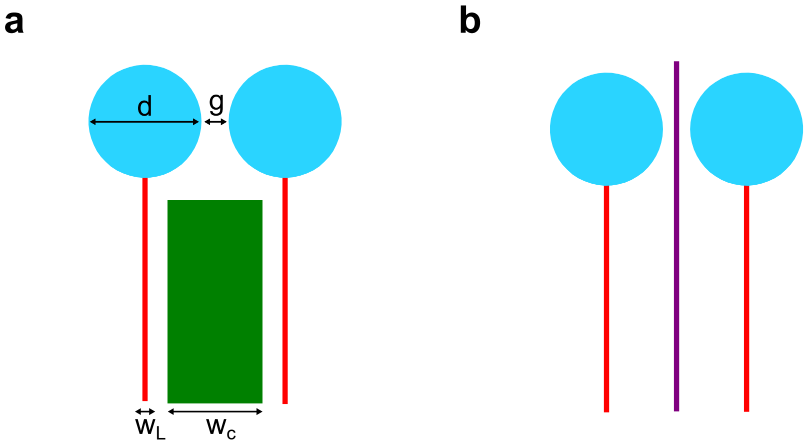

Figure 7.2: **Designs of gate layout for double dot device.** Double dot accumulation gates (blue) and their corresponding leads (red solid line), with a depletion gate (green) in between **(a)** or a barrier gate (purple) in between **(b)**.

model established in Figure 7.3a. Since we are only interested in the physics close to the heterointerface ($\sim$ 60 nm below the surface), we truncated the substrate at a depth of 2 μm below the surface. Applying -0.1 V on the left and right accumulation gate, and 0.5 V on the central gate, the simulated electric potential for the slice at a depth of 61 nm below the surface is shown in Figure 7.3b. In Figure 7.3c, we plot the electric potential across the double gate, where a double well profile is observed and the bottom of the well has a potential of -0.07 V. This result indicates that the lever arm α of the gate is approximately 0.07.

7.1.2 Superconducting resonator for addressing quantum dots

Design

In the proposed platform in Section 6.3, our intention is to use an undoped substrate without ohmic contacts to facilitate charge reservoirs and transport measurements. Therefore a superconducting resonator and cQED readout with microwave are necessary in this architecture. The superconducting resonator used to address quantum dots was designed as a coplanar waveguide (CPW) resonator, as discussed in Section 2.2.1. The goal is to have a planar geometry that is easy to fabricate on GaAs substrate, and to use the resonator fundamental mode to couple the charge electric dipoles within the quantum dots. These quantum dots are placed near the anti-nodes of the mode.

The choice of resonator geometric dimensions needs to satisfy our requirements for three principle resonator parameters: resonant frequency ω_0, impedance Z_0 and resonator linewidth κ. In the following, we will discuss our design considerations for these three parameters.

- **Resonant frequency**. For CPW resonator, the length of the central conductor determines the resonant frequency. The constraints for choosing the proper frequency in our experiment mainly come from the microwave electronic components. For example, the circulators used for noise isolation have a band-

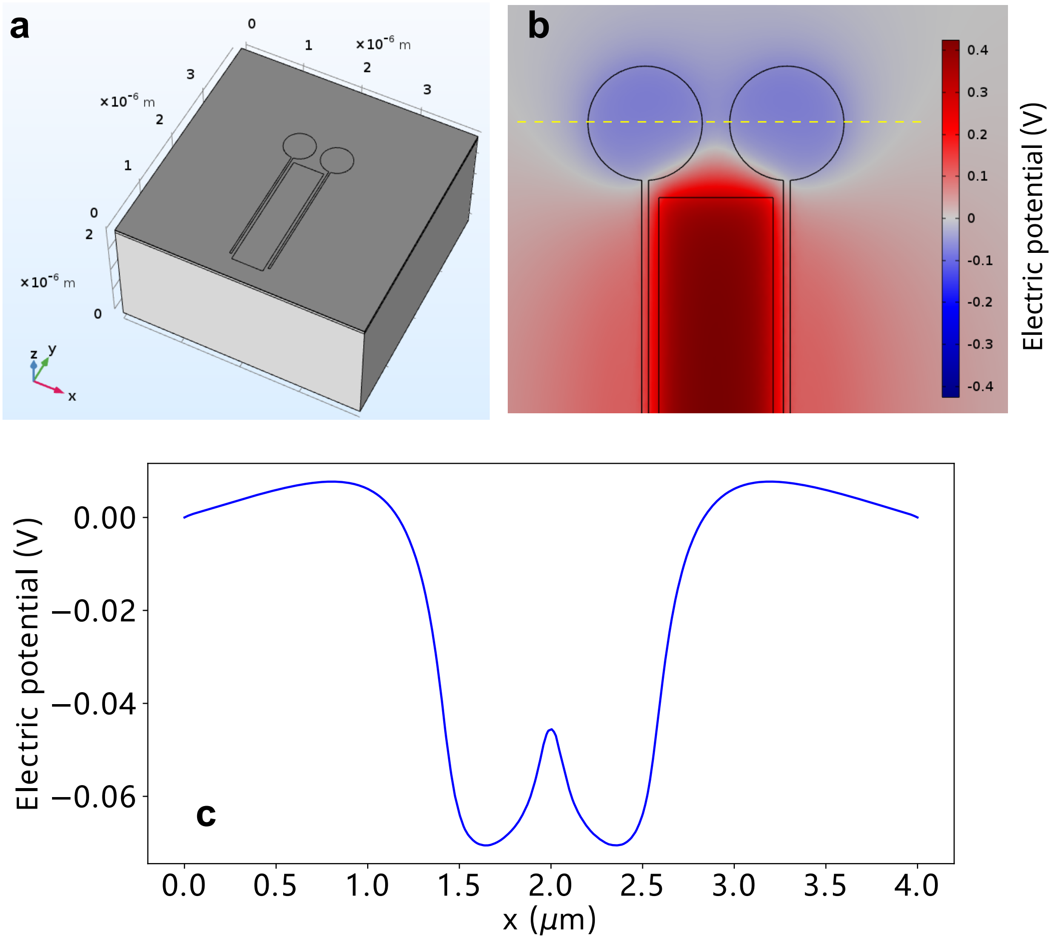

Figure 7.3: **Electrostatic simulation of gate design 1 in COMSOL.** **(a)** Geometric model in COMSOL. The heterostructure substrate is modeled by 3-layer stacks with thicknesses of GaAs(10 nm)/AlGaAl(50 nm)/GaAs(2 μm). The width of the gate lead is 30 nm. **(b)** Distribution of electric potential in the plane of 2-dimensional electron or hole gas (1 nm below the heterointerface and 61 nm below the surface), and the biases on the gates are: -0.1 V on the left and right gates, 0.5 V on the central gate. **(c)** Electric potential across the double gate along the yellow dashed line in panel **b**, showing a double well profile.

width of 4 to 8 GHz, which requires the designed resonator has a frequency in the same range.

- **Characteristic impedance**. Both commercial coaxial cables and transmission lines on printed circuit boards (PCB) used to wire the resonator chip to microwave lines typically have an impedance of 50 Ω. In order to ensure proper signal transmission, we choose to match this 50 Ω impedance in our resonator design. Note that while high impedance resonator can be used to enhance the electric dipole coupling between a resonator mode and a quantum system [10, 80, 86], the coplanar waveguide for external ports should have 50 Ω for impedance matching with the rest of the microwave setup.

- **Linewidth**. The total resonator linewidth is determined by the internal loss and external coupling to the input/output lines ($\kappa = \kappa_i + \kappa_c^{\text{in}} + \kappa_c^{\text{out}}$). The internal loss of a CPW resonator is mainly attributed to the fabrication and material system used, rather than the design parameters; while the external coupling rate is determined by the choice of the input/output capacitors. Working on transmission measurement, an asymmetric coupling capacitor design is preferable. In our case, we choose a larger output capacitance compared to the input one so that a significant proportion of signal will be transmitted out from the output port.

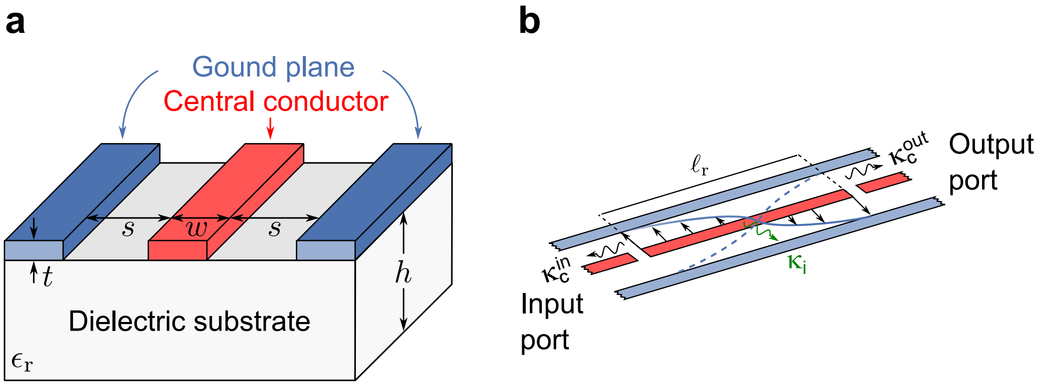

Figure 7.4: **Schematic representation with design parameters for a coplanar waveguide resonator.** **(a)** Cross-section of a CPW resonator composed of a central conductor (red) of width w spaced by a gap spacing s from the ground plane (blue). Both the central conductor and the ground plane have a thickness t. The dielectric substrate with a relative dielectric constant ϵ_r has a thickness h. **(b)** Schematic representation of a two-port half-wavelength CPW resonator of length ℓ_r capacitively coupled to input and output ports at rates κ_c^{in} and κ_c^{out}, respectively. The internal loss rate of the resonator is κ_i.

In terms of design, the resonator ω_0 and Z_0 are determined by the following geometric dimensions (see Figure 7.4): central conductor width w, total length of the resonator ℓ_r, spacing s of the gap between the central conductor and ground plane, thickness t of the conducting metal and thickness h of the dielectric substrate. The following part will establish the link between the geometric parameters and target design considerations.

The characteristic impedance Z_0 and angular frequency of the fundamental mode ω_0 of half-wavelength CPW resonator are given by [154]

$$Z_0 = \sqrt{\frac{L_g + L_k}{C}}, \tag{7.1}$$

$$\omega_0 = \frac{\pi}{\ell_r \sqrt{(L_g + L_k)C}}, \tag{7.2}$$

where L_g and L_k are geometric inductance and kinetic inductance per unit length, respectively, and C the capacitance per unit length. The total inductance and total capacitance are given by $\ell_r(L_g + L_k)$ and $\ell_r C$, respectively.

The capacitance and geometric inductance of the resonator can be expressed as

$$C = 4\epsilon_0\mu_0 \frac{K(k)}{K(k')}, \tag{7.3}$$

$$L_g = \frac{\mu_0}{4}\frac{K(k')}{K(k)}, \tag{7.4}$$

where $K(k)$ is the complete elliptic integral of the first kind defined as

$$K(k) \equiv \int_0^1 \mathrm{d}x \, \left[\left(1-x^2\right)^2 \left(1-(kx)^2\right)^2\right]^{-1/2}, \tag{7.5}$$

with $k = w/(w+2s)$ and $k' = \sqrt{1-k^2}$, determined by the dimensions of CPW resonator.

The kinetic inductance has the form

$$L_k = \mu_0 \frac{\lambda^2}{wt} g(w,s,t), \tag{7.6}$$

where λ is the penetration depth depending on the film thickness of the superconducting material and g(w,s,t) is a geometric filling factor written as

$$g(w,s,t) = \frac{1}{2k^2K^2(k)}\left[-k\ln\left(\frac{t}{4\,(w+2s)}\right) - \ln\left(\frac{t}{4w}\right) + \left(\frac{2\,(w+2)}{w+2s}\right)\ln\left(\frac{s}{w+s}\right)\right]. \tag{7.7}$$

Specifically, for our case of 20 nm thick niobium thin film, the penetration depth is $\lambda = 100$ nm [155]. We can define the kinetic inductance ratio by $\alpha = L_k/(L_g + L_k)$.

With all the equations introduced above, we can calculate ω_0 and Z_0 from geometric dimensions. To reach our design targets ($\omega_0/2\pi \sim 6.2\,\mathrm{GHz}$ and $Z_0 = 50\,\Omega$), we vary the gap spacing s and total resonator length ℓ_r while keeping the chosen width of central conductor $w = 14\,\mu\mathrm{m}$ as a constant. The input and output parameters for the calculation are summarized in Table 7.1 and Table 7.2 respectively.

Parameter	Symbol	SI unit	Design
Resonator angular frequency	ω_0	$2\pi\times$Hz	$2\pi \times 6.2 \times 10^9$
Resonator impedance	Z_0	Ω	50
Relative substrate dielectric constant	ϵ_r	–	12.9 (GaAs)
Width of the central conductor	w	m	14×10^{-6}
Thickness of the dielectric substrate	h	m	500×10^{-6}
Thickness of the superconducting film	t	m	20×10^{-9}
Penetration depth of the superconducting film	λ	m	100×10^{-9}

Table 7.1: **Input parameters of resonator.**

Parameter	Symbol	SI unit	Design
Gap spacing	s	m	4.3×10^{-6}
Resonator length	ℓ_r	m	7.298×10^{-3}
Kinetic inductance ratio	α	–	0.37

Table 7.2: **Output parameters of resonator.**

To make more efficient use of the surface area on chip in practice, we usually construct the resonator by meander segments and flat lines. The final design of the entire resonator is shown in Figure 7.5a.

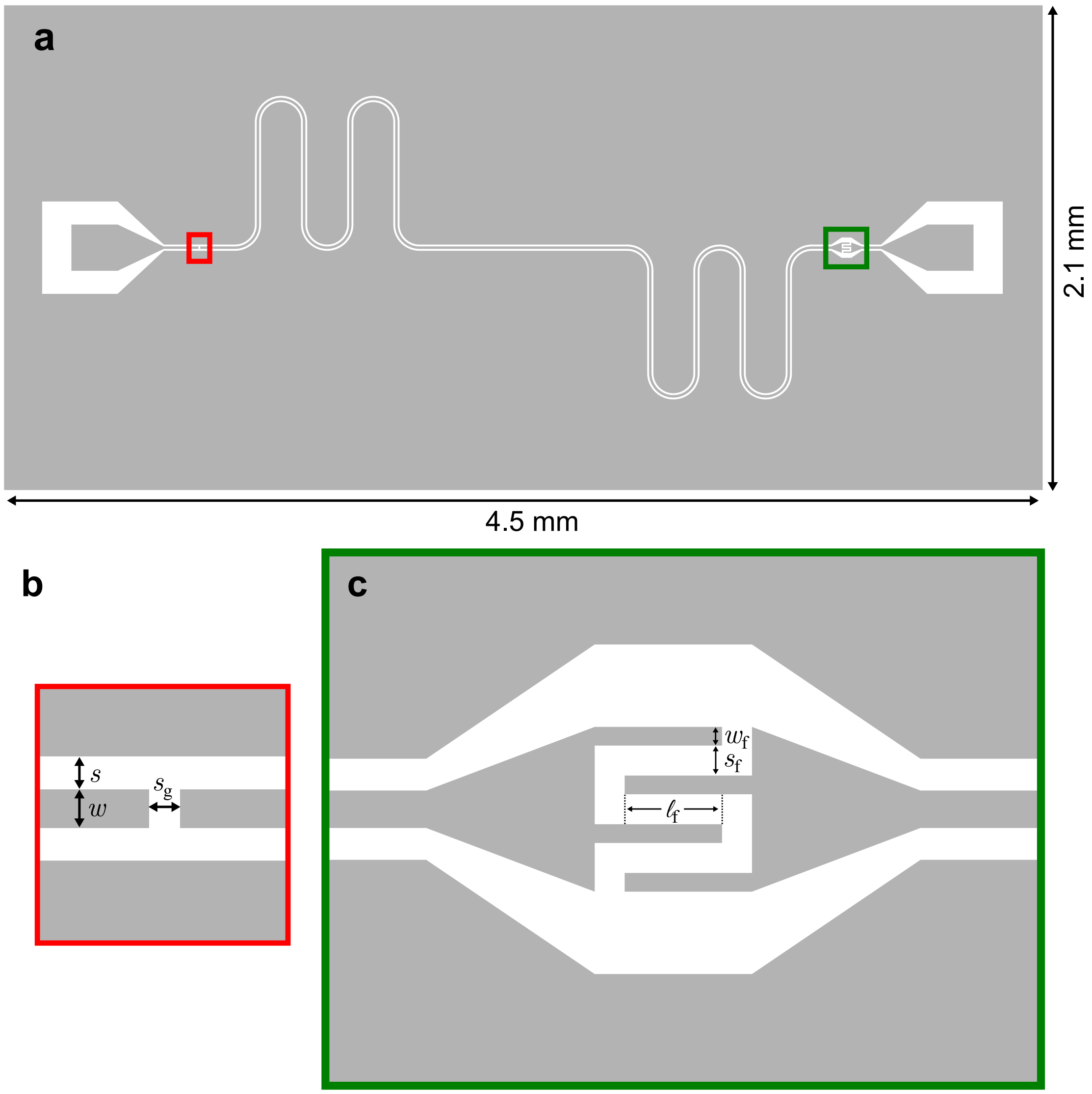

Figure 7.5: **Chip layout of the coplanar waveguide resonator design. (a)** Layout of the entire chip with an input port on the left and an output port on the right. **(b)** Zoom-in on the input capacitor, showing the gap s_g. **(c)** Zoom-in on the output interdigitated capacitor, showing the finger width w_f, spacing s_f and overlap length ℓ_f.

As for the coupling port, the external coupling rate is determined by the coupling capacitor as [156]

$$\kappa_c = \frac{2Z_0^2 C_c^2 \omega_0^3}{\pi}. \tag{7.8}$$

The asymmetric coupling is realized by choosing asymmetric capacitors. At the input side we use a simple gap with a spacing s_g (see Figure 7.5b); at the output side we use interdigitated finger capacitor to increase the coupling with corresponding design parameters: finger width w_f, spacing s_f and overlap length ℓ_f (see Figure 7.5).

Given the difficulty to find the analytical expression of coupling capacitance in terms of geometrical parameters, we rely on the electromagnetic simulation to determine the external coupling rate. Our targets are $\kappa_c^{\text{out}} : \kappa_c^{\text{in}} = 10 : 1$ with $\kappa_c^{\text{out}}/2\pi \sim 1$ MHz.

Finally, to compensate the discrepancy of dimension brought by fabrication (usually the feature size is enlarged due to over-exposure in lithography, see Section 7.2), we need to include the corrections in the design by increasing the gap size and reducing the metal width and length, so that the real dimensions are close to the expected values after fabrication, see Table 7.3. The layout shown in Figure 7.5 is proportional to the real dimension with corrections, which will be used as mask for fabrication. It should be noted that the corrected values in the design are approximations leading towards the desired post-fabrication values and the remaining uncertainties are within the tolerance of our experiment.

Parameter (unit μm)	Symbol	Expected value	Corrected value
Width of the central conductor	w	14	10
Gap spacing	s	4.3	8.5
Input capacitor gap	s_g	5	8
Finger width of output capacitor	w_f	9	5
Finger spacing of output capacitor	s_f	5	8
Finger overlap of output capacitor	ℓ_f	30	26

Table 7.3: **Design parameters with corrections for fabrication.**

Electromagnetic simulations

Similar to what has been done in Section 3.1.2, we use the eigenmode solver in HFSS to precisely find the frequency ω_0 and energy decay rate κ of the designed resonator. The full model is shown in Figure 7.6a, where the following 3 elements are included:

- A GaAs substrate chip ($4.7 \times 2.3 \times 0.5$ mm^3).
- The resonator on top of the GaAs chip, modeled with zero thickness. Its central conductor is assigned with a 2D impedance model: 0 resistance and $0.11\Omega/\square$ reactance (resulting from 2.8 pH/$\square$ at 6.2 GHz).
- A vacuum box enclosure has dimensions of $6.5 \times 5.5 \times 3$ mm^3. (not shown in Figure 7.6a)

The dielectric constant of GaAs used in the simulation is $\epsilon_r = 12.35 \pm 0.09$, which was obtained by extrapolating its temperature dependence to 0 K [157]. Note that all the submicron geometric objects (i.e. quantum dot gates) are removed from simulation to avoid possible meshing issues when simulating together small and large dimensions.

We then use HFSS to solve the eigenmodes of the system. The simulated fundamental mode of the CPW resonator is shown in Figure 7.6b. The magnitude of its electric field is plotted in logarithmic scale for 1 Joule of energy in the mode. Figure 7.6c and d show a magnified view of the input and output coupling capacitor, respectively. The maximized electric field can be observed at the anti-nodes. From the eigenmode study in HFSS, we obtain the resonant frequency $\omega_0/2\pi = 5.72\,\text{GHz}$ and total loss rate $\kappa/2\pi = 1.8\,\text{MHz}$ (quality factor = 3100) for the fundamental mode.

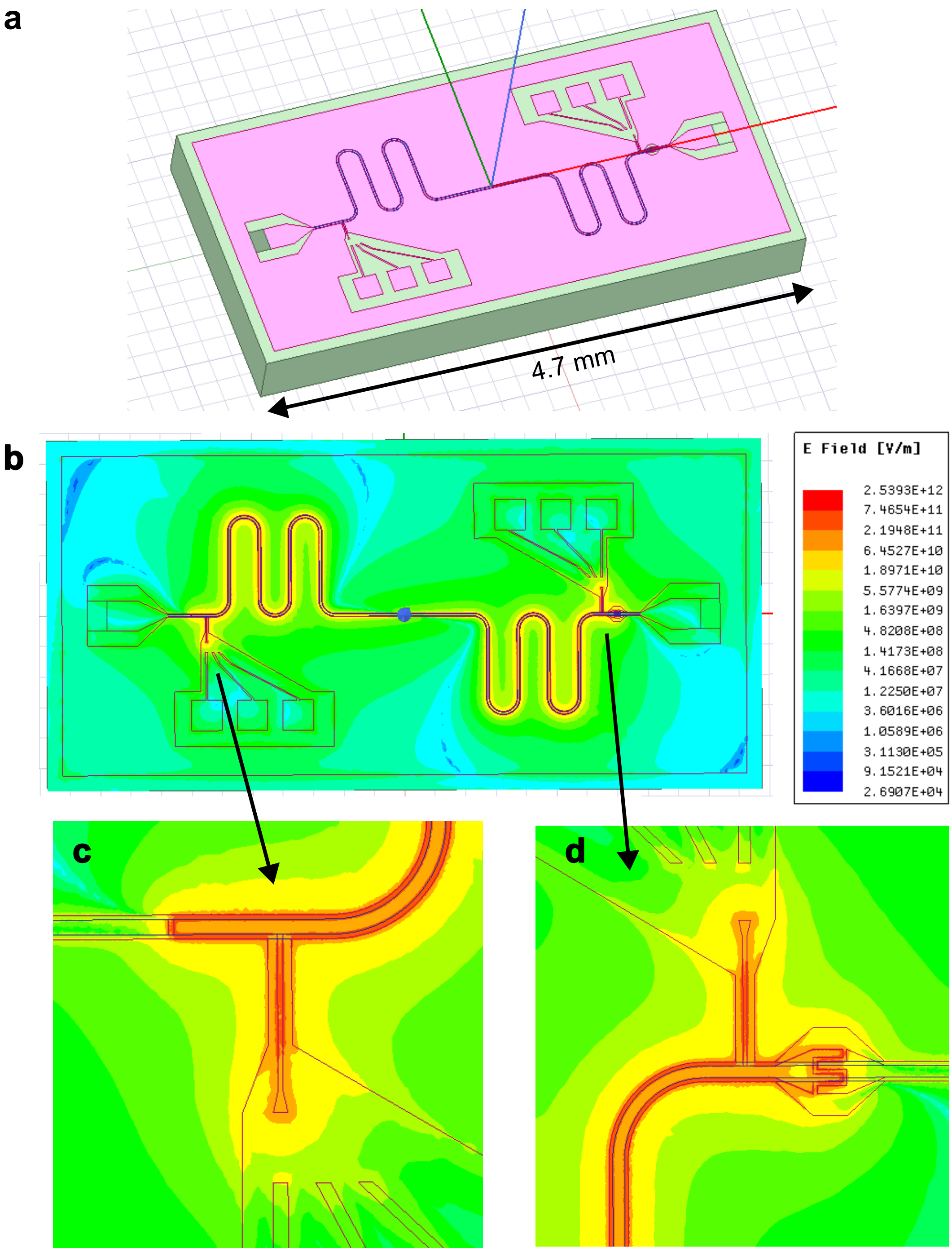

Figure 7.6: **HFSS simulation on $\lambda/2$ CPW resonator.** **(a)** HFSS geometric models of the GaAs substrate ($4.7 \times 2.3 \times 0.5\,\mathrm{mm}^3$) and the resonator created with zero thickness model on top of the GaAs chip. The submicron features of quantum gates are not included in this simulation. **(b)** Simulated electric field amplitude of the resonator fundamental mode in logarithmic scale (1 Joule applied in the mode). **(c)** Zoom-in on the input coupling capacitor. **(d)** Zoom-in on the output coupling capacitor.

7.1.3 Integration of quantum dot with resonator

Having separately discussed the designs of quantum dot gate layout and superconducting resonator, our next step is to integrate them onto the same substrate to create a hybrid device, which will enable us to implement the proposal introduced in Section 6.3.

Based on the resonator design in Figure 7.5, we have removed parts of the ground plane to accommodate the quantum dot gates, and extended the anti-nodes of the resonator near the right accumulation gate of the quantum dot, as depicted in Figure 7.7. The design parameters of the resonator and the quantum dot gates are the same as those discussed in Section 7.1.2 and Section 7.1.1. To increase redundancy and tolerance for potential failures during fabrication, wire bonding and sample mounting, we have placed two identical quantum dot devices on the same chip.

7.2 Fabrication of hybrid device

In this section, we discuss in detail the fabrication process for hybrid device and the encountered issues.

The proposed architecture discussed in Section 6.3 simplifies the fabrication process to three steps of lithography (two steps of optical lithography and one step of electron-beam lithography), compared to a similar reported hybrid cQED-DQD device on AlGaAs/GaAs substrate with five-step-lithography [158, 159], showing the advantage of this proposal.

The entire process flow and corresponding masks used for each lithography step is summarized in Figure 7.8, where two lithography steps create the quantum dot gates and resonator patterns (see Section 7.2.2 and Section 7.2.4), and one lithography step defines the mesa region (a remaining plateau region after etching away heterostructure elsewhere, see Section 7.2.3). With fast e-beam writing, it could be possible to further combine the gate and resonator fabrication in one step. We now give more details on each step.

7.2.1 Substrate preparation

Before fabrication, the wafer with 76 mm diameter is diced into small pieces (15 mm × 15 mm). The space on one piece is sufficient for placing ten chips described in Figure 7.7 with other specific test patterns. The arrangement of the entire layout is shown in Figure 7.9, where we have included two types of quantum dot gate designs in different chips introduced in Figure 7.2 (one with a square depletion gate and another one with a barrier gate).

In order to monitor the success of the fabrication process before mounting the sample, we have added two types of test patterns:

- Test the electrical connection of Au-Nb contact and test the continuity of Nb lines going down the 2 μm-high mesa plateau.
- Identical fine gate structures are created on the mesa plateau outside the resonator chip for the observation with scanning electron microscope.

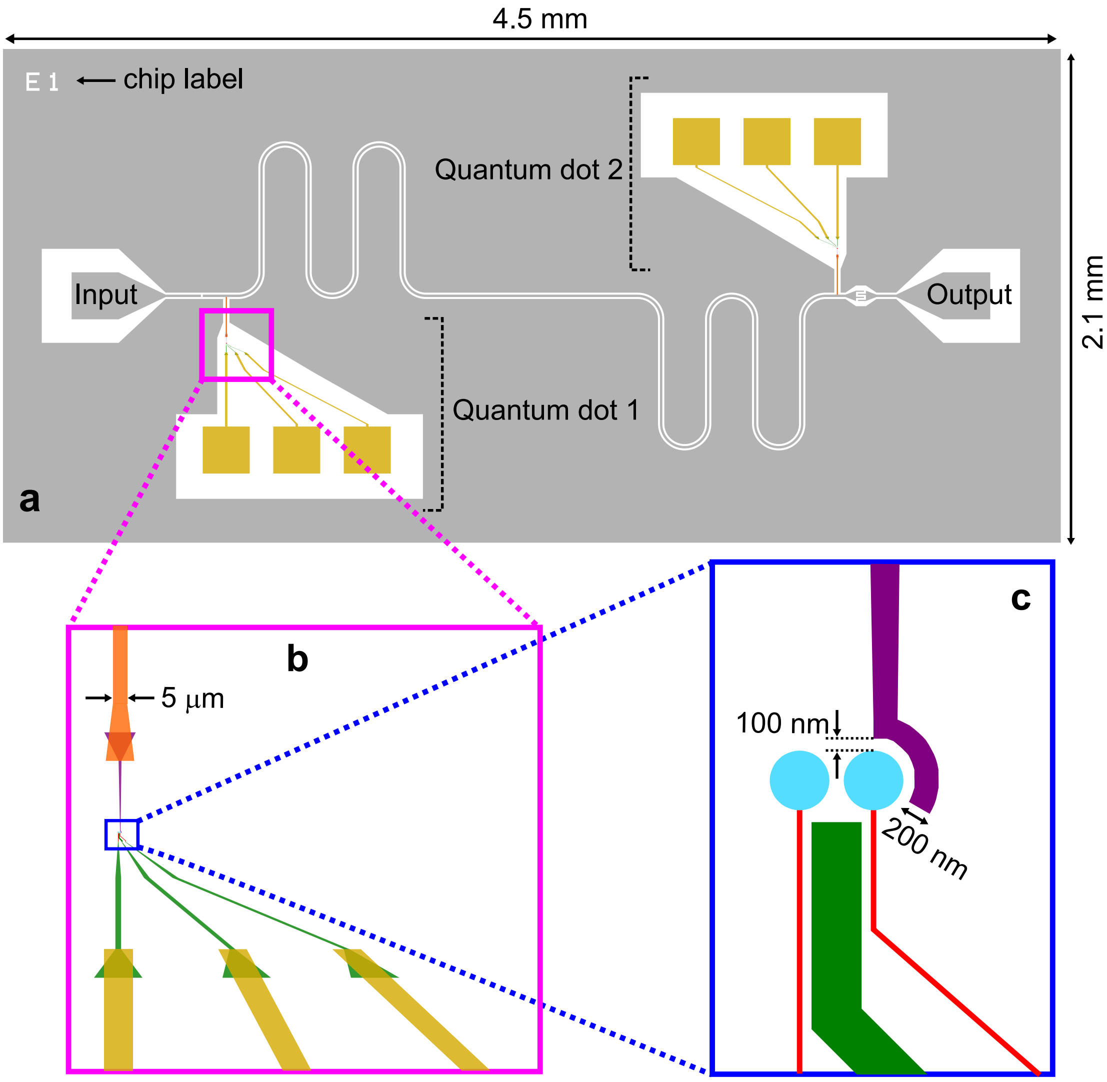

Figure 7.7: **Chip layout of hybrid device.** **(a)** The view of the entire chip layout composed of a CPW resonator and two identical double quantum dot devices placed near the anti-nodes of the resonator. Each double dot device has three electrostatic gates extended towards the chip edge with corresponding pads (yellow) for wire bonding. The resonator design parameters are the same as discussed in Section 7.1.2. **(b)** Zoom-in view on the region of quantum dot 1. The anti-node of the resonator is extended as a $5\,\mu$m-wide wire (orange) to approach the dot accumulation gate. **(c)** Zoom-in on the nanoscale dot gates. The 200 nm-wide lead from the resonator (purple) is placed near the right dot accumulation gate with a gap spacing 100 nm. The quantum dot design parameters are the same as discussed in Section 7.1.1.

At the beginning of the process, we clean the substrate in acetone and isopropanol (IPA) solution with ultrasonic and then it is ready for the first step of e-beam lithography.

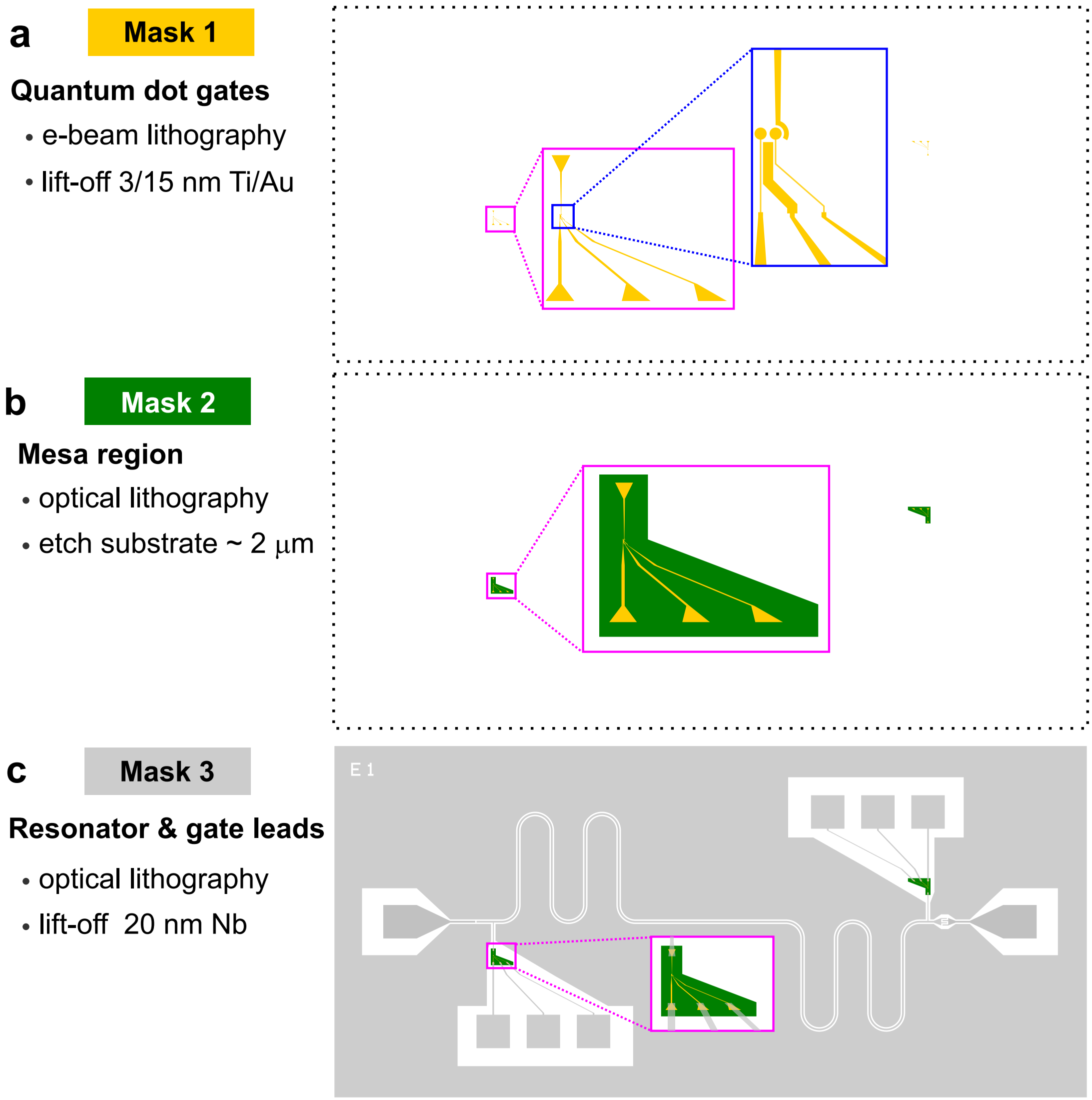

Figure 7.8: **Fabrication process flow and corresponding masks.** **(a)** The mask pattern (yellow) of the first step for fabricating Ti/Au (3/15 nm thick) layer as the quantum dot gates through e-beam lithography, evaporation and lift-off. Inset: zoom-in on the nanoscale dot gates. **(b)** The mask pattern (green) of the second step for defining the mesa region (the untouched area after wet etching) with optical lithography. The region outside the green box is etched by about $\sim 2\ \mu$m. Inset: zoom-in on the mesa region. **(c)** The mask pattern (gray) of the third step for fabricating Nb resonator and leads (20 nm thick) with optical lithography, sputtering and lift-off. Inset: zoom-in on the mesa region, showing the overlap between Nb and Au layer.

7.2.2 Mask 1 - Fine gate structure

To fabricate the nanoscale fine gate structures, the e-beam lithography is used in this step. The metal pattern, Ti/Au (3/15 nm) thin film in our case, can be created by two different approaches: lift-off or etching. In the former approach, the metal is deposited only in the desired place; while in the latter one, the metal is deposited on the whole substrate and etched away in the regions where it is not needed. The dry

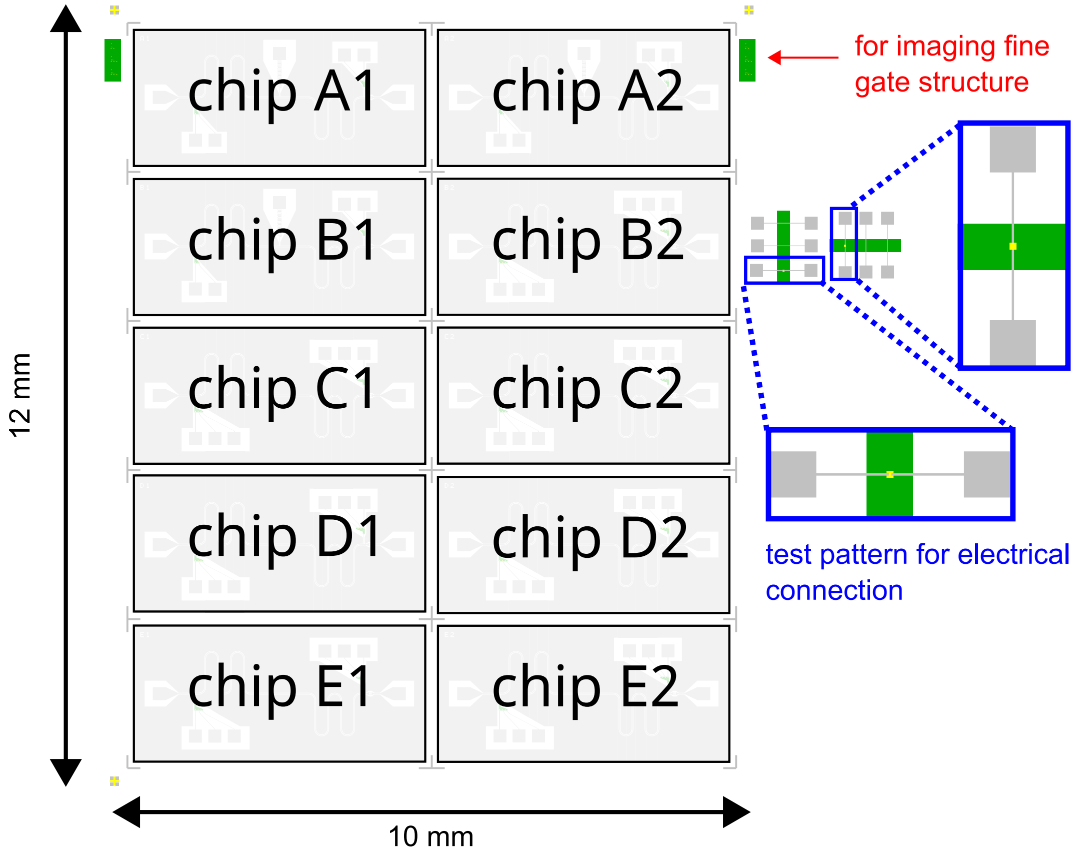

Figure 7.9: The arrangement of chips on a diced substrate (15 mm×15 mm), including test patterns for electrical connection (blue) and imaging fine gate structure (red).

etching technique with plasma is capable of reaching smaller feature size compared to lift-off, but is more brutal for the fragile AlGaAs/GaAs substrate [160]. Since we want to minimize the plasma damage on the heterostructure during fabrication, we choose the lift-off process instead of etching. In our design, two strategies are employed to achieve the requirement of narrow gate wires with width less than 50 nm and dense structures:

- Using single thin layer e-beam resist instead of conventional bi-layer resists for lift-off.
- Creating the narrow leads by assigning line dose to zero-width line-shape patterns in the design. This is in contrast to the typical e-beam patterns of using rectangles with area dose.

The e-beam resist used in this step is a high-resolution and high-contrast resist called AR-P 6200.04 (CSAR 6200.04). After spin-coating with a speed of 2000 rpm and baking on the hot plate at 150 °C for 1 min, a single resist layer with a thickness of 82 ± 3 nm was obtained. Then the sample was mounted in a RAITH-150-Two e-beam writer. The lithography was performed with 10 nm step size under the smallest aperture (10 μm and measured current 0.017 nA) with the dose allocation shown in Figure 7.10. The writing for all the gate structures and alignment marks takes about 60 min.

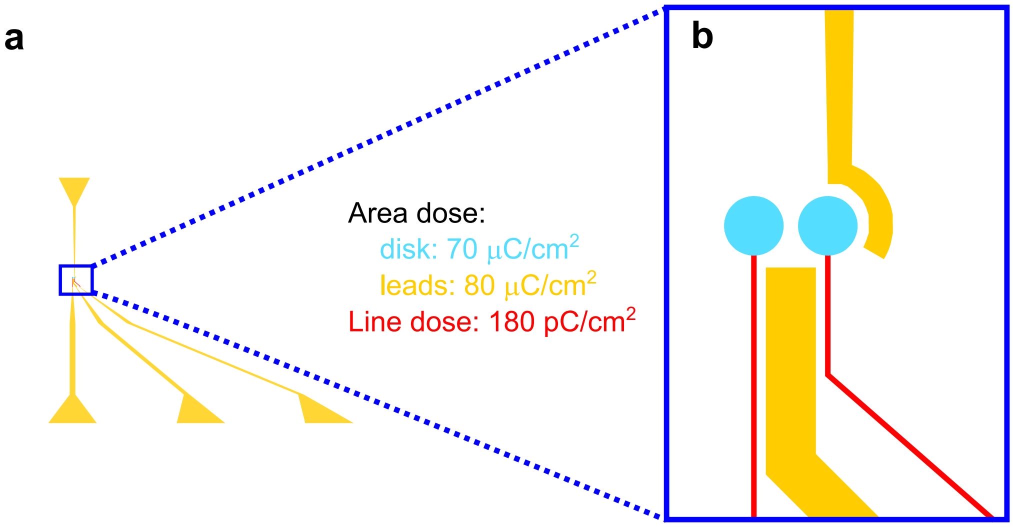

Figure 7.10: **Dose allocation in e-beam lithography for fabricating fine gate structures. (a)** The pattern sent for exposure in e-beam writter. **(b)** Zoom-in on the central region of fine gate structure. The color represents the associated dose in exposure with electron beam: 70 μC/cm^2 area dose for the gate disks (blue), 80 μC/cm^2 area dose for the depletion gate, extended resonator parts and larger wire leads (yellow), and 180 pC/cm line dose for the narrow lines connecting the circular gates and larger leads (red).

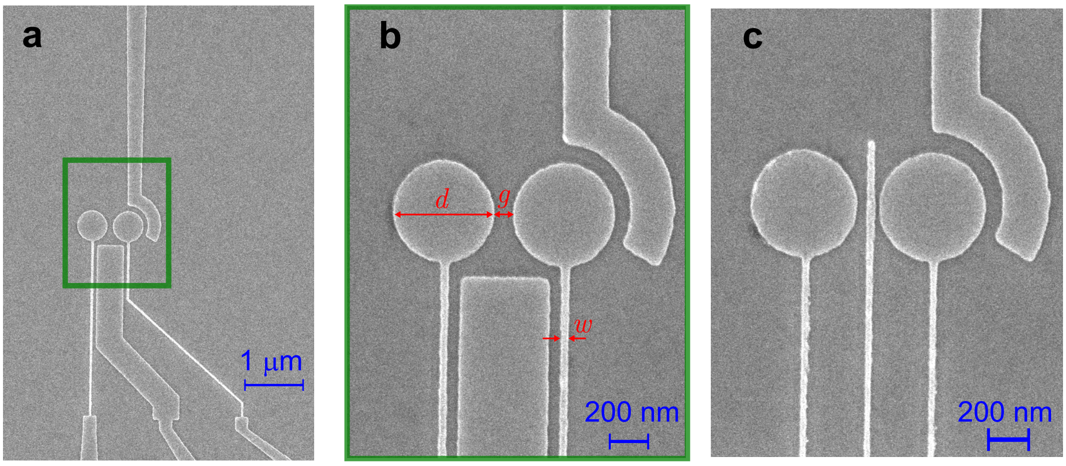

Figure 7.11: **Scanning electron micrographs of the fine gate structures. (a)** Design 1: two accumulation gates, one central depletion gate and one floating gate connected to the resonator. **(b)** Zoom-in on central part of **a**. The measured critical dimensions are: $d = 506$ nm, $g = 93$ nm and $w = 45$ nm. **(c)** Design 2: two accumulation gates, one central barrier gate and one floating gate connected to the resonator.

After the exposure, the development was done in o-Xylene solution for 60 s followed by rinsing successively 30 s in IPA and 30 s in water. Then the sample was put in oxygen plasma asher at 50 W for 30 s to remove the resist residual on the exposed region. The metal deposition of Ti/Au (3/15 nm) was realized by e-beam evaporation in an ultra-high vacuum chamber of Plassys evaporator. The Ti layer is added to enhance the adhesion of Au to the substrate. The lift-off of metal layers was done in hot remover 1165 solution (60 °C) for two-hour immersion followed by rincing in acetone and IPA, and then the sample is ready for the next step.

The images taken with a scanning electron microscope (see Figure 7.11) show the fine gate structures after the e-beam lithography. The 45 nm wide wire extends for 3 μm long and the gap spacing between two accumulation gates is about 93 nm. Figure 7.11c shows the results of another design, where a barrier control is placed in between the circular gates. The difference of gap spacing between the left and the right is possibly due to the spatial drift of the beam during writing or bending of the resist. This process is reproducible with a yield above 90 %.

7.2.3 Mask 2 - Mesa fabrication

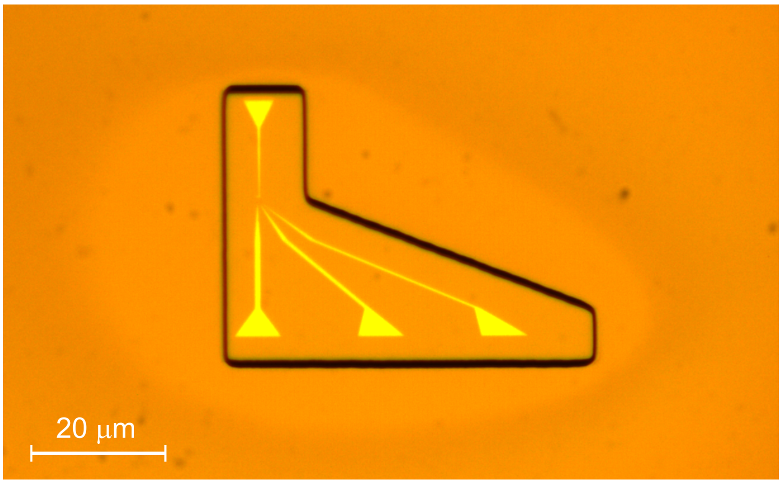

Figure 7.12: Optical micrograph of the sample after mesa fabrication.

Since the charges trapped at the interface of AlGaAs/GaAs heterostructure can move freely in the plane of the interface, they will respond to the oscillating electric field of the resonator and therefore contribute to the resistive loss. It is favorable to etch away the heterostructure below the resonator. A "mesa" defines the region where the heterostructure is kept, typically the region around the electrostatic gates ranging from hundreds of nanometers to a few microns.

The smallest chosen feature size of mesa region in our design is around $\sim 15\,\mu$m and is thus processed with optical lithography. The sample spin-coated with $\sim 1.2\mu$m thick photoresist AZ1512 was exposed with a maskless ultraviolet lithography machine and developed in MF319. We then used diluted Piranha solution (98% H_2SO_4:30% H_2O_2:H_2O=3:1:100) to etch the AlGaAs/GaAs chip for 3 minutes, where a height of $\sim$2.2 μm was obtained. The mesa structure is shown in Figure 7.12. It is noticeable in the image that the top and bottom edges of mesa have different profiles compared to the ones at the left and right. This phenomenon is related to the anisotropic wet etching profile on GaAs and is particularly important concerning the design and process after. We will discuss this in Section 7.2.5.

7.2.4 Mask 3 - Resonator and gate leads

This step introduces patterned Nb layer with optical lithography followed by lift-off, which forms the superconducting resonator and makes the contact with the fabricated Au gates on the mesa. The lithography was performed on the AZ1512/LOR bilayer of resist. After the exposure and development, 20 nm-thick Nb thin film is sputtered followed by lift-off.

After dicing, the chip is ready for mounting in the PCB and wire bonding.

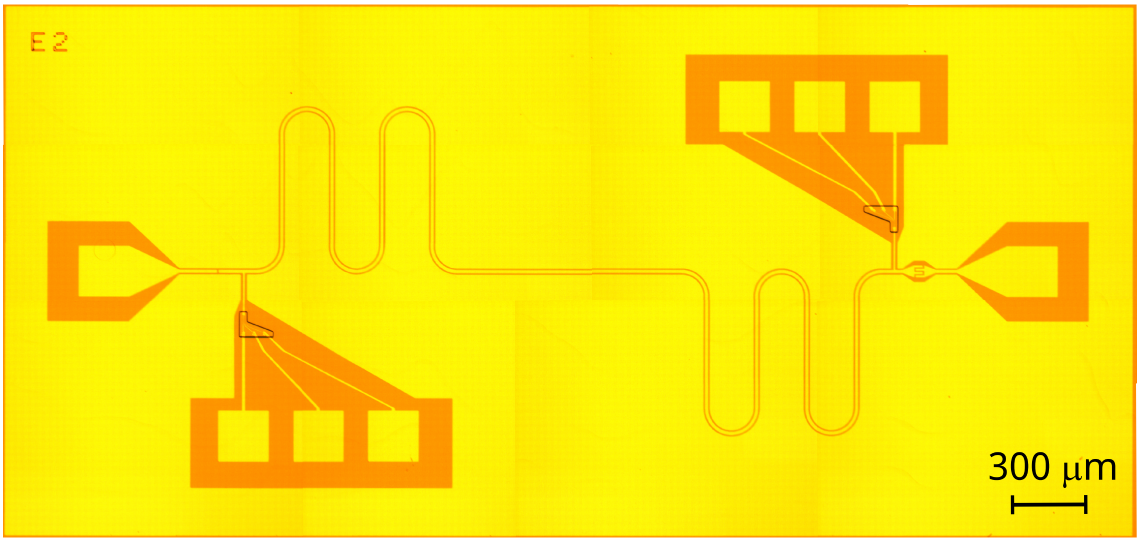

Figure 7.13: Optical micrograph of the hybrid device chip after all the fabrication processes.

7.2.5 Practical issues

Etching profile of mesa

We use diluted Piranha solution (98% H_2SO_4:30% H_2O_2:H_2O=3:1:100) to etch AlGaAs/GaAs substrate. It should be noted that the wet etching on (100) GaAs is highly anisotropic, due to the polar nature of the GaAs lattice [162, 163]. According to the crystal orientation, etching on the (100) chip surface can lead to two different edge profiles along the respective [110] and [$1\bar{1}0$] directions ("V" shape or "dovetail" shape), as shown in the example of Figure 7.14a [161]. This anisotropic feature, depending also on the chosen etchant, poses constraints on the layout design and interconnection of metal in subsequent processes, as the next metal layer used to establish contact with the already fabricated gates must have smooth transition down the mesa plateau.

However, it is important to note that the abrupt edge created along the [$1\bar{1}0$] direction can lead to discontinuity in the metal wires, while the shallow slope along another perpendicular direction is suitable for placing metal thin films. Therefore, before processing the real sample, it is necessary to test the etching profile for AlGaAs/GaAs chip with diluted Piranha solution and make the extension of gate wires along the correct direction.

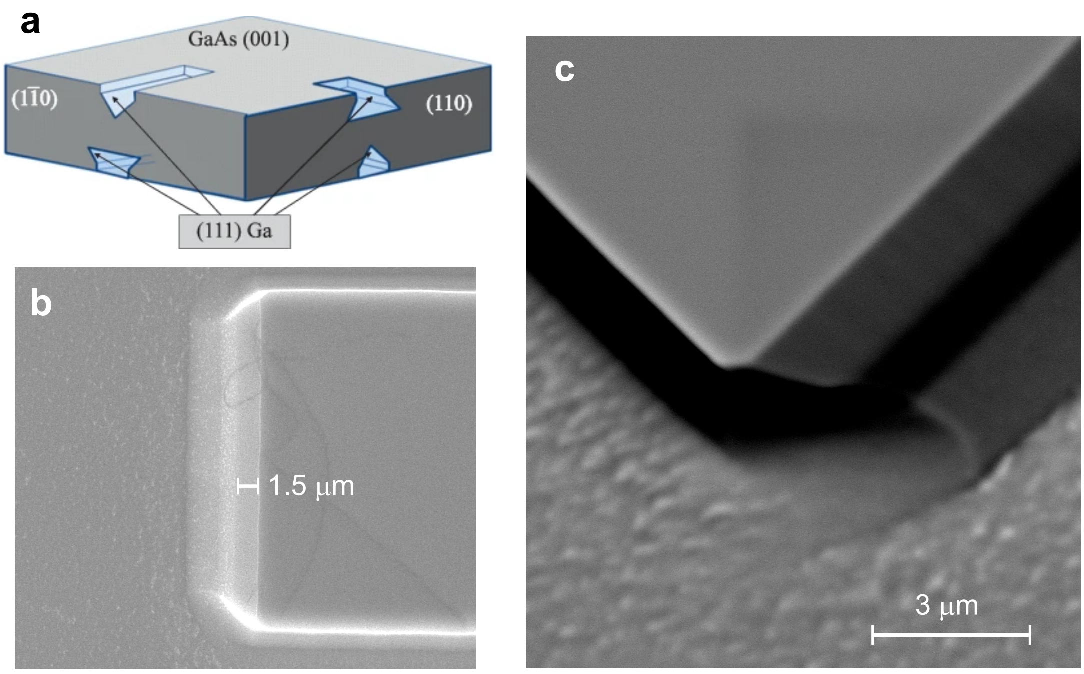

Figure 7.14: **Etching profile of diluted Piranha on AlGaAs/GaAs. (a)** Schematic representation of structures in the direction [110] and $[1\bar{1}0]$ after etching on the (100) GaAs surface [161]. **(b)** Top view of micrograph from scanning electron microscope, showing the etched structure from a rectangular mask on the AlGaAs/GaAs substrate of Figure 7.1. The slope on the horizontal direction has an angle of arctan(1/1.5) $\sim 33°$ while the edge along the perpendicular direction is abrupt. **(c)** Tilted view of micrograph from electron microscope showing the abrupt edge of the etching profile.

7.3 Experimental setup

7.3.1 Sample assembly

After the fabrication, the sample chip of the hybrid device was glued onto a printed circuit board (PCB) with GE Varnish. Aluminum wires were then used to bond the Nb pads on the sample to the Au pads on the PCB. In our design, there are 6 DC lines and 2 RF lines to bond. In addition, the ground plane of the chip was also bonded to the PCB with 6 to 10 bonds on each side, see Figure 7.15.

During the wire bonding and sample mounting, all the DC ports are connected together to PCB ground plane to maintain the same electrostatic potential for the protection from electrostatic discharge (ESD), which can break the fragile quantum dot gates. Once the sample holder is mounted to the dilution refrigerator with all the input DC lines connected to the lab common ground, the piece used to link all the DC lines can then be removed.

The copper-made cover for the PCB was assembled with a frame on top to hold a collimator Figure 7.16a, which turns the input light from the fiber to collimated light and project it on the surface of the cover. As shown in Figure 7.16b,c, there are two tiny holes (diameter 0.3 mm) drilled through the cover (collimator in absence). The light from the collimator can pass through to reach the semiconductor substrate.

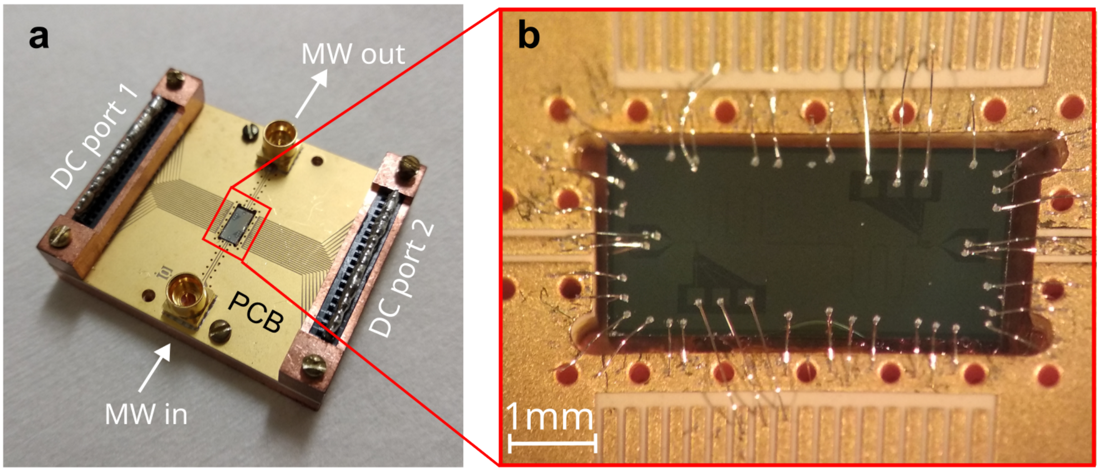

Figure 7.15: **Photos of the sample chip on a PCB after wire bonding.** **(a)** The PCB photo with sample chip at the center, consisting of 2×18 pins DC ports and 2 microwave ports. **(b)** Image from optical microscope showing the aluminum bonding wires connecting the pads on the sample to the gold pads on the PCB.

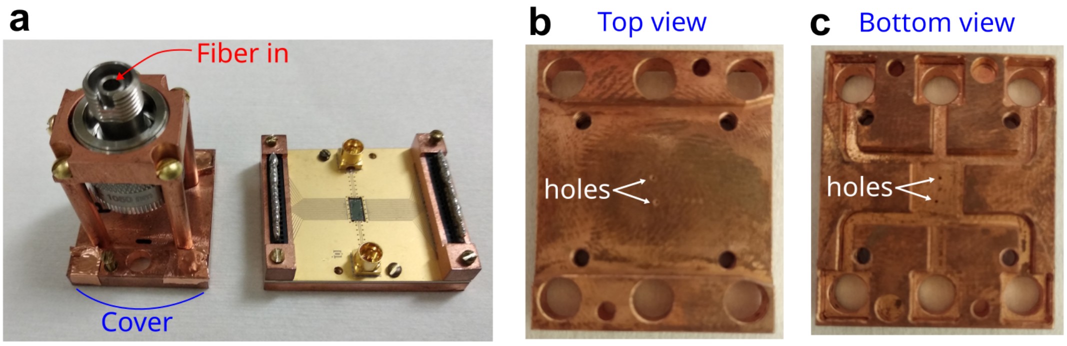

Figure 7.16: **Sample holder of the hybrid device.** **(a)** PCB and its cover assembled with a collimator on top to generate collimated light from a fiber input. **(b,c)** Photos of cover for PCB and sample holder, showing the top view (b) and bottom view (c) of the copper piece. Two holes with a diameter of 0.3 mm are drilled through the cover to let the infrared light from the collimator outside pass through and project onto the quantum dot regions of the chip.

The position of the holes are roughly above the mesa region of the chip.

7.3.2 Low-temperature electrical setup

Once the sample holder is closed with the cover, we mount it to the bottom of a long-extended copper stick (“cold finger”), which is attached to the mixing chamber plate of the dilution refrigerator. The cold finger and mixing chamber plate will reach a base temperature of 10 mK when the refrigerator is cold, see Figure 7.17.

The lines from outside the refrigerator go through several stages of plates with different temperatures to reach the mixing chamber stage at 10 mK. Figure 7.18 shows all the components and wiring used in each stage, along with the associated temperature.

The microwave signal is sent through line number 1 in the figure. This line

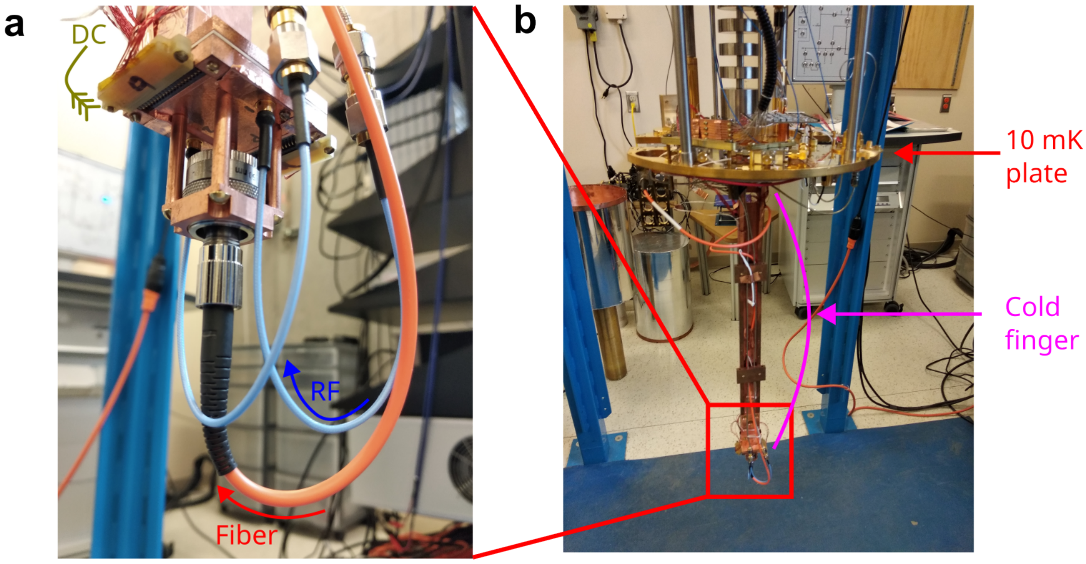

Figure 7.17: **Sample holder mounted in a dilution refrigerator.** **(a)** The complete sample holder (PCB and cover with collimator) is mounted to the bottom of a long extended copper-made stick called "cold finger". The input fiber (red), RF line (blue) and DC lines (olive color) are indicated in the figure. **(b)** The cold finger is attached to the mix chamber plate of a dilution refrigerator. When it cools down to base temperature, the plate and cold finger should reach 10 mK.

is heavily attenuated ($\sim$ 61 dB) to optimize its thermalization and thus reduces thermal noise. The signal sent to the sample is partially reflected from the same port, but most of it will be transmitted to port 2 due to the asymmetric coupling capacitor on the sample (see Section 7.1.2). The transmitted signal propagates to a HEMT amplifier at 4 K and reaches room temperature through line number 2. Between the HEMT and output port of the sample, two circulators with the third port terminated by 50 Ω load and a low-pass filter are added to isolate the sample from the noise of the amplifier.

As for the six DC ports, low-pass filters with cut-off frequency of 10 Hz are added in the lines at 10 mK plate. The cables are connected with a break-out box at room temperature.

The infrared light reaching the sample is provided by a laser through an optical fiber. A collimator is used at 10 mK stage to tune the beam shape.

7.3.3 Room-temperature electrical setup

The room-temperature part of the setup (above the 50 K dilution refrigerator frame in Figure 7.18) uses three types of instruments: a vector network analyser (VNA), source measure units (SMU) and an infrared laser.

The VNA measures the microwave transmission coefficient S_{21} with ports 1 and 2 in the figure, from which we probe the resonator response in frequency domain. The SMUs are used as sources or measurement units for the current or voltage in the given lines. In the experiment, the voltage biases on the electrostatic gates of the sample are provided by SMUs. The laser used in this experiment is a 785 nm diode-laser from Integrated Optics. More details will be given on the characterization of

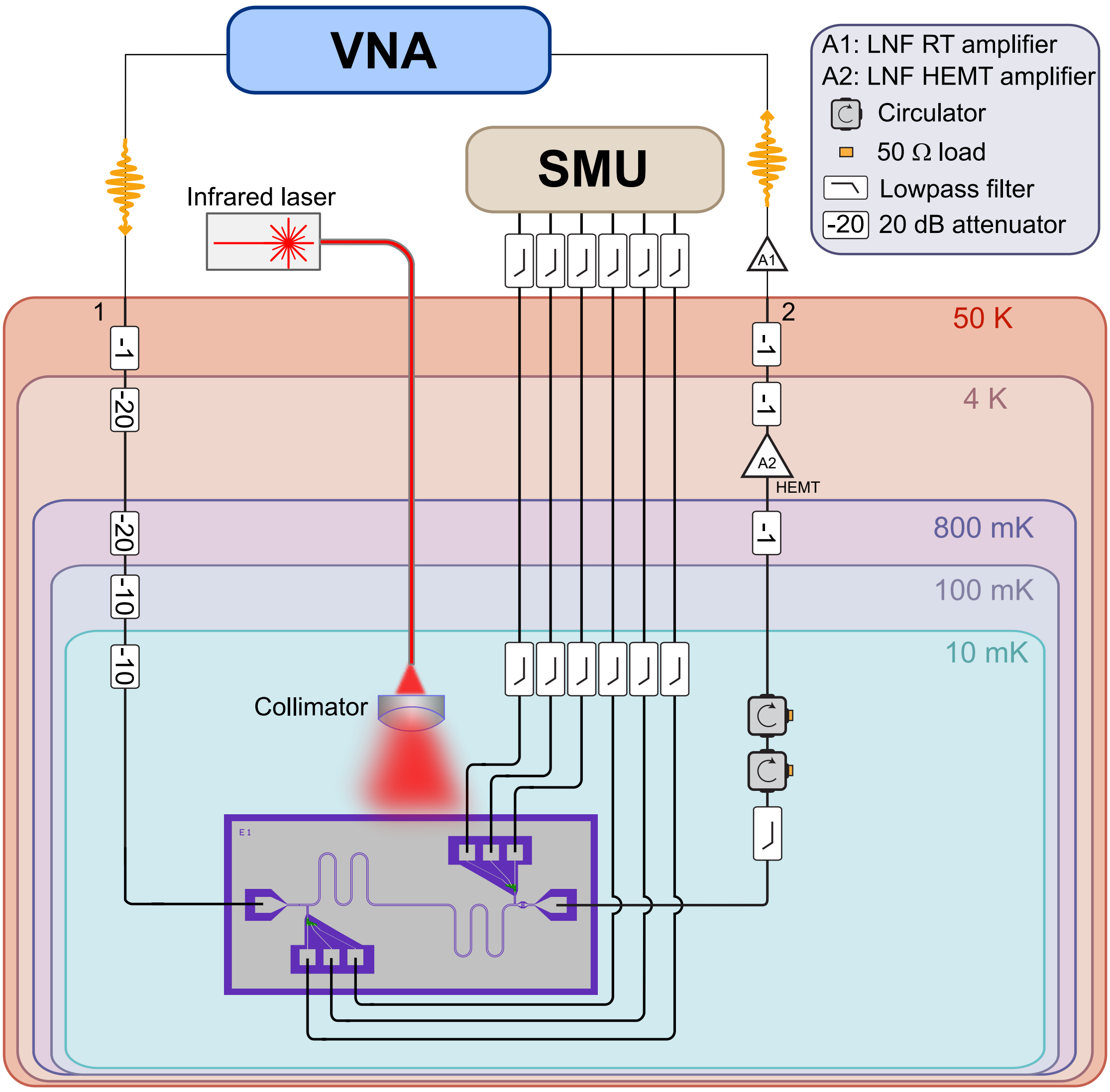

Figure 7.18: **Schematic of the setup**. Wiring and all the components used at cryogenic temperature and room temperature.

optical setup in the next section.

7.3.4 Optical setup

The wavelength of the laser ($\lambda = 785$ nm) is chosen between the bandgaps of GaAs and $Al_{0.33}Ga_{0.67}As$ at 10 mK, such that the optical carriers will only be generated in the GaAs instead of AlGaAs, to avoid the low-mobility carriers appearing in the parallel channel (AlGaAs) [164, 165].

The output light from the laser is coupled to a fiber and finally reaches the adjustable collimator at the end of the fiber. The collimator is installed on the sample holder (see Figure 7.19a) and is set at the mode with maximum allowed divergence in the component. The light exiting the fiber is collimated into a divergent beam and projected onto the surface of the sample holder, as shown in Figure 7.19b. Two tiny holes created on the cover will let the light pass through and reach the semiconductor substrate.

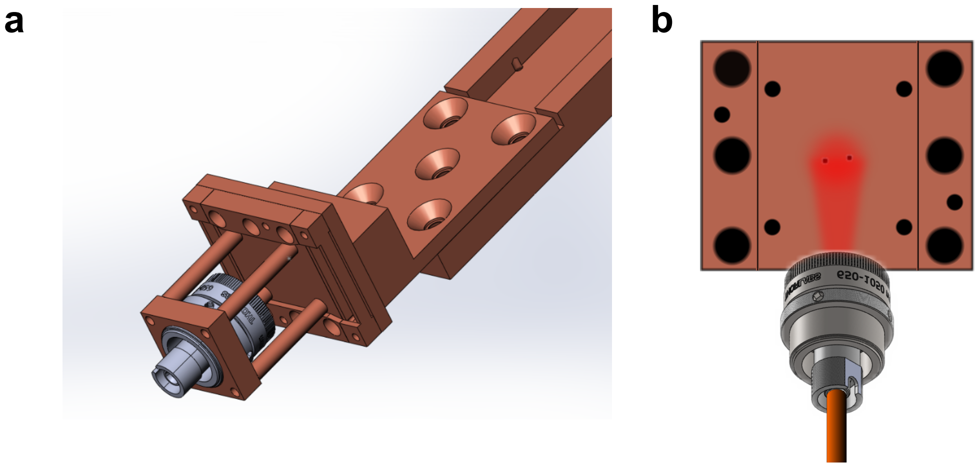

Figure 7.19: **Schematic of installed collimator with sample holder and divergent light beam.** **(a)** Schematic of sample holder model in SolidWorks, showing the collimator assembled in the frame, sample holder for PCB and bottom part of the cold finger. **(b)** Schematic of light beam given by collimator, showing the projection of light onto the holes at the central part of PCB cover.

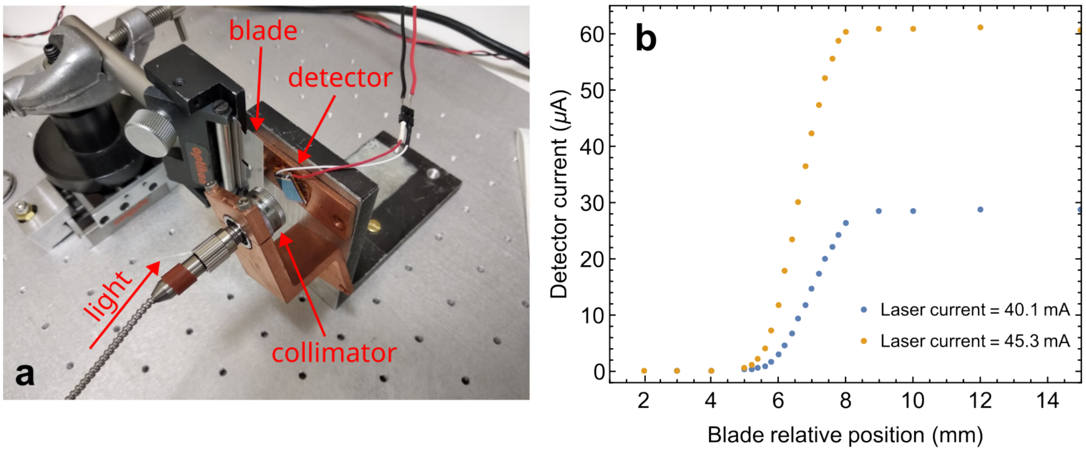

Figure 7.20: **Characterization of the beam spot in front of the PCB cover.** **(a)** Setup for characterizing the beam spot. A position-adjustable blade is placed between the collimator and the optical detector. **(b)** Measured detector current as a function of blade relative position and laser power (laser current).

Before doing quantum dot experiment with this setup, we need to characterize the spot size of the beam at the front and backside of the PCB cover, and to obtain the ultimate photon flux after passing through the holes on the cover. This goal is achieved by using a photo diode (as an optical detector) in the path of the beam and tuning the position of a razor blade placed between the detector and collimator, as shown in the setup of Figure 7.20a. The position of the blade is adjustable so that it can be tuned from blocking the beam to completely open. Measuring the photon current in the detector caused by the light gives the shape of the beam spot in the horizontal direction. When the beam is blocked by the blade, the current in the photo diode is at the background level (contribution from dark current and residual light in the environment).

We have performed the same measurements for two different laser powers (with recorded laser diode current) and the results are shown in Figure 7.20b. When the relative positon of the blade is below 5 mm, the beam is completely blocked and the detector only measures the background current. Between 5 and 8 mm, the beam is partially transmitted and received by the detector. The detector currents show a continuous change as a function of the position. Above 8 mm, the blade no longer blocks the beam. The measurements with two different photon fluxes demonstrate similar results regarding the spot size, except the doubled detector current observed when the laser power is higher. The diameter of the beam spot is roughly 3 mm at the distance of 3 mm away from collimator, which is consistent with the specifications of the component.

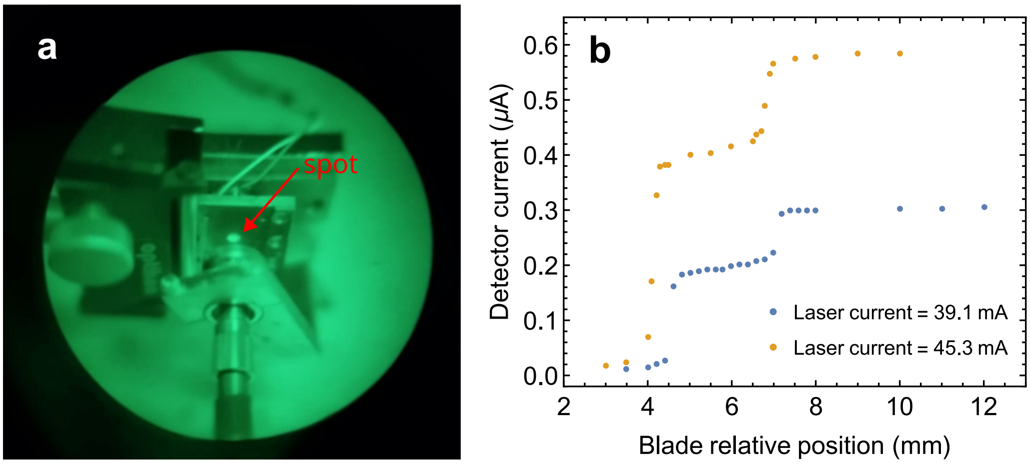

Figure 7.21: **Characterization of the beam spot behind the PCB cover. (a)** Image of the setup through an infrared camera, where the beam spot is “visible” at the center of the PCB cover. **(b)** Measured detector current as a function of blade relative position and laser power (laser current).

We then characterize the beam reaching the backside of the PCB cover after passing through the holes. In this measurement, the detector is placed behind the cover and aligned with the holes on it. The distance between the cover and the collimator is adjusted to $\sim$ 10 mm in order to approach the real spacing when installed in the frame shown in Figure 7.19a. The blade is 3 mm away from the collimator. The photo of the setup through an infrared camera can be seen in Figure 7.21a, where the spot is adjusted to the center of the cover. Using the same method, we measure the detector current while adjusting the blade position and the results are shown in Figure 7.21b. Compared to the gradual change of detector current shown in Figure 7.20b, here the current changes within a similar range of 3 mm but shows a two-step abrupt jump. We attribute this observation to the blockage of holes during the movement of the blade. It should also be noted that the measured detector current behind the holes is reduced by a factor of nearly 100 under a similar laser power.

In the end, it is of interest to test the beam generated with the lowest possible diode current required to switch on the laser, which corresponds to the lowest achievable photon flux with this laser setup (without optical attenuators). We mea-

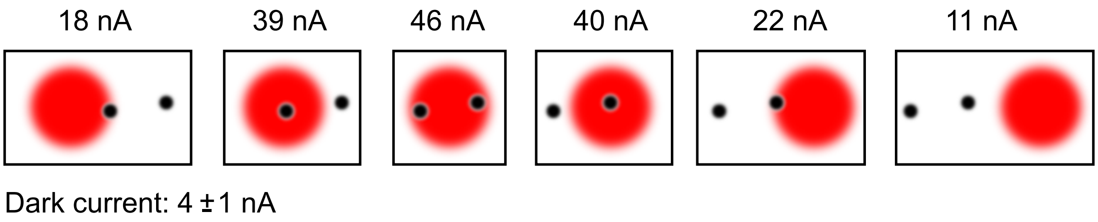

Figure 7.22: **Detector current behind the holes for different relative hole-spot position.**

sured the current of the detector behind the holes for six different hole-spot relative positions, see Figure 7.22. As a reference, we also measured the background current 4 ± 1 nA when the laser is switched off. According to the specification of the detector we use, the measured current can be converted to optical power and photon flux. For the case of a well-centered beam, the flux is about $\sim 10^{11}$ photons/s. This will be approximately the amount of photons reaching the surface of the sample in the following sections.

All these pre-characterization measurements at room temperature regarding the optical setup demonstrate that the method for introducing laser light onto the sample is functioning properly. As a result, the setup is now ready to proceed with the measurements of the resonator and the quantum dots at cryogenic temperature.

7.4 Characterization of test resonator on GaAs at 10 mK

This section presents the characterization results on a “dummy” sample at 10 mK where the design in Figure 7.7 is fabricated on undoped GaAs substrate instead of AlGaAs/GaAs heterostructure. The goal of the measurements are as follows:

- To test the functionality of the experimental setup, particularly the optical components, under cryogenic conditions.
- To evaluate whether the resonator design meets the requirements for the experiment.

Given that the heterostructure of AlGaAs/GaAs substrate is supposed to be etched away in the region underneath the resonator, we can fabricate the resonators on an undoped GaAs substrate as dummy samples. This reproduces a similar electromagnetic environment for testing the resonator design, and the finalized design will be processed on the actual AlGaAs/GaAs substrate. The discrepancy of the resonator frequency observed in the dummy sample is within the tolerance of our design considerations.

The 3-mask process flow described in Figure 7.8 can be used to fabricate the test sample with minor modifications. To begin with, 9 nm thick Al_2O_3 is pre-deposited on the undoped GaAs substrate by the technique called atomic layer deposition. We then follow the process described in Section 7.2 using the same masks but replacing the diluted Piranha etchant in step 2 by MF 319 to remove the 9 nm oxide underneath the resonator. The rest of the process remains the same.

Figure 7.23 shows the image of the sample under an optical microscope when the fabrication is finished. The left gate of quantum dot 1 (QD1) is applied with a voltage bias V_1. The remaining DC ports are grounded, as well as the ground plane of the resonator. Microwave signal is sent from port 1 through the chip and received at port 2.

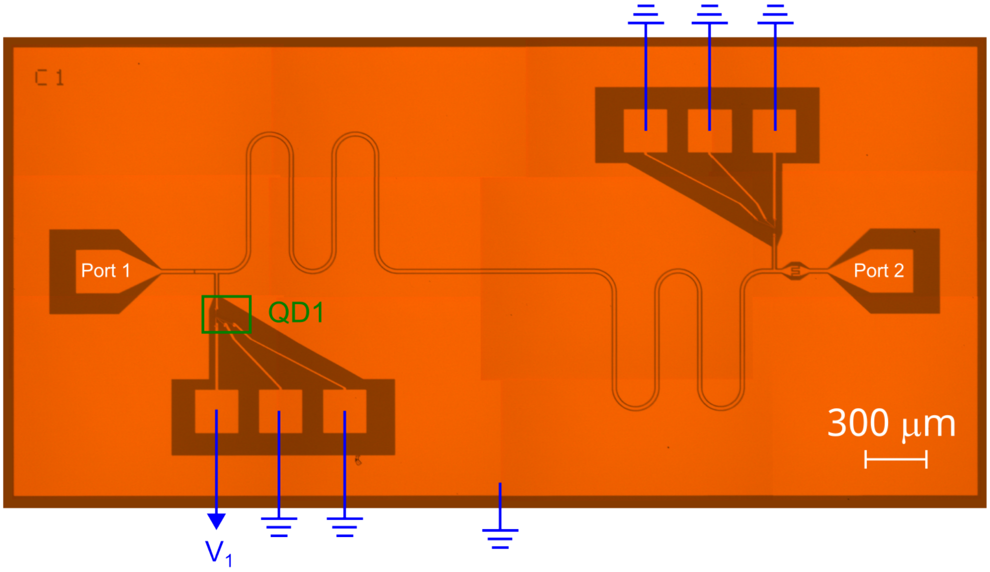

Figure 7.23: **Configuration of electrical connections on the dummy sample.** Optical microscope image of the entire sample chip under measurement. All the DC gates are grounded, as well as the resonator ground plane. The left gate of quantum dot 1 (QD1) is biased with a voltage V_1. The port 1 and port 2 are used as the input and respective output ports for microwave signals to obtain the transmission coefficient S_{21}.

When the sample is assembled and mounted in the setup discussed in the previous section, it is ready to be cooled down to base temperature for characterization.

7.4.1 Standard transmission measurement

The transmission of the CPW resonator is measured with the vector network analyser (VNA) at base temperature 10 mK. The power at the input of the sample holder is around −70 dBm. Because the signal is transmitted from the port 1 to port 2 through the sample (see Figure 7.23), we call this type of measurement transmission and the corresponding coefficient is a complex number S_{21} depending on the probe frequency (see Equation 2.77). Figure 7.24a shows the measured S_{21} of the resonator represented in complex plane. The observed distortion of the resonant circle is caused by cable delay and system attenuation/gain [103]. To fit these data, extra terms are needed in the model of Equation 2.77 to take into account the influence from the environment (contributions from outside the sample), such that

$$S_{21}(\omega) = Ae^{i\varphi}e^{-\omega\tau}\frac{\kappa/2}{\kappa/2 - i(\omega-\omega_0)}, \tag{7.9}$$

where A is an additional amplitude, φ is the extra phase from the impedance mismatch and environmental shift, τ is the electronic delay caused by finite speed of the light and the cable length [103]. The fit with Equation 7.9 to the data yields a resonant frequency $\omega_0/2\pi = 6.275$ GHz and total linewidth $\kappa/2\pi = 6.968$ MHz. The amplitude and phase of S_{21} is shown in Figure 7.24b,c.

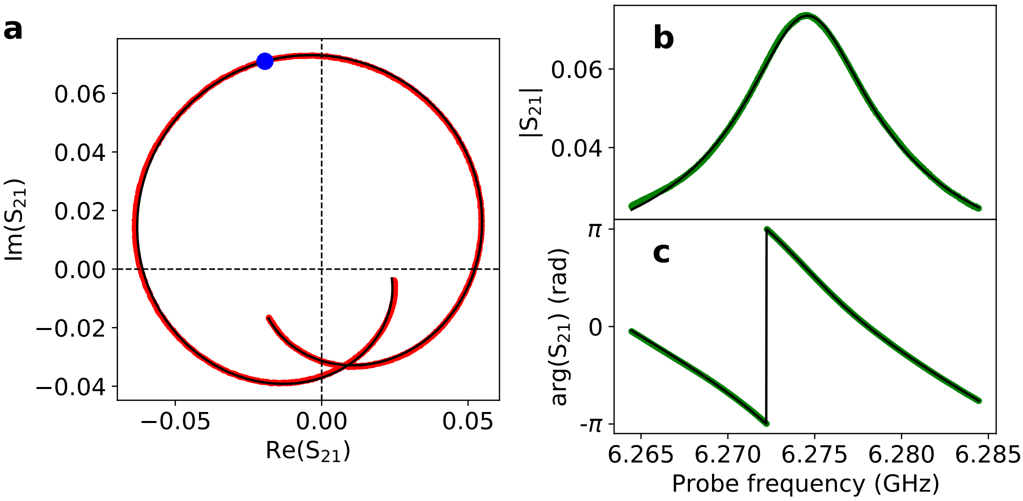

Figure 7.24: **Transmission measurement of the resonator on GaAs.** **(a)** Measured transmission coefficient S_{21} represented with its real and imaginary parts in complex plane as a function of probe frequency. A fit (black solid line) to the data (red) yields a resonant frequency $\omega_0/2\pi = 6.275$ GHz and total linewidth $\kappa/2\pi = 6.968$ MHz. The resonant point is indicated in the figure with blue dot. **(b,c)** Amplitude and phase of transmission coefficient as a function of probe frequency. Solid line is a fit to the data (green).

7.4.2 Transmission measurement under illumination

A superconducting resonator is sensitive to both illumination and charges in the environment. The former property is used to build a special type of photon detector called microwave kinetic inductance detector (MKID) [166], where the incident photons break Cooper pairs into excess quasiparticles to affect the kinetic inductance and resistive loss of the resonator. The excess charges in the environment (such as free carriers, ionized centers, interface charges, etc.) change capacitive part and internal loss of the resonator. In the experiment, the resonator behavior is affected directly by the illumination and indirectly by the charges generated in the semiconductor substrate from illumination, thus it is necessary to characterize the optical response of the resonator.

In the pre-characterization stage at room temperature, the light spot from the collimator is adjusted to be in the center of the sample holder covering both holes in the cover, using a supporting frame shown in Figure 7.19 and the laser is set with the lowest available power. At 10 mK, the transmission coefficient of the resonator is first measured in the dark environment and the results are already shown in Figure 7.24 (see previous section). Next, the laser is turned on for a period of time and then switched off while continuously recording the resonator response S_{21} with VNA. Note that during this measurement, the left dot gate is biased at - 2V and all the other gates are grounded.

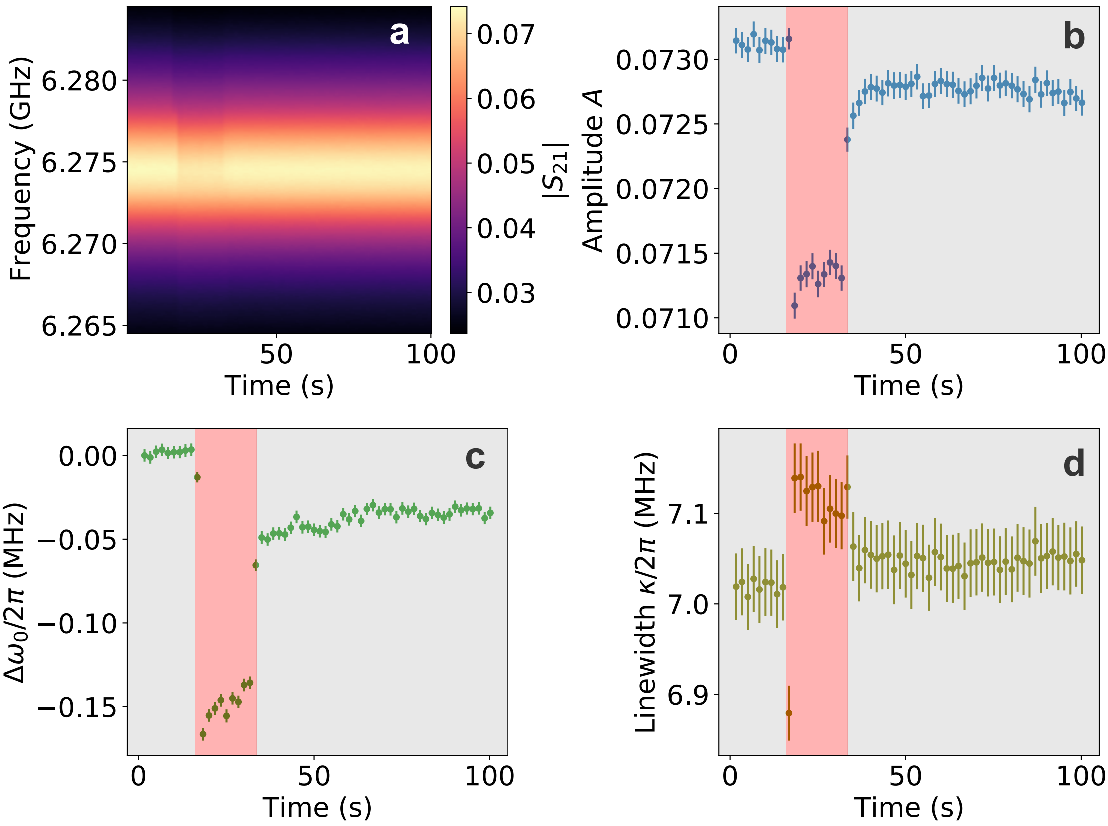

Figure 7.25: **Optical response of the dummy resonator on GaAs.** **(a)** Transmission spectrum of the resonator recorded in time, where the laser is switched on at $\sim 17\,s$ and switched off at $\sim 35\,s$. Colormap represents the amplitude of the transmission coefficient. **(b,c,d)** Fitted amplitude A of S_{21} in Equation 7.9 (b), shift of fitted resonant frequencies $\omega_0(t) - \omega_0(0)$ **(c)** and fitted total loss rates $\kappa/2\pi$ **(d)** as a function of measurement time. Red (resp. gray) boxes are the windows during which the laser is switched ON (resp. OFF).

Once the sample is illuminated, a sudden jump in the transmission spectrum is observed, see Figure 7.25a and red box region in b. During the illumination, the resonant frequency ω_0 shifts downwards to ω_0' and internal loss κ increases (see Figure 7.25c,d). This behavior is expected due to the increased quasiparticle density under illumination, , which leads to an increase in inductance and resistive loss [166].

When the illumination is switched off (gray boxes in Figure 7.25), the ω_0 and κ jump back towards to the initial point at time 0, but maintains the differences $\Delta\omega_0 = \omega_0(t) - \omega_0(0)$ and $\kappa(t) - \kappa(0)$ over a longer timescale (in our case, 100 s of measurement time). Given that the quasiparticle recombination time is on the order of magnitude of $100\,\mu$s [166], we attribute the abrupt change of ω_0 when switching off the light to recombined quasiparticles, while the difference in $\Delta\omega_0$ before and after illumination is due to permanent charges generated in the substrate from illumination.

These measurements prove the functioning of our optical setup described in Section 7.3.4 and that charges can be created in the substrate, as evidenced by the two distinct processes discussed before. Testing the resonator design and functionality on bare GaAs substrate is a quick and cost-effective way to simulate the situation of using AlGaAs/GaAs heterostructure, given their similar dielectric constants. The design meets our requirements for the quantum dot experiment. However, to manipulate the charges in the substrate, the confinement in the substrate depth direction is necessary. In the next section, we will use an identical design as the one tested here but on an AlGaAs/GaAs heterostructure to perform measurements.

Chapter 8

Experimental results on hybrid device

This chapter presents experimental results measured at 10 mK regarding the hybrid device of quantum dot on AlGaAs/GaAs heterostrucure and superconducting resonator. We begin this chapter with basic characterizations on the resonator made from the identical design tested in the previous chapter and then focus on the quantum dot experiments. By using the illumination to introduce charges into the undoped substrate, the initialization of quantum dots with the combined optical-electrostatic approach is demonstrated. The charge detection is achieved by using dispersive measurements on the resonator. Based on the detected single-charge transitions of the hybrid device through microwave, a single-quantum-dot charge stability diagram is observed. These results demonstrate that a quantum dot device can be created and controlled with an optical-electrostatic-cQED approach in an undoped substrate without the need for ohmic contacts. At the end of this chapter, we will discuss the path towards the manipulation of double quantum dot and single hole spin detection.

8.1 Basic characterization

The measurements presented in this chapter were performed on the sample with the design consisting of two accumulation gates and one central depletion gate (see Figure 7.7). The sample is fabricated on AlGaAs/GaAs heterostructure substrate (see Figure 7.1) through the process discussed in Section 7.2.

Figure 8.1 shows the measurement configuration on the sample. Note that only the gates of quantum dot 1 (QD1) are biased in this experiment. The gates of QD2 are all grounded together with the resonator ground plane and are not being measured. We use 3 DC ports in quantum dot 1 (QD1) for applying voltage to control the electrostatic potential underneath the gates. The biases applied on the left dot gate, central gate and right dot gate are V_1, V_C and V_2 respectively. Two RF ports are used as input and output ports for microwave signals to obtain the transmission coefficient of the system.

The device was initially characterized through standard transmission measurements using microwaves to study the resonator, as well as through current-voltage measurements (transport) using the electrostatic gates to test the bias threshold for leakage.

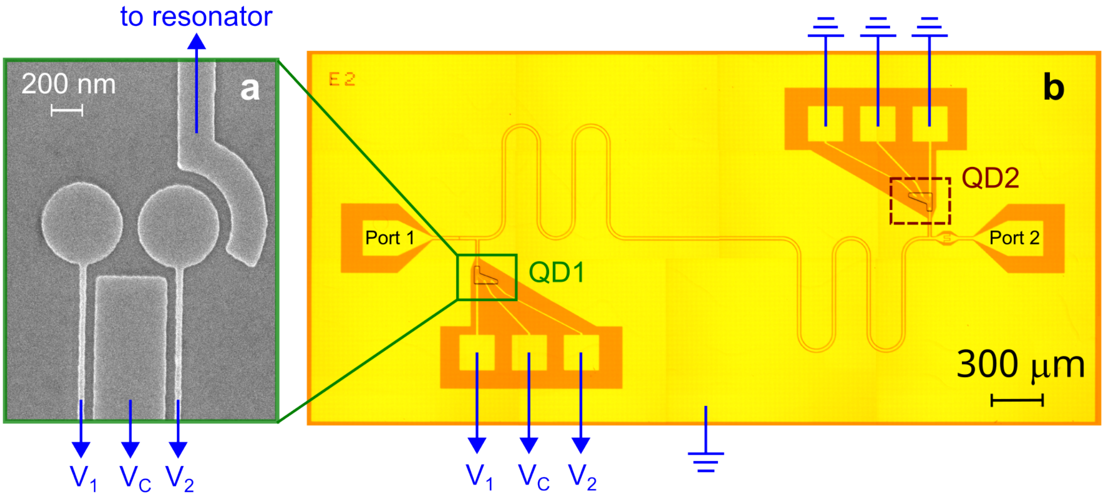

Figure 8.1: **Configuration of electrical connections of the hybrid sample.** **(a)** Scanning electron micrograph of quantum dot 1 (QD1) indicated in the region of green box in (b), where the left dot gate, central gate and right dot gate are biased with the voltages V_1, V_C and V_2 respectively. The floating gate near the right dot gate is connected to the resonator. **(b)** Optical micrograph of the entire sample chip under measurement. All the gates of quantum dot 2 (QD2 in brown dashed box) and resonator plane are grounded, as the reference point “zero” for voltage. Port 1 and port 2 are used as the input and output ports for microwave signals to obtain the transmission coefficient S_{21}.

8.1.1 Resonator characterization

At base temperature 10 mK, we measured with VNA the transmission coefficient S_{21} of the CPW resonator with $V_1 = V_C = V_2 = 0\,\text{V}$. The power at the input of the sample holder is around -70 dBm. Figure 8.2a shows the measured S_{21} of the resonator represented in complex plane. We have observed a distortion of the resonant circle, resulting from the cable delay and system attenuation/gain. The amplitude of the transmission coefficient $|S_{21}|$ (see Figure 8.2b) exhibits a nearly Lorentzian behavior that appears to be “spoiled” compared to the results in Figure 7.24b. We attribute this feature to the imperfections in the sample preparation, such as fabrication defects, issues with sample gluing, wire bonding, or flaws in the holder and PCB. The exact cause of this behavior is currently undetermined. Figure 8.2c shows the phase of S_{21} with the electric delay removed. Fitting the data with Equation 7.9 yields a resonant frequency $\omega_0/2\pi = 6.219$ GHz and total linewidth $\kappa/2\pi = 12.853$ MHz.

Note that the resonator on this sample has a total loss twice larger than the one on GaAs in the previous chapter, due to the increased internal loss. Despite the loss and strong distortion in the resonator behavior, we can still use this resonator to perform the quantum dot experiments.

8.1.2 Transport characterization

In this section, we performed basic current-voltage measurements on the hybrid device to characterize its transport behavior and check for possible leakage through

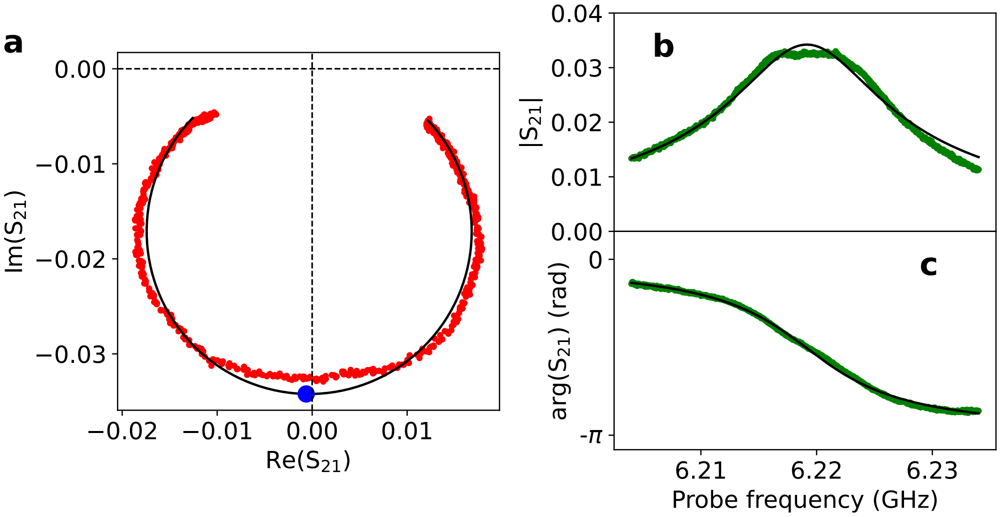

Figure 8.2: **Transmission measurement of the resonator of hybrid device on AlGaAs/GaAs substrate. (a)** Measured transmission coefficient S_{21} represented with its real and imaginary parts in complex plane as a function of probe frequency. A fit (black solid line) to the data (red) yields a resonant frequency $\omega_0/2\pi = 6.219$ GHz and total linewidth $\kappa/2\pi = 12.853$ MHz. The resonant point is indicated in the figure with a blue dot. **(b,c)** Amplitude and phase of transmission coefficient as a function of probe frequency. Solid line is a fit to the data (green).

the electrostatic gates. It should be noted that the hybrid device measured in our experiment has a different reference for the zero potential ("ground"), which is contrary to conventional quantum dot devices.

As shown in Figure 8.3a, conventional quantum dot devices have ohmic contacts between semiconductor and metal, which provide a reservoir of charge carriers that can flow and accumulate underneath the surface control gate. Here the reservoir is referred to as the "source". Typically, the electrode of the source is grounded and the two-dimensional electron gas (2DEG) at the AlGaAs/GaAs interface linked to source also has zero potential. The bias V_g applied to the electrostatic gate at the surface is referred to the 2DEG or source. However in our hybrid device, ohmic contacts do not exist, and 2DEG at the interface is therefore floating (see Figure 8.3b). In this case, the reference point is defined by the resonator ground plane and adjacent grounded gates, as well as the metallic plate at the backside of the sample chip.

The metal-semiconductor Schottky contact between the surface control gate and substrate has a build-in contact barrier for charge carriers [167]. In the case of Figure 8.3b, when the bias difference between the two gates exceeds a certain threshold, the carriers can overcome the Schottky barrier and flow from one gate to the other through the surface GaAs cap layer. Here, we measured current-voltage (I-V) transport behavior of the surface gates to characterize the leakage of the system.

The I-V characteristics for the left dot gate are shown in Figure 8.4, where leakage appears when $|V_1| > 2\,\mathrm{V}$. In order to work in a regime without leakage, we restrict the gate voltage below 1 V for experiments presented in the rest of the chapter.

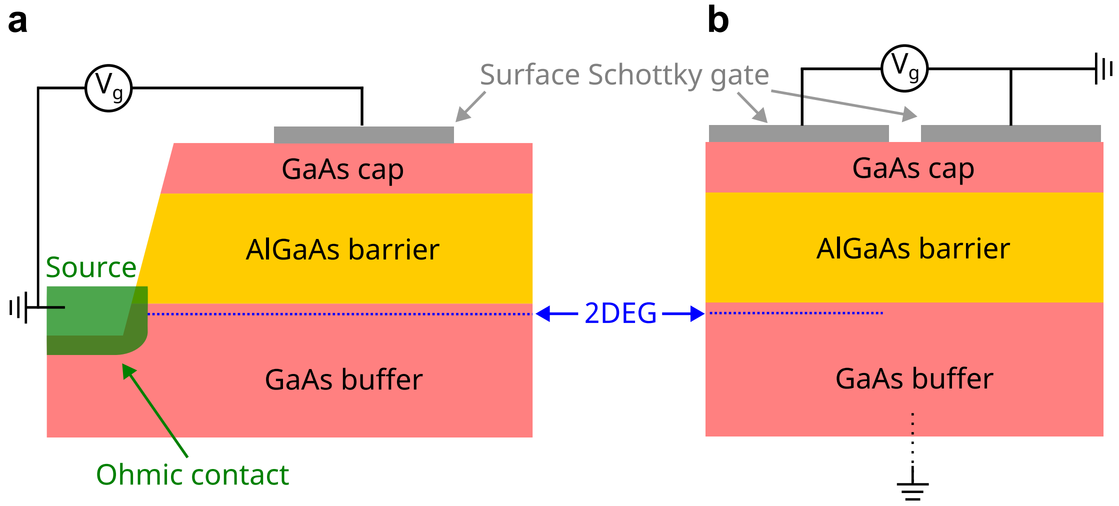

Figure 8.3: **Cross-section schematic of the quantum dot devices with corresponding bias references. (a)** Device with ohmic contact (green). The bias V_g applied on the surface gate (gray) is referred to the grounded ohmic contact of the source. The 2DEG (blue dash line) induced beneath the gate from source reservoir has the same potential as the contact. **(b)** Device without ohmic contact. The grounded surface gates and backside of the substrate are defined as the reference point.

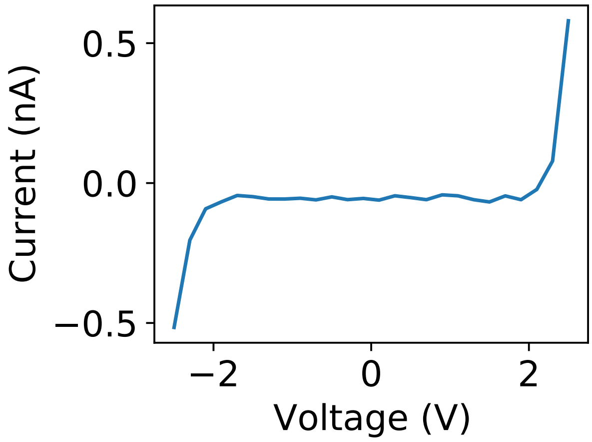

Figure 8.4: **I-V characteristics of surface leakage with quantum dot control gate.** Measured current flowing through the left dot gate as a function of the voltage applied on the same gate.

8.2 Quantum dot

The quantum dot experiment to be discussed in this section consists of two essential steps. In the first step, we use optics to introduce charges into the quantum dots (an optical pumping step). This is done by illuminating the sample with a laser that has energy higher than the bandgap of GaAs. After the absorption of the energy, electron-hole pairs are generated in the substrate and split by electric field from the biased gates.

In the second step, we measure the charge stability diagram of the dots. This is done by applying a voltage to the gates and measuring the resonator transmission. By sweeping the voltage on the gates, the regions where the charge in the dots is stable, as well as the regions where the charge is likely to change due to tunneling events, can be mapped out. The resulting plot is called a charge stability diagram, which provides information about the charging energy of the dots, the capacitances between the dots and gates.

8.2.1 Optical initialization of the quantum dots

Prior to switching on the laser, a voltage of -0.5 V is applied to the left dot gate while all the other gates are grounded ($V_1 = -0.5\,\mathrm{V}$ and $V_C = V_2 = 0$). This creates an electric field between the two dot gates, which can then split the optically generated electron-hole pairs near the gates.

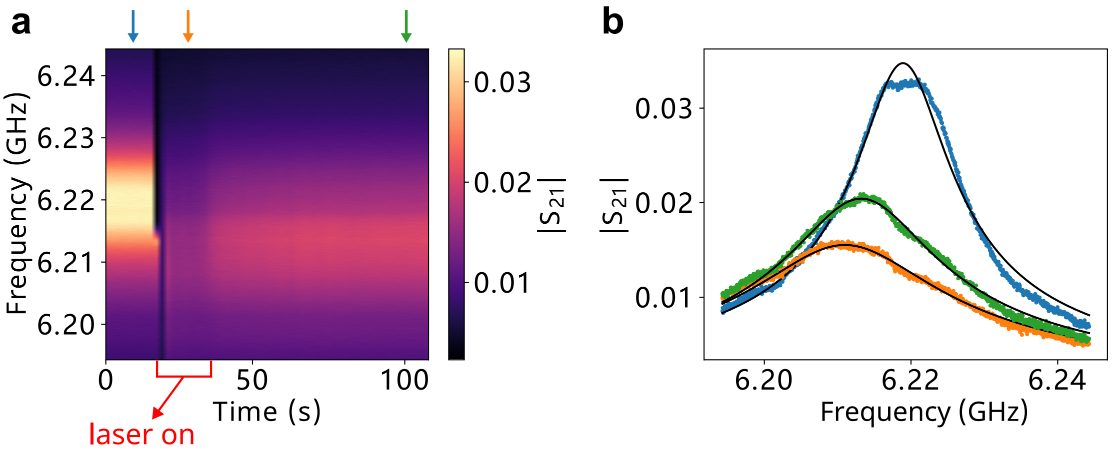

Figure 8.5: **Optical response of the resonator in hybrid device.** **(a)** Transmission spectrum of the resonator recorded in time, where the laser is switched on at $t \sim 18\,\mathrm{s}$ and switched off at $t \sim 36\,\mathrm{s}$. Colormap is the amplitude of the transmission coefficient. The arrow on top indicate three regimes: before (blue), during (orange) and after (green) illumination. **(b)** Amplitude of the transmission coefficient $|S_{21}|$ as a function of probe frequency for the three traces indicated with arrows in (a). The black solid lines are fit to the data.

We use the resonator to monitor the effect of illumination during this process, where a minimal optical power of the laser is applied, as discussed in Section 7.3.4. The resonator transmission spectrum is measured repeatedly through a VNA scan and each repetition takes around 1.8 s. Figure 8.5a shows the continously measured spectrum as a function of time. The spectrum exhibits three distinct regimes: (i) From $t = 0$ to $t \sim 18\,\mathrm{s}$, the laser is off, and the spectrum remains unchanged. (ii) Between $t \sim 18\,\mathrm{s}$ and $t \sim 36\,\mathrm{s}$, the laser is switched on, and the resonant frequency shifts downwards and the linewidth increases. (iii) From $t \sim 36\,\mathrm{s}$ to the end of the measurement, the laser is switched off. The resonant frequency and linewidth return towards their initial values, but remain shifted at the end of the measurement.

Note that the laser is switched on in the middle of VNA scan at $t = 18\,\mathrm{s}$, leading to an abrupt jump in the second half of the spectrum. Then the system reaches a steady state after a few seconds. Typical traces of $|S_{21}|$ as a function of probe frequency in these three regimes acquired at $t = 11\,\mathrm{s}$ (blue), $t = 29\,\mathrm{s}$ (orange) and $t = 101\,\mathrm{s}$ (green) are shown in Figure 8.5b. The fitted resonant frequencies and total linewidths are summarized in Table 8.1.

regime	$\omega_0/2\pi$ (GHz)	$\kappa/2\pi$ (MHz)	comments
i	6.219	12.160	before illumination
ii	6.211	25.005	during illumination
iii	6.213	19.836	after illumination

Table 8.1: **Optical response of resonator in hybrid device and fitted resonator parameters.**

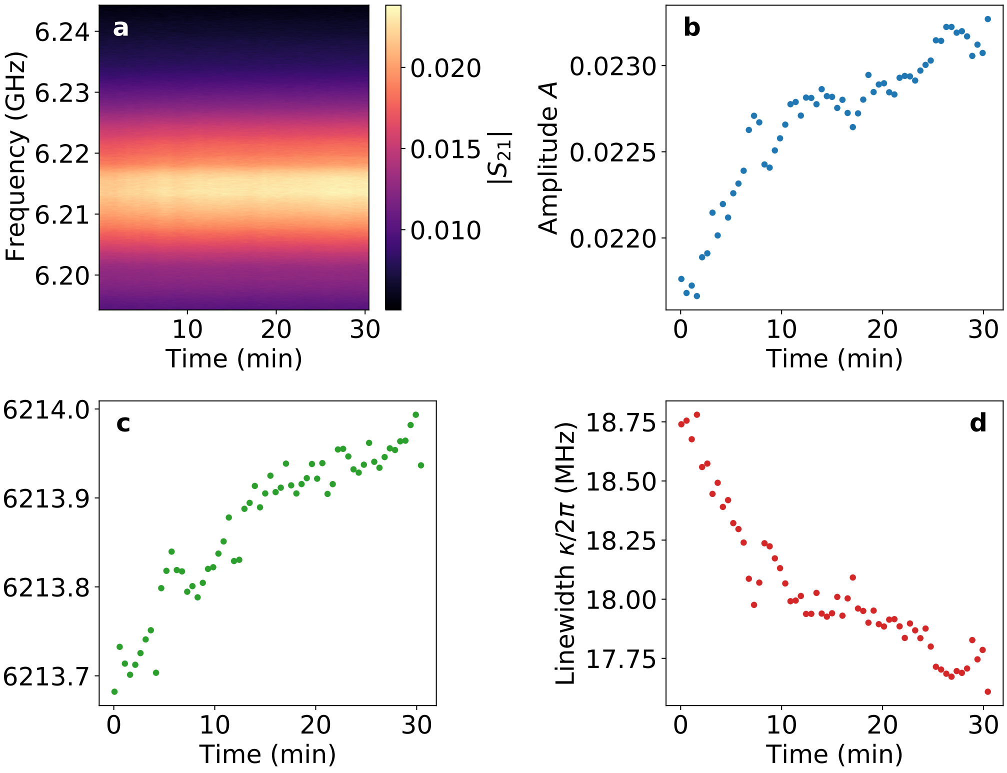

Figure 8.6: **Transmission spectrum after illumination over 30 min.** Transmission spectrum of the resonator recorded in time **(a)**. Colormap shows the amplitude of the transmission coefficient $|S_{21}|$. Fitted amplitude A of S_{21} **(b)**, fitted resonant frequencies ω_0 **(c)** and fitted total linewidth $\kappa/2\pi$ **(d)** as a function of measurement time.

As discussed in Section 7.4.2, the response of the resonator under illumination results from creation and recombination of quasiparticles and of electron-hole pairs. The modifications of the resonator parameters compared to their initial values, which persist when the laser is off, are due to the permanent charges created in the substrate. Since AlGaAs/GaAs heterostructure provides confinement in the substrate depth direction, the newly created charges are more easily trapped at the heterointerface. This leads to a larger effect on the resonator compared to the case of bare GaAs substrate.

Given that our goal is to use the optically-created charges in quantum dot and the measurement timescale usually ranges from several minutes to a few hours, it is of interest to monitor the change of resonator spectrum after illumination over longer timescale. We have measured the transmission spectrum up to 30 min after illumination and the results are shown in Figure 8.6. The resonant frequency gradually increases, and the linewidth decreases, indicating that the movable charges in the environment are slowly vanishing (by recombination) or moving deeper in the substrate bulk, no longer influencing the resonator.

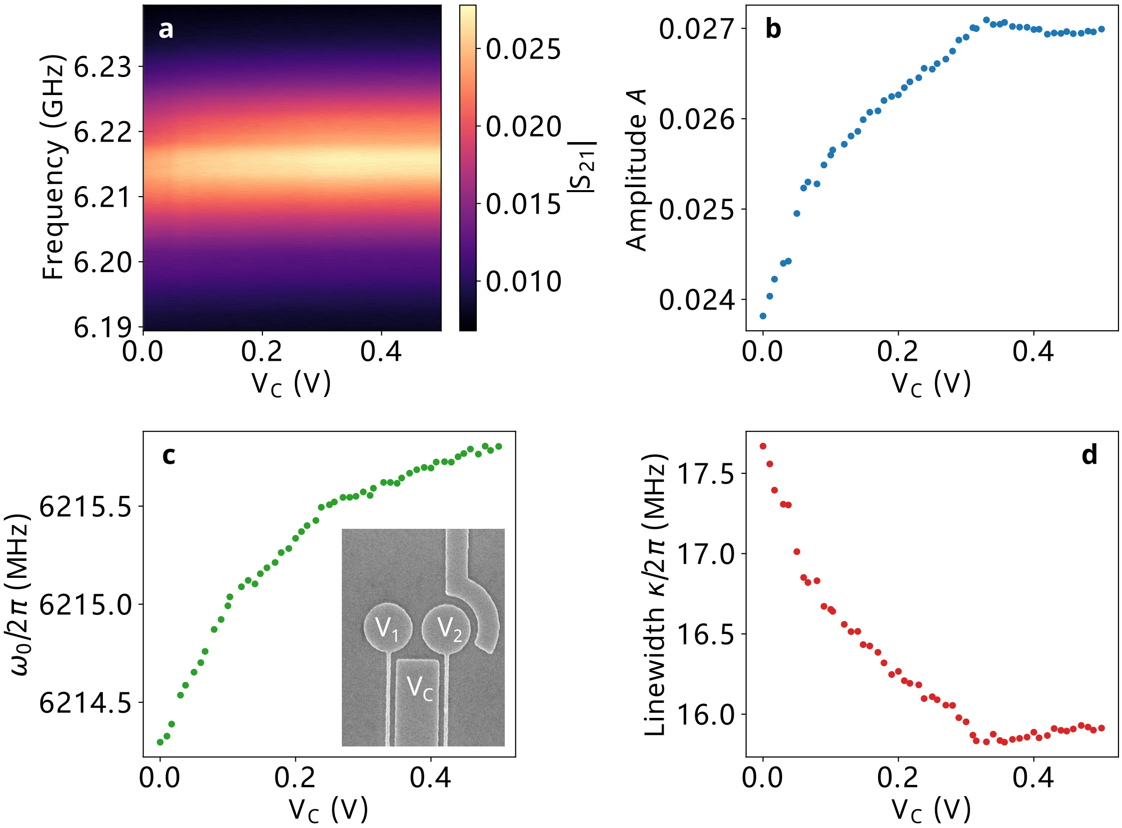

Figure 8.7: **Transmission spectrum as ramping up central gate bias.** Transmission spectrum of the resonator recorded as a function of central gate bias V_C **(a)**. Colormap shows the amplitude of the transmission coefficient $|S_{21}|$. Fitted amplitude A of S_{21} **(b)**, fitted resonant frequency ω_0 **(c)** and fitted total linewidth $\kappa/2\pi$ **(d)** as a function of V_C. The measurement is done under the conditions $V_1 = -0.5\,\mathrm{V}$ and $V_2 = 0$ (see inset of panel **c** for the configuration).

Next, we study the dependence of resonator response on the bias applied to the central depletion gate. The bias V_C is ramped up to deplete the charges below the narrow leads of the left and the right dot accumulation gates. The resonator spectrum is recorded for each voltage value while varying the voltage V_C. This measurement takes only 90 seconds, which is fast enough to neglect the observed change of ω_0 over a longer timescale, as shown in Figure 8.6. The resonator shows a strong dependence on V_C, see Figure 8.7. As V_C is ramping up, the fitted resonator amplitude A and resonant frequency ω_0 increase, and linewidth κ decreases. A plateau of A and κ is reached when V_C is larger than 0.3 V. We are tempted to assume that charges beneath the leads of left and right dot gates are fully depleted as long as $V_C > 0.3\,\mathrm{V}$, which will no longer contribute to resistive loss of the resonator. These results demonstrate the existence of charges in the environment responding to the gate bias. Now the system is ready for quantum dot measurements.

8.2.2 Charge stability diagram

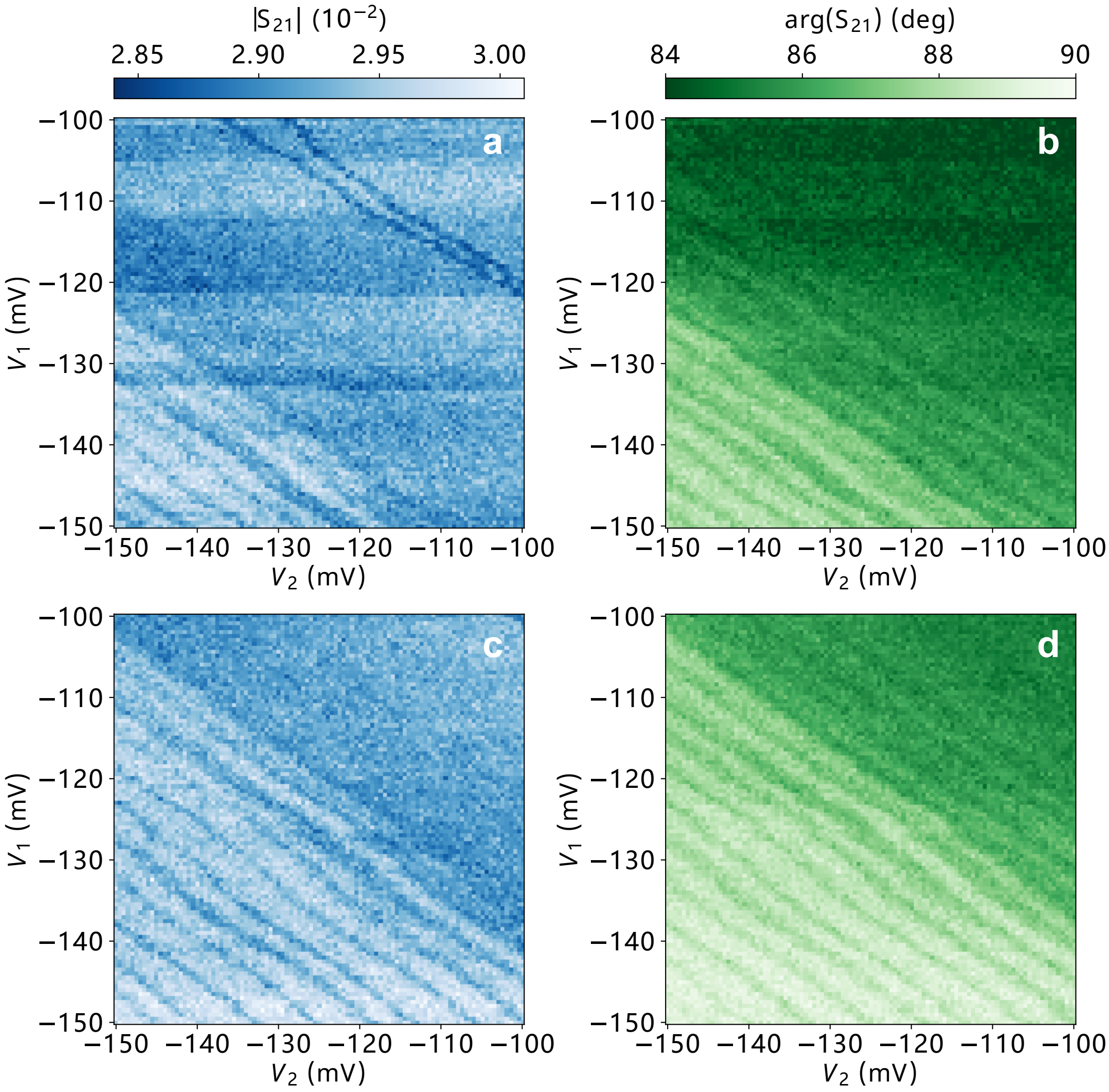

Figure 8.8: **Charge stability diagram probed with resonator.** Amplitude (a,c) and phase (b,d) of the resonator transmission coefficient S_{21} probed at resonance frequency as a function of V_1 and V_2. The central gate bias is fixed at $V_C = 0.5\,\mathrm{V}$. The data in (c,d) are results of repeated measurements as performed in (a,b).

After the optical initialization of the dot, the charge stability diagram can be obtained by measuring the resonator dispersive shift, as discussed in Section 6.2.2, while sweeping the voltages on the dot gates. In practice, we probe the transmission coefficient S_{21} of the resonator at a fixed frequency ω_p with VNA for each bias condition. The choice of probe frequency is normally at or near the resonant frequency

ω_0 of the resonator. Here, $\omega_p/2\pi = 6.21514\,\mathrm{GHz}$ is chosen.

It should be noted that the microwave power is reduced by 20 dBm to observe the single charge dynamics, whereas in the case of obtaining the optical response of the resonator spectrum in the previous chapter, a high power is used for fast measurement with a reasonable SNR.

During the entire scan of measuring charge stability diagram, the central gate is maintained at a fixed voltage ($V_C = 0.5\,\mathrm{V}$). The left and the right dot gates are swept in a range from -150 to -100 mV ($V_1, V_2 \in [-150, -100]\,\mathrm{mV}$) with a step size of 0.5 mV. The measured amplitude and phase of S_{21} as a function of V_1 and V_2 are shown in Figure 8.8a, b, where a series of transition lines are observed in both the amplitude and phase responses of the resonator. Each of these lines corresponds to a tunneling event of a single charge and has an approximate slope of 45°, which is in agreement with the characteristic of a single quantum dot coupled to two gates (as shown in Figure 6.4c). The $\sim 6\,\mathrm{mV}$ spacing of the adjacent lines indicates the charging energy of the system is about $\sim 0.21\,\mathrm{meV}$, using a simulated lever arm $\alpha = 0.07$ associated to the gate (α is a conversion factor between the gate bias and the resulting actual change in the energy of the dot). This charging energy corresponds to a capacitance of about $\sim 760\,\mathrm{aF}$.

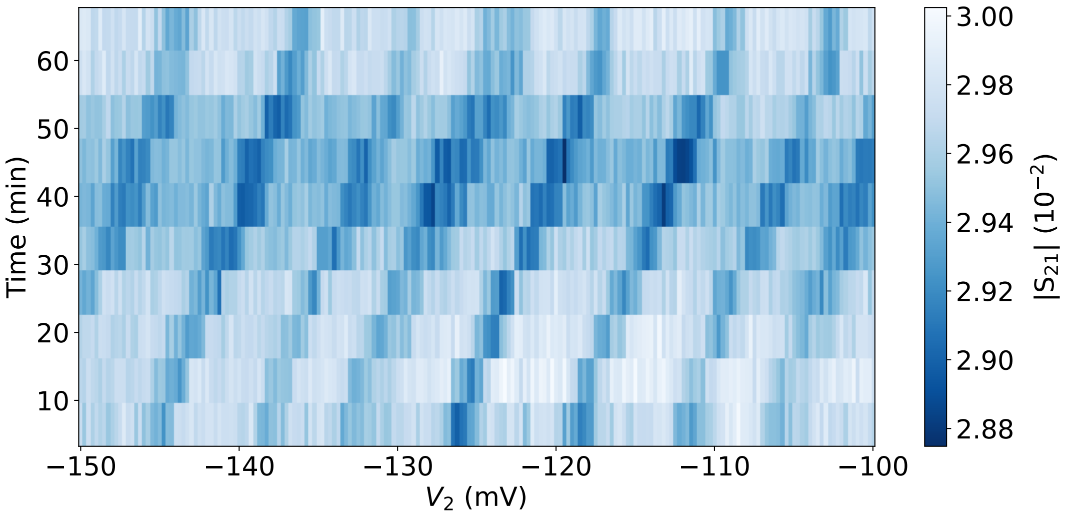

Figure 8.9: **Time drift of charge transition.** Measured amplitude of resonator transmission coefficient $|S_{21}|$ as a function of V_2 and time. Data taken at $V_C = 0.5\,\mathrm{V}$ and $V_1 = -150\,\mathrm{mV}$.

Moreover, to evaluate the stability and reproducibility of the obtained features of single charge transition, the same scan was performed again, and the results are displayed in Figure 8.8c, d, revealing a shifted pattern towards the more positive side of the diagram. The observed features of charge transition regarding the spacing for instance are well reproduced despite the unwanted global drift.

To study the observed temporal drift of the system, we keep $V_1 = -150\,\mathrm{mV}$ and only sweep V_2 repetitively. Figure 8.9 shows the drift of charge transition lines as a function of measurement time. A drift of $\sim 9\,\mathrm{mV/hour}$ is observed in this case. We attribute this phenomenon to the slowly changing charges in the environment, which contribute to an effective global bias on the gates. Since the drift moves towards the positive side, it is reasonable to assume that the positive charges in the environment are pushed further away or screened by the gates under the given bias conditions over a longer timescale.

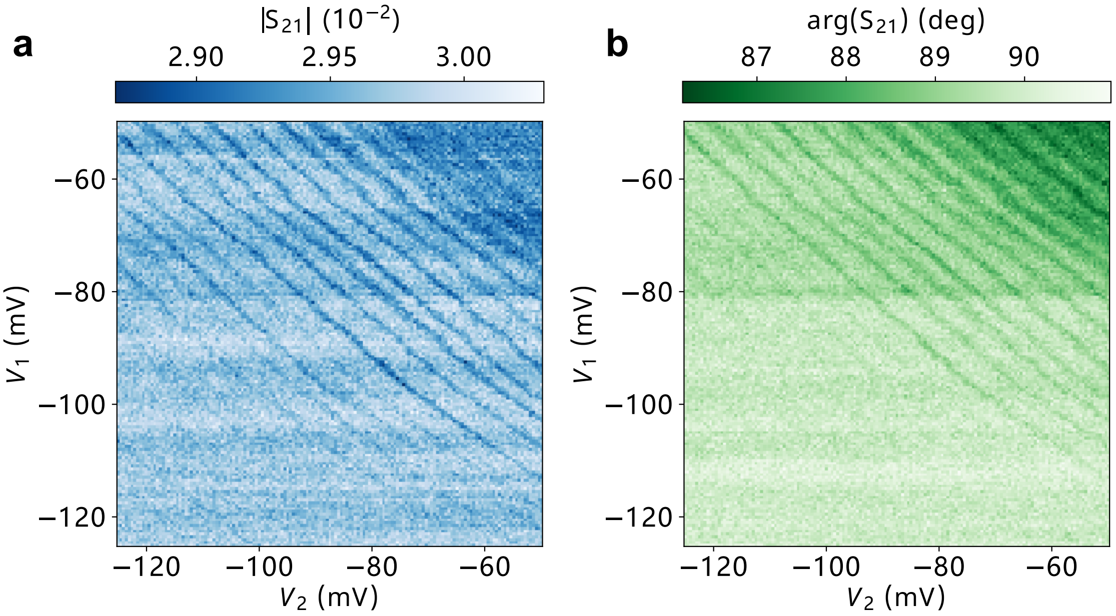

Figure 8.10: **Charge stability diagram probed with resonator.** Amplitude (a) and phase (b) of the measured resonator transmission coefficient S_{21} as a function of V_1 and V_2. The central gate bias is fixed at $V_C = 0.5\,\mathrm{V}$.

Next, to observe the beginning of transition lines on the negative side, a charge stability diagram was measured within an adapted range for V_1 and V_2 (-125 mV to -50 mV), see Figure 8.10. However, there is no clear indication of changes in line spacing to differentiate between different parts of the stability diagram. Since we do not have independent control over the tunnel barrier, the biases applied to the left and right dot gates can also influence the barrier's height, which restricts the observation of charge transition in a certain range with favorable tunnel coupling rates.

In all the previous measurements, the bias voltage on the central gate was maintained at $V_C = 0.5\,\mathrm{V}$. To explore the dependence of charge transitions on V_C, here in this measurement, we sweep V_2 while gradually stepping V_C from 0.5 V to 0 V with V_1 fixed at -70 mV. The results are plotted in Figure 8.11. This measurement takes about 10 hours.

The diagram shows two distinct regions. When V_C is above 150 mV, a series of charge transition lines, as observed previously, shift upon changes in V_C changes. This shift is due to the variation in gate bias and temporal drift that we discussed earlier. When V_C is below 100 mV, no charge transition can be observed within the measurement voltage range. Between 100 and 150 mV, a transition region is observed in which there is a drastic change in the series of lines in terms of their slopes and widths. This behavior is reminiscent to the case of single-dot-reservoir system, as shown in the Fig. 2a of Ref. [168]. In their case, the reservoir of charges was formed electrostatically by biasing an accumulation gate with large area compared to dot gate (similar to the configuration shown in Figure 8.3a). When the bias of the

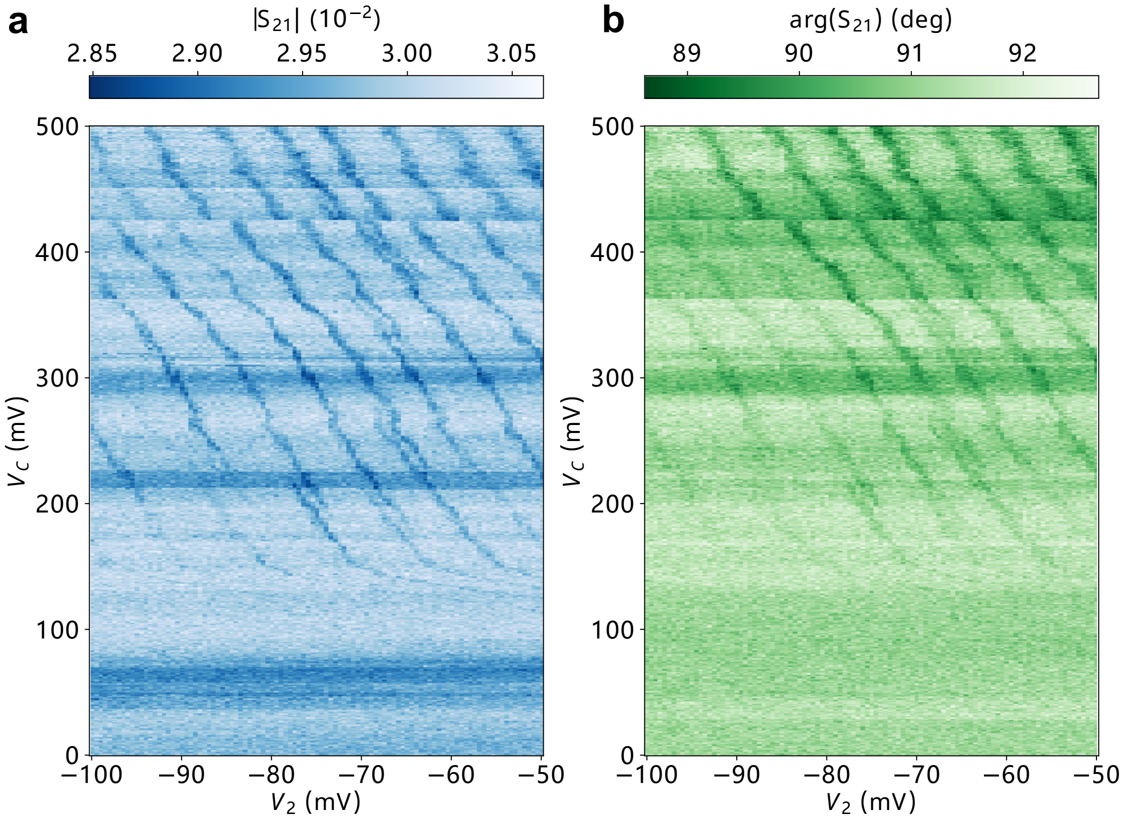

Figure 8.11: **Charge transitions probed with resonator.** Amplitude (a) and phase (b) of the measured resonator transmission coefficient S_{21} as a function of V_2 and V_C. The left gate bias is fixed at $V_1 = -70\,\text{mV}$.

reservoir is changed from high to low, the charge transition lines exhibit decreasing slopes (i.e., becoming more horizontal) and a "speckled" appearance due to the change in the tunneling rate. In our case, the fainted and narrowed appearance in the transition lines, as well as changes in their slopes, indicate a change in the tunneling rate. These features suggest that a charge reservoir was formed electrostatically beneath the central gate, and that this reservoir is emptied when its bias returns to zero.

To confirm the irreversible refilling and emptying of the possible "reservoir" by using only electrostatic gates (the illumination is required to refill the dot or reservoir), we performed two additional measurements. In the first measurement, V_1 is fixed at -70 mV, V_2 is swept between -100 and -50 mV, while stepping V_C from 100 to 400 mV. In the second measurement, we repeat the sweeping of V_1 and V_2 while keeping V_C fixed 0.5 V. As shown in Figure 8.12 and Figure 8.13, no charge transition lines are present in these two scans.

Finally, we measure once again the full resonator transmission spectrum after resetting all the gates back to zero bias, which allows us to compare the results with the initial measurements taken before illumination. After biased illumination, charge stability diagram measurements, and resetting all gates back to zero bias, the resonator frequency and total linewidth now are much closer to the ones measured before illumination (see Figure 8.14), compared to the spectrum right after biased illumination (see green data in Figure 8.5). This suggests the permanent charges in the substrate are reduced when the gate biases are reset to zero, but there is still a

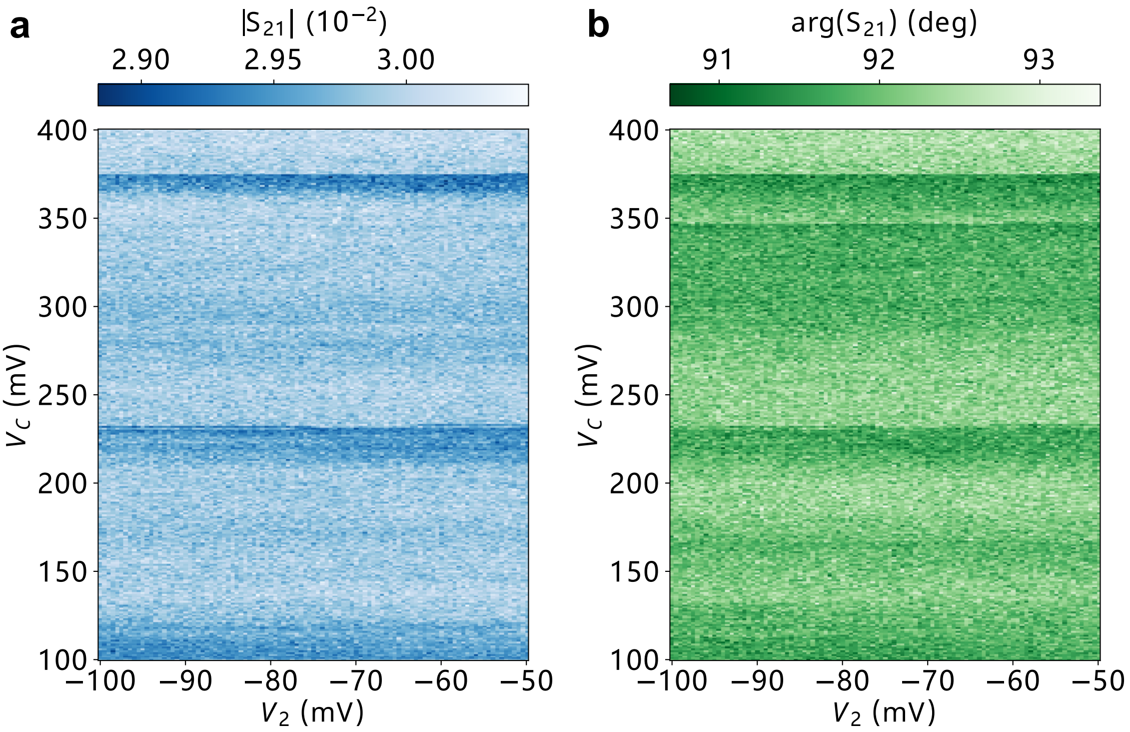

Figure 8.12: **Charge transition map probed with resonator after emptying the central gate.** Amplitude (a) and phase (b) of the measured resonator transmission coefficient S_{21} as a function of V_2 and V_C. The left gate bias is fixed at $V_1 = -70\,\mathrm{mV}$.

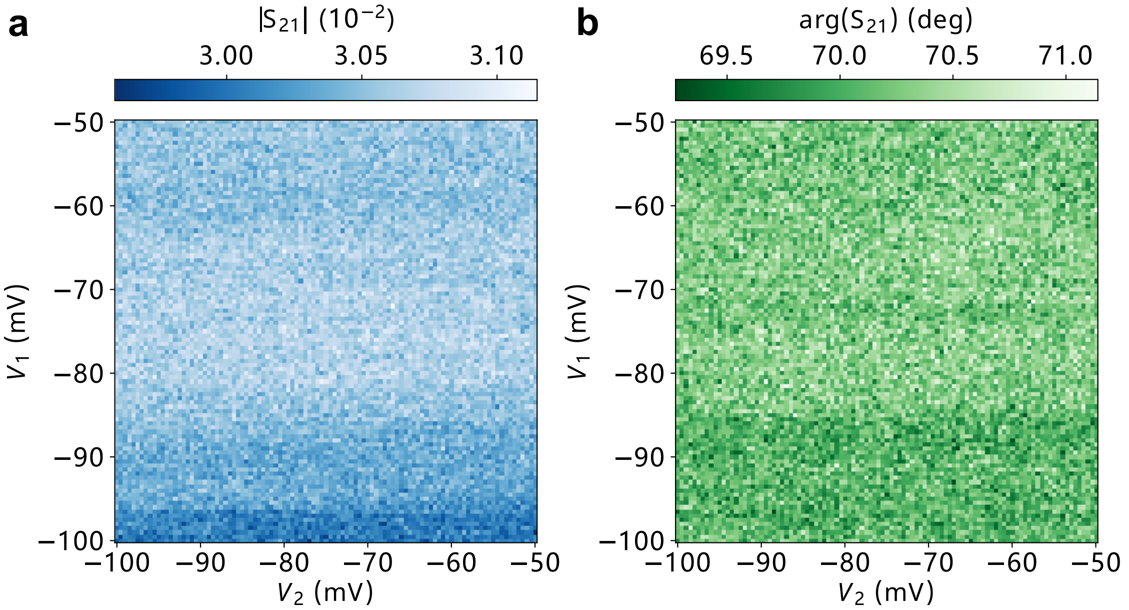

Figure 8.13: **Charge transition map probed with resonator after emptying the central gate.** Amplitude (a) and phase (b) of the measured resonator transmission coefficient S_{21} as a function of V_1 and V_2. The central gate bias is fixed at $V_C = 0.5\,\mathrm{V}$.

small amount of charges that remain.

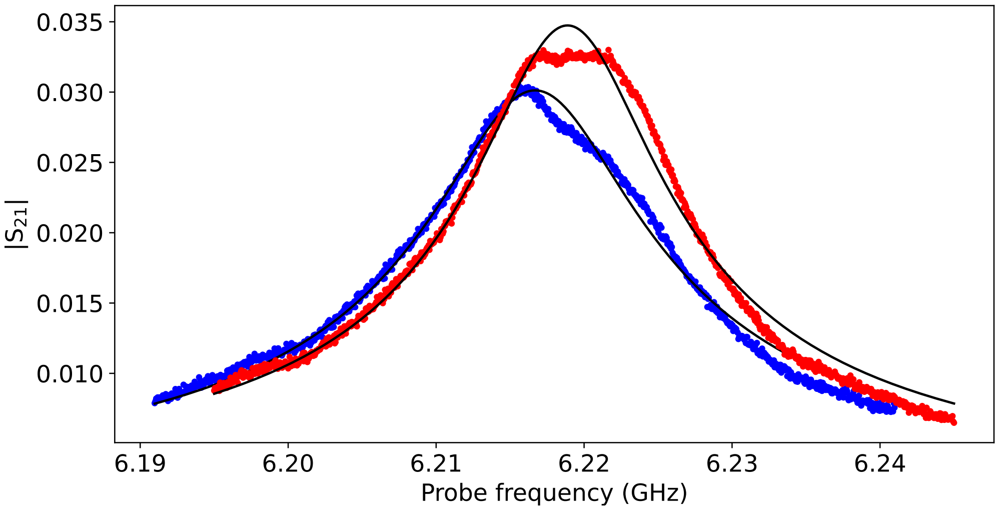

Figure 8.14: **Resonator transmission spectrum after setting all the gates back to zero bias.** Amplitude of the measured resonator transmission coefficient S_{21} as a function of probe frequency for two cases: (i) before illumination (red dots) (ii) after biased illumination, charge stability diagram measurements, and resetting all gates back to zero bias (blue dots). The fitting to the data (solid lines) yields a resonant frequency $\omega/2\pi$ =6.219 GHz and a total linewidth $\kappa/2\pi$ =12.13 MHz for case (i), and $\omega/2\pi$ =6.217 GHz and $\kappa/2\pi$ =13.87 MHz for case (ii).

8.2.3 Possible explanation for the observed features

The observed charge stability diagram shown in Figure 8.8 is associated with the tunneling event between a single quantum dot device and a charge reservoir, where the single dot is controlled by two gates. The results shown in Figure 8.11 further support the existence of the reservoir formed in the given configuration. One possible explanation is depicted in Figure 8.15. In this configuration, two accumulation gates do not create a double quantum dot in the given conditions. Instead, they create a peanut-shaped well (merged from two single wells) forming a single quantum dot that is controlled by both gates. The central gate, designed for depleting charges beneath the leads of accumulation gates, can also act as a reservoir gate.

Upon illumination, electrons are generated and accumulated beneath the central gate to form a reservoir, while in the single dot nearby the charge levels are quantized due to the confinement potential. As shown in the Figure 8.15b, once the level in the quantum dot is adjusted higher than the level of the reservoir, the valence band electrons can tunnel to the conduction band of the reservoir nearby. This results in the loading of holes into the quantum dot, which can be controlled by adjusting the voltages applied to the accumulation gates.

When all the gates are reset to zero, any accumulated charges (both electrons and holes) are released and eventually recombine with their counterparts in the environment, resulting in a reduction of the number of movable charges in the environment and a decrease in the resistive loss in the resonator.

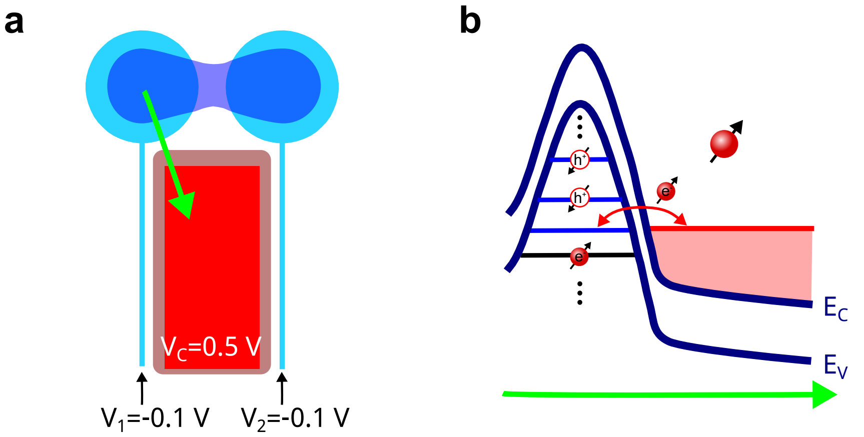

Figure 8.15: **Possible explanations for the observed charge stability diagram.** **(a)** Under the indicated bias configuration, two accumulation gates (blue) generate a peanut-shaped potential well (dark blue) forming a single quantum dot for holes, and the central gate (red) creates a rectangular-shaped well (dark red) acting as a reservoir of electrons. **(b)** The energy band diagram along the green arrow indicated in panel **a**. Conduction band electrons (red) accumulated in the reservoir can tunnel to the single quantum dot in the valence band (hole quantum dot).

8.3 Towards single spin manipulation and detection

This work demonstrates the first detection of charges generated in an undoped substrate through illumination with a superconducting resonator in a cQED platform. In this experiment, a single quantum dot and a reservoir are both created optically-electrostatically, and microwave dispersive measurements are used to probe the single charge transitions of tunneling events between the dot and reservoir.

Moving forward, the next step would be to find the double quantum dot regime for holes using appropriate biases or geometry on the two accumulation gates. Once achieved, the strong intrinsic spin-orbit coupling associated with holes can be leveraged to couple the spin degree of freedom of holes to the resonator during tunneling between the double dots.

A recent work (in Ref. [7]) has demonstrated the strong coupling between a single photon and a single hole spin in silicon, where a spin-photon coupling rate of 330 MHz was achieved. This result shows the potential of hole spin-based cQED platform for quantum computing and spin-photon interface.

This thesis presents a proof-of-principle experiment that establishes a novel platform that combines quantum dots, cQED and optics. This platform offers a versatile framework for studying and manipulating quantum systems. The demonstrated concept is universal and can be extended to other systems beyond the AlGaAs/GaAs material platform that is used in the present study. Specifically, hole spin-based cQED systems in silicon mentioned above are promising candidates for quantum computing due to their exceptional material properties and industrial fabrication platform. The demonstrated concept is expected to work similarly in silicon for creating quantum dots from illumination and performing single spin detection.

Chapter 9

Conclusions and perspectives

This thesis work has explored two hybrid platforms and methods for addressing individual spins in solid-state systems, utilizing circuit quantum electrodynamics. The two distinct but related proof-of-principle experiments demonstrate the potential of these platforms for quantum sensing and quantum computing.

Single electron-spin-resonance detection by microwave photon counting

Part I of the manuscript reports the first measurement of individual electron spins in a solid using magnetic coupling to a microwave resonator. In particular, a single microwave photon detector (SMPD) based on the superconducting transmon qubit is used to detect the microwave fluorescence photons emitted by individual erbium ions in a scheelite crystal, upon radiative relaxation. The measured linewidth of electronic spins of erbium ions in spectroscopy is four orders of magnitude narrower than the inhomogeneously broadened ensemble line, which brings a considerable improvement in spectral resolution. In our experiment, tens of individual spins with coherence times in excess of 1 millisecond are interfaced with the same microwave resonator, which opens new perspectives for hybrid quantum computing. Because of its broad applicability, large detection volume, and spectroscopic capability, our detection method comes close to practical single electron spin resonance at millikelvin temperatures, and may thus open new applications and have a major impact in the fields of magnetic resonance spectroscopy, quantum computing, quantum sensing, and hybrid quantum devices.

In magnetic resonance, existing methods for detecting individual electron spins are either system-specific or have a small detection volume (typically below $10^4\,\mathrm{nm}^3$). In contrast, our method is in principle applicable to arbitrary paramagnetic species, because it only relies on the magnetic dipole coupling between the spin and the resonator, and has a detection volume defined by the mode volume of the spin resonator ($10^{10}\,\mathrm{nm}^3$ in the present experiment). In the spectroscopic measurements, for the first time, we resolve an inhomogeneously broadened spin resonance line into its constituent individual spin peaks using only microwave signals, and show the ability to follow and measure the gyromagnetic tensor of several individual electron spins. These results demonstrate the immense potential of our method for magnetic resonance spectroscopy.

In quantum computing, our results constitute a new method to address individual electron spin qubits. So far, most of the spin qubit experiments use either optical or transport measurements, and these techniques only apply to a very narrow subset of spins. Our method can potentially address all paramagnetic impurities as spin qubits. The success of our method is visible on the long coherence times measured on individual erbium ions, up to 3 ms for the Hahn echo time, on par with the longest ever measured for individual solid-state electron spin qubits. In our experiment, tens of these long-coherence-time spin qubits are addressable. Moreover, excited single spins in Purcell regime, which act as single microwave photon emitters, can be used with SMPD for future implementation of remote entanglement. [169, 170].

In quantum sensing, our results further confirm that superconducting-qubit-based SMPDs enable unprecedented measurement sensitivity, opening the way to the detection of weakly coupled emitters that cannot be detected by other means, such as individual spins. In particular, we present the first measurement of the intensity-intensity correlation function of a single microwave emitter using a SMPD. Our results constitute the first practical use of superconducting qubit for ESR spectroscopy.

Finally, our results demonstrate a new level of control on spin-superconducting hybrid quantum devices, opening perspectives for microwave quantum memories as well as single-spin-based microwave-to-optical conversion.

Towards addressing single hole spin in gate-defined quantum dots initialized by illumination

In Part II of the manuscript, a proof-of-principle demonstration is presented for detecting charges in electrostatically defined quantum dots, which are initialized through illumination in an undoped substrate ; the detection is accomplished via dispersive measurements on a superconducting resonator within a circuit-quantum electrodynamics (cQED) architecture. This novel platform, which combines quantum dots, cQED, and optics, provides new perspectives of development for hybrid quantum systems and quantum technologies.

For the demonstration, we use a hybrid device system that hosts quantum dots in an undoped AlGaAs/GaAs heterostructure and a superconducting resonator. Upon illumination, charges are generated in the substrate and trapped in potential wells created by electrostatic gates, leading to the formation of either a charge reservoir or a quantum dot. We have successfully detected single charge jumps resulting from tunneling events between a single quantum dot and a reservoir, which is a significant step towards the detection and manipulation of individual spins in these nanoscale structures.

The next step in this research direction would be to enter the double quantum dot regime for holes, which is highly desirable for achieving ultimate single spin detection. In this regime, a single hole is shared by two quantum dots (it hops between the two dots), resulting in a large electric dipole moment of the double dot. This dipole moment should interact more strongly with the resonator electric field compared to the case of a localized charge in a single dot. Moreover, the double dot structure provides a way to leverage the strong spin–orbit interaction that is intrinsic to hole spins [171]. With a combination of all these features, the strong spin-photon coupling regime could be eventually reached, a single-spin state being read out dispersively in a single shot, and long-range coupling between two distant spins becoming possible [172]. This would open up new opportunities for quantum information processing with hole spins and cQED.

The concept demonstrated in this thesis is not limited to the AlGaAs/GaAs material platform that we have used, but is rather universal and can be extended to other systems. For instance, hole spin in silicon or germanium [7, 146] are also considered as promising candidates for quantum computing. Detecting single optically-generated hole spins in silicon and germanium systems is expected to be feasible with our approach.

In addition to advancing the field of cQED with spins in semiconductor quantum dots, our platform also creates opportunities for interfacing and establishing quantum transduction between the microwave and optical domains [173], which could tackle the challenges of building long-distance quantum network based on superconducting qubits, spins and optical photons.

Appendix A

Quantization of a transmission line resonator

Given the Hamiltonian of transmission line at a continuum limit

$$H = \int_0^d dx(\frac{Q(x,t)^2}{2c_0} + \frac{(\partial_x \Phi(x,t))^2}{2l_0}) = \int_0^d dx\mathcal{H}, \tag{A.1}$$

one can verify the charge $Q(x,t) = c_0 V(x,t) = c_0 \partial_t \Phi(x,t)$ and the flux $\Phi(x,t)$ are canonical conjugate field variables, and Hamilton equations take the form of functional derivative:

$$\partial_t \Phi(x,t) = \frac{\delta H}{\delta Q(x,t)}, \ \partial_t Q(x,t) = -\frac{\delta H}{\delta \Phi(x,t)}. \tag{A.2}$$

The derivative is given by

$$\frac{\delta H}{\delta \Phi(x,t)} = \frac{\partial \mathcal{H}}{\partial \Phi(x,t)} - \frac{\partial}{\partial x}\frac{\partial \mathcal{H}}{\partial(\partial_x \Phi(x,t))} - \frac{\partial}{\partial t}\frac{\partial \mathcal{H}}{\partial(\partial_t \Phi(x,t))}. \tag{A.3}$$

Therefore we have the equation of motion

$$\partial_t Q(x,t) = \frac{1}{l_0}\frac{\partial^2 \Phi(x,t)}{\partial x^2}, \tag{A.4}$$

and by using the relation $Q(x,t) = c_0 \partial_t \Phi(x,t)$ we find the following wave equation describing the wave in transmission line.

$$\frac{\partial^2 \Phi(x,t)}{\partial t^2} = v_0^2 \frac{\partial^2 \Phi(x,t)}{\partial x^2}, \tag{A.5}$$

where $v_0 = 1/\sqrt{l_0 c_0}$ is the speed of wave in the medium.

We assume the solutions to Equation A.5 take the form of plane wave composed of normal modes

$$\Phi(x,t) = \sum_{m=0}^{\infty} u_m(x)\Phi_m(t), m = 0, 1, 2, 3... \tag{A.6}$$

The function

$$u_m(x) = A_m cos(k_m x + \theta_m) \tag{A.7}$$

gives the mode spacial profile along the transmission line with an amplitude A_m, where k_m is wavevector and θ_m is phase. The time-dependent part $\Phi_m(t)$ satisfying

$$\ddot{\Phi}_m(t) = -\omega_m^2 \Phi_m(t) \tag{A.8}$$

oscillates at the frequency ω_m for a given mode m.

In the example of open-ended transmission line resonator in Figure 2.5c, the boundary conditions for all the normal modes are set by the zero current at two gaps, such that

$$I(x)|_{x=0,d} = \left.\frac{\partial \Phi(x,t)}{l_0 \partial x}\right|_{x=0,d} = 0, \tag{A.9}$$

yielding $\theta_m = 0$ and discret wavevectors $k_m = (m+1)\pi/d$. Moreover, from the orthonormal requirement of the solution

$$\int_0^d \mathrm{d}x \; u_m(x) u_{m'}(x) = \delta_{mm'}, \tag{A.10}$$

we can find the normalization constant $A_m = \sqrt{2/d}$.

Then we can use normal mode expansion to express the Hamiltonian in Equation A.1 into a simpler form

$$H = \sum_{m=0}^{\infty} \left(\frac{Q_m^2}{2C_T} + \frac{1}{2} C_T \omega_m^2 \Phi_m^2\right), \tag{A.11}$$

where $Q_m = C_T \dot{\Phi}_m$ and Φ_m are conjugate charge and flux, with $C_T = dc_0$ being the total capacitance of the resonator. Comparing to the sample LC oscillator Hamiltonian in Equation 2.13, we can find out that the Hamiltonian of a transmission line resonator is a sum over independent harmonic oscillators from fundamental mode ($m = 0$) to infinity. As a result, we can take the same quantization approach used for simple LC oscillator, in which we promote the conjugate variables to non-commuting operators defined as

$$\hat{\phi}_m = \sqrt{\frac{\hbar Z_m}{2}} (\hat{a}_m^\dagger + \hat{a}_m), \tag{A.12}$$

$$\hat{q}_m = i \sqrt{\frac{\hbar}{2 Z_m}} (\hat{a}_m^\dagger - \hat{a}_m), \tag{A.13}$$

where $Z_m = \sqrt{L_m / C_T}$ is the characteristic impedance of mode m and $L_m \equiv 1/C_T \omega_m^2$. The Hamiltonian of the system can be written as

$$H = \sum_{m=0}^{\infty} \hbar \omega_m (\hat{a}_m^\dagger \hat{a}_m + \frac{1}{2}), \tag{A.14}$$

where $\omega_m = (m+1)\omega_0$ is the mode frequency with $\omega_0 / 2\pi = v_0 / 2d$ being the frequency of fundamental mode of open-ended $\lambda/2$ resonator. The flux writes

$$\Phi_m(x) = u_m(x) \hat{\phi}_m. \tag{A.15}$$

Bibliography

[1] Alexandre Blais et al. “Circuit Quantum Electrodynamics”. In: *Reviews of Modern Physics* 93.2 (May 19, 2021), p. 025005. DOI: `10.1103/RevModPhys.93.025005` (cit. on pp. 1, 13, 30).

[2] Guido Burkard et al. “Superconductor–Semiconductor Hybrid-Circuit Quantum Electrodynamics”. In: *Nature Reviews Physics* 2.3 (3 Mar. 2020), pp. 129–140. DOI: `10.1038/s42254-019-0135-2` (cit. on pp. 1, 13).

[3] A. Bienfait et al. “Controlling Spin Relaxation with a Cavity”. In: *Nature* 531.7592 (7592 Mar. 2016), pp. 74–77. DOI: `10.1038/nature16944` (cit. on pp. 3, 13, 17, 42, 43, 103).

[4] Raphaël Lescanne et al. “Irreversible Qubit-Photon Coupling for the Detection of Itinerant Microwave Photons”. In: *Physical Review X* 10.2 (May 18, 2020), p. 021038. DOI: `10.1103/PhysRevX.10.021038` (cit. on pp. 3, 10, 48).

[5] Emanuele Albertinale et al. “Detecting Spins by Their Fluorescence with a Microwave Photon Counter”. In: *Nature* 600.7889 (7889 Dec. 2021), pp. 434–438. DOI: `10.1038/s41586-021-04076-z` (cit. on pp. 3, 13, 19, 21, 48, 81, 92, 96).

[6] Marianne Le Dantec et al. “Twenty-Three–Millisecond Electron Spin Coherence of Erbium Ions in a Natural-Abundance Crystal”. In: *Science Advances* 7.51 (Dec. 15, 2021), eabj9786. DOI: `10.1126/sciadv.abj9786` (cit. on pp. 5, 19, 63, 104).

[7] Cécile X. Yu et al. “Strong Coupling between a Photon and a Hole Spin in Silicon”. In: *Nature Nanotechnology* (Mar. 6, 2023), pp. 1–6. DOI: `10.1038/s41565-023-01332-3` (cit. on pp. 5, 163, 167).

[8] T. Frey et al. “Dipole Coupling of a Double Quantum Dot to a Microwave Resonator”. In: *Physical Review Letters* 108.4 (Jan. 25, 2012), p. 046807. DOI: `10.1103/PhysRevLett.108.046807` (cit. on pp. 6, 22, 119, 120).

[9] Serge Haroche and J.-M. Raimond. *Exploring the Quantum: Atoms, Cavities, and Photons*. OUP Oxford, Aug. 10, 2006. 616 pp. Google Books: `ynwSDAAAQBAJ` (cit. on pp. 9, 42, 43).

[10] Alexandre Blais et al. “Cavity Quantum Electrodynamics for Superconducting Electrical Circuits: An Architecture for Quantum Computation”. In: *Physical Review A* 69.6 (June 29, 2004), p. 062320. DOI: `10.1103/PhysRevA.69.062320` (cit. on pp. 9, 18, 58, 119, 122, 126).

[11] A. Wallraff et al. “Strong Coupling of a Single Photon to a Superconducting Qubit Using Circuit Quantum Electrodynamics”. In: *Nature* 431.7005 (7005 Sept. 2004), pp. 162–167. DOI: `10.1038/nature02851` (cit. on pp. 9, 17, 18).

[12] Bernard Valeur and Mário N. Berberan-Santos. "A Brief History of Fluorescence and Phosphorescence before the Emergence of Quantum Theory". In: *Journal of Chemical Education* 88.6 (June 1, 2011), pp. 731–738. DOI: `10.1021/ed100182h` (cit. on p. 10).

[13] Robert H. Hadfield. "Single-Photon Detectors for Optical Quantum Information Applications". In: *Nature Photonics* 3.12 (12 Dec. 2009), pp. 696–705. DOI: `10.1038/nphoton.2009.230` (cit. on p. 10).

[14] G. A. Morton. "Photomultipliers for Scintillation Counting". In: *R C A Rev.* Vol: 10 (Dec. 1, 1949) (cit. on p. 10).

[15] S. Cova, A. Longoni, and A. Andreoni. "Towards Picosecond Resolution with Single-photon Avalanche Diodes". In: *Review of Scientific Instruments* 52.3 (Mar. 1981), pp. 408–412. DOI: `10.1063/1.1136594` (cit. on p. 10).

[16] G. N. Gol'tsman et al. "Picosecond Superconducting Single-Photon Optical Detector". In: *Applied Physics Letters* 79.6 (Aug. 6, 2001), pp. 705–707. DOI: `10.1063/1.1388868` (cit. on p. 10).

[17] S. Kono et al. "Quantum Non-Demolition Detection of an Itinerant Microwave Photon". In: *Nature Physics* 14.6 (6 June 2018), pp. 546–549. DOI: `10.1038/s41567-018-0066-3` (cit. on pp. 10, 48).

[18] Jean-Claude Besse et al. "Single-Shot Quantum Nondemolition Detection of Individual Itinerant Microwave Photons". In: *Physical Review X* 8.2 (Apr. 3, 2018), p. 021003. DOI: `10.1103/PhysRevX.8.021003` (cit. on pp. 10, 48).

[19] John Clarke et al. "Quantum Mechanics of a Macroscopic Variable: The Phase Difference of a Josephson Junction". In: *Science* 239.4843 (Feb. 26, 1988), pp. 992–997. DOI: `10.1126/science.239.4843.992` (cit. on p. 11).

[20] V. Bouchiat et al. "Quantum Coherence with a Single Cooper Pair". In: *Physica Scripta* 1998.T76 (Jan. 1, 1998), p. 165. DOI: `10.1238/Physica.Topical.076a00165` (cit. on p. 11).

[21] Y. Nakamura, Yu A. Pashkin, and J. S. Tsai. "Coherent Control of Macroscopic Quantum States in a Single-Cooper-pair Box". In: *Nature* 398.6730 (6730 Apr. 1999), pp. 786–788. DOI: `10.1038/19718` (cit. on p. 11).

[22] D. Vion et al. "Manipulating the Quantum State of an Electrical Circuit". In: *Science* 296.5569 (May 3, 2002), pp. 886–889. DOI: `10.1126/science.1069372` (cit. on p. 11).

[23] I. I. Rabi et al. "A New Method of Measuring Nuclear Magnetic Moment". In: *Physical Review* 53.4 (Feb. 15, 1938), pp. 318–318. DOI: `10.1103/PhysRev.53.318` (cit. on p. 11).

[24] Zavoisky E. "Spin-Magnetic Resonance in Paramagnetics". In: *J Phys USSR* 9 (1945), pp. 211–245 (cit. on pp. 11, 54).

[25] Arthur Schweiger and Gunnar Jeschke. *Principles of Pulse Electron Paramagnetic Resonance*. Oxford University Press, 2001. 608 pp. Google Books: `tkvQQElkW1wC` (cit. on p. 11).

[26] M. H. Abobeih et al. "Fault-Tolerant Operation of a Logical Qubit in a Diamond Quantum Processor". In: *Nature* 606.7916 (7916 June 2022), pp. 884–889. DOI: `10.1038/s41586-022-04819-6` (cit. on p. 11).

[27] J. Wrachtrup et al. “Optical Detection of Magnetic Resonance in a Single Molecule”. In: *Nature* 363.6426 (6426 May 1993), pp. 244–245. DOI: `10.1038/363244a0` (cit. on p. 11).

[28] A. Gruber et al. “Scanning Confocal Optical Microscopy and Magnetic Resonance on Single Defect Centers”. In: *Science* 276.5321 (June 27, 1997), pp. 2012–2014. DOI: `10.1126/science.276.5321.2012` (cit. on p. 11).

[29] Mouktik Raha et al. “Optical Quantum Nondemolition Measurement of a Single Rare Earth Ion Qubit”. In: *Nature Communications* 11.1 (1 Mar. 30, 2020), p. 1605. DOI: `10.1038/s41467-020-15138-7` (cit. on pp. 11, 21).

[30] J. M. Elzerman et al. “Single-Shot Read-out of an Individual Electron Spin in a Quantum Dot”. In: *Nature* 430.6998 (6998 July 2004), pp. 431–435. DOI: `10.1038/nature02693` (cit. on p. 11).

[31] Romain Vincent et al. “Electronic Read-out of a Single Nuclear Spin Using a Molecular Spin Transistor”. In: *Nature* 488.7411 (7411 Aug. 2012), pp. 357–360. DOI: `10.1038/nature11341` (cit. on pp. 11, 108).

[32] Jarryd J. Pla et al. “A Single-Atom Electron Spin Qubit in Silicon”. In: *Nature* 489.7417 (7417 Sept. 2012), pp. 541–545. DOI: `10.1038/nature11449` (cit. on pp. 11, 110).

[33] Stefan Thiele et al. “Electrically Driven Nuclear Spin Resonance in Single-Molecule Magnets”. In: *Science* 344.6188 (June 6, 2014), pp. 1135–1138. DOI: `10.1126/science.1249802` (cit. on p. 11).

[34] D. Rugar et al. “Single Spin Detection by Magnetic Resonance Force Microscopy”. In: *Nature* 430.6997 (6997 July 2004), pp. 329–332. DOI: `10.1038/nature02658` (cit. on p. 11).

[35] Susanne Baumann et al. “Electron Paramagnetic Resonance of Individual Atoms on a Surface”. In: *Science* 350.6259 (Oct. 23, 2015), pp. 417–420. DOI: `10.1126/science.aac8703` (cit. on p. 11).

[36] M. S. Grinolds et al. “Subnanometre Resolution in Three-Dimensional Magnetic Resonance Imaging of Individual Dark Spins”. In: *Nature Nanotechnology* 9.4 (4 Apr. 2014), pp. 279–284. DOI: `10.1038/nnano.2014.30` (cit. on p. 11).

[37] Nan Zhao et al. “Sensing Single Remote Nuclear Spins”. In: *Nature Nanotechnology* 7.10 (10 Oct. 2012), pp. 657–662. DOI: `10.1038/nnano.2012.152` (cit. on p. 11).

[38] Shimon Kolkowitz et al. “Sensing Distant Nuclear Spins with a Single Electron Spin”. In: *Physical Review Letters* 109.13 (Sept. 25, 2012), p. 137601. DOI: `10.1103/PhysRevLett.109.137601` (cit. on p. 11).

[39] T. H. Taminiau et al. “Detection and Control of Individual Nuclear Spins Using a Weakly Coupled Electron Spin”. In: *Physical Review Letters* 109.13 (Sept. 25, 2012), p. 137602. DOI: `10.1103/PhysRevLett.109.137602` (cit. on p. 11).

[40] M. H. Abobeih et al. “Atomic-Scale Imaging of a 27-Nuclear-Spin Cluster Using a Quantum Sensor”. In: *Nature* 576.7787 (7787 Dec. 2019), pp. 411–415. DOI: `10.1038/s41586-019-1834-7` (cit. on p. 11).

[41] Heinz-Jürgen Steinhoff et al. “High-Field EPR Studies of the Structure and Conformational Changes of Site-Directed Spin Labeled Bacteriorhodopsin”. In: *Biochimica et Biophysica Acta (BBA) - Bioenergetics* 1457.3 (Apr. 21, 2000), pp. 253–262. DOI: 10.1016/S0005-2728(00)00106-7 (cit. on p. 11).

[42] Olivier Duss et al. “EPR-aided Approach for Solution Structure Determination of Large RNAs or Protein–RNA Complexes”. In: *Nature Communications* 5.1 (1 May 14, 2014), p. 3669. DOI: 10.1038/ncomms4669 (cit. on p. 11).

[43] David Deutsch and Roger Penrose. “Quantum Theory, the Church–Turing Principle and the Universal Quantum Computer”. In: *Proceedings of the Royal Society of London. A. Mathematical and Physical Sciences* 400.1818 (July 8, 1985), pp. 97–117. DOI: 10.1098/rspa.1985.0070 (cit. on p. 12).

[44] P.W. Shor. “Algorithms for Quantum Computation: Discrete Logarithms and Factoring”. In: *Proceedings 35th Annual Symposium on Foundations of Computer Science*. Proceedings 35th Annual Symposium on Foundations of Computer Science. Nov. 1994, pp. 124–134. DOI: 10.1109/SFCS.1994.365700 (cit. on p. 12).

[45] Lov K. Grover. “Quantum Mechanics Helps in Searching for a Needle in a Haystack”. In: *Physical Review Letters* 79.2 (July 14, 1997), pp. 325–328. DOI: 10.1103/PhysRevLett.79.325 (cit. on p. 12).

[46] Frank Arute et al. “Quantum Supremacy Using a Programmable Superconducting Processor”. In: *Nature* 574.7779 (7779 Oct. 2019), pp. 505–510. DOI: 10.1038/s41586-019-1666-5 (cit. on p. 12).

[47] Abhinav Kandala et al. “Hardware-Efficient Variational Quantum Eigensolver for Small Molecules and Quantum Magnets”. In: *Nature* 549.7671 (7671 Sept. 2017), pp. 242–246. DOI: 10.1038/nature23879 (cit. on p. 12).

[48] Guido Burkard et al. *Semiconductor Spin Qubits*. Dec. 16, 2021. DOI: 10.48550/arXiv.2112.08863. arXiv: arXiv:2112.08863. URL: http://arxiv.org/abs/2112.08863 (visited on 12/20/2022). preprint (cit. on pp. 13, 22, 110).

[49] Colin D. Bruzewicz et al. “Trapped-Ion Quantum Computing: Progress and Challenges”. In: *Applied Physics Reviews* 6.2 (June 2019), p. 021314. DOI: 10.1063/1.5088164 (cit. on p. 13).

[50] Pascal Scholl et al. “Quantum Simulation of 2D Antiferromagnets with Hundreds of Rydberg Atoms”. In: *Nature* 595.7866 (7866 July 2021), pp. 233–238. DOI: 10.1038/s41586-021-03585-1 (cit. on p. 13).

[51] Dolev Bluvstein et al. “A Quantum Processor Based on Coherent Transport of Entangled Atom Arrays”. In: *Nature* 604.7906 (7906 Apr. 2022), pp. 451–456. DOI: 10.1038/s41586-022-04592-6 (cit. on p. 13).

[52] Lars S. Madsen et al. “Quantum Computational Advantage with a Programmable Photonic Processor”. In: *Nature* 606.7912 (7912 June 2022), pp. 75–81. DOI: 10.1038/s41586-022-04725-x (cit. on p. 13).

[53] Han-Sen Zhong et al. “Quantum Computational Advantage Using Photons”. In: *Science* 370.6523 (Dec. 18, 2020), pp. 1460–1463. DOI: 10.1126/science.abe8770 (cit. on p. 13).

[54] *IBM Quantum Computing — Roadmap*. Oct. 1, 2015. URL: https://www.ibm.com/quantum/www.ibm.com/quantum/roadmap (visited on 12/20/2022) (cit. on p. 13).

[55] Alexander P. M. Place et al. "New Material Platform for Superconducting Transmon Qubits with Coherence Times Exceeding 0.3 Milliseconds". In: *Nature Communications* 12.1 (1 Mar. 19, 2021), p. 1779. DOI: 10.1038/s41467-021-22030-5 (cit. on p. 13).

[56] Long B. Nguyen et al. "Scalable High-Performance Fluxonium Quantum Processor". In: *PRX Quantum* 3.3 (Aug. 5, 2022), p. 037001. DOI: 10.1103/PRXQuantum.3.037001. arXiv: 2201.09374 [cond-mat, physics:quant-ph] (cit. on p. 13).

[57] Alexei M. Tyryshkin et al. "Electron Spin Coherence Exceeding Seconds in High-Purity Silicon". In: *Nature Materials* 11.2 (2 Feb. 2012), pp. 143–147. DOI: 10.1038/nmat3182 (cit. on p. 13).

[58] Juha T. Muhonen et al. "Storing Quantum Information for 30 Seconds in a Nanoelectronic Device". In: *Nature Nanotechnology* 9.12 (12 Dec. 2014), pp. 986–991. DOI: 10.1038/nnano.2014.211 (cit. on pp. 13, 106).

[59] N. Bar-Gill et al. "Solid-State Electronic Spin Coherence Time Approaching One Second". In: *Nature Communications* 4.1 (1 Apr. 23, 2013), p. 1743. DOI: 10.1038/ncomms2771 (cit. on p. 13).

[60] Miloš Rančić et al. "Coherence Time of over a Second in a Telecom-Compatible Quantum Memory Storage Material". In: *Nature Physics* 14.1 (1 Jan. 2018), pp. 50–54. DOI: 10.1038/nphys4254 (cit. on p. 13).

[61] Ruoyu Li et al. "A Crossbar Network for Silicon Quantum Dot Qubits". In: *Science Advances* 4.7 (July 6, 2018), eaar3960. DOI: 10.1126/sciadv.aar3960 (cit. on p. 13).

[62] Guilherme Tosi et al. "Silicon Quantum Processor with Robust Long-Distance Qubit Couplings". In: *Nature Communications* 8.1 (1 Sept. 6, 2017), p. 450. DOI: 10.1038/s41467-017-00378-x (cit. on p. 13).

[63] Ze-Liang Xiang et al. "Hybrid Quantum Circuits: Superconducting Circuits Interacting with Other Quantum Systems". In: *Reviews of Modern Physics* 85.2 (Apr. 9, 2013), pp. 623–653. DOI: 10.1103/RevModPhys.85.623 (cit. on p. 13).

[64] A. A. Clerk et al. "Hybrid Quantum Systems with Circuit Quantum Electrodynamics". In: *Nature Physics* 16.3 (3 Mar. 2020), pp. 257–267. DOI: 10.1038/s41567-020-0797-9 (cit. on p. 13).

[65] Y. Kubo et al. "Hybrid Quantum Circuit with a Superconducting Qubit Coupled to a Spin Ensemble". In: *Physical Review Letters* 107.22 (Nov. 21, 2011), p. 220501. DOI: 10.1103/PhysRevLett.107.220501 (cit. on p. 13).

[66] B. D. Josephson. "Coupled Superconductors". In: *Reviews of Modern Physics* 36.1 (Jan. 1, 1964), pp. 216–220. DOI: 10.1103/RevModPhys.36.216 (cit. on p. 14).

[67] Jens Koch et al. "Charge-Insensitive Qubit Design Derived from the Cooper Pair Box". In: *Physical Review A* 76.4 (Oct. 12, 2007), p. 042319. DOI: 10.1103/PhysRevA.76.042319 (cit. on pp. 15, 34, 36, 48).

[68] J. Majer et al. “Coupling Superconducting Qubits via a Cavity Bus”. In: *Nature* 449.7161 (7161 Sept. 2007), pp. 443–447. DOI: 10.1038/nature06184 (cit. on p. 15).

[69] E. M. Purcell, H. C. Torrey, and R. V. Pound. “Resonance Absorption by Nuclear Magnetic Moments in a Solid”. In: *Physical Review* 69.1-2 (Jan. 1, 1946), pp. 37–38. DOI: 10.1103/PhysRev.69.37 (cit. on p. 17).

[70] P. Goy et al. “Observation of Cavity-Enhanced Single-Atom Spontaneous Emission”. In: *Physical Review Letters* 50.24 (June 13, 1983), pp. 1903–1906. DOI: 10.1103/PhysRevLett.50.1903 (cit. on p. 17).

[71] J. M. Raimond, M. Brune, and S. Haroche. “Manipulating Quantum Entanglement with Atoms and Photons in a Cavity”. In: *Reviews of Modern Physics* 73.3 (Aug. 28, 2001), pp. 565–582. DOI: 10.1103/RevModPhys.73.565 (cit. on p. 17).

[72] Serge Haroche and Jean-Michel Raimond. “Cavity Quantum Electrodynamics”. In: *Scientific American* (1993) (cit. on p. 18).

[73] C. Monroe et al. “Demonstration of a Fundamental Quantum Logic Gate”. In: *Physical Review Letters* 75.25 (Dec. 18, 1995), pp. 4714–4717. DOI: 10.1103/PhysRevLett.75.4714 (cit. on p. 18).

[74] J. P. Reithmaier et al. “Strong Coupling in a Single Quantum Dot–Semiconductor Microcavity System”. In: *Nature* 432.7014 (7014 Nov. 2004), pp. 197–200. DOI: 10.1038/nature02969 (cit. on p. 18).

[75] T. Yoshie et al. “Vacuum Rabi Splitting with a Single Quantum Dot in a Photonic Crystal Nanocavity”. In: *Nature* 432.7014 (7014 Nov. 2004), pp. 200–203. DOI: 10.1038/nature03119 (cit. on p. 18).

[76] K. J. Satzinger et al. “Quantum Control of Surface Acoustic-Wave Phonons”. In: *Nature* 563.7733 (7733 Nov. 2018), pp. 661–665. DOI: 10.1038/s41586-018-0719-5 (cit. on p. 18).

[77] Dany Lachance-Quirion et al. “Resolving Quanta of Collective Spin Excitations in a Millimeter-Sized Ferromagnet”. In: *Science Advances* 3.7 (July 5, 2017), e1603150. DOI: 10.1126/sciadv.1603150 (cit. on p. 18).

[78] Dany Lachance-Quirion et al. “Entanglement-Based Single-Shot Detection of a Single Magnon with a Superconducting Qubit”. In: *Science* 367.6476 (Jan. 24, 2020), pp. 425–428. DOI: 10.1126/science.aaz9236 (cit. on p. 18).

[79] C. Janvier et al. “Coherent Manipulation of Andreev States in Superconducting Atomic Contacts”. In: *Science* 349.6253 (Sept. 11, 2015), pp. 1199–1202. DOI: 10.1126/science.aab2179 (cit. on p. 18).

[80] A. Stockklauser et al. “Strong Coupling Cavity QED with Gate-Defined Double Quantum Dots Enabled by a High Impedance Resonator”. In: *Physical Review X* 7.1 (Mar. 9, 2017), p. 011030. DOI: 10.1103/PhysRevX.7.011030 (cit. on pp. 18, 126).

[81] X. Mi et al. “Strong Coupling of a Single Electron in Silicon to a Microwave Photon”. In: *Science* 355.6321 (Jan. 13, 2017), pp. 156–158. DOI: 10.1126/science.aal2469 (cit. on p. 18).

[82] P. Scarlino et al. “All-Microwave Control and Dispersive Readout of Gate-Defined Quantum Dot Qubits in Circuit Quantum Electrodynamics”. In: *Physical Review Letters* 122.20 (May 22, 2019), p. 206802. DOI: `10.1103/PhysRevLett.122.206802` (cit. on p. 18).

[83] A. Bienfait et al. “Reaching the Quantum Limit of Sensitivity in Electron Spin Resonance”. In: *Nature Nanotechnology* 11.3 (3 Mar. 2016), pp. 253–257. DOI: `10.1038/nnano.2015.282` (cit. on pp. 19, 20).

[84] J. J. Viennot et al. “Coherent Coupling of a Single Spin to Microwave Cavity Photons”. In: *Science* 349.6246 (July 24, 2015), pp. 408–411. DOI: `10.1126/science.aaa3786` (cit. on pp. 19, 22, 110).

[85] X. Mi et al. “A Coherent Spin–Photon Interface in Silicon”. In: *Nature* 555.7698 (7698 Mar. 2018), pp. 599–603. DOI: `10.1038/nature25769` (cit. on pp. 19, 22).

[86] N. Samkharadze et al. “Strong Spin-Photon Coupling in Silicon”. In: *Science* 359.6380 (Mar. 9, 2018), pp. 1123–1127. DOI: `10.1126/science.aar4054` (cit. on pp. 19, 22, 126).

[87] A. M. Dibos et al. “Atomic Source of Single Photons in the Telecom Band”. In: *Physical Review Letters* 120.24 (June 11, 2018), p. 243601. DOI: `10.1103/PhysRevLett.120.243601` (cit. on pp. 21, 91, 101).

[88] R. L. Bell. “Electric Dipole Spin Transitions in InSb”. In: *Physical Review Letters* 9.2 (July 15, 1962), pp. 52–54. DOI: `10.1103/PhysRevLett.9.52` (cit. on p. 21).

[89] S. Nadj-Perge et al. “Spin–Orbit Qubit in a Semiconductor Nanowire”. In: *Nature* 468.7327 (7327 Dec. 2010), pp. 1084–1087. DOI: `10.1038/nature09682` (cit. on p. 22).

[90] M. Pioro-Ladrière et al. “Electrically Driven Single-Electron Spin Resonance in a Slanting Zeeman Field”. In: *Nature Physics* 4.10 (10 Oct. 2008), pp. 776–779. DOI: `10.1038/nphys1053` (cit. on p. 22).

[91] R. Maurand et al. “A CMOS Silicon Spin Qubit”. In: *Nature Communications* 7.1 (1 Nov. 24, 2016), p. 13575. DOI: `10.1038/ncomms13575` (cit. on p. 22).

[92] N. W. Hendrickx et al. “A Single-Hole Spin Qubit”. In: *Nature Communications* 11.1 (1 July 10, 2020), p. 3478. DOI: `10.1038/s41467-020-17211-7` (cit. on p. 22).

[93] Sergei Studenikin et al. “Electrically Tunable Effective G-Factor of a Single Hole in a Lateral GaAs/AlGaAs Quantum Dot”. In: *Communications Physics* 2.1 (1 Dec. 13, 2019), pp. 1–8. DOI: `10.1038/s42005-019-0262-1` (cit. on p. 22).

[94] Guokui Liu and Bernard Jacquier. *Spectroscopic Properties of Rare Earths in Optical Materials*. Springer Science & Business Media, Jan. 29, 2006. 567 pp. Google Books: `XEArxM4rPv0C` (cit. on p. 27).

[95] Bernal G. Enrique. “Optical Spectrum and Magnetic Properties of Er $^{3+}$ in CaWO $_4$”. In: *The Journal of Chemical Physics* 55.5 (Sept. 1971), pp. 2538–2549. DOI: `10.1063/1.1676445` (cit. on p. 27).

[96] Antipin, A. A et al. "Paramagnetic Resonance and Spin-Lattice Relaxation of Er3+ and Tb3+ Ions in Crystal Lattice of CaWO4". In: *Soviet physics solid state, USSR* 10.2 (1968), pp. 468–+ (cit. on p. 28).

[97] E.T. Jaynes and F.W. Cummings. "Comparison of Quantum and Semiclassical Radiation Theories with Application to the Beam Maser". In: *Proceedings of the IEEE* 51.1 (Jan. 1963), pp. 89–109. DOI: `10.1109/PROC.1963.1664` (cit. on p. 39).

[98] A. A. Houck et al. "Controlling the Spontaneous Emission of a Superconducting Transmon Qubit". In: *Physical Review Letters* 101.8 (Aug. 21, 2008), p. 080502. DOI: `10.1103/PhysRevLett.101.080502` (cit. on p. 42).

[99] Eyob A. Sete, Jay M. Gambetta, and Alexander N. Korotkov. "Purcell Effect with Microwave Drive: Suppression of Qubit Relaxation Rate". In: *Physical Review B* 89.10 (Mar. 21, 2014), p. 104516. DOI: `10.1103/PhysRevB.89.104516` (cit. on p. 42).

[100] Eyob A. Sete, John M. Martinis, and Alexander N. Korotkov. "Quantum Theory of a Bandpass Purcell Filter for Qubit Readout". In: *Physical Review A* 92.1 (July 21, 2015), p. 012325. DOI: `10.1103/PhysRevA.92.012325` (cit. on p. 42).

[101] M. J. Collett and C. W. Gardiner. "Squeezing of Intracavity and Traveling-Wave Light Fields Produced in Parametric Amplification". In: *Physical Review A* 30.3 (Sept. 1, 1984), pp. 1386–1391. DOI: `10.1103/PhysRevA.30.1386` (cit. on p. 43).

[102] C. W. Gardiner and M. J. Collett. "Input and Output in Damped Quantum Systems: Quantum Stochastic Differential Equations and the Master Equation". In: *Physical Review A* 31.6 (June 1, 1985), pp. 3761–3774. DOI: `10.1103/PhysRevA.31.3761` (cit. on p. 43).

[103] S. Probst et al. "Efficient and Robust Analysis of Complex Scattering Data under Noise in Microwave Resonators". In: *Review of Scientific Instruments* 86.2 (Feb. 2015), p. 024706. DOI: `10.1063/1.4907935` (cit. on pp. 46, 146, 147).

[104] Y.-F. Chen et al. "Microwave Photon Counter Based on Josephson Junctions". In: *Physical Review Letters* 107.21 (Nov. 14, 2011), p. 217401. DOI: `10.1103/PhysRevLett.107.217401` (cit. on p. 48).

[105] Kunihiro Inomata et al. "Single Microwave-Photon Detector Using an Artificial -type Three-Level System". In: *Nature Communications* 7.1 (1 July 25, 2016), p. 12303. DOI: `10.1038/ncomms12303` (cit. on p. 48).

[106] A. Opremcak et al. "Measurement of a Superconducting Qubit with a Microwave Photon Counter". In: *Science* 361.6408 (Sept. 21, 2018), pp. 1239–1242. DOI: `10.1126/science.aat4625` (cit. on p. 48).

[107] R. Dassonneville et al. "Number-Resolved Photocounter for Propagating Microwave Mode". In: *Physical Review Applied* 14.4 (Oct. 14, 2020), p. 044022. DOI: `10.1103/PhysRevApplied.14.044022` (cit. on p. 48).

[108] Balembois, Léo. "Towards Hybrid Quantum Calculation from Superconducting Circuit to Nuclear Spins". These de doctorat. Université Paris-Saclay, 2023 (cit. on pp. 48, 62, 72).

[109] X. Y. Jin et al. "Thermal and Residual Excited-State Population in a 3D Transmon Qubit". In: *Physical Review Letters* 114.24 (June 15, 2015), p. 240501. DOI: `10.1103/PhysRevLett.114.240501` (cit. on p. 53).

[110] L. Cardani et al. "Reducing the Impact of Radioactivity on Quantum Circuits in a Deep-Underground Facility". In: *Nature Communications* 12.1 (1 May 12, 2021), p. 2733. DOI: `10.1038/s41467-021-23032-z` (cit. on p. 53).

[111] Eric Billaud et al. *Microwave Fluorescence Detection of Spin Echoes*. Aug. 29, 2022. DOI: `10.48550/arXiv.2208.13586`. arXiv: `arXiv:2208.13586`. URL: `http://arxiv.org/abs/2208.13586` (visited on 02/11/2023). preprint (cit. on pp. 57, 104).

[112] N. Bergeal et al. "Phase-Preserving Amplification near the Quantum Limit with a Josephson Ring Modulator". In: *Nature* 465.7294 (7294 May 2010), pp. 64–68. DOI: `10.1038/nature09035` (cit. on p. 58).

[113] C. Macklin et al. "A near–Quantum-Limited Josephson Traveling-Wave Parametric Amplifier". In: *Science* 350.6258 (Oct. 16, 2015), pp. 307–310. DOI: `10.1126/science.aaa8525` (cit. on p. 58).

[114] Marianne Le Dantec. "Electron Spin Dynamics of Erbium Ions in Scheelite Crystals, Probed with Superconducting Resonators at Millikelvin Temperatures". These de doctorat. Université Paris-Saclay, Jan. 24, 2022 (cit. on pp. 62, 63, 77, 89, 102, 103).

[115] John R. de Laeter et al. "Atomic weights of the elements. Review 2000 (IUPAC Technical Report)". In: *Pure and Applied Chemistry* 75.6 (Jan. 1, 2003), pp. 683–800. DOI: `10.1351/pac200375060683` (cit. on p. 62).

[116] W. S. Brower and P. H. Fang. "Dielectric Constants of PbWO $_4$ and CaWO $_4$". In: *Journal of Applied Physics* 38.5 (Apr. 1967), pp. 2391–2392. DOI: `10.1063/1.1709895` (cit. on p. 65).

[117] J. S. Thorp and E. A. E. Ammar. "The Dielectric Constants of CaWO4, Nd/CaWO4 and Gd/CaWO4". In: *Journal of Materials Science* 10.6 (June 1, 1975), pp. 918–922. DOI: `10.1007/BF00823207` (cit. on p. 66).

[118] Theodore Van Duzer and Charles William Turner. *Principles of Superconductive Devices and Circuits*. Prentice Hall, 1999. 458 pp. Google Books: `uoViQgAACAAJ` (cit. on p. 68).

[119] Jack Y. Qiu et al. "Broadband Squeezed Microwaves and Amplification with a Josephson Travelling-Wave Parametric Amplifier". In: *Nature Physics* (Feb. 9, 2023), pp. 1–8. DOI: `10.1038/s41567-022-01929-w` (cit. on p. 74).

[120] Gheorghe Stan, Stuart B. Field, and John M. Martinis. "Critical Field for Complete Vortex Expulsion from Narrow Superconducting Strips". In: *Physical Review Letters* 92.9 (Mar. 5, 2004), p. 097003. DOI: `10.1103/PhysRevLett.92.097003` (cit. on p. 77).

[121] Jay Gambetta et al. "Qubit-Photon Interactions in a Cavity: Measurement-induced Dephasing and Number Splitting". In: *Physical Review A* 74.4 (Oct. 17, 2006), p. 042318. DOI: `10.1103/PhysRevA.74.042318` (cit. on p. 81).

[122] M. Orrit and J. Bernard. “Single Pentacene Molecules Detected by Fluorescence Excitation in a p -Terphenyl Crystal”. In: *Physical Review Letters* 65.21 (Nov. 19, 1990), pp. 2716–2719. DOI: 10.1103/PhysRevLett.65.2716 (cit. on p. 91).

[123] Jonathan M. Kindem et al. “Control and Single-Shot Readout of an Ion Embedded in a Nanophotonic Cavity”. In: *Nature* 580.7802 (7802 Apr. 2020), pp. 201–204. DOI: 10.1038/s41586-020-2160-9 (cit. on p. 91).

[124] J. J. Pla et al. “Strain-Induced Spin-Resonance Shifts in Silicon Devices”. In: *Physical Review Applied* 9.4 (Apr. 10, 2018), p. 044014. DOI: 10.1103/PhysRevApplied.9.044014 (cit. on p. 91).

[125] V. Ranjan et al. “Spatially Resolved Decoherence of Donor Spins in Silicon Strained by a Metallic Electrode”. In: *Physical Review X* 11.3 (Aug. 16, 2021), p. 031036. DOI: 10.1103/PhysRevX.11.031036 (cit. on pp. 91, 105).

[126] D. A. Broadway et al. “Microscopic Imaging of the Stress Tensor in Diamond Using in Situ Quantum Sensors”. In: *Nano Letters* 19.7 (July 10, 2019), pp. 4543–4550. DOI: 10.1021/acs.nanolett.9b01402 (cit. on p. 92).

[127] Eric Billaud. “Spectroscopie de Résonance de Spin Électronique à l’aide de Détection Fluorescente à Des Températures de l’ordre Du Millikelvin, Appliquer à Des Terres Rares Dans La Scheelite”. These en préparation. université Paris-Saclay, 2019 (cit. on p. 96).

[128] B. A. Myers et al. “Probing Surface Noise with Depth-Calibrated Spins in Diamond”. In: *Physical Review Letters* 113.2 (July 9, 2014), p. 027602. DOI: 10.1103/PhysRevLett.113.027602 (cit. on p. 105).

[129] J. G. Castle and D. W. Feldman. “Resonance Modes at Defects in Crystalline Quartz”. In: *Physical Review* 137 (2A Jan. 18, 1965), A671–A673. DOI: 10.1103/PhysRev.137.A671 (cit. on p. 108).

[130] Jean-Pierre Gayda et al. “Temperature Dependence of the Electronic Spin-Lattice Relaxation Time in a 2-Iron-2-Sulfur Protein”. In: *Biochimica et Biophysica Acta (BBA) - Protein Structure* 581.1 (Nov. 23, 1979), pp. 15–26. DOI: 10.1016/0005-2795(79)90216-2 (cit. on p. 108).

[131] Yi Zhou et al. “Electron Spin Lattice Relaxation Rates for S = 12 Molecular Species in Glassy Matrices or Magnetically Dilute Solids at Temperatures between 10 and 300 K”. In: *Journal of Magnetic Resonance* 139.1 (July 1, 1999), pp. 165–174. DOI: 10.1006/jmre.1999.1763 (cit. on p. 108).

[132] V. Ranjan et al. “Electron Spin Resonance Spectroscopy with Femtoliter Detection Volume”. In: *Applied Physics Letters* 116.18 (May 4, 2020), p. 184002. DOI: 10.1063/5.0004322 (cit. on p. 108).

[133] Bernardo Casabone et al. “Dynamic Control of Purcell Enhanced Emission of Erbium Ions in Nanoparticles”. In: *Nature Communications* 12.1 (1 June 11, 2021), p. 3570. DOI: 10.1038/s41467-021-23632-9 (cit. on p. 108).

[134] J. W. A. Coremans et al. “A W-Band Electron Paramagnetic Resonance Study of a Single Crystal of Azurin”. In: *Journal of the American Chemical Society* 116.7 (Apr. 1, 1994), pp. 3097–3101. DOI: 10.1021/ja00086a044 (cit. on p. 108).

[135] Sabine Van Doorslaer and Evi Vinck. “The Strength of EPR and ENDOR Techniques in Revealing Structure–Function Relationships in Metalloproteins”. In: *Physical Chemistry Chemical Physics* 9.33 (Aug. 15, 2007), pp. 4620–4638. DOI: `10.1039/B701568B` (cit. on p. 108).

[136] Richard J. Warburton. “Single Spins in Self-Assembled Quantum Dots”. In: *Nature Materials* 12.6 (6 June 2013), pp. 483–493. DOI: `10.1038/nmat3585` (cit. on p. 110).

[137] Anasua Chatterjee et al. “Semiconductor Qubits In Practice”. In: *Nature Reviews Physics* 3.3 (Feb. 19, 2021), pp. 157–177. DOI: `10.1038/s42254-021-00283-9`. arXiv: `2005.06564 [cond-mat, physics:quant-ph]` (cit. on p. 110).

[138] F. Pelayo García de Arquer et al. “Semiconductor Quantum Dots: Technological Progress and Future Challenges”. In: *Science* 373.6555 (Aug. 6, 2021), eaaz8541. DOI: `10.1126/science.aaz8541` (cit. on p. 110).

[139] Akito Noiri et al. “Fast Universal Quantum Gate above the Fault-Tolerance Threshold in Silicon”. In: *Nature* 601.7893 (7893 Jan. 2022), pp. 338–342. DOI: `10.1038/s41586-021-04182-y` (cit. on p. 110).

[140] Stephan G. J. Philips et al. “Universal Control of a Six-Qubit Quantum Processor in Silicon”. In: *Nature* 609.7929 (7929 Sept. 2022), pp. 919–924. DOI: `10.1038/s41586-022-05117-x` (cit. on p. 110).

[141] Adam R. Mills et al. “Two-Qubit Silicon Quantum Processor with Operation Fidelity Exceeding 99%”. In: *Science Advances* 8.14 (Apr. 6, 2022), eabn5130. DOI: `10.1126/sciadv.abn5130` (cit. on p. 110).

[142] C. H. Yang et al. “Operation of a Silicon Quantum Processor Unit Cell above One Kelvin”. In: *Nature* 580.7803 (7803 Apr. 2020), pp. 350–354. DOI: `10.1038/s41586-020-2171-6` (cit. on p. 110).

[143] Nico W. Hendrickx et al. “A Four-Qubit Germanium Quantum Processor”. In: *Nature* 591.7851 (7851 Mar. 2021), pp. 580–585. DOI: `10.1038/s41586-021-03332-6` (cit. on p. 110).

[144] R. Hanson et al. “Spins in Few-Electron Quantum Dots”. In: *Reviews of Modern Physics* 79.4 (Oct. 1, 2007), pp. 1217–1265. DOI: `10.1103/RevModPhys.79.1217` (cit. on p. 110).

[145] Xin Zhang et al. “Semiconductor Quantum Computation”. In: *National Science Review* 6.1 (Jan. 1, 2019), pp. 32–54. DOI: `10.1093/nsr/nwy153` (cit. on p. 110).

[146] Giordano Scappucci et al. “The Germanium Quantum Information Route”. In: *Nature Reviews Materials* 6.10 (10 Oct. 2021), pp. 926–943. DOI: `10.1038/s41578-020-00262-z` (cit. on pp. 110, 167).

[147] Félix Beaudoin et al. “Coupling a Single Electron Spin to a Microwave Resonator: Controlling Transverse and Longitudinal Couplings”. In: *Nanotechnology* 27.46 (Oct. 2016), p. 464003. DOI: `10.1088/0957-4484/27/46/464003` (cit. on p. 116).

[148] L. Childress, A. S. Sørensen, and M. D. Lukin. “Mesoscopic Cavity Quantum Electrodynamics with Quantum Dots”. In: *Physical Review A* 69.4 (Apr. 5, 2004), p. 042302. DOI: `10.1103/PhysRevA.69.042302` (cit. on p. 119).

[149] Damaz de Jong et al. “Rapid Detection of Coherent Tunneling in an In As Nanowire Quantum Dot through Dispersive Gate Sensing”. In: *Physical Review Applied* 11.4 (Apr. 19, 2019), p. 044061. DOI: `10.1103/PhysRevApplied.11.044061` (cit. on p. 120).

[150] K. D. Petersson et al. “Charge and Spin State Readout of a Double Quantum Dot Coupled to a Resonator”. In: *Nano Letters* 10.8 (Aug. 11, 2010), pp. 2789–2793. DOI: `10.1021/nl100663w` (cit. on p. 120).

[151] D. J. van Woerkom et al. “Microwave Photon-Mediated Interactions between Semiconductor Qubits”. In: *Physical Review X* 8.4 (Oct. 31, 2018), p. 041018. DOI: `10.1103/PhysRevX.8.041018` (cit. on p. 122).

[152] F. Borjans et al. “Resonant Microwave-Mediated Interactions between Distant Electron Spins”. In: *Nature* 577.7789 (7789 Jan. 2020), pp. 195–198. DOI: `10.1038/s41586-019-1867-y` (cit. on p. 122).

[153] Patrick Harvey-Collard et al. “Coherent Spin-Spin Coupling Mediated by Virtual Microwave Photons”. In: *Physical Review X* 12.2 (May 2, 2022), p. 021026. DOI: `10.1103/PhysRevX.12.021026` (cit. on p. 122).

[154] David Isaac Schuster. “Circuit Quantum Electrodynamics”. Doctoral Thesis. Yale University, 2007 (cit. on p. 127).

[155] Dany Lachance Quirion. “Dispositifs quantiques hybrides basés sur les systèmes de spins et les circuits supraconducteurs”. Université de Sherbrooke, 2018 (cit. on p. 128).

[156] A. Palacios-Laloy et al. “Tunable Resonators for Quantum Circuits”. In: *Journal of Low Temperature Physics* 151.3 (May 1, 2008), pp. 1034–1042. DOI: `10.1007/s10909-008-9774-x` (cit. on p. 129).

[157] Ireneusz Strzalkowski, Sharad Joshi, and C. R. Crowell. “Dielectric Constant and Its Temperature Dependence for GaAs, CdTe, and ZnSe”. In: *Applied Physics Letters* 28.6 (Mar. 15, 1976), pp. 350–352. DOI: `10.1063/1.88755` (cit. on p. 130).

[158] Anna Stockklauser. “Strong Coupling Circuit QED with Semiconductor Quantum Dots”. Doctoral Thesis. ETH Zurich, 2017. DOI: `10.3929/ethz-b-000259894` (cit. on p. 132).

[159] Tobias Sebastian Frey. “Interaction between Quantum Dots and Superconducting Microwave Resonators”. Doctoral Thesis. ETH Zurich, 2013 (cit. on p. 132).

[160] H. Linke et al. “Damage Induced by Plasma Etching: On the Correlation of Results from Photoluminescence and Transport Characterization Techniques”. In: *Applied Physics Letters* 66.11 (Mar. 13, 1995), pp. 1403–1405. DOI: `10.1063/1.113215` (cit. on p. 135).

[161] Yu. N. Drozdov et al. “Features of the Vapor-Phase Epitaxy of GaAs on Nonplanar Substrates”. In: *Semiconductors* 54.9 (Sept. 1, 2020), pp. 1147–1149. DOI: `10.1134/S1063782620090080` (cit. on pp. 138, 139).

[162] Sadao Adachi and Kunishige Oe. “Chemical Etching Characteristics of (001) GaAs”. In: *Journal of The Electrochemical Society* 130.12 (Dec. 1, 1983), pp. 2427–2435. DOI: `10.1149/1.2119608` (cit. on p. 138).

[163] Sheila G. Bailey, Geoffrey A. Landis, and David M. Wilt. "Chemical Etching and Organometallic Chemical Vapor Deposition on Varied Geometries of GaAs". In: Apr. 1, 1989 (cit. on p. 138).

[164] M. Reed, W. Kirk, and P. Kobiela. "Investigation of Parallel Conduction in GaAs/ AlxGa1-xAs Modulation-Doped Structures in the Quantum Limit". In: *IEEE Journal of Quantum Electronics* 22.9 (Sept. 1986), pp. 1753–1759. DOI: `10.1109/JQE.1986.1073155` (cit. on p. 142).

[165] C. M. Hurd et al. "Modeling Parallel Conduction in GaAs/AlxGa1xAs Heterostructures". In: *Journal of Applied Physics* 63.9 (May 1988), pp. 4706–4713. DOI: `10.1063/1.340126` (cit. on p. 142).

[166] Peter K. Day et al. "A Broadband Superconducting Detector Suitable for Use in Large Arrays". In: *Nature* 425.6960 (6960 Oct. 2003), pp. 817–821. DOI: `10.1038/nature02037` (cit. on pp. 147, 148).

[167] J. R. Waldrop. "Schottky-barrier Height of Ideal Metal Contacts to GaAs". In: *Applied Physics Letters* 44.10 (May 15, 1984), pp. 1002–1004. DOI: `10.1063/1.94599` (cit. on p. 152).

[168] S. Rochette et al. "Quantum Dots with Split Enhancement Gate Tunnel Barrier Control". In: *Applied Physics Letters* 114.8 (Feb. 25, 2019), p. 083101. DOI: `10.1063/1.5091111` (cit. on p. 159).

[169] A. Narla et al. "Robust Concurrent Remote Entanglement Between Two Superconducting Qubits". In: *Physical Review X* 6.3 (Sept. 6, 2016), p. 031036. DOI: `10.1103/PhysRevX.6.031036` (cit. on p. 166).

[170] D. L. Moehring et al. "Entanglement of Single-Atom Quantum Bits at a Distance". In: *Nature* 449.7158 (7158 Sept. 2007), pp. 68–71. DOI: `10.1038/nature06118` (cit. on p. 166).

[171] Sergei Studenikin et al. "Single-Hole Physics in GaAs/AlGaAs Double Quantum Dot System with Strong Spin–Orbit Interaction". In: *Semiconductor Science and Technology* 36.5 (Apr. 2021), p. 053001. DOI: `10.1088/1361-6641/abe42d` (cit. on p. 166).

[172] M. Benito, J. R. Petta, and Guido Burkard. "Optimized Cavity-Mediated Dispersive Two-Qubit Gates between Spin Qubits". In: *Physical Review B* 100.8 (Aug. 29, 2019), p. 081412. DOI: `10.1103/PhysRevB.100.081412` (cit. on p. 167).

[173] Yuta Tsuchimoto et al. "Large-Bandwidth Transduction Between an Optical Single Quantum Dot Molecule and a Superconducting Resonator". In: *PRX Quantum* 3.3 (Sept. 9, 2022), p. 030336. DOI: `10.1103/PRXQuantum.3.030336` (cit. on p. 167).